ISSN 1811-1165 (Print)
ISSN 2413-2179 (Online)

EURASIAN PHYSICAL TECHNICAL JOURNAL

VOLUME 21, NO. 4(50), 2024

phtj.buketov.edu.kz

EURASIAN PHYSICAL TECHNICAL JOURNAL

p - ISSN 1811-1165
e - ISSN 2413-2179

Volume 21, No. 4(50), 2024

1st issue – June, 2004

Journal Founder:

NLC "KARAGANDY UNIVERSITY OF THE NAME OF ACADEMICIAN E.A. BUKETOV

https://phtj.buketov.edu.kz

www.facebook.com/groups/1103109540750967

Registration Certificate No.4382-Zh, November 7, 2003.

Re-registration Certificate No.KZ50VPY00027647, October 6, 2020 issued by Information Committee of the Ministry of Information and Public Development of the Republic of Kazakhstan

Contact information:

Editorial board of EAPhTJ
(Build. 2, room 216)
Karaganda Buketov University
Universitetskaya Str.28, Karaganda,
Kazakhstan, 100024
Subscription index: 75240

Tel: +7(7212) 77-04-03
Fax: +7(7212) 35-63-98
E-mail: ephtj@mail.ru,
ephtj2021@gmail.com

Signed to print 24.12.2024
Format 60x84 1/8. Offset paper.
Volume 20.87 p.sh. Circulation 300 copies.
Order No. 143.

Printed in the Publishing House of
Karagandy University of the name
of academician E.A. Buketov

Tel. +7 (7212) 35-63-16.
E-mail: izd_karu@buketov.edu.kz

Eurasian Physical Technical Journal, 2024, Vol. 21, No. 4(50)

CONTENTS

PHYSICS AND ASTRONOMY

.

Dear authors and readers!
Dear colleagues!

Traditionally, in the preface we inform the authors and readers about the most important achievements of the Eurasian Physical Technical Journal as a peer-reviewed open access scientific journal indexed in the SCOPUS database and included in List 1 of the updated List of scientific publications recommended for publishing the main results of scientific works in 4 scientific areas.

In 2024, the indexing of the journal in the Scopus database continues. Eurasian Physical Technical Journal is included in the Q3 quartile in the Engineering direction with a 27 percentile.

As a result of work to optimize online services for editing and preparing articles for publication, the article format was changed in 2024. The interactive OJS journal website allows you to carry out all stages of preparing articles for publication online. When uploading an article, authors are asked to indicate desired and undesirable reviewers, which is a well-known practice of leading journals.

The 2024 was marked by several significant events for our Journal. This year marked 20 years since the publication of the first issue of the journal. In June, an online meeting of the editorial board of the journal was held, where participants, recalling the most important facts of its formation, discussed development prospects and proposals for further promotion of the journal at the international level. Since 2004, 655 articles by authors have been published, of which 37% are articles by foreign authors from more than 30 countries, 33% of the articles were prepared by authors from various universities in Kazakhstan, and 29% of the articles were prepared by employees of our university.

In 2024, along with the 3rd issue, a Special Issue was published, which contains selected articles from the participants of the 7th International Conference on Engineering Sciences and Technology ICEST2024 (Luxor, Egypt, https://ifsdl.org/icest2024/). The invited editors took part in the preparation of the Special Issue: Professor A.L. Kozlovskiy (Institute of Nuclear Physics of the National Nuclear Center of the Republic of Kazakhstan, Almaty) and Dr. Nouby M. Ghazaly, Secretary General of the Conference (Head of the International Foundation for Science and Development (IFSDL), Professor of the Higher Institute of Engineering and Technology El Minya, Egypt).

The year 2024 is marked by another anniversary event - on October 14, Doctor of Physical and Mathematical Sciences, Professor N.Kh. Ibrayev turned 70. Professor N.Kh. Ibrayev has been a permanent member of the editorial board since its foundation, and in the period from 2014 to 2016 he worked as the editor-in-chief. The main area of scientific activity of Professor N.Kh. Ibrayev is the dynamics of electronic excitations in condensed molecular media. As a result of the study of plasmonic effects in nanophotonics, Professor N.Kh. Ibrayev and his colleagues established the patterns of influence of gold and silver nanoparticles on allowed and spin-forbidden radiative transitions, on laser generation of dyes, etc.

Among more than 600 publications of Professor Ibrayev N.Kh. in domestic and foreign rating publications, 13 patents, several textbooks and 2 volumes of "Selected Works". The most valuable result of his multifaceted work is the Institute of Molecular Nanophotonics, the scientific director of which he has been since its inception. Now the structure of the institute includes 12 laboratories with unique electron microscopy equipment for fundamental and applied research in the field of nanotechnology, condensed matter physics, chemical physics. The main scientific areas include: photonics of complex molecular systems; nanoplasmonics: synthesis of nanostructures, plasmon-enhanced photoprocesses; dynamics of electron excitations in nanocomposite functional materials; nanostructured materials for solar and hydrogen energy; functional elements for quantum electronics and optical nanotechnology; synthesis and study of carbon and graphene quantum dots.

It's impossible to describe all the facets of Professor Ibrayev N.Kh.'s work as a scientist and teacher. But it is known that everything is done at a high professional level, which is noted by many state awards. He is winner of the state grant "Best University Teacher" (2006, 2011). Professor Ibrayev N.Kh. holds the title of author with high publication activity in Nature Springer journals (2017), was nominated as “Best

Researcher" (2022), "Most Cited Researcher in Engineering and Technologies" (Scopus Award, Elsevier, 2018), etc.

Ibrayev N.Kh. is actively involved in scientific and organizational activities, is a member of the National Scientific Council "Intellectual Potential of the Country" in the direction of "Natural Sciences". Chairman of the dissertation council for the defense of doctoral dissertations, under his supervision 7 candidate dissertations and more than 10 PhD dissertations were defended. His erudition and dedication to science and such qualities of a research scientist as creative initiative, hard work and desire to understand the laws of physics of complex phenomena at the micro and nano levels are a shining example for students and colleagues. Almost every issue contains articles by Professor Ibrayev N.Kh. or his students, which present new research results.

We wish Ibrayev Niyazbek Khamzinovich good health, creative ideas and great success in work, family well-being, happiness and inexhaustible enthusiasm!

Now let me move on to a brief description of the contents of this issue. The Materials Science section presents new original results on the study of the properties of various materials. The article by authors from Astana presents the results of a study of crystalline graphite powder as a radio-absorbing material in the ultra-high-frequency range. The review article in this section is devoted to the analysis of the influence of the parameters of thermal treatment and chemical modification processes, such as temperature conditions and duration, on the characteristics of synthesized carbon structures used as electrodes for lithium-ion batteries and supercapacitors. As a result of the research conducted by our university researchers, the effect of the Spiro-OMeTAD film thickness on the structural, electrical and transport properties of perovskite solar cells was studied. It was found that with a layer thickness of 260 nm, the efficiency of solar cells reaches its maximum value, and further increase in the layer thickness reduces their efficiency. In a joint paper by Tomsk and Kazakhstani authors, the possibility of synthesizing magnesium fluoride, barium fluoride and magnesium fluoride ceramics activated by tungsten was demonstrated by influencing the charge with an electron flow of a certain energy and power density. It was shown that in the process of radiation synthesis, tungsten enters the ceramics crystal lattice.

In articles in the Energy section, the authors discuss possible ways and methods for solving current problems based on modeling. The first article presents the results of modeling a Stirling engine taking into account temperature changes in the cooler and heater, under the condition of synchronous movement of the piston and the displacer. The possibility of increasing the engine power by reducing the hydraulic resistance in the regenerator is shown. The second article assesses the state of the operating parameters of power systems using telemetry and synchronized vector measurements. The method proposed by the authors improves the accuracy of estimating the voltage in the circuit nodes and active power flows in connections in normal and post-emergency modes.

The Engineering section offers solutions to current automation problems in modern technologies and control and monitoring systems. The article by Azerbaijani authors (Baku) examines the problem of controlling a vacuum technological complex, where the algorithm and principles of control are first applied to analyze the vacuum block of a specific "ELOU-AVT type primary oil refining unit." The proposed method and control algorithm allow "to promptly perform preliminary local correction of control modes, which can help ensure the stability of the quality of the target products obtained."

The article by the authors from the Ghalam Scientific Center (Astana) presents the results of designing, creating and testing a ground station for transmitting and receiving information for low-orbit nanosatellites for remote sensing of the Earth in the S-band using universal inexpensive SDR hardware platforms based on field-programmable gate arrays (FPGA) and microcircuit transceivers. The article by Russian authors shows the results of modeling "technological processes of drawing with wall thinning of hollow axisymmetric parts for various purposes", which in practice are carried out in fairly complex conditions with high loads. An example of "selecting technological conditions of friction and the degree of deformation in the process of drawing with thinning, ensuring the necessary monotony of the process" is given. The article by our university authors presents the results of research into "the features of the processes of squeezing liquid

through throttling holes". The effect of increasing the temperature of the liquid during throttling, which depends on the cross-sectional area of the annular layer of liquid in the heat-generating block, is established, which can contribute to improving the thermal characteristics of the system.

The Physics and Astronomy section features a paper by Nigerian authors that applies the exact quantization rule approach to the analytical solution of the radial Schrödinger equation, specifically by using the inverse square Yukawa potential class. Using this method, they successfully "predicted the mass spectra of heavy mesons over a range of quantum states using energy eigenvalues." "The energy spectrum decreased as the angular momentum quantum number increased in the case where the principal quantum number remained fixed" was found.

The paper by researchers from research centers in Almaty, Astana, and Karaganda is devoted to the problem of increasing the energy conversion efficiency of dye-sensitized solar cells. The authors offer for discussion the results of "GaN synthesis by plasma-enhanced chemical vapor deposition on sapphire and silicon substrates" under certain parameters.

The last two articles are devoted to solving problems of electron optics. In a joint study by authors from Aktobe and Ryazan (Russia), the effect of the width of the interelectrode gap on the focusing quality of electrostatic mirrors with rotational symmetry was investigated. The electrodes are coaxial cylinders of equal diameter, separated by gaps of finite width. Based on the calculations, the geometric and electrical parameters of two- and three-electrode mirrors were determined taking into account the width of the interelectrode gap, ensuring spatial focusing of beams of charged particles and improving the resolving power of mass spectrometers and electron microscopes. In the article by the Almaty authors, a "method for calculating the electrostatic field of multipole systems based on a conducting circular cylinder" was proposed. For the solution, a "method for solving integral equations with singular and quasi-singular kernels was used, ensuring high accuracy of field calculations for electron-optical systems with rectilinear boundaries."

We hope that the articles presented in this issue will be of interest to scientists, teachers, researchers, doctoral and master's students.

We would like to express our deep gratitude to our reviewers for their objective and highly qualified examination of the materials, which helped ensure the quality of the published articles.

We will be glad to see you among our readers and authors of the 2025 issues, in which it is planned to publish articles by leading scientists on the most relevant and priority areas of modern physics and technology.

With respect and best wishes for health and well-being to our authors and readers,

Editor-in-Chief, Professor Sakipova S.E.
December 2024

EURASIAN PHYSICAL TECHNICAL JOURNAL

2024, Volume 21, No.4 (50)

https://doi.org/10.31489/2024No4/7-13

Received: 25/06/2024 Revised: 26/10/2024 Accepted: 12/12/2024 Published online: 25/12/2024

Original Research Article

UDC 538.976

RADIO-ABSORBING MATERIALS BASED ON GRAPHITE PARTICLES IN EPOXY RESIN

Makhanov K.M.[1], Smagulov Zh.K.[2], Burambaeva N.A.[1], Assilbekova A.M.[1], Soldatkhan D.[1], Kuttybek A.A.[1], Suleimenova A.K.[1], Kenes T.K.[1], Kenesbekov S.E.[1], Serikova A.A.[1], Kenesbek B.Sh.[1]

[1] L.N. Gumilyov Eurasian National University, Astana, Kazakhstan

[2] E.A. Buketov Karaganda University, Karaganda, Kazakhstan

*Corresponding author: makanov@inbox.ru

Abstract. *This paper presents the results of a study on radio-absorbing materials in the ultra-high frequency range of 78-118 GHz. Crystalline graphite powder (particle size 0.1 mm) was considered as the main radio-absorbing material. Epoxy resin was used as a substrate and a binder. The samples were prepared by dispersing the graphite powder across the surface of the epoxy resin substrate. The most effective working thickness of epoxy resin has been established experimentally. The geometric dimensions of the arrangement of the installation components at which the most effective signal recording is observed are calculated. The results of the studies showed that a film consisting of graphite particles on the surface of epoxy resin effectively shields radio emissions in the 3-millimeter range.*

Keywords: Radio-absorbing materials, radio frequency range, electromagnetic wave absorption, graphite, attenuator, radio-frequency generator, calorimeter, horn antenna.

1. Introduction

The development of modern radio-electronic technology, especially in the field of ultra-high frequencies (microwave), has led to a global problem of electromagnetic pollution, which can have a negative impact on the operation of radio equipment. The number of different sources of electromagnetic radiation (EMR) is increasing, and the frequency range used is expanding. All this requires addressing issues related to protection from EMI across a wide frequency range [1].

Radio-absorbing materials (RAM), capable of absorbing or attenuating radio wave radiation, are one of the effective means of solving these problems [2]. Such materials include ferrites [2], metal alloys [3], graphite [4], carbon nanotubes [5] and others. Thus, the material can be manufactured using components capable of absorbing or reflecting radio waves. This work aims to develop and study radio materials that effectively absorb EMR in the range of 78 – 118 GHz. The radio materials being developed must satisfy the ratio of "high protection efficiency – low manufacturing costs."

The object of study is graphite particles embedded in the matrix of the binder material. The choice of the object of study is due to the presence of a large number of works devoted to the study of radiophysical parameters of graphite, the prospects of using graphite particles as fillers in the materials under study. In particular, the next stage of research will be devoted to the production of polymer films with fillers from graphite particles of different sizes.

ED-20 epoxy resin was used as the binder. Epoxy resin easily adheres to surfaces requiring emitted electromagnetic interference (EMI) protection and is resistant to various pressures applied to the surface [6]. However, the authors do not consider issues related to the thickness of the epoxy resin. Graphite particles were pre-mixed in a certain proportion in an epoxy resin solution. The film samples under study were obtained by applying a mixture of various volumes (5 ml, 10 ml, and 15 ml) onto glass substrates (9.5x6 cm), transparent in the radio range under consideration.

The determination of the film thickness was carried out by transforming the formula for calculating the volume ($V = abc$, $c = V/ab$), where V is the volume, a is the width, b is the length, and c = h is the thickness of the epoxy resin. The obtained sample thickness values for epoxy resin of various volumes: at V=5 ml, $h_1 = 0.8\ mm$; at V=10 ml, $h_2 = 1.7\ mm$; at V=15 ml, $h_3 = 2.6\ mm$.

2. Material and Methods

The experimental setup consists of a G4-183M signal generator, an AP-20 attenuator, two rectangular horn antennas, and an M1-25 M/03 calorimetric power meter. At the initial stage, work was carried out to determine the optimal relationship between the geometric parameters and frequency characteristics of the experimental setup. When studying the characteristics of radio-absorbing materials, it is necessary to first create conditions that provide the ability to perform various actions to increase the measuring capabilities of the device. For example, to ensure a change in the angle of incidence of the EMR, a change in the frequency of the generator, and the polarization of the electromagnetic wave entering the absorbing layer (material under study). To do this, the first few stages of measurements must be carried out in “empty space”, without objects of study.

An experimental setup was assembled in accordance with the aforementioned requirements. To maintain the stability of the instruments and their position at the same level, the generator and calorimeter were installed on special metal bases. A Standa rotary platform was used to rotate the test sample. The structural diagram of the experimental setup is shown in Figure 1.

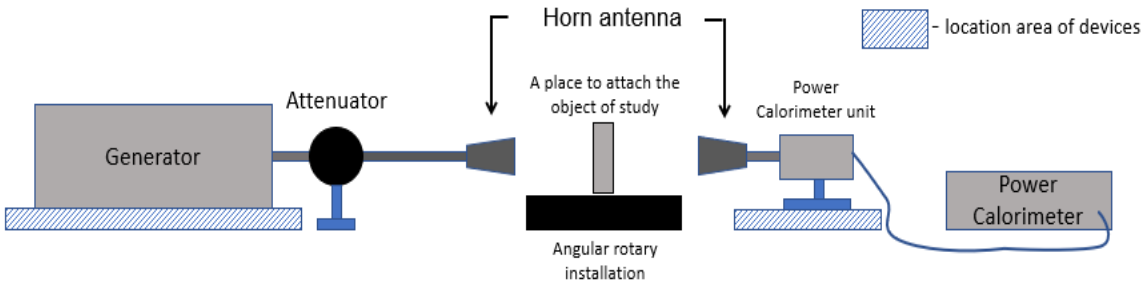

Fig.1. Structural diagram of the experimental setup

In the assembled installation, the angle between the transmitting and receiving horn antennas is small. Therefore, we first determined the radiation pattern of the horn antenna [7, 8]. The studies were carried out at a frequency of 98 GHz. The attenuation level (attenuator) of the original EMR was set to 5 dB. The rotation step of the receiving antenna corresponded to 3-5°.

The results of measurements in the E and H planes, obtained by changing the angle of the receiving antenna, are presented in Table 1.

Table 1. Results of measuring a horn antenna in the E and H planes

Angle		0°	5°	8°	10°	13°	15°	16°	20°
Signal power, dB	E	14.47	12.43	9.54	7.53	1	0	0	0
	H	15.71	14.59	10.21	9.21	6.98	3.01	1	0

The obtained values made it possible to construct a radiation pattern, as well as a 3D model of the antenna and diagram (Figure 2). All charts and graphs presented in the work were constructed using the OriginPro program and the Ansys HFSS environment. Based on the results obtained, the distances corresponding to the effective placement of equipment components were calculated depending on the size of the sample under study. The calculation results are presented in Table 2.

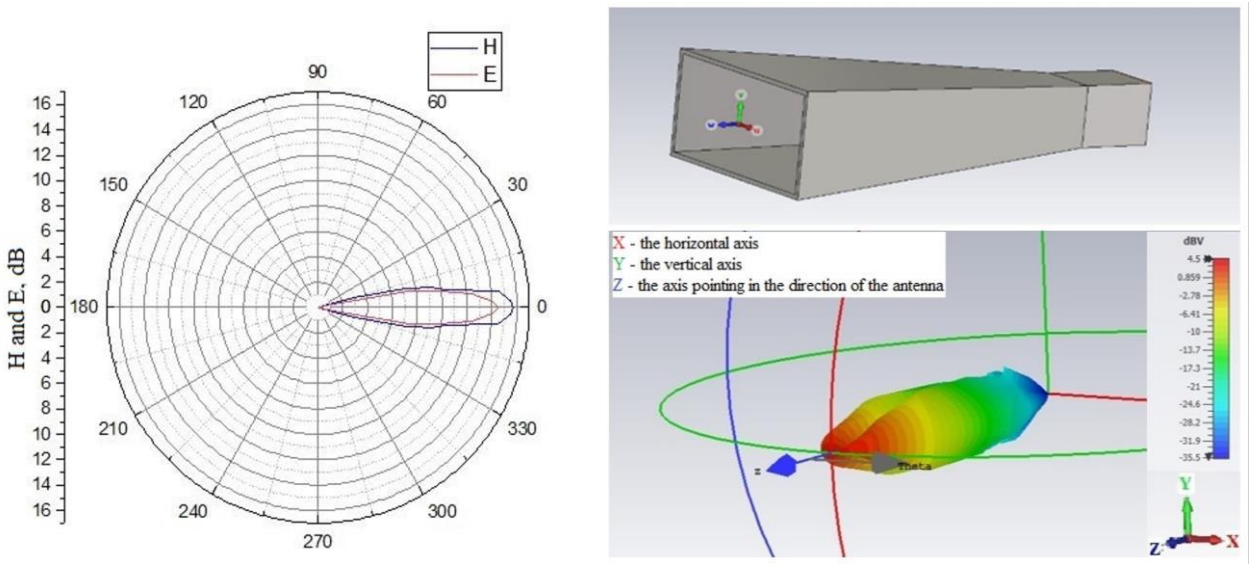

a) b)

Fig.2. Antenna radiation pattern in E and H planes (a), 3D antenna models and radiation patterns (b)

Table 2. Effective distance depending on the width and height of the object under study

Height, cm / Width, cm	4	5	6	7	8	9	10
4	4.66	6.82	8.99	11.15	13.32	15.48	17.65
5	4.71	6.82	8.99	11.15	13.32	15.48	17.65
6	6.46	6.82	8.99	11.15	13.32	15.48	17.65
7	8.20	8.20	8.99	11.15	13.32	15.48	17.65
8	9.95	9.95	9.95	11.15	13.32	15.48	17.65
	Effective distance, cm						

The results presented in Table 2 show the dependence of the distance between the antennas and the sample on the size of the sample itself. Changing the size of one of the sides of the object under study is accompanied by a mandatory adjustment of the distance between the sample and the antenna. This is necessary in order to cover the entire EMR propagation area and eliminate errors in the registration of the useful signal. Based on these results. a block diagram (Figure 3) of the location of the sample relative to the antennas was constructed. Subsequently, the installation was assembled according to this diagram.

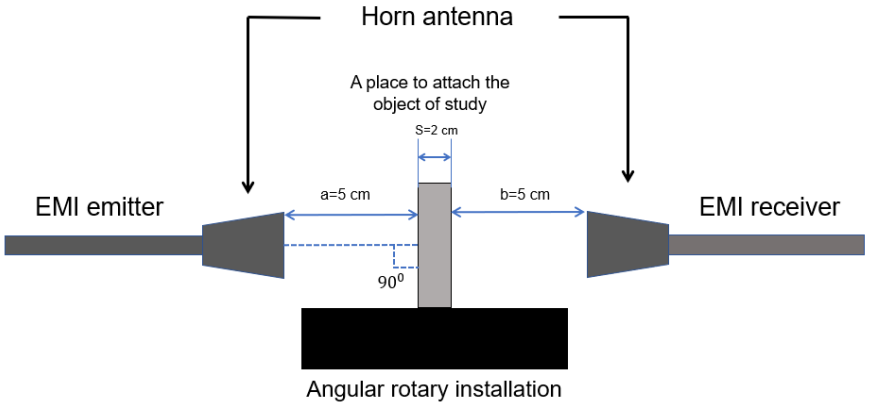

Fig.3. Structural diagram of the sample arrangement relative to the antennas

The distance between the horn antennas and the object was set in strict accordance with the calculation using a caliper. The assembled experimental setup allows for consistent measurements of both transmission and reflection coefficients. This is achieved by using an automated rotating platform (Standa) and a sample holder design. If it is necessary to change the nature of the experimental work, the overall design of the setup is not violated. Accordingly, there is no need for additional work on setting up the devices. The measured data from the recording part can be automatically transferred to a personal computer. Where, subsequently, they can be processed and saved in Excel format. Thus, at this stage, the work on constructing and assembling the experimental installation was completed. The radiation pattern was determined and the geometric position of the installation components relative to each other was calculated.

3. Experimental results and discussion

To establish a safe operating mode of the equipment, the "empty space" measurements were preliminarily carried out at different levels of signal attenuation. The level of attenuation of the power of the initial EMI was set to 25 dB. Then, the attenuator was sequentially opened with a step of 5 dB and the readings were taken from the display of the calorimetric meter. Registration of absorption coefficients was carried out at fixed frequencies of 78.5 GHz, 98 GHz and 118 GHz. Based on the measurement results, a graph of the dependence of the transmitted signal on the frequency and attenuation level of the initial EMI was constructed. The results were processed and presented in 3D format in Figure 4,a. We observe that the level of the emitted signal at the extreme frequencies is lower than the level at 98 GHz. This observed change in signal power is associated with the technical characteristics of the experimental equipment. It was also determined that an EMI attenuation level of 5 dB is the most optimal, as it allows measurements to be conducted without compromising the accuracy of results or the equipment's integrity. Subsequent measurements were conducted at this attenuation level.

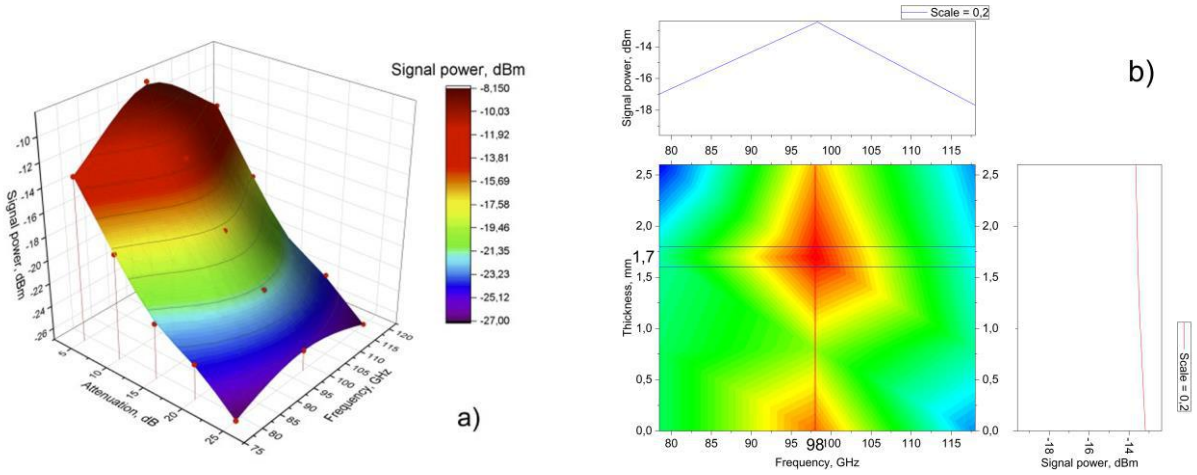

Fig.4. Recording "empty space" (a) and determining the most effective thickness of epoxy resin (b)

The next stage of the study focused on determining the absorption level of pure epoxy resin substrates of varying thicknesses. The purpose of this stage was to select the maximum thickness and determine its absorption properties to ensure that the substrate would not affect the research object. The measurements were carried out for films with a thickness of 0.8 mm, 1.7 mm and 2.6 mm, respectively. Registration was carried out at three discrete frequencies of 78.5 GHz, 98 GHz and 118 GHz. The results obtained are presented in Table 3.

Table 3. Measurement results of epoxy resin films of various thicknesses

f, MHz	Measurements, dBm			
	0 mm	0.8 mm	1.7 mm	2.6 mm
78500	-16.58	-16.58	-16.98	-19.59
98000	-13.19	-14.94	-12.37	-13.67
118000	-18.54	-16.98	-17.69	-18.54

A graphical representation of the dependence obtained after processing the data in Table 3 is shown in Figure 4b. A review of Figure 4b shows that the epoxy resin thickness of 1.7 mm is the most optimal. At this thickness, the substrate has a minimal effect on the magnitude of the EMI. Subsequently, when manufacturing the objects of study, we were guided by these results.

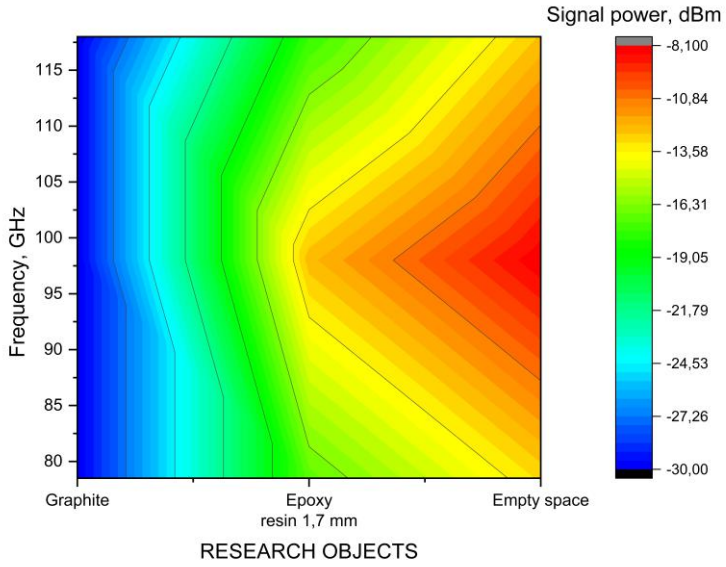

Fig.5. Comparison of study objects

The RAM was manufactured by blowing 10 mg of powdered graphite (grade GL-1) over the surface of the epoxy resin. Registration of the transmission coefficients of the EMI that passed through the samples was carried out at frequencies of 78.5 GHz, 98 GHz and 118 GHz. Figure 5 shows the results of comparing the data obtained for the case of "empty space" and epoxy resin with a thickness of 1.7 mm. From the figure we see that the registered signal that passed through the RAM corresponds to the value of -30 dBm. This indicates complete shielding of the EMI.

4. Conclusion

This study presents the results of measuring the transmission coefficient of graphite particles on the surface of epoxy resin. Signal registration was conducted at three different frequencies: 78.5 GHz, 98 GHz, and 118 GHz. It was determined that the most effective epoxy resin thickness is 1.7 mm, as this thickness has minimal impact on EMI levels across all tested frequencies. The results of experimental measurements of films of graphite particles on the surface of an epoxy substrate were obtained. The films were produced by dispersing 10 mg of graphite particles. The results demonstrated that the tested material completely shields EMI in the millimeter range.

Conflict of interest statement

The authors declare that they have no conflict of interest in relation to this research, whether financial, personal, authorship or otherwise, that could affect the research and its results presented in this paper.

CRediT author statement

Makhanov K.M.: Conceptualization, Methodology, Validation, Investigation, Writing - Original Draft; **Smagulov Zh.K.:** Methodology, Resources, Investigation; **Burambaeva N.A.:** Data Curation, Writing - Original Draft, Supervision; **Assilbekova A.M.:** Writing Review & Editing, Supervision; **Soldatkhan D.:** Development of Facility and Measurements; **Kuttybek A.A.:** Data Curation, Visualization; **Suleimenova A.K.:** Data Curation, Resources; **Kenes T.K., Kenesbekov S.E.:** Development of Facility and Measurements, Investigation, Visualization; **Serikova A.A., Kenesbek B.Sh.**: Investigation, Visualization.

The final manuscript was read and approved by all authors.

Funding

The work was performed as part of the state funding of the Science Committee of the Ministry of Science and Higher Education of the Republic of Kazakhstan (PTF No. BR24993017).

References

1 Ostrovsky O.S., Odarenko E.N., Shmatko A.A. (2003) Protective screens and absorbers of electromagnetic waves. *Physical Surface Engineering*, 1 (2), pp. 161-173. [in Ukrainian]. URL https://clck.ru/3EPCHv

2 Kryukov A.V., Eremeev A.S. (2020) New radio-absorbing flexible materials based on a carbon matrix with various synthetic fillers and evaluation of their absorption properties in the microwave range. *Radioelectronics. Nanosystems. Information Technologies*, 12 (3), pp. 335-340. DOI: 10.17725/rensit.2020.12.335. [in Russian]

3 Gorshenev V.N., Kolesov V.V., Fionov A.S., Erichman N.S. (2016) Multilayer coatings with variable electrodynamic characteristics based on filled polymer matrices. *Journal of Radio Electronics*, 11, pp. 9-9. eISSN: 1684-1719. URL https://elibrary.ru/download/elibrary_28432125_28668191.pdf. [in Russian]

4 Semenets V.V., Stytsenko T.E. (2016) A design of radiation-proof material for protecting the medical staff. *East European Journal of Advanced Technologies*, 2/5 (80), pp. 30-37. ISSN 1729-3774. DOI: 10.15587/1729-4061.2016.63753. [in Russian]

5 Bychanok D.S., Kanygin M.A., Okotrub A.V., Shuba M.V., Poddubskaya O.G., Plyushch A.O., Kuzhir P.P., Maksimenko S.A. (2011) Anisotropy of electromagnetic properties of polymer composites based on multiwall carbon nanotubes in the gigahertz frequency range. *J. Eth. Phys. Letters*, 93 (10), pp. 669-673. DOI: 10.1134/S0021364011100043. [in Russian].

6 Kuzhir P., Paddubskaya A., Bychanok D., Nemilentsau A., Shuba M., Plusch A., Maksimenko S., Bellucci S., Coderoni L., Micciulla F., Sacco I., Rinaldi G., Macutkevic J., Seliuta D., Valusis G., Banys J. (2011) Microwave probing of nanocarbon based epoxy resin composite films: Toward electromagnetic shielding. *Thin Solid Films*, 519 (12), pp. 4114-4118. DOI: 10.1016/j.tsf.2011.01.198.

7 Balanis C.A. (2016) *Antenna theory: analysis and design*. John wiley & sons. ISBN: 978-1-118-64206-1. URL https://books.google.kz/books?id=iFEBCgAAQBAJ

8 Pogrebnoy A. A., Nikitin D. M., Moroz F. V., Maltsev A. N., Poberezhny I. A., Sviridov A. N. (2016) Measurement of the radiation pattern of a two-mirror Cassegrain antenna and calculation of the gain of the studied antenna from the measured radiation pattern. *Young Scientist*, 13 (117), pp.196-200. ISSN 2072-0297. URL https://moluch.ru/archive/117/32396/ [in Russian]

AUTHORS' INFORMATION

Makhanov, Kanat M. – Candidate of Physical and Mathematical Sciences, Senior Lecture, Department of Radio Engineering. Electronics and Telecommunications, L.N. Gumilyov Eurasian National University, Astana, Kazakhstan; Scopus Author ID: 57217354220; https://orcid.org/0000-0002-1263-0734; makanov@inbox.ru

Smagulov, Zhanaidar K. – Candidate of Technical sciences, Associate Professor, E.A. Buketov Karaganda University, Karaganda, Kazakhstan; Scopus Author ID: 35193461600; https://orcid.org/0000-0001-8829-2527, smagul@mail.ru

Burambaeva, Nursaule A. – Candidate of Technical Sciences, Professor, Department of Radio Engineering, Electronics and Telecommunications, L.N. Gumilyov Eurasian National University, Astana, Kazakhstan; Scopus Author ID: 56719699800; https://orcid.org/0000-0003-3029-6474; nursaule.burambaeva.54@mail.ru;

Assilbekova, Aliya M. – Master, Lecture, Department of Radio Engineering. Electronics and Telecommunications, L.N. Gumilyov Eurasian National University, Astana, Kazakhstan; Scopus Author ID: 57202753353; https://orcid.org/0000-0001-5254-5174; asylaliya@yandex.kz

Soldatkhan, Dauren - PhD, Senior Lecture, L.N. Gumilyov Eurasian National University, Astana. Kazakhstan; Scopus Author ID: 57768566200; https://orcid.org/0000-0001-7981-4100; soldathan.dauren@mail.ru;

Kuttybek, Azhar A. - Master, Lecture, Department of Radio Engineering, Electronics and Telecommunications, L.N. Gumilyov Eurasian National University, Astana, Kazakhstan; https://orcid.org/0009-0002-3377-7003; kuttybek.azhar@mail.ru

Suleimenova, Assemgul K. – Master, Lecture, Department of Radio Engineering. Electronics and Telecommunications, L.N. Gumilyov Eurasian National University, Astana, Kazakhstan; https://orcid.org/0009-0005-0280-1148; assemgi1001@gmail.com;

Kenes, Timur K. – Master, Lecture, Department of Radio Engineering. Electronics and Telecommunications, L.N. Gumilyov Eurasian National University, Astana, Kazakhstan; https://orcid.org/0009-0002-7748-0551; timur.kasymuly@mail.ru;

Kenesbekov, Sultan E. – Master, Lecture, Department of Radio Engineering. Electronics and Telecommunications, L.N. Gumilyov Eurasian National University, Astana, Kazakhstan; https://orcid.org/0009-0000-9008-3070; sulaisstambula@mail.ru;

Serikova, Azhar A. – Master, Lecture, Department of Radio Engineering. Electronics and Telecommunications, L.N. Gumilyov Eurasian National University, Astana, Kazakhstan; https://orcid.org/0009-0002-2015-0033; serikovaazhar.0129@mail.com

Kenesbek, Begis Sh. – Master, Lecture, Department of Radio Engineering. Electronics and Telecommunications, L.N. Gumilyov Eurasian National University, Astana, Kazakhstan; https://orcid.org/0009-0003-3828-0351; begis.kenesbek@mail.ru

EURASIAN PHYSICAL TECHNICAL JOURNAL

2024, Volume 21, No.4 (50)

https://doi.org/10.31489/2024N4/14-22

Received: 04/07/2024 Revised: 29/10/2024 Accepted: 12/12/2024 Published online: 25/12/2024

Review Article

UDC 537.22:544.6.076.324.2:546.26 + 621.352.6 + 621.319.4

OVERVIEW OF CARBON MATERIALS FOR USE IN LITHIUM-ION BATTERIES AND SUPERCAPACITORS

Dyussembayev M.[1,4], Khabiyev A.[2,4*], Rafikova Kh.[2,4], Afanasyev D.[3]

[1] Kazakh-British Technical University, Almaty, Kazakhstan
[2] Kazakh National Research Technical University named after K.I. Satpayev, Almaty, Kazakhstan
[3] E.A. Buketov Karaganda University, Karaganda, Kazakhstan
[4] U.A. Joldasbekov Institute of Mechanics and Engineering
*Corresponding author: a.khabiyev@satbayev.university

Abstract. *This review article focuses on the study of carbon materials utilized as electrodes in lithium-ion batteries and supercapacitors. The research examines three primary categories of materials: activated carbon, carbon aerogels, and nanoporous carbon. The article provides a comprehensive explanation of the operational principles of many types of capacitor systems, such as double-layer electrochemical capacitors, pseudo capacitors, and hybrid capacitors. The carbon materials under discussion are thoroughly examined with a focus on their synthesis processes, structural features, and electrochemical properties. The study investigates the impact of pore structure, surface area, and the presence of functional groups on electrode performance. The impact of heat treatment and chemical modification techniques on the properties of synthesized carbon structures has been investigated, specifically examining parameters such as temperature and duration. The text examines the benefits and drawbacks of each material type, taking into account their individual capacity, cyclical stability, and economic efficiency. The study emphasizes the importance of precise adjustment of the synthesis process to enhance the electrochemical characteristics and showcases the possibility of employing these materials in sophisticated energy storage devices. This review serves as a crucial resource for experts engaged in developing cutting-edge materials for lithium-ion batteries and supercapacitors. It also highlights potential topics for future research in the realm of electrochemical energy storage.*

Keywords: lithium-ion battery, supercapacitor, carbon materials, activated carbon, carbon aerogel, nanoporous carbon.

1. Introduction

In the present era, energy technologies are increasingly becoming essential components of both everyday living and several industrial sectors. Lithium-ion batteries and supercapacitors are essential for the storage and utilization of electrical energy, serving as sophisticated electrochemical devices. The efficacy of energy storage and transmission significantly impacts the advancement of contemporary mobile gadgets, electric transportation, and renewable energy sources.

The choice of materials for electrodes plays a vital role in determining the effectiveness of these technologies. This paper offers a comprehensive examination of three primary categories of carbon materials

- activated carbon, carbon aerogels, and nanoporous carbon - focusing on their electrochemical characteristics and potential applications in lithium-ion batteries and supercapacitors.

One category of materials is activated carbon. Activated carbon possesses exceptional electrical conductivity, resistance to corrosion, and affordability as a result of its substantial specific surface area and porous configuration. This article analyses the methods of synthesizing activated carbon-based electrodes, their structural properties, and the impact of activation conditions on their efficiency. Carbon aerogels, a significant category of materials, possess exceptional characteristics in terms of both their lightweight nature and structural strength. An analysis is conducted on the electronic conductivity of carbon aerogels, as well as their potential for increased capacity upon activation. Additionally, this article presents surface modification techniques that are designed to enhance the electrochemical properties of the electrodes.

Nanoporous carbon, which is classified as a third-class material, is formed by carbides. These new materials should be given attention in the development of effective electrodes for supercapacitors and lithium-ion batteries since they have a high specific surface area and porosity. A study was conducted to investigate the impact of temperature, chlorination duration, and synthesis time on the structural features and electrochemical properties of nanoporous carbon.

2. Condenser systems

The Leiden Jar, founded in 1745, is the fundamental model for contemporary electrolytic capacitors. Capacitors are ubiquitous in modern electronic devices and have applications across various domains of electrical engineering. In recent times, a multitude of novel capacitors have been created that function by diverse electrochemical mechanisms. Supercapacitors, sometimes referred to as electrochemical capacitors that utilize the charge energy of a double electric layer (DEL), are rapidly advancing in the realm of contemporary energy storage devices [1]. Electrochemical capacitors, as defined by Brian Evans Conway, are devices that undergo quasi-reversible electrochemical charge-discharge operations. The galvanostatic charge-discharge curves of these devices exhibit a nearly linear shape, indicating that their dependencies are comparable to those of ordinary electrostatic capacitors [2].

Electrochemical supercapacitors function as a bridge between dielectric capacitors, which have the ability to rapidly release a significant quantity of energy, and batteries, which have the capacity to store a substantial amount of energy. Supercapacitors (SC) can be used to complement or replace batteries in situations of high consumption and energy usage. These devices exhibit a greater efficiency in terms of energy conversion or uptake compared to batteries, while they possess a lower energy density. Supercapacitors are essential for controlling and balancing the load, as well as for supplementing or substituting batteries in situations that demand uninterrupted power supply, which is referred to as compensatory power supply [3].

Based on the manner of energy storage, supercapacitors are categorized into distinct classes, each with its own operating principles. These classes include capacitors with a double electric layer, pseudo-capacitors, and hybrid capacitors. Currently, the prevailing devices are capacitors equipped with a dual electric layer. These devices produce energy by creating an electric charge on highly porous materials in the active section of the electrodes. These devices do not experience oxidation/reduction events, which are referred to as Faraday processes. Instead, the charge builds up in pseudo capacitors or redox supercapacitors as a result of fast and reversible reactions that occur on the surface or near the surface. However, both batteries and pseudo capacitors frequently lack enough stability during cycling as a result of redox processes.

Hybrid capacitors are a novel integrated circuit (IC) that merges a battery electrode with either a capacitive or pseudo-capacitive electrode. These capacitors have the characteristics of both a capacitor and a battery. Capacitors can be categorized as symmetrical or asymmetrical based on the design of the cell [4].

2.1 Double-layer electrochemical capacitors

In 1957, Becker initially described the concept of DEL SC in a patent [5]. N.S. Lidorenko spearheaded the creation of the domestic DEL SC at the All-Union Scientific Research Institute of Current Sources. The devices were referred described as "molecular energy storage devices".

The charge builds up in the capacitors of the double electric layer as a result of the reversible adsorption of electrolyte ions by stable electrochemically active materials with a large specific surface area. During polarization at the electrode-electrolyte interface, there is no transfer of charge across the boundary between the electrode and the electrolyte. The charge mechanism involves the surface dissociation of the electrolyte and the adsorption of ions from the solution into the pores of the electrode. Consequently, there is either an

abundance or a deficiency of charge on the electrode's surface. Simultaneously, ions of opposite charge migrate towards the interface between the electrode and the electrolyte to uphold electroneutrality [6].

Helmholtz formulated the initial hypothesis regarding a double electric layer and drew a parallel between the double electric layer and a planar capacitor. Gui-Chapman, Stern, and Grem provided additional support for the concept [7].

During the charge-discharge cycle of supercapacitors, Faraday processes are absent. Instead, energy is solely accumulated by the electrostatic charges present on the opposing surfaces of the double electric layer. Consequently, these devices have the ability to operate for an extended period without experiencing a decrease in active mass, a phenomenon commonly seen in chemical power sources [8]. Although the electrochemical processes in secondary current sources are irreversible, the active mass of the electrodes is steadily diminishing. Therefore, the number of charge/discharge cycles that a battery can undergo during its lifespan varies, ranging from several thousand cycles, depending on the specific type of battery. The DEL SC exhibits excellent reversibility and may undergo a cyclic life of 10^5-10^6 cycles without forming new phases or intercalating [9]. The system exhibits quick charge and discharge capabilities with large currents, as it is not affected by polarization issues.

Figure 1 illustrates the structure of symmetrical double-layer electrochemical capacitors, which have two electrodes immersed in an electrolyte and separated by a membrane or separator. Separators are commonly employed in the utilization of diverse polymers, paper, or fiberglass. The electrodes consist of metal current collectors, often composed of aluminum or stainless steel, that have an active mass placed onto them. The active mass comprises a binder and a carbon substance with a highly developed surface. An electrically conductive additive, sometimes referred to as soot, may be added to the active mass in certain circumstances.

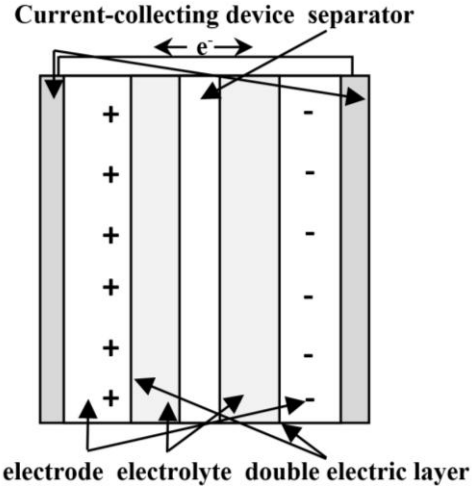

Fig.1. Schematic representation of double electric layer supercapacitor

The electrochemical process in DEL SC can be represented as follows:

- The positive electrode $E_s + A^- \leftrightarrow E_s^+ \parallel A^- + e^-$;
- Negative electrode $E_s + K^+ + e^- \leftrightarrow E_s^- \parallel K^+$;
- Total reaction $E_s + E_s + K^+ + A^- \leftrightarrow E_s^- \parallel K^+ + E_s + \parallel A^-$.

The surface of the electrode is denoted as Es, and there is a double electric layer, represented by ||, where charge accumulates on both sides of the electrode. The cations and anions of the electrolyte are denoted as K^+ and A^-, respectively [10]. When the integrated circuit is charged, the electrons are facilitated by the external environment to travel from the positive electrode to the negative electrode. The ions migrate towards the electrodes from within the electrolyte. Due to the load during discharge, electrons migrate from the negative electrode to the positive electrode, while ions reenter the electrolyte's volume and return to the surface. The electrolyte-impregnated separator prevents a short circuit between the electrodes while the supercapacitor is charged or discharged, while still allowing the passage of cations and anions. The charge density and electrolyte concentration fluctuate during the process of charging and discharging. The capacitance of a capacitor is determined by the surface area of its plates and the separation distance between them.

$$C = \frac{\varepsilon_0 \varepsilon S}{d}, \quad (1)$$

where ε_o is the dielectric constant, ε is the relative permittivity, S is the surface area of the lining, d is the distance between the plates, C is the capacitance of the capacitor.

In the design of a supercapacitor, the distance between the electrodes is equivalent to the thickness of the double electric layer, which is similar in size to the dimensions of molecules. The magnitude of this value is roughly a few angstroms, contingent upon the dimensions of the ions and the concentration of the electrolyte. The capacitance of these capacitors is significantly lower compared to electrolytic capacitors that utilizes aluminum foil, in which a thin oxide film on the metal surface acts as a dielectric (with a thickness of approximately 10 nm). Furthermore, the utilization of contemporary carbon materials with a substantial specific surface area (ranging from 1500 to 2500 m^2/g) enables the attainment of the most extensive surface area for the lining of the capacitor [11].

Figure 1 depicts a SC model comprising two capacitors connected in series. The porous electrodes facilitate the formation of electrical layers that enable current collection. The reason for this is that the ion layer created in the liquid at the interface serves as one of the plates of the supercapacitor. However, it is challenging to get a current collector with such characteristics from the liquid. The formation of the double electric layer occurs on a non-uniform surface, and not all parts of the electrode are equally accessible for wetting with electrolyte [12]. Currently, one of the key areas of research is the investigation of the relationship between the SC capacitance and the features of the electrode surface, including wettability, zero charge potentials, and the presence or absence of functional groups [13].

2.2 Pseudocapacitors

Pseudo capacitors are distinct from double-layer capacitors in that their capacitance is influenced by both electrostatic mechanisms and rapid Faraday reactions involving charge transfer. In this scenario, the active materials' surfaces undergo reversible redox reactions, resulting in "pseudo-intensive" behavior. The operation basis of capacitors of this sort involves the combination of two energy conservation mechanisms: electrostatic contact, which is comparable to what happens in capacitors with a double electric layer, and Faraday reactions, which are similar to what happens in batteries and accumulators [14].

Pseudo capacitor electrodes undergo a variety of Faraday processes, including those that are repeatable.

- For instance, the process of depositing lead or hydrogen onto the surface of titanium or aluminum, as well as the occurrence of redox processes involving transition metal oxides.
- For instance, compounds such as IrO_2, RuO_2, and different combinations of oxides [15] can be used.
- Additionally, electrodes made from conductive polymers can undergo repeated electrochemical doping and dedoping procedures [16].

Ruthenium oxide-based pseudo capacitors exhibit a substantial capacity; nevertheless, their practical application is constrained by the exorbitant cost of the constituent raw ingredients. Experiments are carried out utilizing inexpensive substances such as iron, vanadium, nickel, cobalt, and manganese oxides [17]. Interest in carbon materials that utilize a charge accumulation mechanism in a double electric layer is justified due to their increased pseudo-capacity. However, both batteries and pseudo capacitors are frequently regarded as unstable during cycling as a result of redox processes [18].

2.3 Hybrid capacitors

Hybrid systems employ a solitary electrode with a "Faraday function" rather than two carbon electrodes that are identical, in contrast to double-layer electrochemical capacitors. Asymmetric hybrid supercapacitors possess two primary benefits. One reason is the higher specific energy resulting from the battery electrode, and another one is the higher specific power resulting from the capacitor type electrode [19]. When employing a non-polarizable electrode, the voltage of an individual component rises, resulting in an expansion of the operational voltage range. Removing the second capacitor that is linked in series in an equivalent circuit enhances the overall electrical capacitance of the capacitor. This combination of adjustments enhances the specific energy by a factor of two to five when compared to a symmetrical design. An advantage of an asymmetric system is its low self-discharge rate. This is due to the presence of only one carbon electrode in the cell, as opposed to two in a symmetrical capacitor. The carbon electrode is primarily responsible for the self-discharge in the system [20].

Hybrid capacitors encompass the subsequent systems:

- Examples of metal oxides used with aqueous electrolyte solutions include NiOOH|KOH|C [21] and $PbO_2|H_2SO_4|C$ systems. Regarding the latter system, the overall reaction can be expressed as follows:

$$PbO_2 + 2H_2SO_4+(H^+)_{ad}/e \leftrightarrow PbSO_4+2H_2O+(HSO_{4-})_{ad}/-e.$$

The DES (Dual Energy Storage) system undergoes recharging at the negative electrode [22].

Graphite [4], $LiMnO_2$, $Li_2\ MnSiO_4$, $Li_4Ti_5O_{12}$, and other related compounds have the ability to reversibly intercalate lithium ions in non-aqueous electrolytes. These systems closely resemble normal lithium-ion systems. One instance is the suggestion of a hybrid electrode utilizing nanostructured β-Fe OOH [23]. The development of hybrid systems has resulted in the creation of novel electrode materials for lithium-ion batteries. As an illustration, the system consists of nanostructured $Li_4Ti_5O_{12}$ and a positive electrode composed of activated carbon [24]. Figure 2 illustrates the operational principle of these systems.

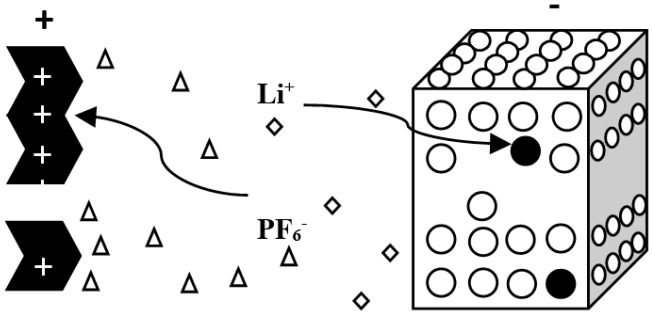

Fig.2. Schematic representation of a hybrid integrated circuit [24]

The lithium titanate electrode offers high power output without the formation of a "solid electrolyte" layer. Furthermore, $Li_4Ti_5O_{12}$ exhibits minor changes in volume during the charging/discharging process, making it highly resistant to cycling [25]. Following the examination of $Li_4Ti_5O_{12}$, numerous subsequent experiments were carried out utilizing different combinations of lithium-containing electrodes in conjunction with capacitive carbon electrodes. The emergence of nanomaterials and significant advancements in lithium-ion battery technology are expected to drive the creation of high-performance hybrid supercapacitors. These supercapacitors will utilize a lithium-containing electrode to enable fast charging and discharging.

3. Materials of DEL SC electrodes

Carbon's distinctive chemical and physical properties make carbon compounds appealing for use as electrodes. The properties of this material encompass excellent conductivity, resistance to corrosion, stability under high temperatures, the capacity to regulate the porous structure, affordability, eco-friendliness, and potential for utilization in composite materials. Double layer charging enables the utilization of electrodes that possess highly advanced characteristics such as specific surface area, open porosity, electronic conductivity, and electrochemical stability. This allows for the attainment of a high and reversible capacitance. Currently, ongoing research involves the utilization of activated carbons, nanoporous carbon derived from carbides, carbon fabric, nanotubes and nanofibers, spheroidal carbon structures, aerogels, and other materials [26].

3.1 Activated carbon

Activated carbons (AC) are widely used materials due to their abundant availability, large surface area, and affordable price. Various affordable and readily available raw materials such as rice husks, coconut fibre, sunflower cake [27], animal bones, apricot kernels, straw [28], etc., can be utilized for the manufacturing. The two prerequisites for eliciting a response from an asynchronous machine are carbonation and activation. Conversely, carbonation refers to the transformation of organic matter into carbon through the application of heat in an oxygen-free environment. During the carbonization process, hydrolysis occurs, resulting in the creation of graphite plane pieces. The temperature ranges from 300 to 500 °C. During the carbonization process, it may be necessary to use elevated temperatures, such as 600-1000 °C. The temperature at which carbonation occurs has a significant impact on the composition and arrangement of coal (table 1).

Table 1. Properties of carbon materials after their processing.

Method	Result
Oxidation in the liquid phase (by oxygen-containing acids)	An increase in surface area and porosity, a decrease in density, an increase in the concentration of surface functional groups.
Oxidation in the gas phase (O_2, H_2O)	An increase in surface area and porosity, a decrease in density, an increase in the concentration of surface functional groups.
Plasma treatment	Increased surface area and porosity, improved wettability, increased concentration of surface functional groups, reduced electrical resistance, increased electrocatalytic activity for the oxygen reduction process.
Heat treatment in an inert environment (argon, nitrogen)	Increase in surface area and porosity, increase in density, decrease in the concentration of surface functional groups, increase in the degree of graphitization.

Functional groups have the ability to influence several characteristics of the supercapacitor, such as the rate at which it discharges on its own, the ability of the electrode to absorb the electrolyte, the resistance at the contact points, and the angle at which the electrolyte wets the electrode surface. Functional groups present at the interface of coal, electrolyte, and current collector might induce chemical reactions, resulting in self-discharge currents and degradation of the electrolyte. Faraday reactions occurring in symmetrical capacitors of the double electric layer typically result in a reduction in the cyclic lifespan of the system. The surface of activated carbon materials may contain functional groups that contain oxygen and hydrogen, small amounts of sulphur, nitrogen, halides, and remnants of organic precursors resulting from incomplete carbonation.

3.2 Carbon Aerogel

Carbon aerogel-based supercapacitors have gained significant popularity. This material possesses exceptional characteristics of both lightness and strength, making it highly distinctive. Additionally, it exhibits an extraordinarily porous surface with a surface area ranging from 400 to 2000 square meters per gramme (m^2/g). Aerogels can be produced through the pyrolysis of formaldehyde polycondensation products. The porosity structure of aerogels is determined by modifications in the parameters of the polycondensation process. Aerogels are solid, film-like structures composed of interconnected polymer chains. After pyrolysis, the polymer chains undergo a transformation and are converted into carbon, while maintaining the same structure. Aerogel exhibits a considerably greater level of electronic conductivity compared to activated carbon. Upon activation of the aerogel, there is a significant increase in surface area, resulting in a corresponding rise in capacity. Nevertheless, the holes generated during the activation phase can be excessively narrow for the electrolyte to reach. The literature also presents information regarding the potential for altering the surface of activated aerogel. This modification enhances the ability of the material's pores to be wetted by electrolyte, resulting in improved electrochemical properties of the supercapacitor [29].

3.3 Nanoporous carbon

Nanoporous carbon, also known as NPC or CDC-carbide generated carbon, is a novel carbon material characterized by its exceptionally large specific surface area and porosity. These properties make it highly appropriate for utilization in the electrodes of double-layer supercapacitors and hybrid SC systems. NPC is produced through the process of chlorinating carbides of elements like Al, Ti, B, Si, Mo. This involves exposing the carbides to a continuous flow of chlorine while heating them to a temperature range of 600-1200 °C. In this reaction, the metal is separated from the carbide as a result of the creation of chlorides that have a low boiling point. The carbon rearranges itself into structures that are predominantly amorphous, disordered, and composed mostly of sp^2 bonds.

For example, for titanium carbide: $TiC + 2Cl_2 \rightarrow C + TiCl_4\uparrow$.

For aluminum carbide: $Al_4C_3 + 6Cl_2 \rightarrow 3C + 4AlCl_3\uparrow$.

The pore size is determined by the composition of the original carbide and can be modified through technological means such as adjusting temperature or chlorination duration. The surface area of these materials, as determined by the BET technique, ranges from 1000 to 2000 m^2/g. Micropores, with a size

ranging from 0.7 to 1 nm, mostly develop at a temperature of 800 °C. Mesopores, with a size ranging from 2 nm, are also generated under the same temperatures. As an illustration, the NPC derived from TiC had a pore size ranging from 0.7 to 1.1 nm, and a specific surface area (S_{BET}) of 1000-1600 m^2/g. Simultaneously, the specific surface area exhibited an increase as the average pore size decreased.

The scientists from the University of Tartu conducted research where they acquired and examined the characteristics of NPC that were synthesized from various carbides, including TiC, Al_4C_3, B_4C, α-SiC, MO_2C, VC, WC, TaC, NbC, HfC and ZrC. The nanoporous materials derived from vanadium, niobium, tantalum, hafnium, and zirconium carbides exhibit optimal characteristics for use in DES supercapacitors, owing to the favorable ratio between nanopore dimensions and surface area. Simultaneously, the surface area of tantalum carbide NPC (2275 m^2/g) ranks among the greatest among nanoporous carbons [30].

Considering the high cost and limited availability of these materials, as well as the combination of surface area and pore size, the most appropriate mass electrical material is NPC derived from titanium carbide at temperatures ranging from 700 to 900 °C.

It is important to mention that, similar to the materials mentioned earlier, not all holes of nanoporous carbon are suitable for usage with solvents. As a consequence of the electrolyte's inability to moisten some pores, a portion of the surface may stay inactive. Therefore, the computed capacity of the double layer on a highly porous carbon material does not align with the real value. Deviation in the incomplete wetting of pores can typically be attributed to the presence of numerous flaws, closed pores, a disordered structure, and surface heterogeneity. To enhance the electrochemical characteristics of the completed supercapacitor, it is imperative to select carbon materials that possess an appropriate porosity configuration for the specific electrolyte. In order to achieve complete infiltration of ions into the electrode's pores and the creation of a deep eutectic solvent, it is necessary for the minimum radius of the pores to align with the significant dimensions of the electrolyte ions. In order to generate a concentrated and spread out section of the double electric layer, it is imperative to augment the size and surface area of the active pores. The presence of larger mesopores also plays a role in the formation of DEL.

4. Conclusions

Ultimately, the authors stress the necessity for additional investigation to optimize the efficiency of carbon material synthesis for the purpose of attaining superior electrochemical characteristics. The article discusses the potential of carbon materials in lithium-ion batteries and supercapacitors, emphasizing the need for a careful balance between specific surface area, porosity, and structural stability in order to develop efficient electrodes. This review article not only provides information for present researchers, but also highlights essential issues for future research focused on creating novel materials for sophisticated electrochemical devices like lithium-ion batteries and supercapacitors.

Conflict of interest statement

The authors declare that they have no conflict of interest in relation to this research, whether financial, personal, authorship or otherwise, that could affect the research and its results presented in this paper.

CRediT author statement:

Dyussembayev M.Sh.: writing—original draft preparation; Khabiev A.T.: supervision; Rafikova Kh.S.: Conceptualization; Afanasyev D.A.: writing—review and editing.

The final manuscript was read and approved by all authors.

Funding

This study was funded by the Committee on Science of the Ministry of Science and Higher Education of the Republic of Kazakhstan (grant AP22783377 of the Ministry of Education and Science of the Republic of Kazakhstan).

References

1 Truong T.T.T., Le. L.T.M., Tran M.V., Vu P.T., Phung Q., Truong D.Q., Le P.M.L. (2004) Conventional supercapacitor electrolytes: aqueous, organic, and ionic. *Supercapacitors,* 245 – 265. DOI: 10.1016/b978-0-443-15478-2.00010-3.

2 Ding R., Chagnot M., Saeed S., Augustyn V. (2023) Nanostructured materials for electrochemical capacitors. *In Comprehensive Inorganic Chemistry*, Part III. Elsevier, 570. DOI: 10.1016/b978-0-12-823144-9.00128-x.

3 Mandal M., Chattopadhyay K., Mitra A., Haider D. (2024) 4.16-Micro-supercapacitors based on thin films: Journey so far. *Comprehensive Materials Processing*, Elsevier, 418. DOI: 10.1016/b978-0-323-96020-5.00092-3.

4 Callahan C.L., Cameron A.P., Forghani M., Donne S.W. (2024) Analysis of voltametric data from electrochemical capacitor electrode materials: Method refinement for improved outcomes. *Electrochimica Acta*, 475, 143619. DOI: 10.1016/j.electacta.2023.143619.

5 Sammed K.A., Farid A., Mustafa S., Kumar A., Tabish M., Khan A.A., Ajmal S., Mo Z., Akbar A.R., Yasin G., Zeng Y.J., Zhao W. (2023) Developing next-generation supercapacitor electrodes by coordination chemistry-based advanced functional carbon nanostructures: Progress, Current challenges and prospects. *Fuel Processing Technology*, 250, 107896. DOI:10.1016/j.fuproc.2023.107896.

6 Dong H., Sun K., Li X., Li H., You P., Chen S., Zhou J. (2024). Effects of organic acid and phosphoric acid at the low-voltage stage of the high-voltage forming process for the anode dielectric film of an aluminum electrolytic capacitor. *International Journal of Electrochemical Science*, 19(6), 100587. DOI: 10.1016/j.ijoes.2024.100587.

7 Chen C., Wei S., Zhang Q., Yang H., Xu J., Chen L., Liu X. (2024) High-performance VO_2/CNT@PANI with core-shell construction enable printable in-planar symmetric supercapacitors. *Journal of Colloid and Interface Science*, 664, 53–62. DOI:10.1016/j.jcis.2024.03.012.

8 Arulepp M., Leis J., Lätt M., Miller F., Rumma K., Lust E., Burke A.F. (2006) The advanced carbide-derived carbon based supercapacitor. *Journal of Power Sources*, 162(2), 1460–1466. DOI 10.1016/j.jpowsour.2006.08.014.

9 Kaiser, T., von der Höh, N., Menzel, A. (2024). Computational multiscale modelling of material interfaces in electrical conductors. *Journal of the Mechanics and Physics of Solids*, 186, 105601. DOI: 10.1016/j.jmps.2024.105601.

10 Panda P., Mishra R., Panigrahy S., Barman S. (2021) Design of $Co_1Al_3(OH)_m$/carbon nitride hybrid nanostructures for enhanced capacitive energy storage in an alkaline electrolyte. *Materials Advances*, 2(23), 7671–7680. DOI: 10.1039/d1ma00665g.

11 Du Y., Liu W., Cui Y., Fan H., Zhang Y., Wang T., Wang H., Jin Y., Liu S., Feng W., Chen M. (2021) Microzone-explosion synthesis of porous carbon electrodes for advanced aqueous solid-state supercapacitors with a high-voltage gel electrolyte. *Journal of Energy Chemistry*, 60, 95–103. DOI: 10.1016/j.jechem.2020.12.015.

12 Chauhan P.S., Sengupta R., Kumar S., Panwar V., Sahoo S., Bose S., Misra A. (2023) Role of graded microstructure and electrolyte distribution in electrochemical capacitance of compressible three-dimensional carbon nanotubes-polymer foam based supercapacitor. *Electrochimica Acta*, 461, 142595. DOI:10.1016/j.electacta.2023.142595.

13 Liu Y.-S., Ma C., Wang K.-X., Chen J.-S. (2023) Recent advances in porous carbons for electrochemical energy storage. *New Carbon Materials*, 38(1), 1–15. DOI: 10.1016/s1872-5805(23)60710-3.

14 Chen Y., Ma Y., Huang J., Xu H. (2022) Fabricating dual redox electrolyte to achieve ultrahigh specific capacitance and reasonable Coulombic efficiency for biomass activated carbon. *Electrochimica Acta*, 414, 140215. DOI:10.1016/j.electacta.2022.140215.

15 Abareghi M., Mohsen Saeidi S., Keshavarzi E. (2023) Effect of solvent on electric double layer capacitance and over screening inside spherical cavity by density functional theory. *Journal of Molecular Liquids*, 383, 122080. DOI: 10.1016/j.molliq.2023.122080.

16 Kazari H., Pajootan E., Sowa M., Coulombe S., Hubert P. (2023) Plasma-enhanced atomic layer deposition of ruthenium metal on free-standing carbon nanotube forest for 3D flexible binder-less supercapacitor electrodes. *Journal of Energy Storage*, 64, 107049. DOI: 10.1016/j.est.2023.107049.

17 Lai H., Li W., Zhou Y., He T., Xu L., Tian S., Wang X., Fan Z., Lei Z., Jiao H. (2019) Hydrophilically engineered polyacrylonitrile nanofiber aerogel as a soft template for large mass loading of mesoporous poly(3,4-ethylenedioxythiophene) network on a bare metal wire for high-rate wire-shaped supercapacitors. *Journal of Power Sources*, 441, 227212. DOI: 10.1016/j.jpowsour.2019.227212.

18 Krishna B.H., Reddy C.P., Munirathnam K., Yusuf K., Nagajyothi P.C., Shim J. (2024) In-situ synthesis of coral reef-like synergistic zinc cobalt oxide and zinc manganese oxide composite as a battery-type electrode material for supercapacitors. *Colloids and Surfaces. A, Physicochemical and Engineering Aspects*, 694, 134148. DOI: 10.1016/j.colsurfa.2024.134148.

19 Bao C., Chu P., Xu C., Yuan J., Si L., Bo Z., Ostrikov K., Yang H. (2024) More disorder is better: Cutting-edge progress of high entropy materials in electrochemical energy storage applications. *Energy Storage Materials*, 69, 103408. DOI: 10.1016/j.ensm.2024.103408.

20 Murovhi P., Tarimo D.J., Oyedotun K.O., Manyala N. (2020) High specific energy asymmetric supercapacitor based on alpha-manganese dioxide/activated expanded graphite composite and activated carbon-polyvinyl alcohol. *Journal of Energy Storage*, 32, 101797. DOI: 10.1016/j.est.2020.101797.

21 Eroglu O., Kizil H. (2023) Pseudocapacitive sodium-ion storage in one-dimensionally structured anatase TiO2 nanofiber anode for high performance sodium-ion batteries. *The Journal of Physics and Chemistry of Solids*, 178, 111352. DOI: 10.1016/j.jpcs.2023.111352.

22 Huo J., Xue Y., Wang X., Liu Y., Zhang L., Guo S. (2020) TiO_2/carbon nanofibers doped with phosphorus as anodes for hybrid Li-ion capacitors. *Journal of Power Sources*, 473, 228551. DOI: 10.1016/j.jpowsour.2020.228551.

23 Reddy H.P.C., Amalraj J., Ranganatha S., Patil S.S., Chandrasekaran S. (2023) A review on effect of conducting polymers on carbon-based electrode materials for electrochemical supercapacitors. *Synthetic Metals*, 298, 117447. DOI: 10.1016/j.synthmet.2023.117447.

24 Yang J.W., Kwon H.R., Seo J.H., Ryu S., Jang H.W. (2024) Nanoporous oxide electrodes for energy conversion and storage devices. *RSC Applied Interfaces*, 1, 11-42. DOI: 10.1039/d3lf00094j.

25 Bhowmik S., Bhattacharjee U., Ghosh S., Martha S.K. (2023) Evaluating the feasibility of the spinel-based $Li_4Ti_5O_{12}$ and $LiNi_{0.5}Mn_{1.5}O_4$ materials towards a battery supercapacitor hybrid device. *Journal of Energy Storage*, 73(C), 109099. DOI: 10.1016/j.est.2023.109099.

26 Seenath J.S., Pech D., Rochefort D. (2022) Investigation of protic ionic liquid electrolytes for porous RuO_2 micro-supercapacitors. *Journal of Power Sources*, 548, 232040. DOI: 10.1016/j.jpowsour.2022.232040.

27 Huang B., Liu W., Lan Y., Huang Y., Fu L., Lin B., Xu C. (2024) Highly ion-conducting, robust and environmentally stable poly(vinyl alcohol) eutectic gels designed by natural polyelectrolytes for flexible wearable sensors and supercapacitors. *Chemical Engineering Journal*, 480, 147888. DOI: 10.1016/j.cej.2023.147888.

28 Schrade S., Zhao Z., Supiyeva Z., Chen X., Dsoke S., Abbas Q. (2022) An asymmetric MnO_2|activated carbon supercapacitor with highly soluble choline nitrate-based aqueous electrolyte for sub-zero temperatures. *Electrochimica Acta*, 425, 140708. DOI: 10.1016/j.electacta.2022.140708.

29 Xia G., Liu Z., He J., Huang M., Zhao L., Zou J., Lei Y., Yang Q., Liu Y., Tian D., Shen F. (2024) Modulating three-dimensional porous carbon from paper mulberry juice by a hydrothermal process for a supercapacitor with excellent performance. *Renewable Energy*, 227, 120478. DOI: 10.1016/j.renene.2024.120478.

30 Wang X., Chang K.-C., Zhang Z., Liu Q., Li L., Ma S., Zhang M. (2021) Performance enhancement and mechanism exploration of all-carbon-nanotube memory with hydroxylation and dehydration through supercritical carbon dioxide. *Carbon*, 173, 97–104. DOI: 10.1016/j.carbon.2020.10.084.

AUTHORS' INFORMATION

Dyussembayev, Medet – Doctoral Student, Kazakh-British Technical University; Research Associate, U.A. Joldasbekov Institute of Mechanics and Engineering, Almaty, Kazakhstan; https://orcid.org/0000-0003-2071-7191; m.dyussembayev@gmail.com

Khabiyev, Alibek – PhD, Associate Professor, Department of Chemical and Biochemical Engineering, Satbayev University; Leading Researcher, U.A. Joldasbekov Institute of Mechanics and Engineering, Almaty, Kazakhstan; https://orcid.org/0000-0001-9397-2367; alibek1324@mail.ru

Rafikova, Khadichakhan – PhD, Associate Professor, Department of Chemical and Biochemical Engineering, Satbayev University; Leading Researcher, U.A. Joldasbekov Institute of Mechanics and Engineering, Almaty, Kazakhstan; https://orcid.org/0000-0001-8028-2244; hadichahan@mail.ru

Afanasyev, Dmitriy – PhD, Professor, Department of Radiophysics and Electronics, E.A. Buketov Karaganda University, Karaganda, Kazakhstan; https://orcid.org/0000-0002-0437-5315; a.d.afanasyev2@gmail.com

EURASIAN PHYSICAL TECHNICAL JOURNAL

2024, Volume 21, No.4 (50)

https://doi.org/10.31489/2024No4/23-34

Received: 22/07/2024 Revised: 14/11/2024 Accepted: 13/12/2024 Published online: 25/12/2024

Original Research Article

UDC 538.9; 535.215; 539.23; 535.3

INFLUENCE OF SPIRO-OMETAD FILM THICKNESS ON THE STRUCTURAL AND ELECTRICAL PROPERTIES OF PEROVSKITE SOLAR CELLS

Tazhibayev S.K.[1], Alekseev A.M.[2], Aimukhanov A.K.[1], Ilyassov B.R.[3], Beisembekov M.K.[1], Rozhkova X.S.[1], Mussabekova A.K.[1], Zeinidenov A.K.[1]*

[1] E.A. Buketov Karagandy University, Karaganda, Kazakhstan
[2] Kazan Federal University, Kazan, Russia
[3] Astana IT University, Expo C1, Astana, Kazakhstan
* *Corresponding authors*: a.k.zeinidenov@gmail.com

Abstract. *This work investigates the effect of the hole transport layer (HTL) thickness of Spiro-OMeTAD on the electrical transport properties in perovskite solar cells (PSCs). Spiro-OMeTAD films were obtained by the spin-coating method at centrifuge rotation speeds from 2000 to 7000 rpm. The thickness and morphology of the Spiro-OMeTAD films were studied by atomic force microscopy (AFM). From the obtained AFM image data, an increase in the surface root mean square (rms) value is observed with decreasing film thickness. A decrease in film thickness leads to an increase in Energy gap ($E_{g)}$ from 2.97 eV to 3.01 eV. We observe that at a layer thickness of 260 nm, the efficiency of the cells reaches its maximum value; further increasing the layer thickness reduces the efficiency. Analysis of the impedance spectra of PSCs showed that the optimal layer thickness reduces the HTL resistance and increases the recombination resistance at the perovskite/HTL interface, which increases the effective lifetime of charge carriers. Images of the surface and current distribution of Spiro-OMeTAD on the surface of the perovskite layer were studied. A non-uniform current distribution on the surface of the samples was revealed, the observed spots with high conductivity are interpreted as perovskite quantum dots, which have better photovoltaic characteristics.*

Keywords: Perovskite solar cells, hole transport layer, Spiro-OMeTAD, conductive-AFM, current-voltage characteristics, impedance measurements.

1. Introduction

In recent years, organic-inorganic perovskite solar cells have attracted much attention from the global scientific community. The unprecedented development of PSCs is driven by their high optical absorption coefficient, tunable bandgap, low cost, ease of fabrication, and great potential to achieve higher efficiency compared to c-Si solar cells [1–3]. To increase the efficiency and stability of PSCs, work is being done to search and optimize the composition of all parts of the solar cell, not only the perovskite itself, but also the so-called transport layers. The hole-conducting transport layer plays an important role in the efficiency of charge transfer and extraction of photoexcited perovskite, HTL is important for power conversion efficiency (PCE) and stability in PSCs. Transport layers typically consist of small organic molecules, polymers, or inorganic materials such as oxides. The energy level of the HTL material must coincide with the maximum

of the perovskite valence band. The difference between these two energy levels allows for hole transport, but too large a difference in energy levels can lead to energy loss [4-6]. Thus, when using a hole transport material in PSCs, various basic requirements must be met, such as solubility, suitable energy level, and high hole mobility [7]. The organic molecule Spiro-OMeTAD (2,20,7,70-tetrakis (N, N-di-p-methoxyphenylamine)-9,90-spirobifluorene) is the most abundant HTL material in PSCs. This is due to its suitable glass transition temperature, high transparency in the visible spectrum and almost perfect energy band matching with $MAPbI_3$ [8, 9]. The Spiro-OMeTAD layer above the photoactive layer is used as an HTL to block electrons and pass holes to the bottom electrode. In addition to transporting holes into PSCs, Spiro-OMeTAD avoids direct contact between the photoactive layer and the bottom electrode. Currently, the efficiency of converting light energy into electrical energy in PSCs exceeds 25%. These indicators were obtained as before using HTL based on Spiro-OMeTAD [10,11].

Studies have shown that charge transport properties at the perovskite/HTL interface are the main factor limiting the efficiency and stability of high-performance PSCs [12,13]. It was shown in [14] that recombination between holes in HTL and electrons in perovskite is the main mechanism of recombination losses in PSCs. The amount of interfacial recombination can be influenced by the electronic coupling between the HTL and the perovskite, the number of trap states in the HTL, and the conductivity of the HTL [15–17]. Fast charge transfer through HTL is also important for the efficiency of PSCs; the conductivity of hybrid perovskites is orders of magnitude higher than that of used HTLs, which can cause the accumulation of high hole densities at the interface [18]. Therefore, the reduction in the transit time of charges through the HTL can be increased due to the optimal thickness of the HTL, or by increasing its conductivity by doping with various materials, which will significantly improve both the fill factor (FF) and V_{oc} of the device by improving charge extraction and reducing the probability of passage recombination in HTL [19]. Various thicknesses of perovskite and HTM layers have been reported, and an optimal value is required for each layer. A thick perovskite layer greater than 1000 nm results in decreased hole collection efficiency due to increased resistance and recombination within the perovskite layer. Thin perovskite layers less than 100 nm cause low photocurrent due to lower photo-absorption. The likelihood of recombination is reduced because the holes travel a shorter distance to reach the electrode. Device performance improves when using a thinner HTM. The probability of hole accumulation depends on the thickness of the HTL. Therefore, an ideal HTL thickness is required for a high-performance device. In addition, since the perovskite surface contains crystallites, which can protrude through the HTM and contact the electrode if a very thin HTL is used [20, 21]. In addition to this, concomitant light absorption by HTL can also reduce the efficiency of PSCs by negatively affecting the short-circuit current density (J_{sc}) [22]. Therefore, ideal HTL thickness is required for high-performance PSCs.

Thus, the use of Spiro-OMeTAD as HTL is extremely popular for perovskite solar cells, making the study of charge transfer and recombination dynamics at the perovskite/HTL interface a highly relevant task. Optimizing the thickness of the hole transport layer is an important procedure for the fabrication of high-performance PSCs. Despite the fact that work has already been carried out around the world to optimize the thickness of HTL, studies that include various characterization methods that provide a complete understanding of the processes of hole transport in PSCs remain relevant. In this work, we fabricated Spiro-OMeTAD-based solar cells and studied the effect of HTL thickness on the electrical transport performance in PSCs.

2. Experimental part. Materials and Methods

2.1. Sample preparation and deposition process

Solar Cell Fabrication. Perovskite solar cells were constructed on glass substrates coated with a thin conductive layer of FTO (15 Ohm/cm^2), which acted as an external electrode (cathode). A TiO_2 film (Ti-Nanoxide BL/SC-Solaronix) was applied to the surface of the FTO substrate using the spin-coating method from a solution at a rotation speed of 5000 rpm, followed by annealing at a temperature of 500℃ for 60 minutes. Next, a perovskite layer and a Spiro-MeOTAD hole-transport layer were sequentially deposited on the TiO_2 surface. Spiro-OMeTAD films were obtained at different centrifuge speeds of 2000, 3000, 4000, 5000, 6000 and 7000 rpm. Finally, an Ag electrode was deposited onto the surface of the films in a vacuum atmosphere at a pressure of 10^{-3} Pa.

Perovskite Materials. $PbCl_2$ (Sigma Aldrich) and Methylammonium iodide (MAI, Sigma Aldrich) were used to prepare perovskite. Solutions were prepared by dissolving weighed portions of $PbCl_2$ (230 mg) and

MAI (394 mg) powder in 1 ml of N, N-Dimethylformamide (Sigma Aldrich). The resulting solution was stirred on a magnetic stirrer at a temperature of 60°C for 2 hours. To ensure complete crystallization, after deposition, the perovskite films were annealed for 2 hours at 100 °C. The crystallization process is accompanied by a change in the color of the film from yellow to dark brown.

Composition of HTM. The hole transport layer was made from 1 ml chlorobenzene (Sigma Aldrich) and 75 mg Spiro–OMeTAD. The resulting solution was stirred on a magnetic stirrer at a temperature of 30°C for 1 hour. To reduce the oxidation process, all operations were carried out in a sealed glove box with an inert atmosphere. Structural formulas (a) and a scheme for producing perovskite solar cells (b) are shown in Fig.1.

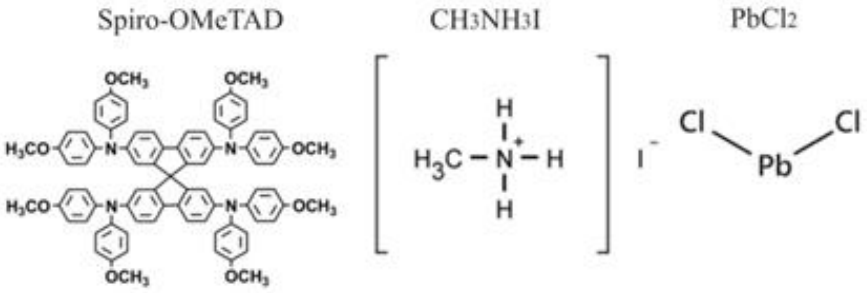

a)

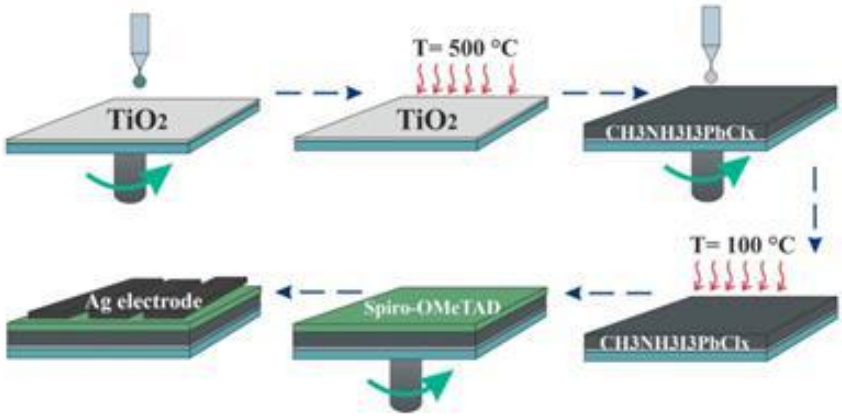

b)

Fig.1. Structural formula (a) and preparation scheme perovskite solar cells (b)

2.2. Analysis methods

The surface topography and thickness of the samples were studied using a JSPM-5400 atomic force microscope (AFM, JEOL). To process the AFM images, a modular program for analyzing scanning probe microscopy data (Win SPMII Data-Processing Software) was used. A SolverP47 (NT-MDT) AFM was used to measure the local current distribution. When measuring current, a voltage was applied to the sample, while a conductive probe coated with a gold film was grounded. To measure surface topography and determine rms, a semi-contact scanning mode was used (NSC14 probe, Micromash); current measurements were carried out in contact mode (CSC37/Au probe, Micromash). The thickness of the deposited layers and the distribution of PSCs elements were measured using a scanning electron microscope (SEM, MIRA 3 LMU, Tescan). The absorption spectra of Spiro-OMeTAD thin films were investigated on an AvaSpec-ULS2048CL-EVO spectrometer (Avantes). A combined deuterium-halogen light source AvaLight-DHc (Avantes) with a working range of 200-2500 nm was used as probing radiation.

Thermal deposition of films was carried out using a vacuum deposition machine CY-1700x-spc-2 (Zhengzhou CY Scientific Instruments Co., Ltd). The preparation and assembly processes of PSCs were carried out in a glove box with an inert atmosphere. Impedance spectra were measured using a P45X potentiostat-galvanostat in impedance mode. The current-voltage characteristics of photosensitive cells were determined using a Sol3A Class AAA Solar Simulators (Newport) with PVIV-1A I-V Test Station device.

3. Results and Discussion

3.1. Structural analysis of the prepared films

Figure 2 shows AFM images of the surface of the HTL layer of Spiro-OMeTAD, obtained at different centrifuge rotation speeds. As can be seen from Figure 2a, the surface morphology of the HTL layer obtained at the lowest rotation speed is uniform and smooth. The rare pores observed are apparently associated with the evaporation of the solvent when the film dries. As the rotation speed increases, a structure with characteristic sizes of regions of several hundred nanometers appears on the surface of the film (Figures 2b-2f). The appearance of such a structure can be explained by the influence of the FTO substrate surface.

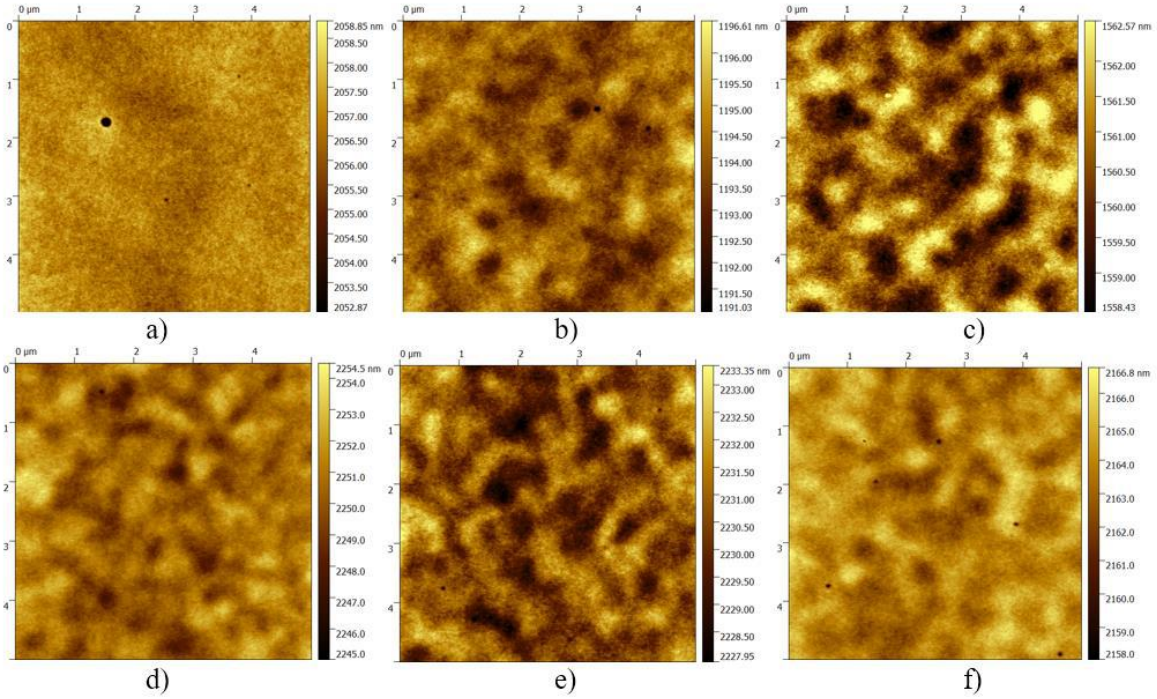

Fig.2. Surface morphology of Spiro-OMeTAD films, obtained at different substrate rotation speeds: a) 2000 rpm.; b) 3000 rpm.; c) 4000 rpm.; d) 5000 rpm.; e) 6000 rpm.; f) 7000 rpm.

Figure 3a shows the dependence of the thickness of Spiro-OMeTAD films on the centrifuge rotation speed. The thickness was determined from the step height obtained by scratching the surface of the film by measuring the height difference using statistical analysis. The solid line in the figure shows the well-known dependence of thickness on centrifugation speed t~1/√w, fitted to the data obtained using the least squares method.

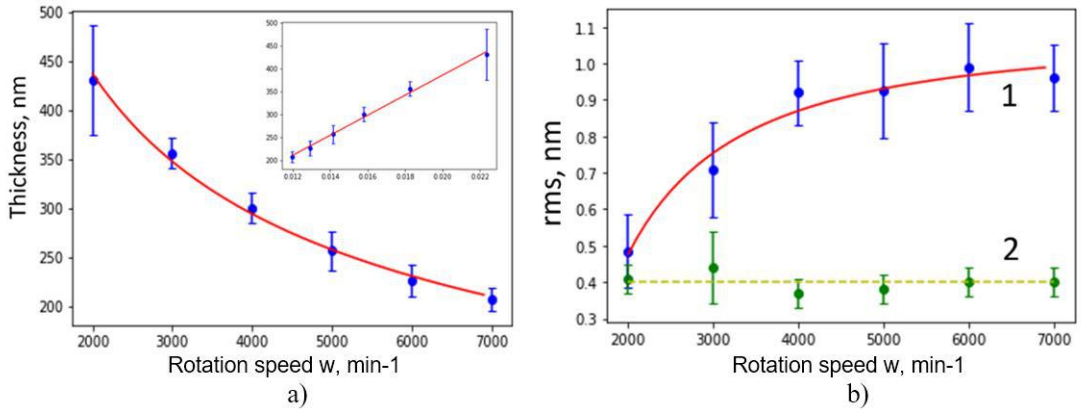

Fig.3. Thickness (a) and standard deviation (b) of the surface of the spin-coated Spiro-OMeTAD film as a function of rotation speed: a) blue symbols – experimental data, red line – dependence $t \sim 1/w^{0.5}$; in the inset - the same data in coordinates $t\ (1/w^{0.5})$; b) data 1 – for FTO film, data 2 – for film on glass; the lines show the average value for 2 and the $rms \sim w^{0.5}$ dependence for 1.

It can be seen that the obtained thicknesses are in good agreement with the theoretical dependence and decrease monotonically with increasing rotation speed. Apparently, as the rotation speed increases, the film thickness decreases and the structure of the substrate appears in the AFM image.

Figure 3b shows surface root mean square deviation (rms) versus spin speed for Spiro-OMeTAD films deposited on FTO and glass. For a film on FTO, a sharp increase in surface rms is observed when the rotation speed increases to 4000 rpm, then the dependence saturates. The stabilization of rms can be explained by the stabilization of thickness at high speeds: the structure of the substrate appears approximately the same for samples obtained at speeds from 4000 rpm. The rms dependence for FTO films is well approximated by the $rms \sim w^{0.5}$ dependence. Thus, dependences of thickness and rms on rotation speed are inverse for FTO substrate. For Spiro-OMeTAD films deposited on glass, no dependence of rms on rotation speed is observed; the average rms value of films on glass is close to the rms value of the thickest film on FTO. The SEM image of the cross-cleavage and the element distribution of PSCs are shown in Figure 4. From the figure 4, it can be seen that the thickness of the FTO film is 360 nm, the thickness of the TiO_2 film is 65 nm, the perovskite layer is 340 nm, the Spiro-OMeTAD layer is 260 nm, the Ag electrode layer is 70 nm.

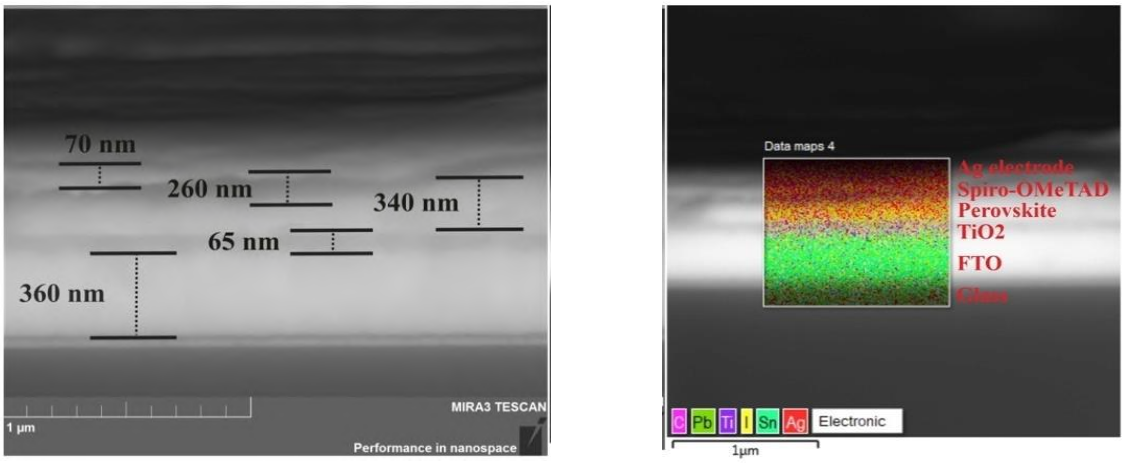

a) b)

Fig.4. SEM images of transverse cleavage a) and distribution of PSCs elements b)

3.2. Optical properties

Figure 5a shows the absorption spectra of Spiro-OMeTAD films. The absorption spectrum of Spiro-OMeTAD has three maxima, the most intense is at a wavelength of λ=228 nm, and the other two maxima are less intense and are located at λ=308 nm and λ=373 nm.

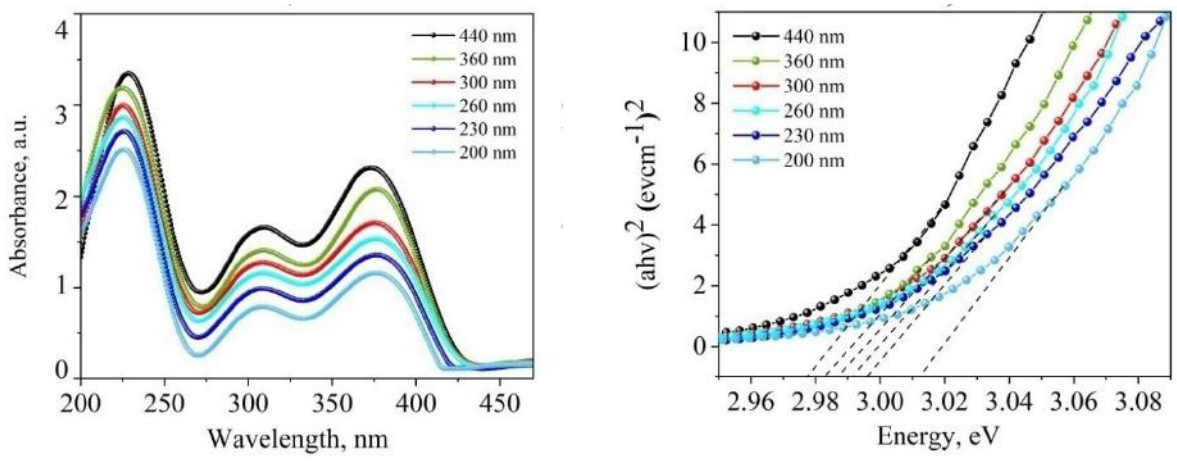

a) b)

Fig.5. Absorption spectra (a) and band gap (b) Spiro-OMeTAD films with different thicknesses

As the film thickness decreases, a shift in the absorption edge of Spiro-OMeTAD is observed. This shift to short wavelengths is associated with a change in the surface structure of Spiro-OMeTAD films. In addition, decreasing the film thickness leads to a decrease in the optical density of Spiro-OMeTAD.

From the absorption spectra of the films, the energy gap (E_g) of Spiro-OMeTAD was determined using the TaucPlot method (Figure 5 b). Analysis of the data shows that with a decrease in film thickness, an increase in the band gap is observed, respectively, from E_g = 2.97 eV to Eg = 3.01 eV. The optical characteristics of Spiro-OMeTAD films are presented in Table 1.

Table 1. Optical characteristics of the Spiro-OMeTAD transport layer at different thicknesses

Film thickness, nm	D_1, A.U. (λ=228 nm)	D_2, A.U. (λ=308 nm)	D_3, A.U. (λ=373 nm)	Bandgap, eV
440	3.49	1.68	2.39	2.977
360	3.39	1.41	2.13	2.982
300	3.03	1.23	1.72	2.987
260	2.95	1.14	1.54	2.991
230	2.79	0.96	1.35	2.995
200	2.57	0.73	1.14	3.012

3.3. Electrophysical characterizations

To study the current-voltage characteristics, perovskite solar cells with the FTO/TiO_2/$CH_3NH_3I_3PbClx$/Spiro-OMeTAD/Ag structure with different HTL layer thicknesses were constructed. To study the effect of Spiro-OMeTAD thickness on photovoltaic properties, solar cell layers were prepared under the same conditions except for the Spiro-OMeTAD layer. The current-voltage characteristics of PSCs and the energy diagram of the components are presented in Figure 6. From Figure 6 and Table 2 it can be seen that with a decrease in the thickness of the Spiro-OMeTAD film from 200 to 230 nm, an increase in the transmission coefficient of up to 8.6% is observed. The solar cell with Spiro-OMeTAD, obtained with an HTL layer thickness of 260 nm, showed the highest energy conversion efficiency characteristics, reaching 9%. Further increase in the thickness of the Spiro-OMeTAD layer to 440 nm. results in lower photovoltaic performance values of PCSs compared to cells with thin layers of Spiro-OMeTAD.

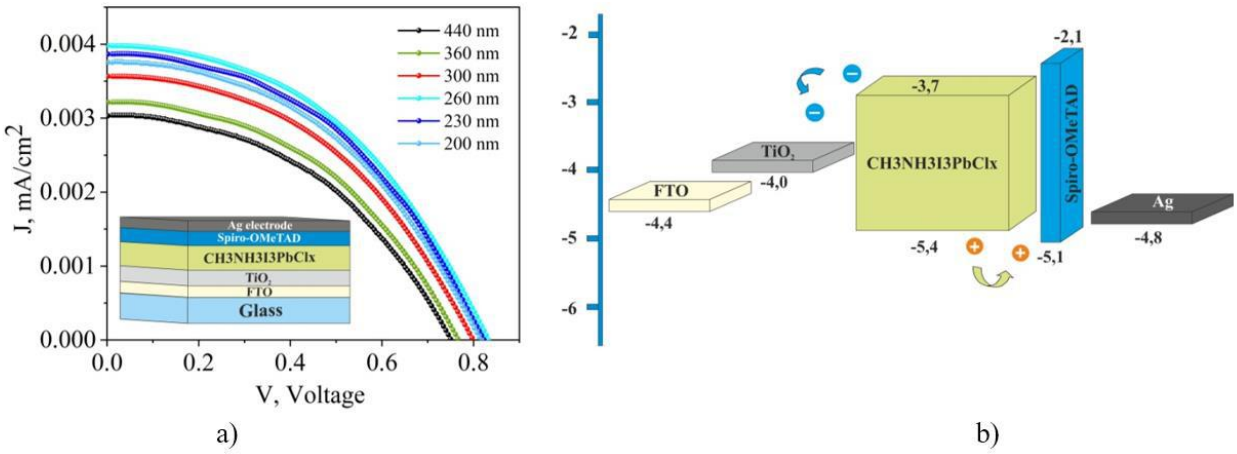

Fig.6. Current-voltage characteristics (a) and energy diagram (b) of perovskite solar cells

The current-voltage characteristics show that the current density increases with increasing Spiro-OMeTAD thickness; the highest current density value J_{sc} = 24.94 mA/cm^2 is found in PSCs with a Spiro-OMeTAD film with a thickness of 260 nm. A further decrease in the thickness of the HTL films leads to a decrease in the current density to the value J_{sc} = 23.41 mA/cm^2. The findings indicate that the optimal thickness of Spiro-OMeTAD, obtained at a thickness of 260 nm, increases the charge transfer efficiency and reduces the recombination of charge carriers in the transport layer of PSCs.

The change in fill factor (FF) with Spiro-OMeTAD thickness is an indication of a change in series resistance. As the Spiro-OMeTAD thickness decreases to 260 nm, cell efficiency increases from 6.0% to 9.0% due to an increase in fill factor from 0.43 to 0.47 (Table 2). Further reduction in thickness from 230 to 200 nm. Reduces the fill factor to 0.46 and efficiency to 8.3%, respectively.

Table 2. Photovoltaic characteristics of perovskite solar cells

Film thickness, nm	V_{oc}(V)	J_{sc}(mA/cm^2)	V_{max} (V)	J_{max}(mA/cm^2)	FF	PCE %
440	0.74	19	0.50	12.6	0.43	6.0
360	0.76	20.1	0.51	13.5	0.44	6.8
300	0.80	22.3	0.53	14.8	0.45	7,8
260	0.83	24.9	0.55	16.5	0.47	9.0
230	0.82	24.1	0.54	16.1	0.46	8.6
200	0.81	23.4	0.54	15.5	0.46	8.3

To understand the influence of the thickness of the HTL layer of Spiro-OMeTAD on the charge carrier transport mechanisms, measurements of the impedance spectra of PSCs were carried out (Figure 7a). The impedance spectra were analyzed using standard equivalent electrical circuitry, where R_s is the high-frequency resistance, R_{rec} is the low-frequency bulk recombination resistance, and CPE is the phase constant between layers (Figure 7a - insert).

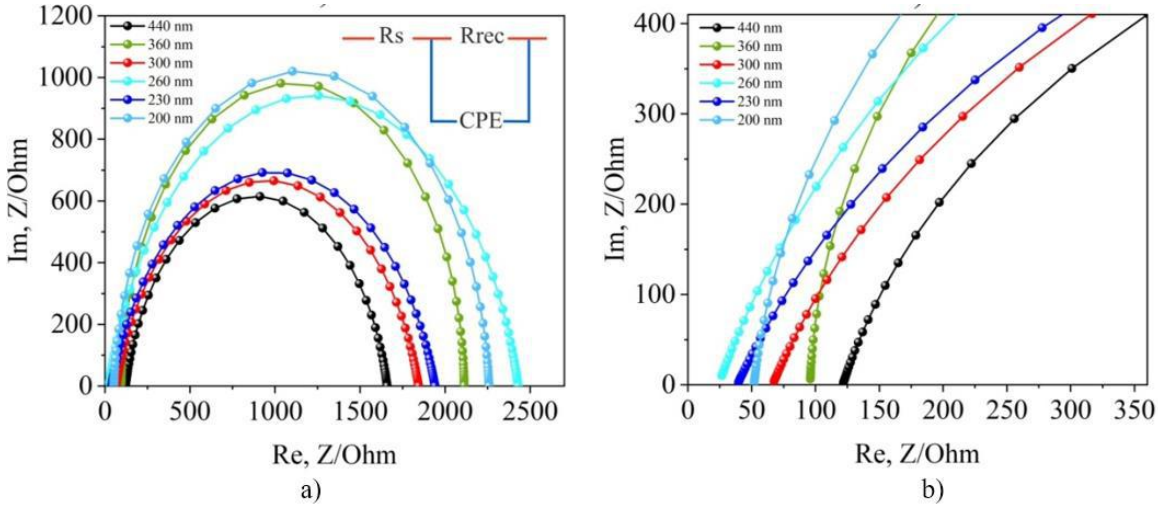

Fig.7. Impedance hodographs in Nyquist coordinates (a) for PSCs with different Spiro-OMeTAD thicknesses, equivalent electrical circuit in the inset; (b) enlarged image of the initial values of the impedance hodographs

The value of the effective charge carrier recombination rate k_{eff} was determined from the maximum arc of the hodograph using the formula:

$$\omega_{eff} = k_{eff} \quad (1)$$

$$\omega = 1/rc,$$

where is angular frequency, rc is a time characteristic of a simple electrical circuit in which the charge of capacitor C changes due to its discharge through resistance R.

The effective lifetime of charge carriers in films is calculated using the formula:

$$\tau_{eff} = 1/k_{eff} \quad (2)$$

The effective free path of charge carriers was calculated using the formula:

$$D_{eff}=R_s/R_{rec}\cdot k_{eff}\cdot L^2 , \quad (3)$$

where L is the film thickness.

As a result of the analysis of impedance spectra, the following electrical transport characteristics were determined: R_s – a parameter characterizing the series resistance of all functional layers of the cell; R_k is the resistance characterizing the recombination channels of charge carriers; τ_{eff} is the effective lifetime of charge carriers, Table 3 shows the parameters listed. P - parameter of constant phase element (CPE), preexponential factor, n is the number of points in the impedance spectrum. Figure 7 b shows an enlarged image of the initial values of the hodographs characterizing the values of the parameter R_s.

Table 3. Parameters of charge injection and transport in perovskite solar cells

Film thickness, nm	R_s, Ohm	R_k, Ohm	R_k/R_s	n	P	k_{eff}, s^{-1}	τ_{eff}, ms
440	121.9	1537.6	12.6	0.86	$1.18*10^{-8}$	501.1	1.9
360	96.1	2016.1	20.9	0.98	$3.25*10^{-9}$	251.1	3.9
300	67.5	1777.8	26.3	0.81	$1.67*10^{-8}$	645.6	1.5
260	26.7	2405.4	90.1	0.84	$2.38*10^{-8}$	158.5	6.3
230	39.6	1901.6	48.1	0.80	$3,33*10^{-8}$	301.9	3.3
200	51.9	2206.1	42.5	0.95	$5.80*10^{-9}$	234.4	4.3

As can be seen from Table 3, the R_s value is the lowest for a cell with a Spiro-OMeTAD HTL layer with a thickness of 260 nm. Further increase in layer thickness leads to an increase in the value of R_s. Since all functional cell layers were obtained under the same conditions, the decrease in R_s is due to the improvement in the efficiency of injection and hole transport. As can be seen from the energy diagram in Figure 6 (b), the positions of the $CH_3NH_3I_3PbCl_x$ cost center are more negative compared to the Spiro-OMeTAD cost center, which generates a stronger built-in electric field for efficient extraction of holes into the anode.

Resistance R_k is also an important parameter characterizing the recombination of charge carriers. From the fitting data it follows that R_k has a low value for cells with a Spiro-OMeTAD HTL layer with a thickness of 440 nm. As the HTL thickness decreases, R_k for cells with an HTL layer of Spiro-OMeTAD at a thickness of 360 nm. and 300 nm increased by 30% and 15%, respectively. At an HTL thickness of 260 nm, R_k reached a maximum value of 2405.4 Ohm, which led to an increase in the resistance efficiency in the charge carrier recombination channels. With further reduction in thickness to 200 nm. there is a decrease in the value of R_k, which in turn leads to a deterioration in the performance of the solar cell. Thus, the Spiro-OMeTAD film, with a thickness of 260 nm, contributes to efficient electron blocking.

A significant increase in the effective lifetime of charge carriers (τ_{eff}) is three orders of magnitude higher for films with a thickness of 260 nm. The significant increase in τ_{eff} can be explained by a decrease in the recombination of charge carriers due to the blocking effect and partly by an improvement in hole transport. When comparing the photovoltaic and electrical transport parameters of cells with an HTL layer of Spiro-OMeTAD, with a thickness of 200 nm up to 440 nm, the following features are observed: a cell with an HTL layer with a thickness of 260 nm. showed an efficiency of 40% more compared to a cell with an HTL layer with a thickness of 440 nm, which is largely due to an increase in photovoltage and fill factor. In cells of the ITO/TiO_2/$CH_3NH_3I_3PbCl_x$/Spiro-OMeTAD/Ag structure, the photovoltage is caused by the difference between the Fermi level of electrons in TiO_2 and the Fermi level of Spiro-OMeTAD holes.The lower position of the quasi-Fermi level of the Spiro-OMeTAD holes gives an increase in the observed photovoltage. The higher fill factor is largely due to the lower R_s. According to the impedance spectra, the lifetime of charge carriers in a cell with a Spiro-OMeTAD HTL layer with a thickness of 260 nm is almost 3 times greater than τeff in a cell with a Spiro-OMeTAD HTL layer with a thickness of 430 nm. As described earlier, the optical band gap width of a hole-transport layer film with a thickness of 260 nm is almost 0.02 eV greater than that of a film with a thickness of 440 nm, which is due to the lower position of the valence band maximum. This generates a stronger built-in electric field to effectively extract holes into the anode, thereby reducing the likelihood of charge carrier recombination.

Figure 8 shows images of the surface and current distribution of Spiro-OMeTAD on the surface of the peroskite layer. The use of conductive-AFM (CAFM) made it possible to identify a significantly inhomogeneous current distribution on the surface of the samples. In addition to inhomogeneities associated with the perovskite structure, current images of some samples show spots with increased conductivity, which stand out sharply against the general background and are located along the boundaries of crystallites.It was shown in [23] that when this type of AFM is used, the probe-sample contact area is illuminated by the microscope laser. The instrument used to measure the current distributions shown in Figure 8 uses a laser with a wavelength of 650 nm, which falls within the absorption spectrum of the perovskite used in the work.

Thus, the contrast in Figures 8b and 8d contains both dark current and potentially photocurrent. The observed spots of increased conductivity can presumably be interpreted as perovskite quantum dots, which have better photovoltaic characteristics compared to the bulk material. For this reason, research into perovskite quantum dots is currently being actively carried out [24, 25]. We do not know the results of direct observation of the electrical properties of perovskite quantum dots; therefore, our results may be the first visualization of the current distribution on quantum dots.

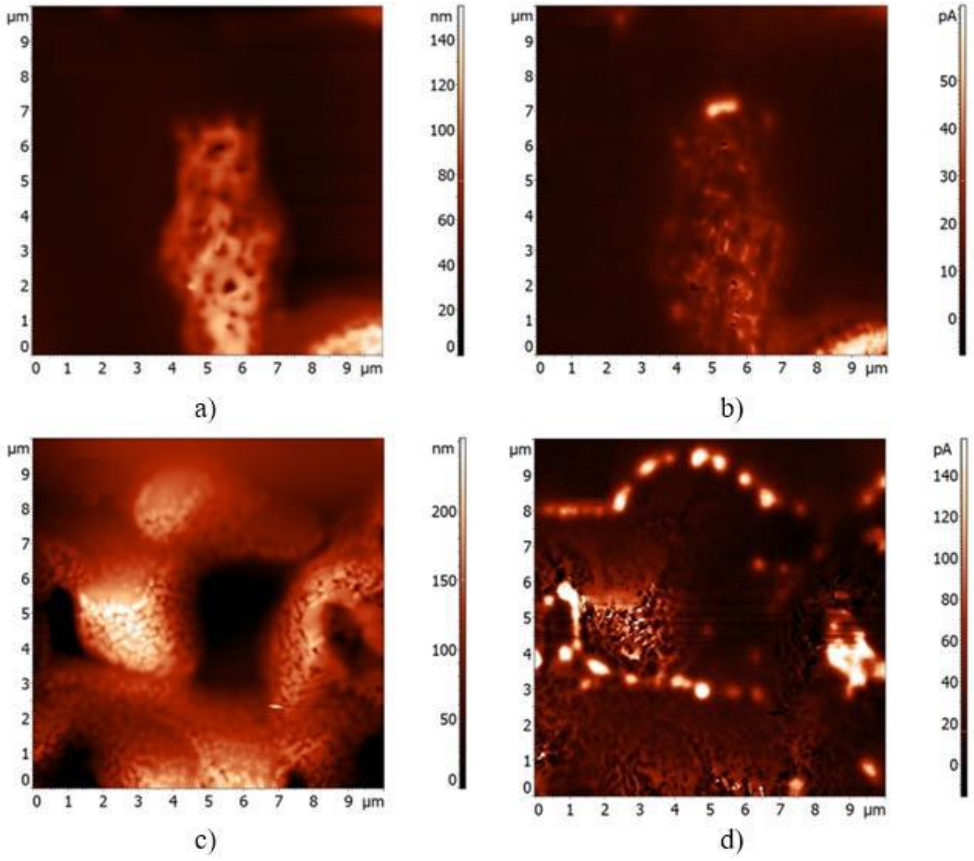

Fig.8. Images of the surface (a, c) and current distribution (b, d). Samples obtained at different centrifuge rotation speeds: a, b) – 2000 rpm, c, d) –5000 rpm. Images of the surface (a, c) and current distribution at a voltage across the sample of +5 V (b, d)

From the data obtained, we can make an assumption about the possible influence of the number of quantum dots on the efficiency of the resulting cells: the largest number of them was observed in sample 4, which shows an efficiency close to the maximum (see Table 2). At the same time, the small size of the scanning area of the AFM used in the work does not allow us to estimate the statistics of the distribution of quantum dots over the samples. Currently, the authors are conducting a more detailed study of perovskite quantum dots using electrical AFM methods.

4. Conclusions

In these studies, perovskite solar cells with FTO/TiO_2/$CH_3NH_3I_3PbCl_x$/Spiro-OMeTAD/Ag architecture were fabricated. The effect of the Spiro-OMeTAD layer density on the photovoltaic characteristics of PSCs was investigated.

The Spiro–OMeTAD hole-transport layer was obtained by the Spin-coating method. The thickness of the Spiro–OMeTAD layer was controlled by changing the centrifugation rotation speed. It was revealed that a monotonic decrease in the thickness of the Spiro–OMeTAD film leads to a sharp increase in the rms of the surface when the rotation speed increases to 4000 rpm, then the dependence saturates.

The dependences of thickness and rms on rotation speed for films on FTO are inversed: $\sim 1/w^{0.5}$ and $\sim w^{0.5}$, correspondingly. As the film thickness decreases, a decrease in the optical absorption density in the spectrum and an increase in the optical band gap of Spiro–OMeTAD films are observed. Electrical impedance spectra were measured for PSCs with different Spiro-OMeTAD thicknesses. It is shown that the series resistance of the functional layers of the cell depends on the thickness of the Spiro–OMeTAD layer. With thin layers, a decrease in resistance is observed; the lowest value is observed in a cell with an HTL layer of Spiro-OMeTAD with a thickness of 260 nm. A further increase in the thickness of the layer leads to an increase in resistance.

The use of conductive-AFM (CAFM) made it possible to identify a significantly inhomogeneous current distribution on the surface of the samples. In addition to inhomogeneities associated with the perovskite structure, current images of some samples show spots with increased conductivity, which stand out sharply against the general background and are located along the boundaries of crystallites. The observed spots of increased conductivity can presumably be interpreted as perovskite quantum dots, which have better photovoltaic characteristics compared to the bulk material.

Conflict of interest statement

The authors declare that they have no conflict of interest in relation to this research, whether financial, personal, authorship or otherwise, that could affect the research and its results presented in this paper.

CRediT author statement

Tazhibayev S.K.: Writing – original draft, Conceptualization; **Alekseev A.M.:** Investigation, Formal analysis; **Aimukhanov A.K.:** Supervision, Data curation; **Ilyassov B.R.:** Visualization; **Beisembekov M.K**.: Data curation; **Rozhkova X.S.:** Resources; **Mussabekova A.K.:** Investigation; **Zeinidenov A.K.:**Project administration, Methodology. The final manuscript was read and approved by all authors.

Funding

This research is funded by the Science Committee of the Ministry of Science and Higher Education of the Republic of Kazakhstan (Grant No. AP19576784).

References

1 Devadiga D., Nagaraja A.T., Devadiga Dh., Selvakumar M. (2024) Minireview and Perspectives of Liquid Crystals in Perovskite Solar Cells. *Energy & Fuels*, 38 (2), 854 - 868. DOI: 10.1021/acs.energyfuels.3c04050.

2 Sha W.E.I., Ren X., Chen L., Choy W.C.H. (2015) The efficiency limit of $CH_3NH_3PbI_3$ perovskite solar cells. *Appl. Phys. Lett*., 106, 221104. DOI: 10.1063/1.4922150.

3 Saliba M., Correa-Baena J.-P., Gratzel M., Hagfeldt A., Abate A. (2018) Perovskite Solar Cells: From the Atomic Level to Film Quality and Device Performance. *Angew. Chem., Int. Ed.*, 57, 2554–2569. DOI:10.1002/anie.201703226.

4 Aristidou N., Eames C., Sanchez-Molina I., Bu X., Kosco J., Islam M. S., Haque S.A. (2017) Fast oxygen diffusion and iodide defects mediate oxygen-induced degradation of perovskite solar cells. *Nat. Commun.*, 8, 15218. DOI: 10.1038/ncomms15218.

5 Wolff C.M., Caprioglio P., Stolterfoht M., Neher D. (2019) Nonradiative Recombination in Perovskite Solar Cells: The Role of Interfaces. *Adv. Mater.*, 31, 1902762. DOI: 10.1002/adma.201902762.

6 Jeong J., Kim M., Seo J., Lu H., Ahlawat P., Mishra A., Yang Y., Hope M. A., Eickemeyer F.T., Kim M., Yoon Y. J., Choi I. W., Darwich B.P., Choi S. J., Jo Y., Lee J. H., Walker B., Zakeeruddin S.M., Emsley L., Rothlisberger U., Hagfeldt A., Kim D. S., Gra¨tzel M., Kim J.Y. (2021) Pseudo-halide anion engineering for a-FAPbI3 perovskite solar cells. *Nature*, 592, 381–385.DOI: 10.1038/s41586-021-03406-5.

7 Guan-Woo K., Hyuntae C., Minjun K., Lee J., Son S.Y., Park T. (2020) Hole transport materials in conventional structural (n-i-p) perovskite solar cells: from past to the future. *Adv Energy Mater.*, DOI:10.1002/aenm.201903403.

8 Jeyakumar R., Bag A., Nekovei R., Radhakrishnan R. (2019) Interface studies by simulation on methylammonium lead iodide based planar perovskite solar cells for high efficiency. *Sol. Energy*, 104-111. DOI:10.1016/j.solener.2019.07.097.

9 Tumen-Ulzii G., Matsushima T., Adachi C. (2021) Mini-Review on Efficiency and Stability of Perovskite Solar Cells with Spiro-OMeTAD Hole Transport Layer: Recent Progress and Perspectives. *Energy & Fuels*, 35 (23), 18915-18927. DOI: 10.1021/acs.energyfuels.1c02190.

10 Yoo J.J., Wieghold S., Sponseller M.C., Chua M. R., Bertram S.N., Hartono N.T.P., Tresback J.S., Hansen E.C., Correa-Baena J.-P., Bulovic´V., Buonassisi T., Shin S.S., Bawendi M.G. (2019) An interface stabilized perovskite solar cell with high stabilized efficiency and low voltage loss. *Energy Environ. Sci*., 12, 2192–2199. DOI:10.1039/C9EE00751B.

11 Jiang Q., Zhao Y., Zhang X., Yang X., Chen Y., Chu Z., Ye Q., Li X., Yin Z., You J. (2019) Surface passivation of perovskite film for efficient solar cells. *Nat. Photonics*, 13, 460–466. DOI: 10.1038/s41566-019-0398-2.

12 Stolterfoht M., Caprioglio P., Wolff C., Ma´rquez Prieto J., Nordmann J., Zhang S., Rothhardt D., Ho¨rmann U., Amir Y., Redinger A., Kegelmann L., Zu F., Albrecht S., Koch N., Kirchartz T., Saliba M., Unold T., Neher D. (2019) The impact of energy alignment and interfacial recombination on the internal and external open-circuit voltage of perovskite solar cells. *Energy Environ. Sci.*, 12, 2778–2788. DOI: 10.1039/C9EE02020A.

13 Hawash Z., Ono L. K., Qi Y. (2018) Recent Advances in SpiroMeOTAD Hole Transport Material and Its Applications in Organic-Inorganic Halide Perovskite Solar Cells. *Adv. Mater. Interfaces*, 5, 1700623. DOI: 10.1002/admi.201700623.

14 Gelmetti, Montcada N., Pe´rez-Rodrı´guez A., Barrena E., Ocal C., Garcı´a-Benito I., Molina-Ontoria A., Martı´n N., Vidal-Ferran A., Palomares E. (2019) Energy Alignment and Recombination in Perovskite Solar Cells: Weighted Influence on the Open Circuit Voltage. *Energy Environ. Sci.*, 12, 1309–1316. DOI: 10.1039/C9EE00528E.

15 Wolff C.M., Caprioglio P., Stolterfoht M., Neher D. (2019) Nonradiative Recombination in Perovskite Solar Cells: The Role of Interfaces. *Adv. Mater*., 31, 1902762. DOI: 10.1002/adma.201902762.

16 Wang J., Liu K., Ma L., Zhan X. (2016) Triarylamine: Versatile Platform for Organic, Dye-Sensitized, Perovskite Solar Cells. *Chem. Rev*., 116, 14675–14725. DOI: 10.1021/acs.chemrev.6b00432.

17 Le Corre V.M., Stolterfoht M., Perdigo´n Toro L., Feuerstein M., Wolff C., Gil-Escrig L., Bolink H. J., Neher D., Koster L. J. A. (2019) Charge Transport Layers Limiting the Efficiency of Perovskite Solar Cells: How To Optimize Conductivity, Doping, and Thickness. *ACS Appl. Energy Mater*., 2, 6280–6287. DOI:10.1021/acsaem.9b00856.

18 Grill I., Aygu¨ler M. F., Bein T., Docampo P., Hartmann N. F., Handloser M., Hartschuh A. (2017) Charge Transport Limitations in Perovskite Solar Cells: The Effect of Charge Extraction Layers. *ACS Appl. Mater. Interfaces*, 9, 37655–37661. DOI: 10.1021/acsami.7b09567.

19 Stolterfoht M., Wolff C. M., Amir Y., Paulke A., Perdigon L., Caprioglio P., Neher D. (2017) Approaching the Fill Factor Shockley Queisser Limit in Stable, Dopant-Free Triple Cation Perovskite Solar Cells. *Energy Environ. Sci.*, 10, 1530. DOI: 10.1039/C7EE00899F.

20 Das A.K., Mandal R., Mandal D.K. (2022) Impact of HTM on Lead-free Perovskite Solar Cell with High Efficiency. *Optical and Quantum Electronics*, 07. DOI: 10.1007/s11082-022-03852-z.

21 Bag A., Radhakrishnan R., Nekovei R., Jeyakumar R. (2020) Effect of absorber layer, hole transport layer thicknesses, and its doping density on the performance of perovskite solar cells by device simulation. *Solar Energy*, 196, 177-182. DOI: 10.1016/j.solener.2019.12.014.

22 Da Y., Xuan Y., Li Q. (2018) Quantifying energy losses in planar perovskite solar cells. *Sol. Energy Mater. Sol. Cells*, 174, 206–213. DOI: 10.1016/j.solmat.2017.09.002.

23 Aimukhanov A.K., Rozhkova X.S., Ilyassov B.R., Omarbekova G.I., Seisembekova T.E. (2022) Effect of alcohol solvents on the structural, optical and electrical characteristics of PEDOT:PSS polymer films annealed at low atmospheric pressure. *Eurasian physical technical journal*, 19, 2 (40), 35-41. DOI: 10.31489/2022No2/35-41.

24 Hedley G., Ward A., Alekseev A., Calvyn T., Howells E.R., Serrano L., Cooke G., Ruseckas A., Samuel I.D. (2013) Determining the optimum morphology in high-performance polymer-fullerene organic photovoltaic cells. *Nature Communications*, 4, 2867. DOI: 10.1038/ncomms3867.

25 Han R., Zhao Q., Hazarika A., Li J., Cai H., Ni J., Zhang J. (2022) Ionic Liquids Modulating CsPbI3 Colloidal Quantum Dots Enable Improved Mobility for High-Performance Solar Cells. *ACS Appl. Nano Mater.*, 5, 10, 14092–14132. DOI: 10.1021/acsami.1c20274.

AUTHORS' INFORMATION

Tazhibayev, Serzhan Kozhanuly – Master (Sci.), Senior lecturer, E.A. Buketov Karaganda University, Karaganda, Kazakhstan. Scopus Author ID: 58170071100; https://orcid.org/0000-0001-9059-2975: tazh1981@gmail.com

Alekseev, Alexander Mikhailovich – Candidate of Phys. and Math. Sciences, Lead engineer, Kazan Federal University, Kazan, Russia. Scopus Author ID: 55286055800; https://orcid.org/0000-0002-2800-6047; alalrus@gmail.com

Aimukhanov, Aitbek Kalievich – Candidate of Phys. and Math. Sciences, Professor, E.A. Buketov Karaganda University, Karaganda, Kazakhstan. Scopus Author ID: 58493008700; https://orcid.org/0000-0002-4384-5164, a_k_aitbek@mail.ru

Ilyassov, Baurzhan Rashidovich – PhD, Associate Professor, Astana IT University, Expo C1, Astana, Kazakhstan. Scopus Author ID: 56669724700; https://orcid.org/0000-0003-4563-2004; baurdinho@mail.ru

Beisembekov, Meirkhan Kurmangazyuly – Master, E.A. Buketov Karaganda University, Karaganda, Kazakhstan. Scopus Author ID: 58984780800; https://orcid.org/0000-0003-2788-1699; baiboldy_han@mail.ru

Rozhkova, Xenia Sergeevna – PhD, Senior Lecturer, E.A. Buketov Karaganda University, Karaganda, Kazakhstan. Scopus Author ID: 57219053347; https://orcid.org/0000-0003-3048-6171; ksusharogovaya@mail.ru

Mussabekova, Assel Kanatkyzy – Master (Eng.), Senior Lecturer, E.A. Buketov Karaganda University, Karaganda, Kazakhstan. Scopus Author ID: 58429663700, https://orcid.org/0000-0003-3452-4622; assel501vremennyi@mail.ru

Zeinidenov, Assylbek Kalkenovich – PhD, Professor, E.A. Buketov Karaganda University, Karaganda, Kazakhstan. Scopus Author ID: 56386144000; https://orcid.org/0000-0001-9232-8406; asyl-zeinidenov@mail.ru

EURASIAN PHYSICAL TECHNICAL JOURNAL

2024, Volume 21, No.4 (50)

https://doi.org/10.31489/2024No4/35-48

Received: 20/07/2024 Revised: 13/10/2024 Accepted: 18/12/2024 Published online: 25/12/2024

Original Research Article

UDC 535.37

RADIATION SYNTHESIS OF BARIUM MAGNESIUM FLUORIDE ACTIVATED BY TUNGSTEN CERAMICS: STRUCTURE AND LUMINESCENCE

Lisitsyn V.M.[1], Vaganov V.A.[1], Alpyssova G.K.[2]*, Kaneva E.V.[3], Lisitsyna L.A[4]., Strelkova A.V.[5], Denisov I.P.[1]

[1] National Research Tomsk Polytechnic University, Tomsk, Russia
[2] E.A. Buketov Karagandy University, Karaganda, Kazakhstan
[3] Vinogradov Institute of Geochemistry SB RAS, Irkutsk, Russia
[4] Tomsk State University of Architecture and Building, Tomsk, Russia
[5] L.N. Gumilyov Eurasian National University, Astana, Kazakhstan
*Corresponding author: gulnur-0909@mail.ru

Abstract. *In the work on the example of barium magnesium fluoride activated by tungsten system the existence of possibility of introduction of activators, modifiers into the formed ceramics are shown. Using unique properties of radiation synthesis of high synthesis rate is happened. The possibility of synthesis of magnesium fluoride activated by tungsten, barium fluoride activated by tungsten and barium magnesium fluoride activated by tungsten ceramics by impact on the charge of a stream of electrons with energy 1.4 MeV with power density 15 kW/cm^2 is shown. The X-ray diffraction, photoexcitation and luminescence spectra, integral spectra of pulsed cathodoluminescence and its decay kinetics have shown that during radiation synthesis tungsten centers the crystal lattice of ceramics. The formed volatile compounds of hexafluoride tungsten do not have time to leave the reaction zone during the synthesis. The efficiency of synthesis reaches 99%. Addition of tungsten oxide to the charge in the amount of up to 2% of the total weight does not affect the formation of ceramics*

Keywords: ceramics; luminescence; radiation-assisted synthesis, X-ray diffraction spectra, optical properties of ceramics.

1. Introduction

Prospective scintillators are materials based on alkaline earth and alkali metal fluorides activated by polyvalent ions [1]. Introducing activators into the crystal lattice of these materials is a complex task. Metal fluoride crystals like LiF, MgF_2, and BaF_2 exhibit a high degree of structural perfection. Activators, being polyvalent ions, have difficulty incorporating into the lattice due to differences in charge and size [2]. Therefore, additional elements are introduced to compensate for this difference in order to incorporate the activator ions into the lattice. Facilitating the introduction of activators into crystals can be achieved by creating conditions that distort the lattice and promote the formation of a complex lattice structure. Examples of such crystals include $LiYF_4$ [3, 4], $NaYF_4$ with activators [5, 6], and $NaGdF_4$ [7]. A complex structure is obtained in the synthesis from LiF (NaF) and YF3 (GdF_4) with cubic and rhombohedral symmetries and similar systems [8]. Another possible matrix for obtaining activated material is $BaMgF_4$, which is derived

from BaF2 with a fluorite lattice and MgF_2 with a rutile lattice [9]. Effective activators (modifier) in metal fluoride-based materials include W, U, and Ti ions. However, their introduction into the crystalline lattice is challenging. At high temperatures of a thermal synthesis, fluoride compounds are formed with low melting points: 2.3, 64, 426°C, and boiling points: 17, 56, 285°C for W, U, Ti fluorides, respectively. Activators W, U, Ti are extracted from the melt. Therefore, the synthesis of activated materials based on them is carried out in an oxidative atmosphere, and LiOH is added to the mixture to facilitate the process. The introduction of substances that aid in synthesis into the initial charge affects the properties of the resulting materials.

A promising method for producing ceramics based on refractory materials is radiation synthesis. Radiation synthesis is carried out solely using a radiation energy, from charge materials of stoichiometric composition without additives, and without the use of any materials that facilitate synthesis, within a time frame of less than 1 second, in an air environment [10]. It can be expected that during radiation synthesis, tungsten ions will not have the opportunity to leave the area where ceramic formation occurs and will be incorporated into the lattice. The possibility of using radiation for the synthesis of MgF_2: W ceramics was demonstrated in a study [11]. The results presented in [12] indicate the possibility of obtaining tungsten-activated ceramics based on alkali earth and alkali metal fluorides.

2. Materials and methods

Ceramic synthesis was achieved by direct electron beam irradiation of the initial mixture of a specified composition using the UNU Stand ELV6 accelerator at the Budker Institute of Nuclear Physics, Siberian Branch of the Russian Academy of Sciences. High-energy electron beams with energy of 1.4 MeV were utilized for synthesis. The beam, extracted through a differential pumping system, had a Gaussian cross-sectional shape with an area on the target surface of 1 cm². The synthesis occurs when the threshold power density of the energy flux is exceeded. At the electron energy of 1.4 MeV, electron beams with a power density on the target surface of 15-23 kW/cm² were used for the synthesis of alkaline earth metal fluoride-based ceramics.

A charge of fluorine powders was prepared for synthesizing ceramics of the desired composition. Tungsten oxide powders were added in an amount of 2.0% of the total charge mass for activate the sensitized ceramics. The charge was poured into a massive copper crucible with a surface area of 10x5 cm² and a depth of 7 or 10 mm. The crucible's depth for synthesis was chosen to ensure the complete absorption of the electron beam energy flux by the charge. The crucible was placed on a massive metal table under the accelerator's output orifice. During radiation synthesis, the electron beam was scanned at a frequency of 50 Hz in the transverse direction of the crucible, and the crucible was moved relative to the scanning beam at a speed of 1 cm/s. The total exposure time of the electron beam on the target surface of the charge in the crucible always amounted to 10 seconds, which was due to the design features of the accelerator and the subject table. Since the beam had a size in the target plane of 1 cm², the crucible was moved relative to the scanning beam. Each elementary area of the charge surface was exposed to the action of a 1-second pulse with a rising and falling Gaussian-shaped envelope, lasting 2 ms with a 10 ms period under these conditions.

The samples were synthesized from powders supplied by «Chemreactiv» shops and Hebei Suoyi New Material Technology Co., Ltd. Note that the efficiency of radiation synthesis of alkaline earth metal fluoride ceramics depends on the background of the starting materials. It was shown in [13] that the efficiency of synthesis strongly depends on the size and aspect ratio of the powder particles used for synthesis. Studies on the dispersion of the initial powders used for synthesis to obtain ceramic samples were conducted using laser diffraction with the Shimadzu SALD-7101 laser particle size analyzer. Figure 1 (a, b) provides information on the dispersion composition of the initial materials used for synthesis.

Ceramic synthesis was achieved solely through the energy of radiation flux, using only raw materials without the addition of other facilitating substances. The synthesis resulted in obtaining samples in the form of plates with dimensions similar to the crucible: 10x5 cm². The typical appearance of inactivated and activated W ceramic samples of BaF_2, MgF_2, $BaMgF_4$, synthesized under the influence of an electron beam with E=1.4 MeV, P=15 kW/cm², is shown in Figure 2. Tungsten oxide powder (WO3) was used as an activator. The particle size is given in [14].

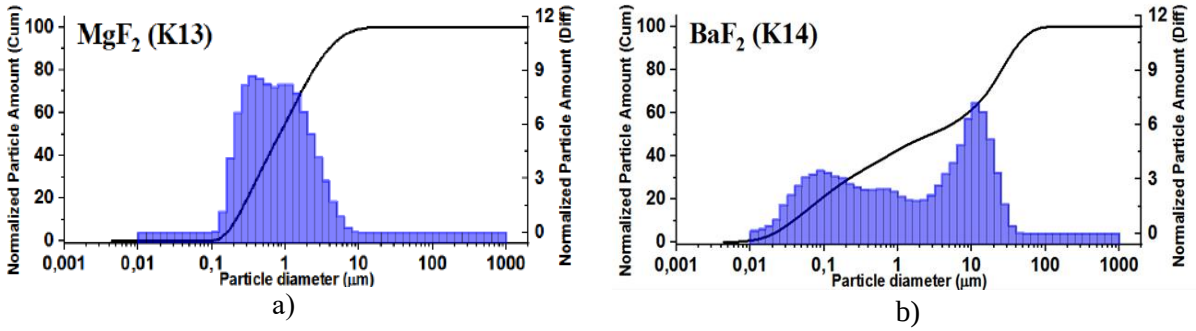

Fig.1. Dispersion composition of MgF_2 (a) and BaF_2 (b) used for powder synthesis.

All samples are solid, glassy and white with shades. The thickness of the samples varies across the area and ranges from 2-4 mm. When struck, the samples shatter like glass. In contrast to solid ceramic materials based on yttrium aluminum garnet, there are no characteristic large voids in the fracture of the described samples, typical of ceramics made of YAG and spinel. The density of the samples of the obtained MgF_2, BaF_2 ceramics is 3.0±0.3 g/cm^3 and 4.8±0.5 g/cm^3, which is close to the density of the corresponding single crystals (3.15 g/cm^3 for MgF_2 and 4.89 g/cm^3 for BaF_2). The surface of the fracture plane is rough, solid. It is worth noting that voids were observed by us earlier during the synthesis of ceramics of alkali-earth metal fluorides from charge materials of different histories. It was assumed that the presence of a significant volume of air in the charge, which does not have time to escape from the reaction zone during the short synthesis time. It is the cause of the void formation inside the synthesized samples. Table 1 provides information on the change in material density during synthesis: the density of the charge used for synthesis ρ_m, the density of the obtained ceramics ρ_{cr} g/cm^3. Here, the density of crystals ρ_{cr} [15] in g/cm^3 is also provided accordingly. The densities of the ceramics obtained by the radiation method were determined with an accuracy of 10%. The sample number in Table 1 represents the experiment number in the system adopted by the authors for record-keeping.

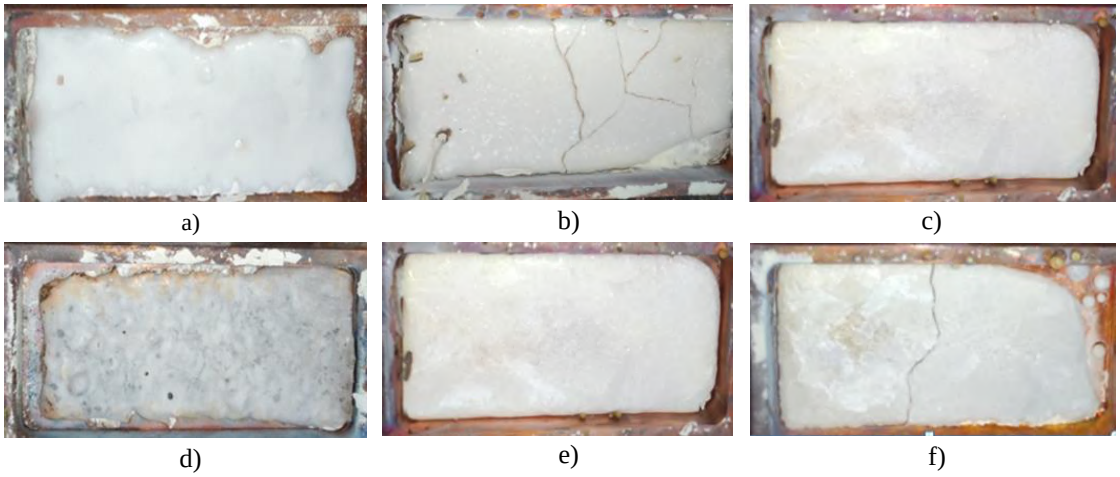

Fig.2. Photos of ceramics samples MgF_2, BaF_2, $BaMgF_4$ (a, b, c), and activated MgF_2:W, BaF_2:W, $BaMgF_4$:W (d, e, f) synthesized under the influence of an electron beam with E=1.4 MeV, P=15 kW/cm^2.

Table 1. Densities of mixture obtained by radiation method of ceramics, crystal in g/cm^3.

No Sample	Composition	ρ_m	ρ_{ce}	ρ_{cr}
516	MgF_2	0.85	2.97	3.15
517	MgF_2:WO_3	0.85	2.97	3.15
519	BaF_2	1.56	4.9	4.89
520	BaF_2:WO_3	1.56	4.8	4.89
521	$BaMgF_4$	1.63	4.5	4.53
522	$BaMgF_4$:WO_3	1.55	4.65	4.53

As can be seen from the results presented in Table 1, the density of the obtained ceramics is equal to the density of the corresponding crystal. The air volume in the BaF_2 and $BaMgF_4$ mixtures is 50% and 70% in MgF_2. However, empty voids are not formed in the ceramics. The same air volumes are present in the mixtures for making ceramics based on YAG, alumina-magnesium spinel, in which voids make up half of the volume.

Table 2 provides information on the synthesis efficiency of the described ceramics when processed with electron beams at an energy of 1.4 MeV and a power density of 15 kW/cm^2. Here, the synthesis efficiency is defined as the ratio of the mass of the synthesized sample to the mass of the charge placed in the crucible.

Table 2. Synthesis efficiency of the studied ceramics.

No Sample	Sample, description	Weight sample, g	Mass loss ΔM, %	Synthesis efficiency
516	MgF_2	42.21	0.40	99.6
517	MgF_2:WO_3	39.26	0.97	99.0
519	BaF_2	66.97	0.75	99.3
520	BaF_2:WO_3	75.9	0.53	99.5
521	$BaMgF_4$	75.71	0.53	99.5
522	$BaMgF_4$:WO_3	75.53	0.56	99.4

As indicated by the presented results, the efficiency of radiation synthesis of ceramics from the used raw materials is very high. The ceramic samples have a weight of up to 75 grams. There are the results of particle distribution based on volume only in figure 1, the relationship between the total volume of particles and their sizes. In MgF_2, the primary range of particle volumes is between 0.2 and 5 micrometers. In BaF_2, the range of particle volumes is much broader, ranging from 0.03 to 30 micrometers. However, the synthesis efficiencies of MgF_2 and BaF_2 ceramics are similar. The quantity of small particles, nano- and sub-micron-sized, in the examined powders is much greater than for micron-sized particles. Nevertheless, their proportion in the overall powder volume is small. Since the synthesis efficiency is 99%, it can be confidently assumed that the ceramics were primarily formed from micron-sized particles. The conclusion is also interesting that ceramics of $BaMgF_4$ are also produced with high efficiency (see Table 2).

3. Results and discussions

3.1. Structure of ceramics

X-ray diffraction patterns were collected using a Bruker D8 ADVANCE (AXS, Berlin, Germany) diffractometer equipped with a scintillation detector. The measurements were performed in step-scan mode over a diffraction angle range (2θ) of 10 to 90° 2θ, employing a CuKα radiation source. The experiments were conducted at room temperature with a flat sample in Bragg-Brentano geometry. The experimental conditions were as follows: 40 kV, 40 mA, exposure time - 2 seconds, step size - 0.02° 2θ. Data processing was conducted using the DIFFRAC plus software package. Sample identification was performed using the Powder Diffraction File (PDF-2) database (ICDD, 2007) and indexing was carried out using the EVA software (Bruker, 2007). The TOPAS 4.2 software package (Bruker, 2008) was used for Rietveld profile fitting, degree of crystallinity, crystallite size and unit cell parameters calculation. Rietveld refinements provided agreement factors, R_{wp}, in the range from 4.9 to 8.4%. The diffraction patterns of the samples (Figures 3-5) have small peaks, indicating the possibility of the presence of certain impurity phases in small quantities.

Figures 3-5 X-ray diffraction pattern of MgF_2 (a) and MgF_2:W (b), BaF_2 (a) and BaF_2:W (b), $BaMgF_4$ (a) and $BaMgF_4$:W (b) samples. The hkl indices of the reflexes of $BaMgF_4$ are marked. Reflections belonging to $BaMgF_4$ and $Ba_6Mg_7F_{26}$ are marked with ◊ and o, respectively.

The results of the study are presented in Table 3 (Appendix). The following data from the PDF-2 database (ICDD, 2007) were used for qualitative phase analysis and indexing of the diffraction patterns:

PDF 01-070-0212 «Magnesium fluoride (MgF_2)», symmetry is tetragonal lattice, space group is *P*42/*mnm* (#136), a = 4.6213 Å, c = 3.0519 Å.

PDF 00-004-0452 «Barium fluoride (BaF_2)», symmetry is face-centered cubic lattice, space group is *Fm–3m* (#225), a = 6.2001 Å.

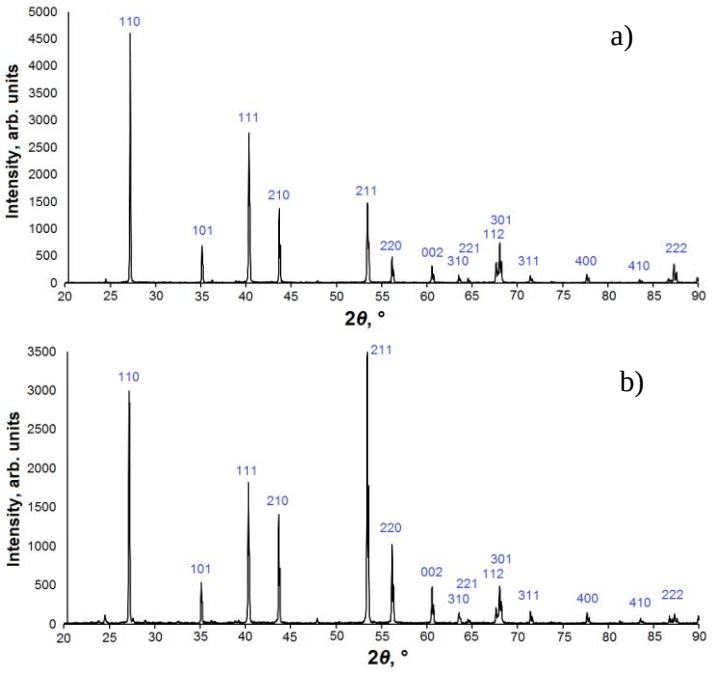

Fig.3. X-ray diffraction pattern of MgF_2 (a) and MgF_2:W (b) samples. The hkl indices of the reflexes of MgF_2 are marked.

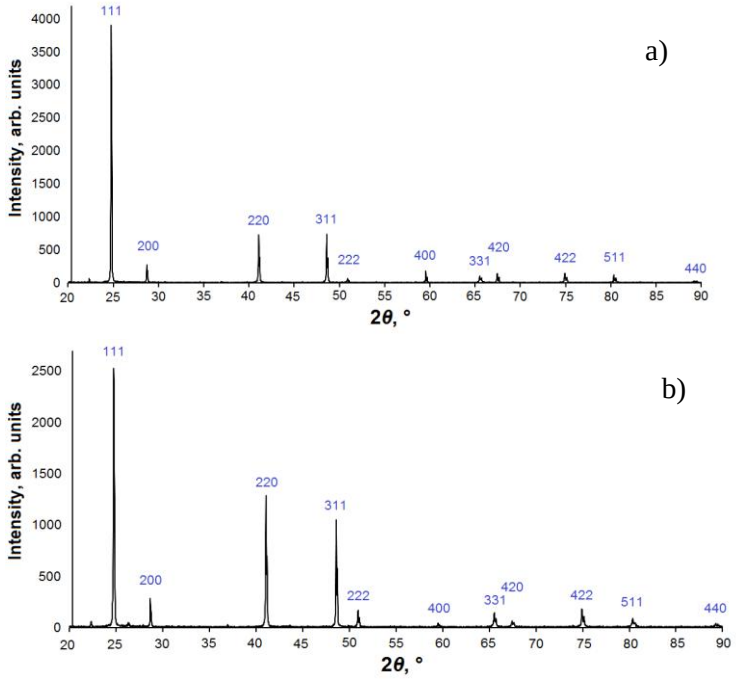

Fig.4. X-ray diffraction pattern of BaF_2 (a) and BaF_2:W (b) samples. The hkl indices of the reflexes of BaF_2 are marked.

PDF 01-087-0201 «Barium magnesium fluoride ($BaMgF_4$)», symmetry – base-centered orthorhombic lattice, space group is *Cmc*21 (#36), $a = 4.126$ Å, $b = 14.518$ Å, $c = 5.821$ Å.

PDF 01-087-0192 «Barium magnesium fluoride ($Ba_6Mg_7F_{26}$)», symmetry is body-centered orthorhombic lattice, space group – *Immm* (#71), $a = 5.8535$ Å, $b = 12.1495$ Å, $c = 15.1109$ Å.

The diffraction patterns of the samples (Figures 3-5) have small peaks, indicating the possibility of the presence of certain impurity phases in small quantities. In all synthesized samples, the dominant phase is the crystalline phase of the corresponding composition, regardless of the presence of tungsten oxide in the charge.

In addition, the precursor phase is detected in all samples. The WO_3 phase is found in MgF_2, BaF_2 is retained along with the $BaMgF_4$ phase. The MgO phase is found in some samples. The appearance of this phase can be explained by oxidation because the synthesis is carried out in an open atmosphere. However, the results of XRD studies show that during radiation treatment, the indicated crystalline phases, including solid solutions, are formed in ceramics.

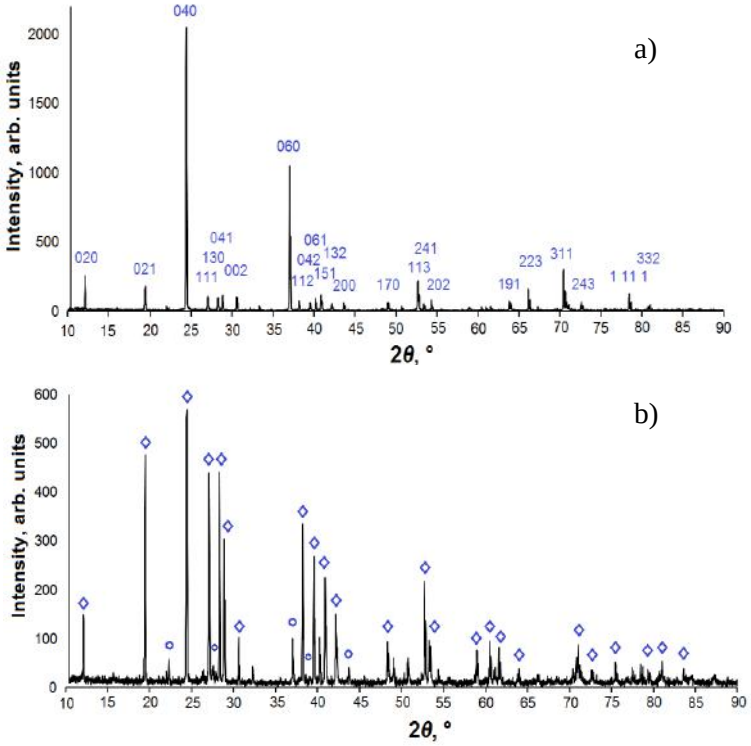

Fig.5. X-ray diffraction pattern of $BaMgF_4$ (a) and $BaMgF_4$:W (b) samples.

Thus, at radiation treatment by powerful flows of high-energy electrons of the charge based on alkaline-earth metal fluorides with tungsten oxide for activation, ceramics with the presence of crystalline phase is formed. Note that the synthesis results depend on the prehistory of the starting substances. The surface microstructure of alkaline earth metal fluorides was studied using a MIRA 3 LMU scanning electron microscope (SEM) (TESCAN). The elemental composition of the samples was obtained using an INCA PentaFET-x3 analyzer (Oxford Instruments, England). To study the surface, a small amount of sample was applied on a conductive carbon tape. A nanometer-thin layer of carbon was applied to the surface of the samples from above by thermal deposition.

The results of composition analysis of synthesized samples of MgF_2, BaF_2, MgF_2:W, BaF_2:W, $BaMgF_4$ and $BaMgF_4$:W fluorides are shown in Fig. 6. In samples MgF_2, BaF_2 the main elements of composition are dominant: Mg, Ba and F. In addition, some amount of oxygen is found in the composition of the ceramic samples. Its presence is explained by the fact that the synthesis is carried out in an open atmosphere, oxygen can enter the pores of the sample. In samples MgF_2:W, BaF_2:W tungsten is detected. We emphasise that tungsten oxide was added to the charge in an amount of 2% of the total mass. The detection of tungsten in ceramics indicates that a significant part of it does not have time to leave the synthesis zone for less than 1 s. and remains in the sample.

Fig. 7 presents SEM images of samples MgF_2:W, BaF_2:W with presentation of the map of distribution of elements by volume. From the presented results it can be seen that part of tungsten is included in the crystallites, but a significant part is concentrated in the intercrystalline space.

As follows from the presented results, the injected activator is distributed very unevenly over the volume of ceramics. The inhomogeneous distribution of the activator is also evident in the measured distribution maps. The main significant conclusion for the method is that after radiation synthesis a part of tungsten was retained in the formed ceramics.

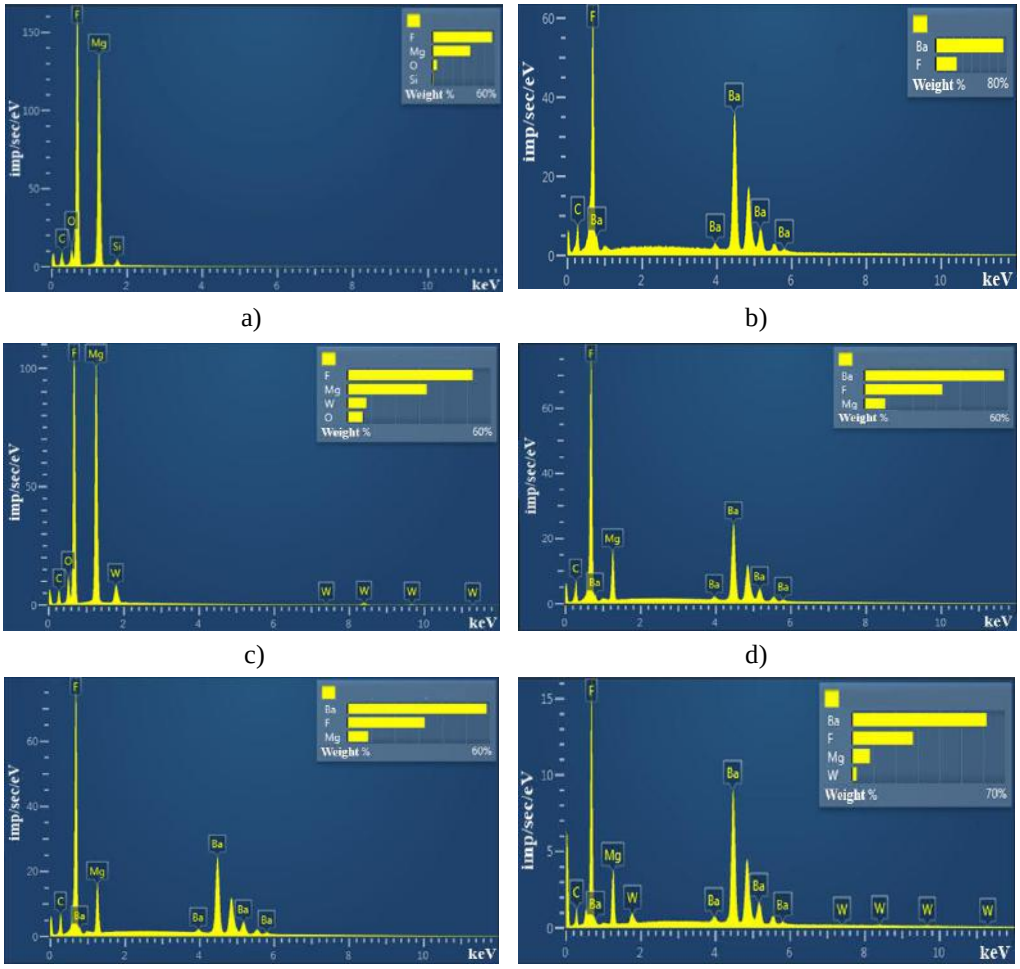

Fig.6. Composition results of MgF_2 (a) and BaF_2 (b) samples (top), MgF_2:W (c), BaF_2:W (d), and $BaMgF_4$ (e), $BaMgF_4$:W (f) (bottom).

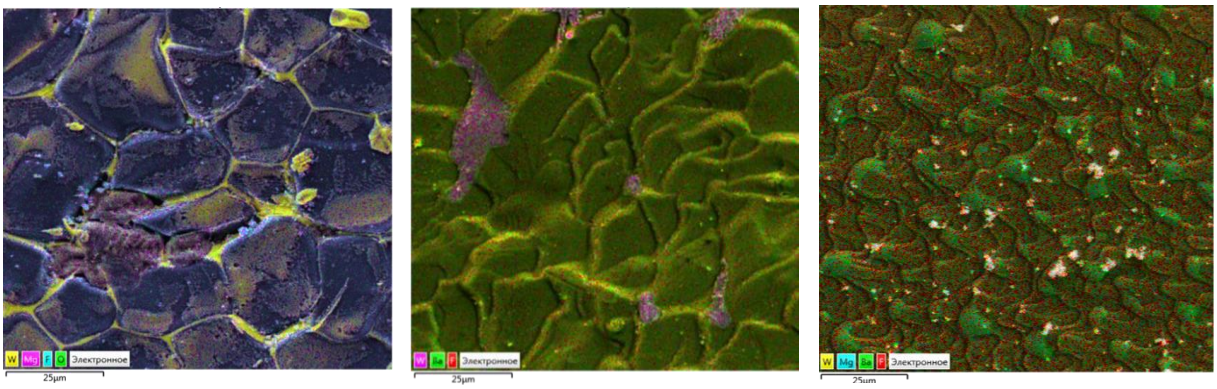

Fig.7. Mappings of the distribution of elements in the samples MgF_2:W (a), BaF_2:W (b), $BaMgF_4$:W (c).

3.2. Luminescence of ceramics

A study cycle of the luminescent properties of tungsten-activated samples of BaF_2, MgF_2 and $BaMgF_4$ synthesized ceramics was carried out, including the spectra of photoexcitation and photoluminescence (PL) under stationary conditions using a SOLAR SM2203 spectrometer. In a summarized form, the spectra are presented in Figure 8.

The figures depict series of luminescence spectra taken from various sections of synthesized ceramic samples. The spectra of all fragments from each sample are similar. Measurements were conducted under identical conditions. Therefore, the presented results can provide an idea of the variation in their intensities over the sample area. We emphasize that the shapes of the bands do not change. In the samples of ceramics synthesized from the charge containing tungsten oxide and without it, the luminescence bands are usually slightly different in position. The luminescence bands in the activated samples are slightly shifted to the long-wave region of the spectrum. The luminescence excitation spectra differ significantly. In non-activated samples luminescence is excited by ultraviolet (UV) radiation in the range from 200 to 260 nm. With the introduction of the activator the excitation band becomes wider. The luminescence is excited by UV radiation in the region up to 300 nm. Changes in the excitation spectra of luminescence and the positions of the bands indicate that with the introduction of tungsten in the crystalline phase of ceramics there is a transformation of the structure of the luminescence centers or, more likely, the local structure in their surroundings. Consequently, tungsten enters the ceramics during synthesis.

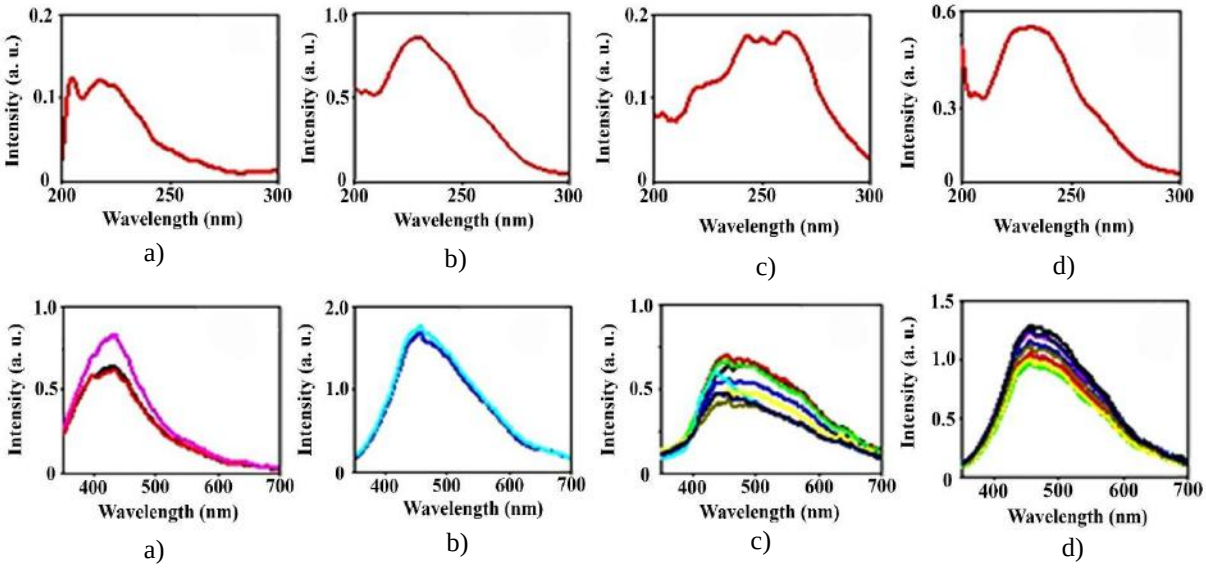

Fig.8. Excitation (top row) and luminescence (bottom row) spectra of $BaMgF_4$ samples (a) when excited at 220 nm, and $BaMgF_4$:W (b), BaF_2:W (c), MgF_2:W3 (d) when excited in the 260 nm range.

Impulse cathodoluminescence (ICL) studies of synthesized ceramic samples have been conducted. An electron accelerator, generating single pulses with the following characteristics, was used as the excitation source for cathodoluminescence: electron energy = 0.25 MeV, pulse duration at half-height = 10 ns, current density at the maximum up to 100 A/cm², and the excitation energy density could vary in the range from 1 to 50 mJ/cm². Luminescence registration was performed using a photomultiplier tube PMT-97 with the use of a monochromator MDR-23 (spectral range 200-2000 nm, linear dispersion 1.3 nm/mm) and a digital oscilloscope Tektronix DPO3034 (300 MHz). Registration of integrated emission spectra of the ICL was carried out using an optical fiber spectrometer AvaSpec-2048 (200 - 1100 nm). The emission spectrum was corrected for the spectral sensitivity of the optical path.

The results of measurements of integrated emission spectra of ICL samples of synthesized ceramics are presented in Fig. 9. The spectra were not normalized for intensity and are presented in a form convenient for comparison. Cathodoluminescence of ceramic samples synthesized from raw materials containing tungsten differs significantly from the luminescence of ceramic samples from raw materials that do not contain tungsten oxide. The cathodoluminescence spectrum of MgF_2: W shows a wide and complex band with a maximum around 570 nm. In ICL spectrum of MgF_2 ceramics, a band with a maximum around 400 nm is observed. In the spectra of ICL of BaF_2 and BaF_2: W ceramics, a band around 390 nm is observed. There is an additional wide band in the range of 520-620 nm in the BaF_2: W spectrum. In the ICL spectrum of $BaMgF_4$ ceramics, a wide band in the range of 400-500 nm is observed, and in $BaMgF_4$: W, the band significantly broadens in the 500-650 nm range. Thus, luminescence in the 520-620 nm range is observed in all ceramic samples synthesized from raw materials containing tungsten oxide.

Some difference of luminescence spectra under photo- and cathode excitation may be due to the following. At optical excitation in PL measurements, the energy is transferred directly to the luminescence center or absorption center with subsequent transfer to the luminescence center. At excitation by high-energy electrons not less than 99% of all absorbed energy of the flux is spent on the creation of electron-hole excitations in the matrix, the created electron-hole excitations transfer energy to the luminescence centers. The influence of the method of excitation energy transfer to the luminescence center can be explained by the complex structure of the luminescence centers, the presence of their own lattice defects in their structure.

The nature of luminescence in tungsten-activated crystals and ceramics of alkaline and alkaline-earth metal fluorides is unknown. However, a significant increase of luminescence intensity by introducing metal ions of tungsten, uranium, titanium into the lattice of metal fluorides is supposed to be promising for obtaining effective scintillators. It should be noted that for introduction of tungsten at thermal synthesis in the charge additionally oxides and hydrides of metals are added. Their introduction contributes to the preservation of tungsten in the reaction zone. Probably, the formation of luminescence centers in the ceramics synthesized by us is promoted by oxygen introduced with tungsten.

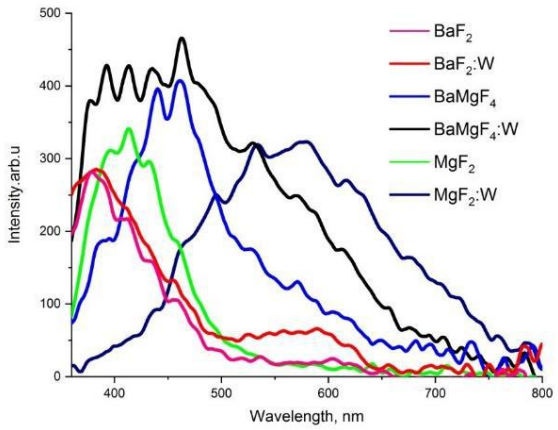

Fig.9. Integral spectra of impulse cathodoluminescence of ceramic samples.

It is possible that oxygen from the environment is involved in the synthesis: the synthesis is carried out in an open atmosphere. Obviously, the active element of the structure of the luminescence centers are anionic vacancies [16], which are always present in metal oxides or as part of anions in the lattice of crystals. Anionic vacancies with trapped electrons in LiF (M centers) are one of the most effective luminescence centers. The assumption that oxygen-vacancy complexes in the crystal lattice can be effective luminescence centers was suggested in [17]. Luminescence of oxygen-vacancy complexes is also observed in other materials, for example, in quartz [18] existing in different phase states [19], in topaz [20, 21], corundum [22], magnesium oxide [23]. Kinetic decay curves after excitation by electron pulses with an energy of 250 keV and a duration of 10 ns were measured. The results of luminescence decay kinetics for BaF_2 and BaF_2:WO_3 are presented in Figure 10.

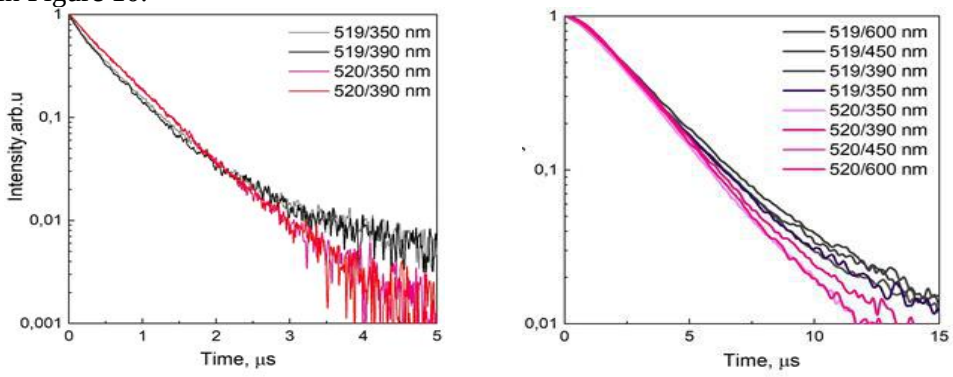

a) b)

Fig.10. Kinetic decay curves of cathodoluminescence for BaF_2 (a) and BaF_2 (b):W

The luminescence spectra are complex and different for all studied ceramic samples. Measurements of kinetic decay curves provide some insight into the change in spectra over time in different spectral regions. The inserts in the figures show sample numbers and the wavelengths of the luminescence spectra at which the measurements were performed. In the time range up to 4 μs, the decay of luminescence in BaF_2: W ceramic samples can be described as a linear function in logarithmic coordinates, while the decay of luminescence in BaF_2 ceramic samples is nonlinear. Differences in kinetic curves over time are also observed for longer times. In the time range of 5-15 μs, the decrease in luminescence intensities is nearly linear in semi-logarithmic coordinates. The rate of luminescence decay in activated ceramic samples is higher than in non-activated ones across the entire measured spectral range (Figure 11).

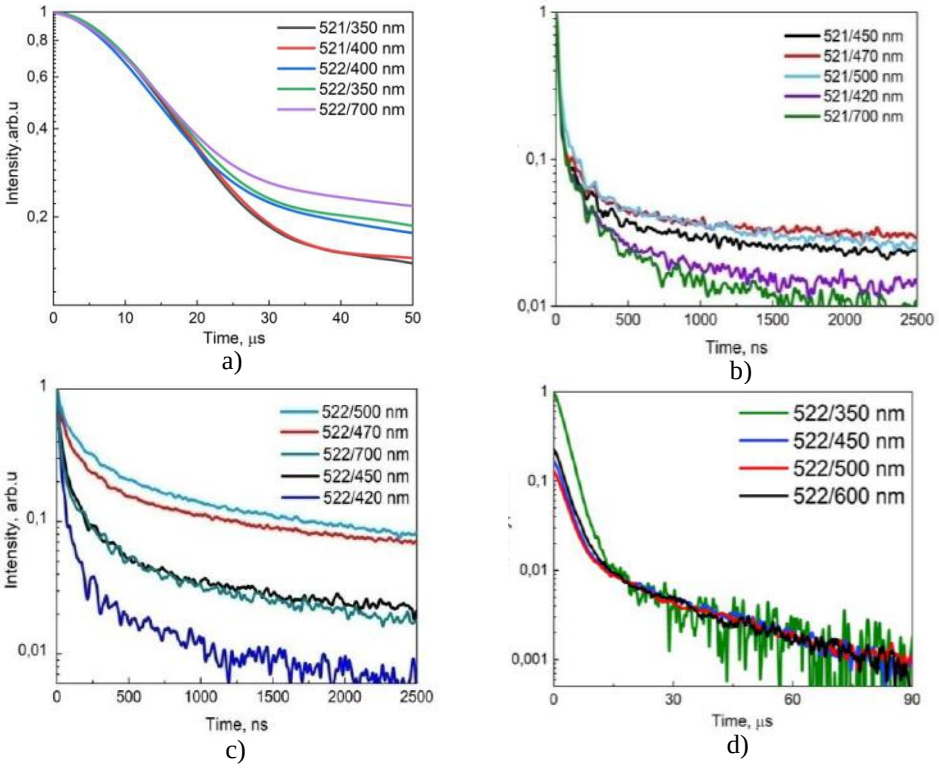

Fig.11. Kinetic decay curves of cathodoluminescence for $BaMgF_4$, BaMgF4:W (a), $BaMgF_4$ (b), BaMgF4:W (c), BaMgF4:W (d) in the nanosecond range.

The decrease in luminescence continues throughout the entire measured spectrum range and within the time range of several microseconds. In the time range of 50 to 500 nanoseconds, a significant difference in the intensity decay of $BaMgF_4$ and $BaMgF_4$:W luminescence is observed in different parts of the spectra, which persist up to 10 microseconds. Thus, the kinetic characteristics of cathodoluminescence in the investigated samples of solid solutions of alkaline earth metal fluorides in activated and non-activated synthesized ceramics are different.

4. Conclusion

Radiation synthesis method for ceramics made from dielectric refractory materials is characterized by high speed, high efficiency, and the absence of the need for additional substances to form new phase structures. The development and establishment of this method are currently in the process of exploring its potential for expanding the range of ceramics that can be synthesized through radiation methods, studying the dependence of synthesis efficiency on radiation processing parameters, the properties of the starting materials for synthesis, and the nature of the processes that facilitate ceramic formation in the presence of intense radiation flux. In this study, using the example of the $Ba_xMg_{(2-x)}F_4$:W system, it is demonstrated that it is possible to introduce activators and modifiers into the forming ceramics, leveraging the unique qualities of radiation synthesis.

The possibility of synthesizing MgF_2 and BaF_2 ceramics by directly exposing the material to an electron beam with an energy of 1.4 MeV and a power density of 15 kW/cm² has also been shown. Samples with

dimensions of up to 10x5x0.4 cm³ and weights of up to 40 g (MgF_2) and 70 g (BaF_2) have been obtained. The density of the synthesized ceramic samples is 3.0±0.3 g/cm³ and 4.8±0.5 g/cm³, which is equivalent to the density of the corresponding single crystals. In cross-section, the samples are solid and do not contain voids, as observed in YAG ceramics [10]. The efficiency of synthesis, defined as the ratio of the mass of the ceramic sample to the mass of the row charge, depends on the characteristics of the starting materials used, primarily their particle size distribution [14]. When using powders of MgF_2 and BaF_2 for synthesis with particle sizes of 0.2-4 μm and a peak distribution at ~0.8 μm and 0.04-25 μm with a peak distribution at ~10 μm, the synthesis efficiency reaches 99%. Adding tungsten oxide (WO_3) to the charge in an amount of up to 2% of the total weight does not affect the formation of MgF_2:W and BaF_2:W ceramics.

Ceramics with complex compositions, such as $BaMgF_4$ and $BaMgF_4$:W, are also efficiently formed in the presence of intense radiation flux, with densities comparable to those of crystals. It appears that the particle size distribution functions of the used powders are sufficient to avoid the creation of local non-stoichiometry during the formation of the crystalline phase. The X-ray diffraction patterns of $BaMgF_4$:W ceramics, attributed to $BaMgF_4$ phase lines with local non-stoichiometry $Ba_6Mg_7F_{26}$, have very low intensity.

Ceramic materials are highly defective. Their luminescence upon excitation is mainly due to the presence of defects in the crystal lattice and impurities. Synthesizing ceramics with activators leads to changes in their luminescent properties. Research has shown that adding tungsten oxide (WO_3) to the charge for ceramic synthesis in amounts up to 2% does not affect synthesis efficiency but results in changes in luminescent properties. The excitation and emission spectra are altered, with shifts towards longer wavelengths. When excited by nanosecond electron beam pulses with an energy of - 0.25 MeV, the ceramic samples exhibit luminescence with specific properties. In the integrated spectra of samples synthesized from charges with WO_3, shifts or new bands in the long-wavelength region are observed. In MgF_2:W, BaF_2:W, and $BaMgF_4$:W ceramics, luminescence in the 450-700 nm range appears.

The luminescence decay kinetics after excitation by nanosecond electron beam pulses also vary. Up to 4 μs, the luminescence decay of BaF_2:W ceramics follows a linear function in logarithmic coordinates, whereas the decay of BaF_2 luminescence is nonlinear. Differences in the kinetic curves are observed even at longer times. In activated samples, the linear decay range in the 5-25 ns range in semi-logarithmic coordinates is wider than in $BaMgF_4$, and the intensity decay is greater. In the 50-500 ns range, significant differences in the intensity decay magnitude between $BaMgF_4$ and $BaMgF_4$:W are observed in various parts of the spectra, which persist up to 10 μs.

The combination of the results of the studies on ceramics synthesized from alkali-earth metal fluorides allows the conclusion that it is possible to introduce tungsten into the ceramic lattice during synthesis in the presence of intense radiation flux. Tungsten does not have time to leave the synthesis zone during the short synthesis time and remains in the lattice.

Conflict of interest statement

The authors declare that they have no conflict of interest in relation to this research, whether financial, personal, authorship or otherwise, that could affect the research and its results presented in this paper.

CRediT author statement

Alpyssova G.K., **Lisitsyn V.M.:** Conceptualization, Data Curation, Writing Original Draft, Supervision**; Vaganov V.A.:** Visualization, Methodology; **Kaneva E.V.:** Formal analysis, Investigation; **Lisitsyna L.A.:** Writing Review & Editing, Supervision; **Strelkova A.:** Writing – Review & Editing, Validation; **Denisov I.P.:** Investigation.
The final manuscript was read and approved by all authors.

Funding

This research has been funded by TPU and INP SB RAS under the project of the Russian Science Foundation of the Russian Federation. (Grant No. 23-73-00108)

Acknowledgements

Work on the study of morphology, photoluminescence, SEM was carried out by in E.A. Buketov Karaganda University under the project of the Science Committee of the Ministry of Science and Higher Education of the Republic of Kazakhstan (Grant No. AP19579177).

References

1 Atroshchenko L.V., Burachas S.F., Gal'chinetskii L.P., Grinev B.V., Ryzhikov V.D., Starzhinskiy N.G. (1998) Kristally scintilljatorov i detektory ionizirujushhih izluchenij na ih osnove [Scintillator crystals and detectors of ionizing radiations on their base]. *Naukova dumka*, 312 Available at: www.irbis-nbuv.gov.ua/cgi-bin/irbis64r_81/cgiirbis_64.exe?Z21ID=&I21DBN=REF&P21DBN=REF&S21STN=1&S21REF=10&S21FMT=fullw [in Russian].

2 Fumiya N., Takumi K., Go O., Naoki K., Noriaki K., Kentaro F., Takayuki Y. (2018) Scintillation, Dosimeter and Optical Properties of MgF2 Transparent Ceramics Doped with Gd3+. *Mater. Res. Bull.*, 98, 83–88. DOI: 10.1016/j.materresbull.2017; 09: 058.

3 Renfro G., Halliburton L., Sibley W., Belt R. (2000) Radiation Effects in LiYF4. *J. Phys. C Solid State Phys.*, 13, 1941. DOI: 10.1088/0022-3719/13/10/013.

4 Morato S.P., Macedo T.C. (1983) F and photochromic Centers in LiYF4: Nd Crystals *Radiat. Eff.*, 72, 229–235. DOI: 10.1080/00337578308218647.

5 Wang M., Mi C.C., Wang W.X, Liu C.H.Y., Wu F., Xu Z.R., Mao C.B., Xu S.K. (2009) Immunolabeling and NIR-excited fluorescent imaging of hela cells by using NaYF4:Yb, Er upconversion nanoparticles. *ACS Nano.*, 3, 1580-1586. DOI: 10.1021/nn900491j.

6 Li Z.Q., Zhang Y., Jiang S. (2008) Multicolor core/shell-structured upconversion fluorescent nanoparticles. *Adv. Mater*., 20, 4765–4769. DOI: 10.1002/adma.200801056.

7 Ma J.J., Zhu W.J., Lei L., Deng D.G., Hua Y.J., Yang Y.M., Xu S.Q., Prasad P.N. (2021) Highly efficient NaGdF4:Ce/Tb nanoscintillator with reduced afterglow and light scattering for high-resolution X-ray imaging. *ACS Appl. Mater. Interfaces*, 13, 44596–44603. DOI: 10.1021/acsami.1c14503.

8 Yang B., Yin L.X., Niu G.D., Yuan J.H., Xue K.H., Tan Z.F., Miao X.S., Niu M., Du X.Y., Song H.S. Lifshitz E., Tang J. (2019) Lead-free halide Rb2CuBr3 as sensitive X-ray scintillator. *Adv. Mater.*, 31, 1904711. DOI: 10.1002/adma.201904711.

9 Buchter S., Fan T., Liberman V., Zayhowski J., Rothschild M., Mason E., Cassanho A., Jenssen H., Burnett J. (2001) Periodically Poled BaMgF4 for Ultraviolet Frequency Generation. *Opt. Lett.*, 26, 1693–1695. DOI:10.1364/OL.26.001693.

10 Lisitsyn V., Mussakhanov D., Tulegenova A., Kaneva E., Lisitsyna L., Golkovski M., Zhunusbekov A.M. (2023) The Optimization of Radiation Synthesis Modes for YAG:Ce Ceramics. *Materials*, 16, 3158. DOI: 10.3390/ma16083158.

11 Karipbayev Zh., Alpyssova G., Mussakhanov D., Kukenova A., Tulegenova A. (2020) Time-resolved luminescence excited with N_2 laser of YAG:CE Ceramics formed by electron beam assisted synthesis. *Eurasian Physical Technical Journal*, 17, 73 – 76. DOI: 10.31489/2020NO1/73-76.

12 Lisitsyn V., Golkovski M., Lisiysyna L., Dauletbekova A., Mussakhanov D., Vaganov V., Tulegenova A., Karipbayev Z. (2019) MgF_2-Based Luminescing Ceramics. *Russ. Phys.J.*, 61. DOI: 10.1007/s11182-019-01617-y.

13 Lisitsyn V., Polisadova E., Lisitsyna L., Tulegenova A., Denisov I., Golkovski M. (2023) Efficiency Dependence of Radiation-Assisted Ceramic Synthesis Based on Metal Oxides and Fluorides on Initial Powder Particle Sizes. *Photonics*, 10: 1084. DOI: 10.3390/photonics10101084.

14 Alpyssova G., Lisitsyn V., Bakiyeva Zh., Chakin I., Kaneva E., Afanasyev D., Tussupbekova A., Vaganov V., Tulegenova A., Tuleuov S. (2024) Characterization of ZnWO4, MgWO4, and CaWO4 Ceramics Synthesized in the Field of a Powerful Radiation Flux. *Ceramics*, 7, 1085-1099. DOI: 10.3390/ceramics7030071.

15 Gingl F. (1997) $BaMgF_4$ and $Ba_2Mg_3F_{10}$: New Examples for Structural Relationships Between Hydrides and Fluorides. Z. Anorg. *Allg. Chem*., 623, 705–709. DOI: 10.1002/zaac.199762301112.

16 Kotomin E.A., Popov A.I. (1998) Radiation-induced point defects in simple oxides. *Nuclear Instruments and Methods in Physics Research B*, 141 (1), 1-15. DOI: 10.1016/S0168-583X(98)00079-2.

17 Lisitsyna L., Lisitsyn V. (2013) Composition Nanodefects in Doped Lithium Fluoride Crystals. *Phys. Solid State*, 55. DOI: 10.1134/S1063783413110139.

18 Garmysheva T., Shendrik R., Paklin A., Shalaev A., Kaneva E., Nepomnyashchikh A. (2022) Luminescence of Oxygen-Deficient Centers in Quartz Glasses. *Glass Phys. Chem.*, 48, 232–235. DOI: 10.1134/S1087659622030038.

19 He J., Jusnes K.F., Tangstad M. (2021) Phase transformation in quartz at elevated temperatures. *Aspects Min Miner Sci.*, 6(1), 691 – 698. DOI: 10.31031/AMMS.2021.06.000629.

20 Bernal R., Souza D., Valerio M., Cruz-Vázquez C., Barboza-Flores M. (2006) Optically Stimulated Luminescence Dosimetry Performance of Natural Brazilian Topaz Exposed to Beta Radiation. *Radiat. Prot. Dosimetry*, 119, 161–163. DOI: 10.1093/rpd/nci677.

21 Priest V., Cowan D., Yasar H., Ross F. (1991) ESR, Optical Absorption, and Luminescence Studies of the Peroxy-Radical Defect in Topaz. *Phys. Rev. B Condens. Matter.*, 44, 9877–9882. DOI: 10.1103/PhysRevB.44.9877.

22 Surdo A., Pustovarov V.A., Kortov V., Kishka A., Zinin E. (2005) Luminescence in Anion-Defective α - Al_2O_3 Crystals over the Nano-, Micro- and Millisecond Intervals. *Nucl. Instrum. Methods Phys. Res. Sect. -Accel. Spectrometers Detect. Assoc. Equip*., 543, 234–238. DOI: 10.1016/j.nima.2005.01.189.

23 Nikiforov S., Lisitsyn V., Ananchenko D.V., Kasatkina Y.P, Golkovski M.G., Ishchenko A. (2022) Luminescent and Dosimetric Properties of Magnesium Oxide Ceramics Synthesized by a High-Energy Electron Beam. *Tech. Phys. Lett.*, 48(6):8. DOI: 10.21883/TPL.2022.06.53454.19174.

AUTHORS' INFORMATION

Lisitsyn, Victor M. – Doctor of Physical and Mathematical Sciences, Professor, Department of Materials Science, National Research Tomsk Polytechnic University, Tomsk, Russia; Scopus Author ID: 35577898600, https://orcid.org/0000-0002-2075-4796; lisitsyn@tpu.ru

Vaganov, Vitalii A. – Master (Eng.), Researcher, Department of Materials Science, Engineering School, National Research Tomsk Polytechnic University, Tomsk, Russia; Scopus Author ID: 56545484700; https://orcid.org/0000-0002-4644-9095; nba_vitas@mail.ru

Alpyssova, Gulnur K. – PhD, Associate Professor, Department of Radiophysics and Electronics, E.A. Buketov Karaganda University, Karaganda, Kazakhstan; Scopus Author ID: 57204979025, https://orcid.org/0000-0002-7164-2188; gulnur-0909@mail.ru

Kaneva, Ekaterina V. – PhD, Candidate of Geological and Mineralogical Sciences, Senior Researcher, X-ray Analysis Laboratory, Vinogradov Institute of Geochemistry SB RAS, Irkutsk, Russia. Scopus Author ID: 54883446000; https://orcid.org/0000-0001-7155-6784; kev604@mail.ru

Lisitsyna, Liudmila A. – PhD, Professor, Department of Physics, Chemistry and Theoretical Mechanics, Tomsk State University of Architecture and Building, Tomsk, Russia; Scopus Author ID: 6602905153; lisitsyna@mail.ru

Denisov, Igor P. – Researcher, Department of Materials Science, National Research Tomsk Polytechnic University, Tomsk, Russia. Scopus AuthorID: 58713871500; dip@tpu.ru

Strelkova, Assel – Master (Sci.), Department of Technical Physics, L.N. Gumilyov Eurasian National University, Astana, Kazakhstan; Scopus Author ID:: 696600x0, https://orcid.org/0000-0002-8437-811X; a.strelkova@nurorda.kz

Appendix

Table 3. The results of the phase composition investigation.

Sample	Main Phase	Degree of crystallinity	Crystallite size	Cell parameters from database	Refined cell parameters
MgF_2	MgF_2	99.9 (±5) %	413 (±25) nm	PDF 01-070-0212(MgF_2), *P*42/*mnm* (#136), *a* = 4.6213 Å, *c* = 3.0519 Å.	*P*42/*mnm*, *a* = 4.620(5) Å, *c* = 3.050(6) Å, *V* = 65.1(1) Å^3
MgF_2: WO_3	MgF_2	99.6 (±5) %	296 (±35) nm	PDF 01-070-0212(MgF_2), *P*42/*mnm* (#136), *a* = 4.6213 Å, *c* = 3.0519 Å.	*P*42/*mnm*, *a* = 4.619(6) Å, *c* = 3.050(6) Å, *V* = 65.1(1) Å^3
BaF_2	BaF_2	99.9 (±5) %	221 (±22) nm	PDF 00-004-0452 (BaF_2), *Fm–3m* (#225), *a* = 6.2001 Å.	*Fm–3m*, *a* = 6.230(5) Å, *V* = 241.8(1) Å^3
BaF_2:WO_3	BaF_2	99.9 (±5) %	123 (±10) nm	PDF 00-004-0452 (BaF_2), *Fm–3m* (#225), *a* = 6.2001 Å.	*Fm–3m*, *a* = 6.228(4) Å, *V* = 241.6(1) Å^3
$BaMgF_4$	$BaMgF_4$	99.9 (±5) %	92 (±15) nm	PDF 01-087-0201 ($BaMgF_4$), *Cmc*21 (#36), *a* = 4.126 Å, *b* = 14.518 Å, *c* = 5.821 Å.	*Cmc*21, *a* = 4.136(7) Å, *b* = 14.490(5) Å, *c* = 5.830(7) Å, *V* = 349.4(1) Å^3
$BaMgF_4$:WO_3	$BaMgF_4$	89.2 (±5) %	87 (±11) nm	PDF 01-087-0201 ($BaMgF_4$), *Cmc*21 (#36), *a* = 4.126 Å, *b* = 14.518 Å, *c* = 5.821 Å.	*Cmc*21, *a* = 4.134(6) Å, *b* = 14.490(3) Å, *c* = 5.827(7) Å, *V* = 349.0(2) Å^3
	$Ba_6Mg_7F_{26}$		352 (±44) nm	PDF 01-087-0192 ($Ba_6Mg_7F_{26}$), *Immm* (#71), *a* = 5.8535 Å, *b* = 12.1495 Å, *c* = 15.1109 Å.	*Immm*, *a* = 5.825(6) Å, *b* = 12.159(10) Å, *c* = 15.147(13) Å, *V* = 1072.8(9) Å^3

EURASIAN PHYSICAL TECHNICAL JOURNAL

2024, Volume 21, No. 4(50)

https://doi.org/10.31489/2024No4/49-60

Received: 24/06/2024 Revised: 10/08/2024 Accepted: 17/12/2024 Published online: 25/12/2024

Original Research Article

UDC 536.8

SIMULATION OF CONDITIONS FOR ACHIEVING HIGH ELECTRICAL POWER AND EFFICIENCY IN A STIRLING ENGINE WITH A FREE WORKING PISTON

Sabdenov K. O.[1]*, Erzada M.[1], Zholdybaeva G.T.[2]

[1] L.N. Gumilyov Eurasian National University, Astana, Kazakhstan

[2] M. Saparbaev South Kazakhstan Humanitarian Institute, Shymkent, Kazakhstan

Corresponding author: sabdenovko@yandex.kz

Abstract. *A simulation of the Stirling engine was carried out, where the temperature variability in the cooler and heater is taken into account, and the engine itself generates electric current. The study was carried out in the temperature range when the piston and displacer move synchronously. The possibility of increasing engine power by reducing hydraulic resistance in the regenerator is shown. It was also discovered that as the electrical load on the generator increases, the work produced by the engine can also increase. This indicates that there is a maximum of electrical energy production depending on the load. The increased rigidity of the displacer spring contributes to an increase in engine power and its efficiency.*

Keywords: free-piston Stirling engine, regenerator, displacer, efficiency.

1. Introduction

Due to the limited reserves of oil, gas and high-quality coal on the planet, the problem of energy shortages will arise in the near future. Therefore, new thermodynamic cycles and the possibility of creating heat engines based on them are being sought [1–4]. In this context, the Stirling engine deserves attention; it unites a large family of devices whose operation is based approximately on the thermodynamic Stirling cycle [5, 6]. It belongs to a wide class of low-power motors for producing mechanical work and/or electrical energy from low-potential heat sources [7–11]. Based on the Stirling engine, it is possible to create an energy system with distributed generation [12, 13]. This is important for Kazakhstan, which has a low population density and rich solar energy resources. Mathematical modeling of the Stirling engine makes it relatively easy to find the most important conditions and parameters necessary to create devices with the highest efficiency.

Widely used isothermal models [1–3, 6, 13–15] have low accuracy and are not convenient for designing real Stirling engines, although they allow us to understand their basic properties. Therefore, a model is needed that takes into account the temperature change in all parts of the engine, since the temperature changes greatly and this factor can have a significant impact on the physical characteristics of the designed devices.

In addition, there is another important question about the role of spring 4 (Fig. 1) in the engine operation. The fact is that the Stirling engine can operate without this spring, and no separate studies devoted to its influence on such important characteristics as power and efficiency can be found.

The proposed work analyzes the operation of a Stirling engine with a free working piston; in contrast to earlier works, the temperature variability in the heater and cooler is taken into account. This is very important, since widespread isothermal models [1–3, 7, 14, 15] are not convenient for designing real engines, although they allow one to understand their basic properties.

An attempt to take into account the temperature variability in work [14] does not solve the problem, since it uses approximate equations that are valid only for the steady-state heat exchange mode. The same is done in [1-3, 6]. It is not possible to find other studies that describe in detail the temperature change over time in a Stirling engine. In addition, the proposed study, unlike [1-3, 6, 14], is based on a simpler and at the same time more advanced model [13]; in it, the engine is considered to consist of three parts (instead of five) — a heater, cooler and regenerator. There is another difference: a non-stationary equation of conservation of momentum is used for the regenerator. This equation more accurately takes into account the momentum transfer in the regenerator and, for a steady gas flow, goes over to the Darcy-Weisbach equation from works [1-3, 6, 14].

2. Engine design diagram and model equations

In Fig. 1 shows a diagram of the design of a Stirling machine with a free piston [14, 15]. Compression volume 6 is a cooler and is designated V_c, expansion volume 7 is a heater with volume V_e. This means that the volumes V_c and V_e are essentially a cooler and a heater, they are cylindrical in shape with a diameter d_2. Accordingly, their temperatures are T_c and T_e. Volumes V_c and V_e are in contact with "external environments" with minimum $T_{\min}$ and maximum $T_{\max}$ temperatures. The gas masses in each of the indicated volumes are equal to m_c and m_e.

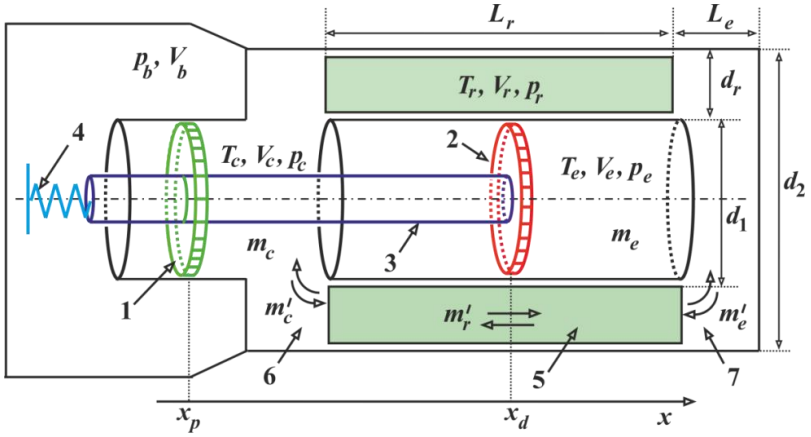

Fig. 1. Simplified diagram of the structure of a Stirling engine with a free piston and the direction of the x coordinate: 1 – working piston; 2 – displacer; 3 – displacer rod; 4 – displacer spring; 5 – regenerator; 6 – cooling area; 7 – heating area

The origin of coordinates x coincides with the initial position of the working piston when it is in the equilibrium position $x_p = 0$. This state corresponds to the initial position of the displacer $x_d = x_{d,0}$. Regenerator 5 is a narrow and long channel in the space between two coaxial cylinders with diameters d_1 and $d_2 = d_1 + 2d_r$. In it, gas moves in the direction of coordinate x with a cross-sectional average speed u and density ρ_r. The buffer space includes volume V_b, pressure p_b in it, according to the results of [15], it does not play a big role.

The displacer and the working piston have the shape of a disk of equal diameter d_1. The working piston 1 moves freely along the rod 3 of the displacer 2, the last two are rigidly connected to each other, and one of the ends of the rod is attached to the spring 4 with a stiffness coefficient k_d. The displacer can move freely inside the cylinder, surrounded by a cylindrical regenerator with length L_r and working space thickness d_r. When the piston moves, an electric current is generated, the linear generator in Fig. 1 is not shown, but its reverse effect on the operation of the machine is taken into account by the damping coefficient D_p [14].

A new isothermal model of the engine is presented in [15], it includes the equations of motion of the displacer, piston and gas in the regenerator, and takes into account the relaxation property of the regenerator of a hydrodynamic nature. The coordinate of the displacer x_d with mass m_d is measured from the equilibrium position $x_{d,0}$, the initial state of the piston coordinate x_p and mass m_p coincides with the x coordinate. The gas in the buffer volume compresses and expands under adiabatic conditions with index γ. External and initial pressure p_0. The equations of motion of the displacer and piston have the form

$$m_d \frac{d^2 x_d}{dt^2} + k_d (x_d - x_{d,0}) = p_b A_{rod} + p_c A_p - p_e A_d , \quad (1)$$

$$m_p \frac{d^2 x_p}{dt^2} + D_p \frac{dx_p}{dt} = (p_b - p_c) A_p . \quad (2)$$

They are supplemented by formulas for determining pressures:

$$p_b = p_0 \left(\frac{V_{b,0}}{V_b} \right)^{\gamma}, \qquad p_c = \frac{R_g T_c}{V_c} m_c , \qquad p_e = \frac{R_g T_e}{V_e} m_e . \quad (3)$$

The volumes contained here are found by the equations

$$V_c = V_{c,0} + A_p (x_d - x_{d,0} - x_p), \qquad V_e = V_{e,0} - A_d (x_d - x_{d,0}), \quad (4)$$

$$V_{e,0} = X_{e,0} \frac{\pi d_1^2}{4} + L_e \frac{\pi d_2^2}{4}, \quad V_b = V_{b,0} + A_{rod} (x_d - x_{d,0}) + A_p x_p .$$

Here $X_{e,0}$ is the distance from the right wall of the heater to the equilibrium position of the displacer; A_{rod} is the cross-sectional area of rod of the displacer; A_d is the cross-sectional area of the displacer, and $A_d = \pi d_1^2 / 4$.

In equations (1) and (2) there are no reaction forces from the walls that arise when the piston and displacer reach the extreme positions on the left $x_{d,\min}$, $x_{p,\min}$ and on the right $x_{d,\max}$, $x_{p,\max}$. In this study, only such operating modes are considered when such values of the coordinates of the piston and displacer are not achieved. The gas masses in the displacer m_c and heater m_e are determined by solving the equations (further, the top stroke means the derivative with respect to time)

$$\frac{dm_c}{dt} = -m_r', \quad \frac{dm_e}{dt} = m_r' . \quad (5)$$

Let $m_{c,0}$ and $m_{e,0}$ are the initial values of the gas masses in the cooler and heater, then from the sum of equations (5) and after integration the equality follows

$$m_c - m_{c,0} = -(m_e - m_{e,0}) . \quad (6)$$

The pressure p_r and temperature T_r in the regenerator are taken to be the average values in the heater and cooler:

$$p_r = \frac{p_e + p_c}{2}, \quad T_r = \frac{T_e + T_c}{2} . \quad (7)$$

Equalities (7) mean accepting a linear dependence on the x coordinate of changes in pressure and temperature in the regenerator. Then the average gas density in the regenerator ρ_r is determined from the equation of state

$$\rho_r = \frac{p_e + p_c}{(T_e + T_c) R_g} . \quad (8)$$

For the gas mass flow rate in the regenerator $m'_r(t) = u(t)\rho_r A_r$, the equation is used [15]

$$\frac{dm_r'}{dt} = \frac{A_r}{L_r} \Delta p - \frac{1}{2} \frac{K_\Sigma |m_r'|}{m_r} m_r', \quad (9)$$

$$K_\Sigma = K_r + \frac{L_r}{2 d_r} \zeta, \quad m_r = \rho_r L_r A_r = \rho_r V_r, \quad V_r = L_r A_r . \quad (10)$$

According to the diagram in Fig. 1, the positive direction of gas movement corresponds to the positive sign of the pressure drop Δp, therefore $\Delta p = p_c - p_e$.

Writing the energy equation comes down to finding an equation for the temperature of the heater T_e and cooler T_c; these parts of the machine are surrounded by media with temperatures $T_{\max}$ and $T_{\min}$. In real devices, $T_{\max}$ is the temperature of the liquid or gaseous medium that serves as a heat supplier for the machine; $T_{\min}$ is the ambient temperature.

Heat exchange with the external environment occurs according to Newton's law with heat transfer coefficients α_e and α_c through the wall surfaces with the contact area S_e and S_c. Using Newton's law does not

accurately model heat transfer through the wall during fast transient processes, but is acceptable as a first approximation.

The heat capacity of a gas at a constant volume c_υ = const, the mass of the gas m, the internal energy of the gas $U = c_\upsilon mT$, when a small heat dQ is supplied, its volume changes by the value dV, then the law of conservation of energy is written as the equality

$$\frac{dU}{dt} = -p\frac{dV}{dt} + \frac{dQ}{dt}.$$

The rate of heat supply/removal Q' is determined by the sum of the following factors:
- convective transfer across the boundaries of the volume under consideration Q'_c (or, Q'_e),

$$Q'_c = \begin{cases} c_\upsilon m'_r T_c, & \text{if } m'_r \geq 0; \\ c_\upsilon m'_r T_r, & \text{if } m'_r < 0; \end{cases} \qquad Q'_e = \begin{cases} c_\upsilon m'_r T_r, & \text{if } m'_r \geq 0; \\ c_\upsilon m'_r T_e, & \text{if } m'_r < 0; \end{cases}$$

- exchange of heat with the external environment Q'_{in} (or, Q'_{out}).

$$Q'_{in} = \alpha_e S_e (T_{\max} - T_e), \quad Q'_{out} = \alpha_c S_c (T_c - T_{\min});$$

here is the surface area of the heater

$$S_e = \frac{\pi d_2^2}{4} + L_e \pi d_2.$$

- thermal equivalent of the operation of an electric generator Q'_{gen},

$$Q'_{gen} = D_p \left(\frac{dx_p}{dt} \right)^2; \tag{11}$$

- thermal equivalent of the work of pushing gas through the regenerator $Q'_{r,c}$ (or, $Q'_{r,e}$),

$$Q'_{r,c} = \begin{cases} \dfrac{p_c - p_e}{\rho_r} m'_r, & \text{if } m'_r \geq 0; \\ 0, & \text{if } m'_r < 0; \end{cases} \qquad Q'_{r,e} = \begin{cases} 0, & \text{if } m'_r \geq 0; \\ \dfrac{p_c - p_e}{\rho_r} m'_r, & \text{if } m'_r < 0. \end{cases} \tag{12}$$

Thermal powers $Q'_{r,c}$ and $Q'_{r,e}$ always have a positive sign; if the gas flows from left to right, then the pushing work is performed by the coolant gas; if the gas flows in the opposite direction, then it is the heater gas. The rates of change in the volumes of the cooler and heater are equal

$$\frac{dV_c}{dt} = A_p \left(\frac{dx_d}{dt} - \frac{dx_p}{dt} \right), \qquad \frac{dV_e}{dt} = A_d \frac{dx_d}{dt}.$$

Then, from the law of conservation of energy, the rates of temperature changes T_c and T_e are determined,

$$c_\upsilon m_c \frac{dT_c}{dt} = -c_\upsilon T_c \frac{dm_c}{dt} - p_c A_p \left(\frac{dx_d}{dt} - \frac{dx_p}{dt} \right) - Q'_{out} - Q'_c - Q'_{gen} - Q'_{r,c},$$

$$c_\upsilon m_e \frac{dT_e}{dt} = -c_\upsilon T_e \frac{dm_e}{dt} - p_e A_d \frac{dx_d}{dt} + Q'_{in} + Q'_e - Q'_{r,e}.$$

Using equalities (4) allows the temperature equations to be written in a convenient form:

$$\frac{dT_c}{dt} = \frac{T_c}{m_c} m_r' - \frac{p_c A_p}{c_\upsilon m_c}\left(\frac{dx_d}{dt} - \frac{dx_p}{dt}\right) - \frac{Q_{out}' + Q_{gen}' + Q_{r,c}' + Q_c'}{c_\upsilon m_c},$$

$$\frac{dT_e}{dt} = -\frac{T_e}{m_e} m_r' - \frac{p_e A_d}{c_\upsilon m_e}\frac{dx_d}{dt} + \frac{Q_{in}' + Q_e' - Q_{r,e}'}{c_\upsilon m_e}.$$

Here, the first terms on the right sides of the equalities have the same structure, so they can be combined with convective heat sources. After simple transformations, the final forms of the equations for temperatures are obtained:

$$\frac{dT_c}{dt} = -\frac{p_c A_p}{c_\upsilon m_c}\left(\frac{dx_d}{dt} - \frac{dx_p}{dt}\right) - \frac{Q_{out}' + Q_{gen}' + Q_{r,c}'}{c_\upsilon m_c} + \tilde{Q}_c', \tag{13}$$

$$\frac{dT_e}{dt} = -\frac{p_e A_d}{c_\upsilon m_e}\frac{dx_d}{dt} + \frac{Q_{in}' - Q_{r,e}'}{c_\upsilon m_e} + \tilde{Q}_e',$$

$$\tilde{Q}_c' = \begin{cases} 0, & \text{if } m_r' \geq 0; \\ \dfrac{T_c - T_r}{m_c} m_r', & \text{if } m_r' < 0. \end{cases} \qquad \tilde{Q}_e' = \begin{cases} \dfrac{T_r - T_e}{m_e} m_r', & \text{if } m_r' \geq 0; \\ 0, & \text{if } m_r' < 0. \end{cases}$$

The inclusion of thermal powers (11) and (12) explicitly in the temperature equations (13) makes it possible to more accurately determine the temperature in the cooler and heater.

3. Modeling tools, construction of computational grid and verification of model accuracy and adequacy

The solution of equations (1), (2), (5), (9) and the system of equations (13) was carried out using the numerical Runge-Kutta method with second order accuracy [19]. The computational grid is taken from the same book. The program code for implementing the computational algorithm was written by one of the authors in C++ using the DevCpp 5.11 package.

The integration step is $\Delta t = 10^{-5}$ s; such a small value allows one to obtain reliable results with wide variations in engine parameters. The accuracy of the model was verified by decreasing the integration step Δt; the invariance of the results at different steps indicates the accuracy of the calculations [19]. The adequacy of the model was verified by checking the coincidence of the results with the results from work [15], obtained in the isothermal approximation.

4. Stirling machine simulation results

The analysis of its operation was carried out with the following set of input parameters:

– displacer mass m_d = 0.1 kg;
– heater length L_e = 0.17 m;
– spring stiffness k_d = 500 N/m;
– cross-sectional area of the displacer rod A_{rod} = 0.01 m^2;
– diameter d_1 = 0.24 m and displacer cross-sectional area A_d = 0.045 m^2;
– piston area $A_p = A_d - A_{rod}$ = 0.035 m^2;
– piston mass m_p = 0.2 kg;
– damping coefficient (characterizes the reverse effect of an electric generator on a machine) D_p = 8.0 N·s/m;
– initial pressure $p_0 = 10^5$ Pa;
– working gas: adiabatic index (air) γ = 1.4, gas constant R_g = 287 J/(kg·K), heat capacity at constant volume c_υ = 710 J/(kg·K);
– heat transfer coefficients $\alpha_c = \alpha_e$ = 250 Вт/(м^2·K);

– heat exchange surface area of the cooler S_c = 0.65 m^2;
– heater heat exchange surface area S_e = 0.19 m^2;
– heat source temperature T_{max} = 593 K (320 ºC);
– cooler (ambient) temperature T_{min} = 293 K (20 ºC);
– distance $X_{e,0}$ = 0.26 м;
– initial volumes $V_{e,0} = 1.46 \cdot 10^{-2}$ m^3, $V_{b,0} = 2.5 \cdot 10^5$ m^3, $V_{c,0} = 5.7 \cdot 10^{-3}$ m^3;
– neutral position of the displacer $x_{d,0}$ = 0.15 m;
– geometric parameters of the regenerator L_r = 0.18 m, d_r = 0.01 m, $A_r = 7.85 \cdot 10^{-3}$ m^2; $V_r = 1.4 \cdot 10^{-3}$m^3;
– hydraulic parameters of the regenerator K_r = 0.5, ζ = 0.06.

The volume of the buffer space is taken to be very large, $V_{b,0} = 2.5 \cdot 10^5$ m^3; in fact, it is excluded from consideration. High values of the heat transfer coefficients α_c and α_e suggest a rough account of the convective movement of the gas. But such movement is not considered in detail here, so as not to complicate the analysis of engine operation. The accepted value ζ corresponds to the weak porous structure of the regenerator; ζ = 0.03 is realized in the free space of a channel with smooth walls [18].

The following was discovered during the simulation:

– the time it takes to reach a steady state of engine operation depends on the initial conditions for the differential equations;

– oscillations with very different frequencies occur in the system, so numerical integration of the equations must be carried out with a small-time step;

– under certain initial conditions, oscillations with very large amplitudes may occur in the first 0.01...0.1 s;

– with low spring stiffness k_d, the displacement of the displacer x_d may not correspond to the design of the engine and then the displacer rod may rest against the right or left wall. Sometimes this appears as a negative volume value V_e.

Results in Fig. 2–4 were obtained with initial conditions

$t = 0$: $x_p = 0$; $dx_p/dt = 0$; $x_d = x_{d,0}$; dx_d/dt = 1 m/s; $m'_r = 0$.

In addition to them, at the initial pressure p_0 and temperatures $T_e(t = 0) = T_{max}$, $T_c(t = 0) = T_{min}$, the gas masses in the cooler and displacer are equal

$$m_{c,0} = \frac{p_0 V_{c0}}{R_g T_c}, \quad m_{e,0} = \frac{p_0 V_{e0}}{R_g T_e}.$$

4.1. Methodology for calculating the generated power of electricity

Since the reverse influence of the electric current generator on the operation of the Stirling engine lies in the $D_p x'_p$ complex, it characterizes the production of electrical energy. The coefficient D_p depends on the properties of the generator [14]. The $D_p x'_p$ complex is the resistance force resulting from self-induction in the generator windings. Then the instantaneous electrical power is equal to

$$P = Q'_{gen} = D_p \left(x'_p\right)^2.$$

To assess the efficiency of the engine, the amplitude, or the average value over several periods of oscillation <P> in a steady state, is of interest. The positions of the displacer and piston (Fig. 2) are gradually established to a periodic oscillation mode with constant amplitudes. Clock frequency of oscillations in steady state ν = 12.3 Hz. The piston and the displacer perform synchronous oscillations; the presence of a noticeable phase shift between x_d and x_p is not detected. Such a small phase shift exists in the model [14], but not between pressure fluctuations in the heater and cooler.

Within one period of oscillation, the maximum speed of the piston is greater when moving to the right than in the opposite direction. Since the piston stroke is the same in both directions, the travel time is different. Due to the indicated difference in velocity amplitudes, the power graph (Fig. 3) in steady-state mode shows two maximum points $P_{max,1}$ = 427 W and $P_{max,2}$ = 598 W. Thus, the greatest engine power is developed when cold gas expands.

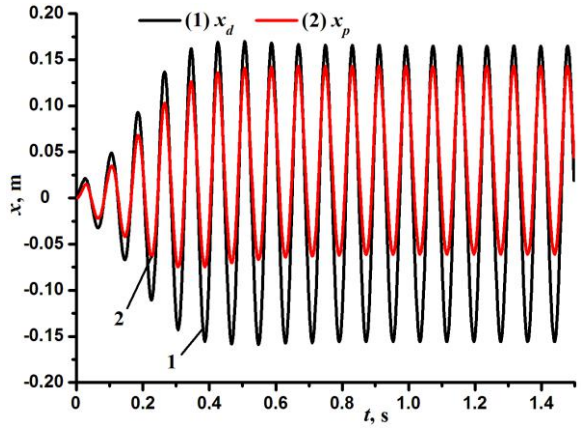

Fig. 2. Changes in the coordinates of the displacer x_d and piston x_p over time

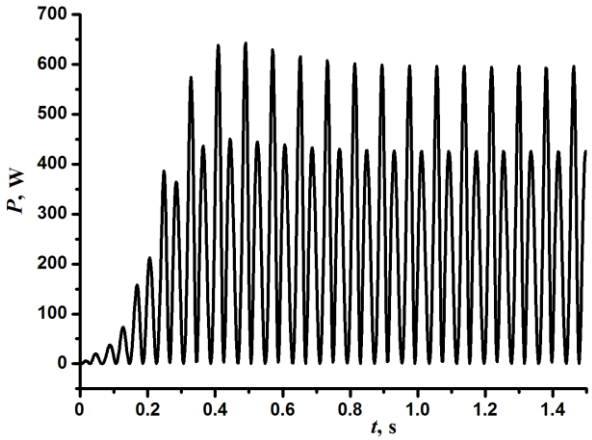

Fig. 3. Dependence of electrical power P on time t

The gas temperature in the heater T_e at certain moments of time exceeds T_{max} (Fig. 4). This occurs as a result of adiabatic compression of the gas under the influence of the inertia force of the displacer mass. But the average value $<T_e>$ is always less than T_{max}. The gas temperature in the cooler T_c can increase both due to the incoming mass from the heater and as a result of adiabatic compression. In addition, T_c oscillations have a weakly expressed relaxation character, when the temperature increases faster than the decrease. Temperature data $<T_e>$ allows an approximate estimate of the electrical efficiency of the engine η. The temperature difference between the heater and the external temperature T_{max} is $\Delta T = T_{max} - <T_e> = 84$ K. Then the heat entering the engine is $Q'_{in} = \alpha_e S_e \Delta T = 4012$ W. The net power produced is approximately $<P> = 254$ W, and then the efficiency is $\eta = 0.063$, or 6.3%.

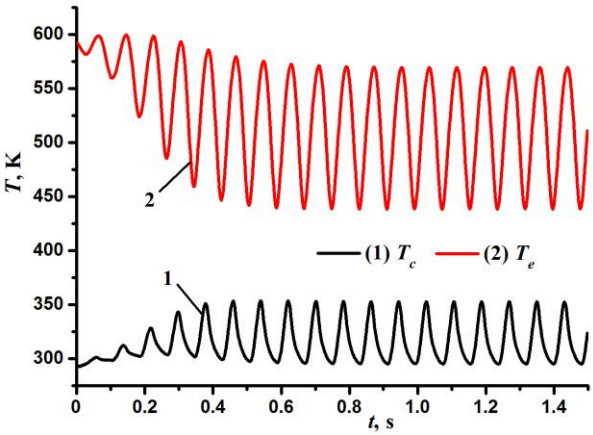

Fig. 4. Dependence of the temperature of the refrigerator T_c and the heater T_e on time t

It should be noted that the use of values with a temperature difference Q'_{in} (or Q'_{out}) is inconvenient, since the value ΔT is much smaller than the temperatures themselves, so they must be calculated with high accuracy. Various thermodynamic cycles are realized in the heater and cooler; in the *p-V* coordinates one close to the Stirling cycle is observed, and in the cooler its almost mirror image is observed relative to the vertical axis (Fig. 5). A special feature of them is the presence of a small loop in the upper part of the figure; in addition, line 1 is not a Stirling cycle, since a decrease in pressure corresponds to an increase in volume. An increase in the hydraulic resistance coefficient K_r leads to a decrease in engine efficiency η (Fig. 6) and average power <*P*> (Fig. 7), the opposite phenomenon is observed depending on D_p.

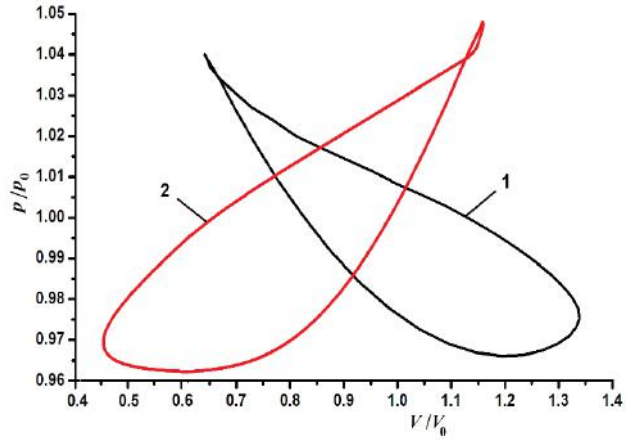

Fig. 5. Image in *p-V* coordinates of cycles in the heater (line 1) and cooler (line 2) in steady-state engine operation

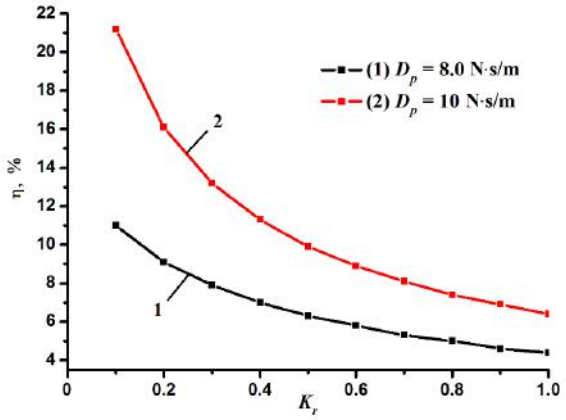

Fig. 6. Dependence of the electric efficiency of the engine η on the parameter K_r

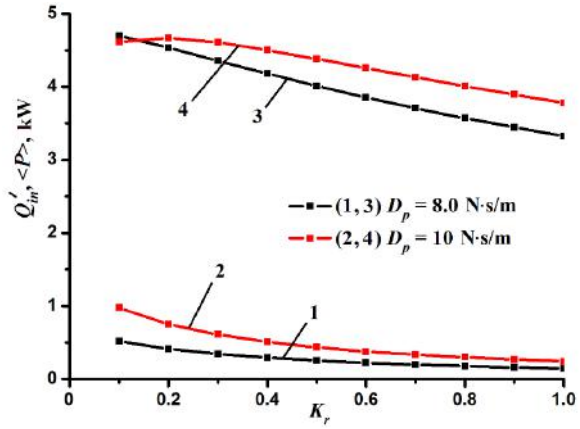

Fig. 7. Dependences of electric power <*P*> (lines 1, 2) and incoming heat Q'_{in} (lines 3, 4) on the K_r parameter

The power of heat supplied to the engine Q'_{in} decreases at low K_r, and the observed increase in <P> means a more efficient conversion of heat into mechanical work. However, at low values of K_r, excessively large displacements of the displacer may be observed due to low spring stiffness k_d or small volume V_e, which do not correspond to the engine design. As the damping coefficient D_p increases, the pressure in the heater and cooler, as well as the difference between them, increases. This is explained by an increase in resistance to the movement of the piston, which leads to more mechanical work and the production of electrical power P.

In this regard, it would seem that the coefficient of hydraulic resistance K_r should have the same effect, but here the opposite phenomenon is observed (Fig. 7) the power <P> drops. The reason for this is a reduction in the exchange of heat and mass between the heater and cooler, which is fundamentally necessary in the Stirling cycle. An increase in engine power and efficiency can also be achieved by increasing the rigidity of the displacer spring, and at the same time this leads to an increase in the oscillation frequency (Fig. 8). Over the range of k_d changes indicated here, the power <P> increases from 64 to 251 W.

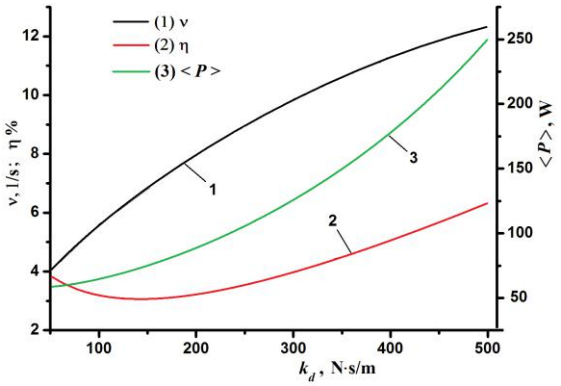

Fig. 8. Changes in frequency, efficiency and power when spring stiffness changes; K_r = 0.5, D_p = 8.0 N·s/m

The above results indicate the existence of an optimal operating mode for the Stirling engine depending on the spring stiffness, the hydraulic resistance of the regenerator, the connected electrical load and the geometric characteristics of the heater. The optimization procedure necessary in this case was not carried out; this is a separate and complex task due to the presence of a large number of parameters.

Here, the increase in efficiency η and power P depending on the load parameter k_d deserves special attention. Obviously, an unlimited increase in k_d will ultimately lead to the engine stopping. This means that the functions η(k_d) and P(k_d) must have a maximum point.

5. Comparison with the isothermal model [15]

Now temperatures $T_c = T_{\min}$, $T_e = T_{\max}$, equations (1.13) are not considered. In the isothermal approximation, the efficiency calculation is performed based on the value of the total engine power Pm (or the rate of production of mechanical work), it is equal to

$$P_m = \left|(p_c - p_e)\frac{dV_c}{dt}\right| + \left|(p_e - p_0)\frac{dV_e}{dt}\right| = \left|(p_c - p_e)A_p\left(\frac{dx_d}{dt} - \frac{dx_p}{dt}\right)\right| + \left|(p_e - p_0)A_d\frac{dx_d}{dt}\right|.$$

The necessity of the module sign is explained by the fact that useful work is performed both during expansion and compression of gas in volumes. The engine efficiency η was determined by the average values of power $\langle P \rangle$ and $\langle P_m \rangle$:

$$\eta = \frac{\langle P \rangle}{\langle P_m \rangle}.$$

The initial physical parameters remain the same as those used to construct Figures 6 and 7. Changing the resistance coefficient K_r from 0.1 to 0.9 does not change the efficiency, but the power is constantly reduced. And this result does not depend on the generator electrical load characteristic D_p. The obtained data are placed in Table 1.

Table 1. Dependence of average electrical power on the resistance coefficient K_r

D_p = 8 N·s/m									
K_r	0.1	0.2	0.3	0.4	0.5	0.6	0.7	0.8	0.9
η	17 % (for all K_r)								
$\langle P \rangle$, W	28	21	16	13	10	9	7	6	5
D_p = 10 N·s/m									
η	19 % (for all K_r)								
$\langle P \rangle$, W	53	40	31	24	20	17	14	12	10

It is also worth paying attention to the decrease $\langle P \rangle$ when switching to an isothermal model (power in Table 1 is measured in watts), but at the same time the efficiency increases. The constancy of the efficiency η found here is another distinctive feature of the isothermal model. It is generally accepted that friction always reduces the efficiency of the engine, but this is not observed in Table 1. Apparently, this is a shortcoming of the isothermal approximation.

6. Conclusion

Simulation of the Stirling engine showed a strong dependence of the results (temperatures in the heater and cooler, power and frequency) on the geometric and physical properties of the regenerator and the amount of work generated by the electric generator. In this case, the engine power increases with a decrease in the coefficient of hydraulic resistance in the regenerator and an increase in the load of the electric generator. An increase in power is also observed with an increase in the spring stiffness of the displacer, leading to an increase in the oscillation frequency. It was also found that the greatest power is observed in the absence of a phase shift between the oscillations of the displacer and the piston. The motor cannot run when the phase shift gets close to π. Increasing the stiffness of the displacer spring also leads to an increase in oscillation frequency, power and efficiency. Thermodynamic processes according to the Stirling cycle occur in the heater; in the cooler, a cycle is implemented that is close to mirror reflection relative to the pressure axis in *p*-*V* coordinates.

Comparison with an earlier isothermal model showed the following:

1) taking into account the change in temperature (in contrast to the isothermal model) in the engine leads to an increase in its power (for example, approximately 8.9 times with a spring stiffness of k_d = 500 N/m and D_p = 8 N·s/m);

2) but at the same time the efficiency of the engine increases for example, approximately 2.74 times with a spring stiffness of k_d = 500 N/m and D_p = 8 N·s/m);

3) in the isothermal approximation, the efficiency can remain constant with an increase in the hydraulic resistance of the regenerator K_r from 0.1 to 0.9, and this result does not depend on the damping coefficient D_p.

The obtained data are the result of calculations (simulation) under the specified simulation conditions and will be further analyzed for compliance with experimental data under similar operating conditions of the Stirling engine.

Notation

A_d – the cross-sectional area of the displace, m^2;
A_p – the cross-sectional area of the working piston, m^2;
A_{rod} – the cross-sectional area of the rod (displacer), m^2;
A_r, L_r – cross-sectional area and length of the regenerator, m^2 and m;
D_p – the coefficient characterizing the electric generator, N·s/m;
d_r – the height of the working section of the regenerator, m;
d_1 – the diameter of the piston and displacer, m;
d_2 – diameter of the heater and cooler, m;
k_d – spring stiffness coefficient, N/m;
m_c – the mass of gas in the cooler, kg;
m_e – the mass of gas in the heater, kg;
m_r, m'_r – mass and mass flow rate of gas in the regenerator, kg and kg/s;
P – electric power of the generator, W;

p_b, V_b – pressure and volume of buffer space, Pa and m^3;
p_0 – initial and external pressure, Pa;
Q'_{in} and Q'_{out} – heat input and output power in the engine, W;
$Q'_{r,c}$ and $Q'_{r,e}$ – thermal equivalents of the work of pushing gas through the regenerator, W;
Q'_c and Q'_e – thermal capacities of convective transfer across the boundaries of the cooler and heater, W;
R_g – gas constant, J/(kg·K);
T_{min}, T_{max} – minimum and maximum temperature, K;
t – time, s;
V_c, p_c and T_c – volume, m^3, pressure, Pa, and gas temperature, K, in the cooler;
V_e, p_e and T_e – volume, m^3, pressure, Pa, and gas temperature, K, in the heater;
V_r, p_r and T_r – volume, m^3, pressure, Pa, and gas temperature, K, in the regenerator;
x_d, x_p – the coordinates of the displacer and piston, m;
u – gas velocity in the regenerator, m/s;
α_c, α_e – heat transfer coefficients in the cooler and heater, W/(m^2·K);
γ – adiabatic index;
η – electrical efficiency;
ρ_r – gas density in the regenerator, kg/m^3;
ν – the oscillation frequency of the piston and the displacer, s^{-1};
ζ, K_r – hydraulic resistance coefficients.
Subscripts: *c* – compression; *e* – expansion; *b* – buffer; *d* – displacer; *gen* – generator; *in* – inlet; *out* – output; *p* – piston; *r* – regenerator; *g* – gas.

Conflict of interest statement
The authors declare that they have no conflict of interest in relation to this research, whether financial, personal, authorship or otherwise, that could affect the research and its results presented in this paper.

CRediT author statement
Sabdenov K.O.: Conceptualization, Methodology, Writing-Review & Editing; **Erzada, M.:** Original Draft, Visualization, Software; **Zholdybaeva G.T.:** Conceptualization, Methodology.
The final manuscript was read and approved by all authors.

References

1 Ruihua Chen, Weicong Xu , Shuai Deng, Ruikai Zha, Siyoung Q. Choi, Li Zhao. (2023) Towards the Carnot efficiency with a novel electrochemical heat engine based on the Carnot cycle: Thermodynamic considerations. *Energy*, 284, 128577. DOI: 10.1016/j.energy.2023.128577.

2 Xu W, Deng S, Zhao L, Zhang Y, Li S. (2019) Performance analysis on novel thermodynamic cycle under the guidance of 3D construction method. *Applied Energy*, 250, 478 – 492. DOI: 10.1016/j.apenergy.2019.05.081.

3 Sabdenov K.O. (2021) The Thermodynamic Brayton Cycle with a Reversible Chemical Reaction. *Technical Physics*, 66, 1275 – 1283. Available at: https://link.springer.com/article/10.1134/S1063784221090164.

3 Sabdenov K. (2023) The Thermodynamics Cycles with a Reversible Chemical Reaction. *Americ. Journ. Mod. Phys.* (*AJMP*), 12, 2, 14 – 20. Available at: http://ajmp.org/article/10.11648/j.ajmp.20231202.11

4 Walker G. (1973) *Stirling-cycle machines*. Clarendon Press, Oxford, 156. Available at: https://www.amazon.com/Stirling-Cycle-Machines-Graham-Walker/dp/0198561121.

6 Reader G.T., Hooper Ch. (1982) *Stirling engines*, 424. Spon Press. Available at: https://www.abebooks.co.uk/9780419124009/Stirling-Engines-Reader-G.T-Hooper-0419124004/plp

7 Valenti G., Campanari S., Silva P., Ravida A., Macchi E., Bischi A. (2015) On-off cyclic testing of a micro-cogeneration Stirling unit. *Energy Procedia*, 75, 1197–1201. Available at: https://www.researchgate.net/publication/281373930_On-off_Cyclic_Testing_of_a_Micro-cogeneration_Stirling_Unit

8 Sabdenov K.O., Erzada M., Suleimenov A.T. (2019) The Possibility of Converting Energy in Space with the Aid of a Chain Heat Machine Operating on Methane and Nitrogen. *Journ. Eng. Phys. Therm.*, 92, 3, 574-584. Available at: https://link.springer.com/article/10.1007/s10891-019-01965-z#citeas

9 Konyukhov G.V., Bukharov A.V., Konyukhov V.G. (2020) On the Problem of Rejection of Low-Potential Heat from High-Power Space Systems. *Journ. Eng. Phys. Therm.*, 93, 16–27. Available at: https://doi.org/10.1007/s10891-020-02086-8

10 Vikulov A.G., Morzhukhina A.V. (2021) Controlling the Power of the Internal Heat Sources of Space Vehicles. *Jour. Eng. Phys. Therm.*, 94, 1101–1109. DOI: 10.1007/s10891-021-02390-x.

11 Xu W, Deng S, Zhao L, Zhang Y, Li S. (2019) Performance analysis on novel thermodynamic cycle under the guidance of 3D construction method. *Applied Energy*, 250, 478-492. DOI: 10.1016/j.apenergy.2019.05.081.

12 Jenkins N., Ekanayake J.B., and Strbac G. (2010) *Distributed Generation*. The Institution of Engineering and Technology, London. Available at:

https://web.nit.ac.ir/~shahabi.m/M.Sc%20and%20PhD%20materials/DGs%20and%20MicroGrids%20Course/Books/Distributed%20Generation%20by%20N.Jenkins%20IET%20press/Distributed.pdf.

13 Dulau L. I., Abrudean M., Bica D. (2014) Effects of Distributed Generation on Electric Power Systems. *Procedia Technology*, 12, 681–686. Available at: https://www.researchgate.net/publication/270916389_Effects_of_Distributed

14 Langlois, Justin L.R. (2006) Dynamic computer model of a Stirling space nuclear power system. *Trident Scholar project report no. 345*. Annapolis, US Naval Academy. Available at: https://www.semantic scholar.org/paper/Dynamic-Computer-Model-of-a-Stirling-Space-NuclearLanglois/0e513dee372464b9d6807efb9717e 934af1c4df1

15 Sabdenov K.O. (2024) A simple model of a Stirling machine (engine) with a free working piston. *Journ. Eng. Phys. Therm.*, 97, 4. P. 1034-1041. DOI: 10.1007/s10891-024-02974-3.

16 Zhiwen Dai, Chenglong Wang, Dalin Zhang, Wenxi Tian, Suizheng Qiu, G.H. Su. (2021) Design and analysis of a free-piston Stirling engine for space nuclear power reactor. *Nucl. Eng. Techn*., 53, 2, 637–646. DOI:10.1016/j.net.2020.07.011.

17 Fr. Catapano, C. Perozziello, B. M. Vaglieco. (2021) Heat transfer of a Stirling engine for waste heat recovery application from internal combustion engines. *Appl. Therm. Eng*., 198, 5, 117492. DOI:10.1016/j.applthermaleng.2021.117492.

18 Ukhin B.V., Gusev A. A. (2010) *Hydraulics*. Moscow, 432. Available at: https://www.ibooks.ru/products/360607? Category id=12968 [in Russian]

19 Kalitkin N.N. (2011) *Numerical methods*. Moscow, 592. Available at: https://bhv.ru/wp-content/uploads/wpallimport/ filespdfk i/view_1768_978-5-9775-5000.pdf?srsltid=AfmBOoq6JfthMR60no1rnchXvS2xar [in Russian]

AUTHORS' INFORMATION

Sabdenov, K.O. - Doctor of Phys.- Math. Sciences, Professor, Electrical Engineering Department, Transport and Energy Faculty, L.N. Gumilyov Eurasian National University, Astana, Kazakhstan; https://orcid.org/0009-0008-4733-6667; sabdenovko@yandex.kz

Erzada, M. - Doctor (Eng.), Associate Professor, Electrical Engineering Department, Transport and Energy Faculty, L.N. Gumilyov Eurasian National University, Astana, Kazakhstan; https://orcid.org/0000-0002-3943-651X; mayira76@yahoo.co.jp

Zholdybaeva G.T. – Master (Eng.), Teacher, Mathematics Department, M. Saparbaev South Kazakhstan Humanitarian Institute, Shymkent, Kazakhstan; https://orcid.org/0009-0008-4733-6667; gulnur_rashid@mail.ru

EURASIAN PHYSICAL TECHNICAL JOURNAL

2024, Volume 21, No.4 (50)

https://doi.org/10.31489/2024No4/61-70

Received: 24/06/2024 Revised: 25/11/2024 Accepted: 18/12/2024 Published online: 25/12/2024

Original Research Article

UDC 537.3.311, 621.311.004.13:51

STATE ESTIMATION OF POWER SYSTEM MODE PARAMETERS BY TELEMETRY AND SYNCHRONIZED PHASOR MEASUREMENTS

Batseva N.L., Foos J.A.

National Research Tomsk Polytechnic University, Tomsk, Russia
*Corresponding author: JuliaAlekseevna6797@gmail.com

Abstract. *Real time hardware and software systems are operated at centers of a power system operation. The key unit of these systems is the state estimation block since, based on the results of mode parameters derived from this block, parameters that are more comprehensive can be calculated. These parameters are considered for system stability and reliability. Currently, not only telemetry but also synchronized phasor measurements can be used for a state estimation. Therefore, the development of state estimation methods is the relevant task. The proposed method allows improving the estimation accuracy and the quality of decisions, related to system stability and reliability. The method is based on mathematical frameworks of the Gauss-Newton method and extended Kalman filter, when telemetry and synchronized phasor measurements arrays are used simultaneously. It is confirmed, that the given method increases an accuracy of the voltage and active power flow estimation at steady state and post-accident modes, in contrast to the standard state estimation method. The developed algorithm enables the implementation of this method into the state estimation block of real time hardware and software systems. The upcoming trends for the development of state estimation methods in the event of dynamic processes in power system areas are also formed.*

Keywords: state estimation, Gauss-Newton method, extended Kalman filter, telemetry, synchronized phasor measurements.

1. Introduction

Automated dispatch management systems, for instance, Centralized Emergency Control Systems (CECSs), System Integrity Protection Schemes control modes operate in high voltage power systems based on state estimation (SE) results [1-4]. To obtain SE results, telemetry of mode parameters is often used. It has major sample spacing, and the parameters are asynchronous in time. Moreover, telemetry does not involve such parameters as voltage and current vectors. These factors reduce the accuracy of solutions to technological tasks, particularly, when calculating power flows before electrical switching operations, identifying maximum and emergency allowed power flows, and making an expert analysis of emergency states, which requires a proximity control of a current mode.

Wide-Area Measurement Systems (WAMSs) are embedded at power system facilities [5, 6]. Synchronized phasor measurements (SPMs) of mode parameters, received from WAMSs, are timed by Global Positioning System (GPS), updated before 50 cycles per second. SPMs include measurements of direct voltage and current vectors. The high update rate ensures control of sudden changes in a power system structure and its mode; records of voltage and current vectors improve the Jacobian and computing process stability; high accuracy of SPMs increases SE results veracity [7–9]. Figure 1 illustrates telemetry and SPMs acquisition and transition.

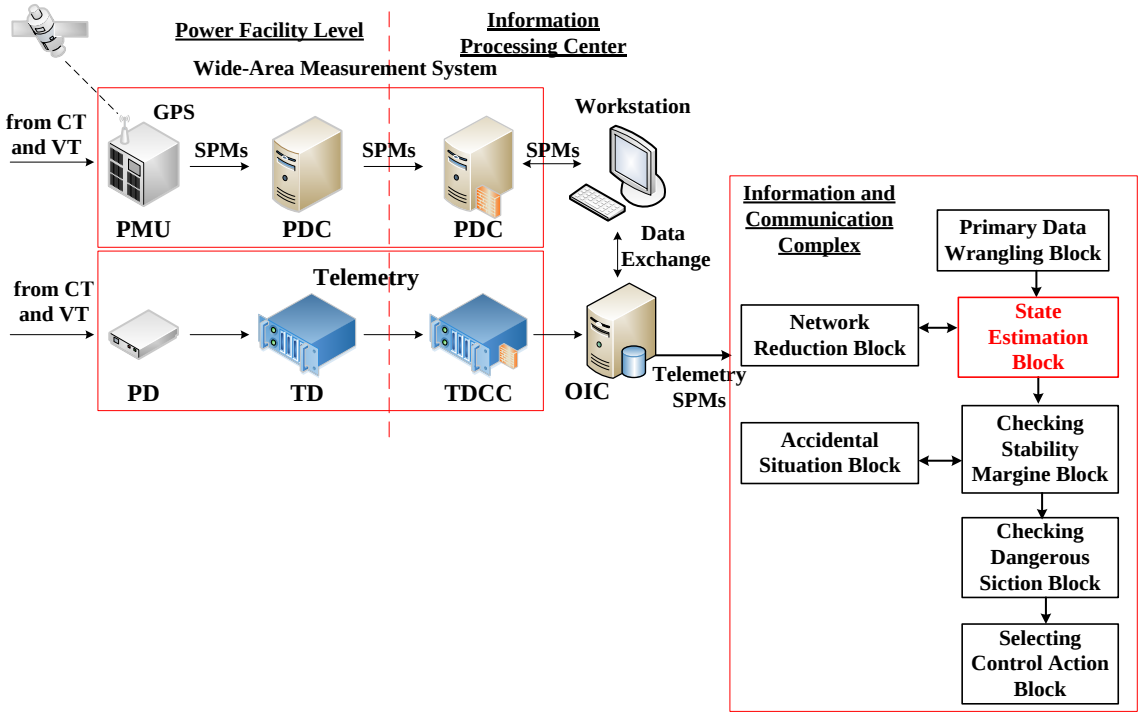

Fig.1. Scheme of telemetry and SPMs acquisition and transition

In the telemetry system, a primary detector (PD) does not guarantee that telemetry is bound to Coordinated Universal Time. As a result, telemetry is asynchronously transferred to a telemetry device (TD), then to a telemetry device of a control center (TDCC) and an Operative information complex (OIC). Time irregularity of the parameters recording falsifies SE results.

WAMSs involve two types of facilities: phasor measurement systems (PMUs) and phasor data concentrators (PDCs). PMUs record mode parameters, received from voltage (VT) and current (CT) transformers, and provide label binding to SPMs by GPS. PDCs receive SPMs from PMUs, save them and process SPMs consistency. After that, SPMs are transmitted to the Information Processing Center (IPC) via the communication network. Subsequently, telemetry and SPMs arrive at the OIC and they are transmitted to the Information and Communication Complex (ICC). According to figure 1, ICC software includes some blocks, where the SE block is the primary unit, as an accidental situation simulation and checking stability margin are performed on the basis of the mode, estimated in the SE block.

Significantly, WAMSs are installed only at 220 kV and above power system facilities. Therefore, SPMs and telemetry can be consistently used for obtaining more precise SE results. Combining SPMs and telemetry enables to develop SE methods [10-12].

Currently, in the modern automated dispatch management systems the SE is achieved by the standard static method, when telemetry is only used as the data, for the reason that this method is not adapted for SPMs [13].

It is reported in [14-21], that dynamic SE methods demonstrate greater accuracy at steady state conditions than the standard static SE method. However, authors stated, that the accuracy of dynamic SE methods is spiraled downward, when sudden changes in a power system are occurred, but no solutions have been proposed [15, 20].

All in all, despite the development of SE methods, the issue of the adequate combining static and dynamic SE methods for the improvement of the SE quality has not yet been come to a decision.

In this paper, the SE method combining sophisticated static and dynamic SE methods in line with the Gauss-Newton mathematical method and extended Kalman filter (EKF) is proposed and tested. This method provides high-quality SE results at various power structures and modes. This is crucial for identifying technological tasks in real-time.

2. Theory of the Method

The SE method is based on the following principles:

1. SE operates in polar coordinates to consider voltage and current angles;
2. It is offered to calculate SPMs weight factors with the formula, which gives a reliable repeatability of an iterative process.

Generally, the static SE method is formalized by the Newton or the Gauss-Newton methods [12, 13]. The Gauss-Newton method is used to solve nonlinear systems of equations and it differs from the Newton method in that the Jacobian is used for approximation instead of the Hessian matrix. Hence, the iterative process time is decreased for the calculation of large-scale systems of equations, such as power system mode equations. For that reason, the Gauss-Newton method is the most relevant for SE. This fact is especially important for automated dispatch management systems. It should be noted that, the Gauss-Newton method is already implemented in the algorithm of the State Estimation Block (fig.1). For that reason, it remains only to modify these method and algorithm for the simultaneous using telemetry and SPMs with economically justifiable expenses.

Dynamic SE methods rest on Kalman filters: *EKF*, *Unscented Kalman Filter (UKF*) and others [12, 15-20]. UKF ensures higher accuracy than *EKF, if a mathematical model is* non-linear. This is due to the fact that at UKF nonlinear predictive functions are plotted by sigma-points, while a model can be linearized in each iteration by the Jacobian at EKF.

However, it is required to define additional model parameters for UKF. Indeed, it is impossible to predetermine additional model parameters in advance for all schemes and modes, therefore, EKF is preferred.

If a scheme and a mode are rapidly changed, then in the proposed method a state estimation is provided by the static SE method during the specified time Δt to configure an amplification matrix. Further, the matrix is applied as initial data for SE by the dynamic SE method.

2.1 Transition to the polar coordinate system and development of the mathematical framework for SPMs

The mathematical statement of SE task comes down to identification of the state vector $\boldsymbol{u}$, with 2N-1 dimension, where N is the number of nodes. In the current SE blocks the state vector components are longitudinal and transversal components of the node voltages: E_1, V_1; E_2, V_2;…, E_{N-1}, V_{N-1}; E_N, V_N.

Every measured mode parameter r_i =1…M, where M is the number of measurements, is an explicit function from voltage $r_i(U)$, and the analytical form of this function corresponds to Ohm's law and Kirchhoff's law. The calculation results of the mode parameters $r_i(U)$ and r_i are inconsistent with each other, due to measurement errors, resulting from imperfection of measuring equipment and irregularity of mode parameters measurements. The proximity measure of calculated and measured parameters can be identified by means of the formula (1):

$$\boldsymbol{r} = \boldsymbol{r}(U) \pm \boldsymbol{f}(U), \tag{1}$$

where $\boldsymbol{r} = \{U_i, P_i, Q_i, P_{ij}, Q_{ij}\}$ is a mode parameters vector; $\boldsymbol{r}^T(U) = \{U_i, P_i(U), Q_i(U), P_{ij}(U), Q_{ij}(U)\}$ is a vector-function, defining mode parameters with node voltages; $\boldsymbol{f}^T(U) = [r_1(U) - r_1; r_2(U) - r_2; \ldots; r_m(U) - r_m]$ is a vector of measurement errors; P_{ij}, Q_{ij} are active and reactive power flows from node i to node j; T is an attribute of the conjugation.

Absolute magnitudes and angles of node voltages U_1,δ_1; U_2,δ_2;…,U_{N-1},δ_{N-1}; U_N, δ_N are implemented to the state vector $\boldsymbol{u}$ for SPMs accounting purposes. This approach significantly enhances the Jacobian condition, accelerates a convergence of a computation process and reduces SE time.

At nodes, where SPMs are measured, voltage and angle measurements are given as $U_i = U_i^{SPM}$ and $\delta_i = \delta_i^{SPM}$, and, at nodes, where telemetry is measured, as $U_i = U_i^{telemetry}$ and δ_i=0 respectively. If a voltage measurement is not available at a node, it is necessary to assume that $U_i^k = U_i^{nominal\ voltage}$ and δ_i=0. The vector and the vector-function of mode parameters are expanded for SPMs accounting purposes (2), (3):

$$\boldsymbol{r} = \left\{U_i, \delta_i, P_i, Q_i, I_{ij}, \sigma_{ij}, P_{ij}, Q_{ij}\right\}, \tag{2}$$

$$\boldsymbol{r}(U) = \left\{U_i, \delta_i, P_i(U), Q_i(U), P_{ij}(U), Q_{ij}(U), I_{ij}(U), \sigma_{ij}(U)\right\}, \tag{3}$$

where U_i, δ_i are the voltage absolute magnitude and angle at the node i; $I_{ij} = \sqrt{\left(C_{ij}^2 + D_{ij}^2\right)}$ and $\sigma_{ij} = \text{arctg}\left(D_{ij} \div C_{ij}\right)$ are the current absolute magnitude and angle in the ij connection; $P_{ij} = C_{ij} \cdot \sqrt{3} \cdot U_i$ and $Q_{ij} = D_{ij} \cdot \sqrt{3} \cdot U_i$ are the active and reactive power flows in the ij connection; $P_i = \sqrt{3} \cdot U_i \cdot \sum_{j \in N}^{N} C_{ij}$ and $Q_i = \sqrt{3} \cdot U_i \cdot \sum_{j \in N}^{N} D_{ij}$ are injections of active and reactive powers at the node i, if $C_{ij} = U_i \cdot (g_{ii} + g_{ij}) - U_j (g_{ij} \cdot \cos\delta_{ij} - b_{ij} \cdot \sin\delta_{ij})$ and $D_{ij} = U_i \cdot (b_{ii} + b_{ij}) - U_j (g_{ij} \cdot \sin\delta_{ij} + b_{ij} \cdot \cos\delta_{ij})$, where g_{ii}, b_{ii} are active and reactive self-conductivity of the node i; g_{ij}, b_{ij} are active and reactive conductivities of the ij connection; $\delta_{ij}=\delta_i - \delta_j$ is the voltage reciprocal phase shift between nodes i and j; δ_i, δ_j are the voltage angle at nodes i and j. The Jacobian is also expanded for:

current absolute magnitude and angle (4):

$$\frac{\partial I_{ij}}{\partial U_i}, \frac{\partial I_{ij}}{\partial U_j}, \frac{\partial I_{ij}}{\partial \delta_i}, \frac{\partial I_{ij}}{\partial \delta_j}, \frac{\partial \sigma_{ij}}{\partial U_i}, \frac{\partial \sigma_{ij}}{\partial U_j}, \frac{\partial \sigma_{ij}}{\partial \delta_i}, \frac{\partial \sigma_{ij}}{\partial \delta_j}, \tag{4}$$

active and reactive power flows (5):

$$\frac{\partial P_{ij}}{\partial U_i}, \frac{\partial P_{ij}}{\partial U_j}, \frac{\partial P_{ij}}{\partial \delta_i}, \frac{\partial P_{ij}}{\partial \delta_j}, \frac{\partial Q_{ij}}{\partial U_i}, \frac{\partial Q_{ij}}{\partial U_j}, \frac{\partial Q_{ij}}{\partial \delta_i}, \frac{\partial Q_{ij}}{\partial \delta_j}, \tag{5}$$

injections of active and reactive powers (6):

$$\frac{\partial P_i}{\partial U_i}, \frac{\partial P_i}{\partial U_j}, \frac{\partial P_i}{\partial \delta_i}, \frac{\partial P_i}{\partial \delta_j}, \frac{\partial Q_i}{\partial U_i}, \frac{\partial Q_i}{\partial U_j}, \frac{\partial Q_i}{\partial \delta_i}, \frac{\partial Q_i}{\partial \delta_j}, \tag{6}$$

Accordingly, the transition from the rectangular coordinate system to the polar coordinate system with SPMs is provided.

2.2 Calculation of SPMs weight factor

In the SE block the weight factor matrix recognizes the importance and quality of a measured mode parameter in reference to the other mode parameters. It is complicated by user's configurations resulting in frequent failure of an iterative process. Therefore, the formula (7) is suggested

$$c_{ij} = \frac{1}{\sum_{i=1}^{M} j_{ij}^2}, \tag{7}$$

where j_{ij} is the Jacobian component.

This approach guarantees a monotonous reduction of the weighted sum of the voltage square imbalance.

2.3 Algorithm of the method

The algorithm flow-chart of the proposed SE method is presented in figure 2, where k_{max} is the limit number of iterations; ε is the reasonable error of the voltage vector estimation, calculated as the difference of estimated voltage values at power system nodes on k and k+1 iterations, representative of an iteration convergence; t is the time interval, when a measurement array is formed; t_1 is the calculation time; t_0 is the time, when the last hard change of a topology and a mode is recorded. Diagonal entries of the covariance matrix of the process noise $\boldsymbol{Q}$ equal the measurement variance σ^2: σ=0.02 for telemetry and σ=0.005 for SPMs [20].

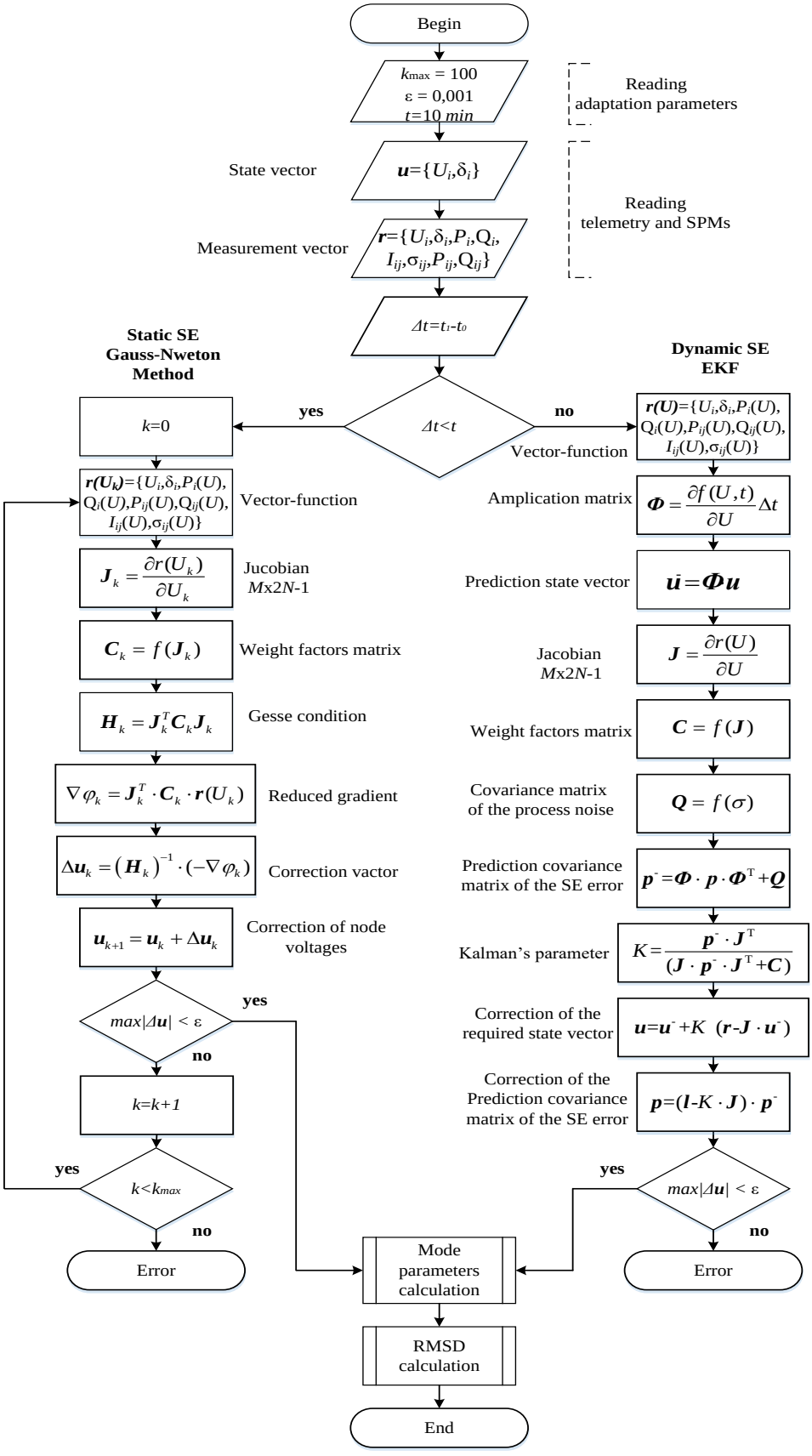

Fig.2. The algorithm flow-chart.

A root-mean-square deviation (RMSD) of mode parameters from a reference parameter is calculated by formula (8):

$$\sigma = \sqrt{\frac{\sum_{i=1}^{n}(r_i - \overline{r})^2}{n-1}}, \tag{8}$$

where r_i is a mode parameter value; $\overline{r}$ is the mean mode parameter value in a data selection; n is the number of values in a data selection.

3. Practical approbation and results

Figure 3 shows the part of the equivalent topology of 500 kV Siberian united electrical grid. This model is implemented to the automated dispatch management system. The following legends are assumed: a State Regional Power Plant (SRPP), a Hydro Power Plant (HPP), and a Power Substation (PS). The telemetry and SPMs are collected from OIC.

PMUs are located on connections: SRPP-1 – PS-4, SRPP-2 – HPP-2, PS-14 – HPP-2, PS-14 – PS-15, HPP-3 – PS-19, PS-20 – PS-19, PS-20 – PS-21, PS-18 – PS-20, PS-21 – PS-18, PS-21 – PS-20, PS-21 – HPP-4, PS-21 – HPP-5, PS-21 – PS-22. They are marked with a grey circle.

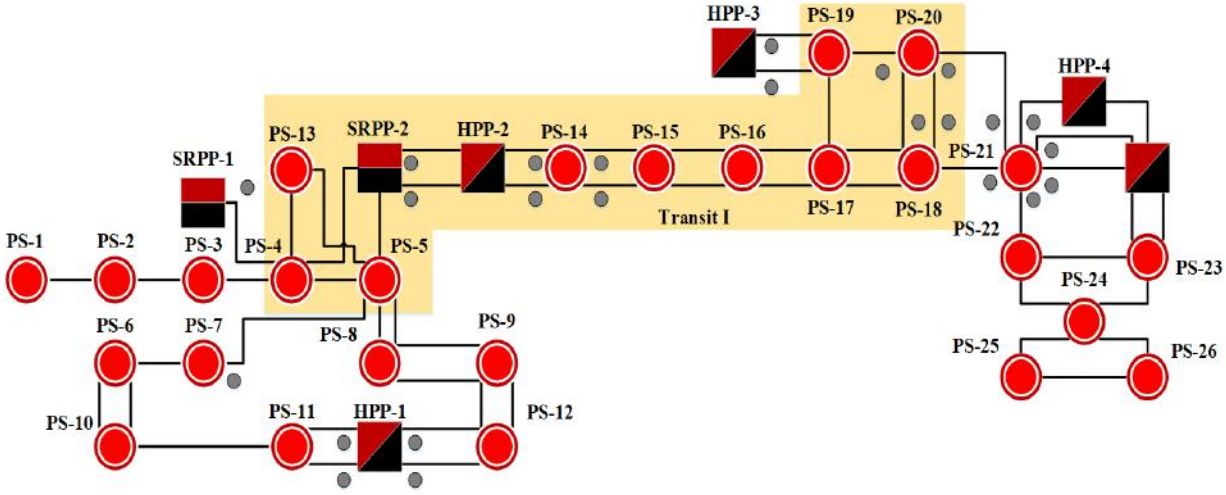

Fig.3. Equivalent topology of 500 kV united power system electrical grid.

Steady state and post-accident modes are studied. The post-accident mode is aligned with the shutdown of 500 kV power line PS-19 – PS-17 by a relay protection. SE is completed by the standard static SE method by telemetry and the suggested method by telemetry and SPMs. According to the nodes of Transit I, figures 4 – 7 demonstrate the RMSD sharing for an active power and voltage measured and estimated values from control values, obtained in the steady state and post-accident modes.

The active power RMSD mean value equals 1.62 MW for measured values, for estimated values by the standard static SE method by telemetry is 1.51 MW and for estimated values by the suggested method by telemetry and SPMs equals 0.86 MW. The voltage RMSD mean value equals 1.91 kV for measured values, for estimated values by standard static SE method by telemetry is 1.32 kV and 1.15 kV for estimated values by suggested method by telemetry and SPMs.

The active power RMSD mean value equals 3.68 MW for measured values, for estimated values by standard static SE method by telemetry is 3.15 MW and 2.11 MW for estimated values by suggested method by telemetry and SPMs. The voltage RMSD mean value equals 3.65 kV for measured values, for estimated values by standard static SE method by telemetry is 2.12 kV and 2.07 kV for estimated values by suggested method by telemetry and SPMs. In the mode, when PS-19 – PS-17 power line is shutdown, active power flows are rerouted between PS-20 – PS-19, PS-18 – PS-20, PS-17 – PS-18 power lines. In this case, the SE accuracy is notably higher for the nearby nodes, where the structure of a power system and the mode are changed.

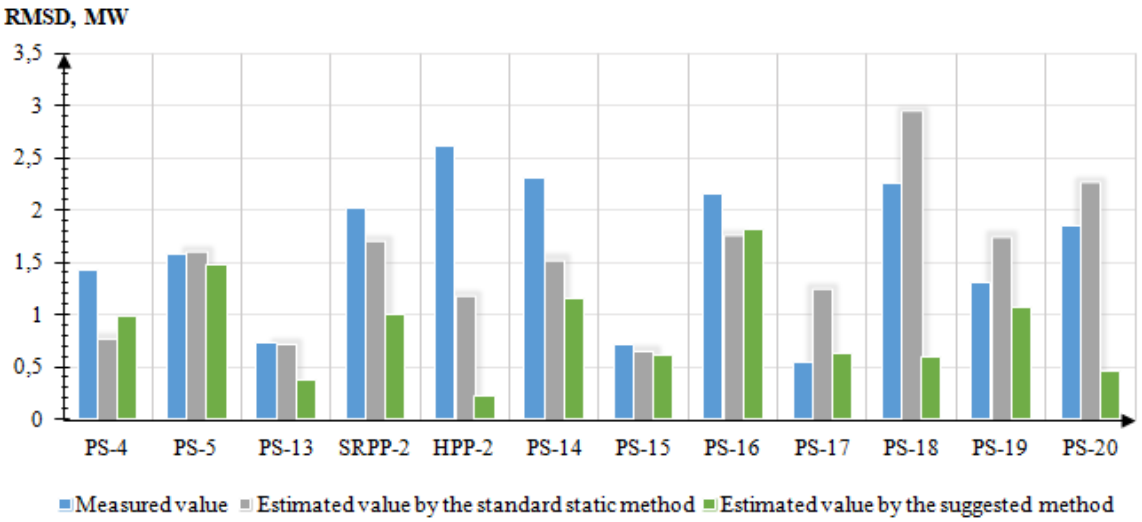

Fig.4. Active power RMSD sharing at the steady state mode

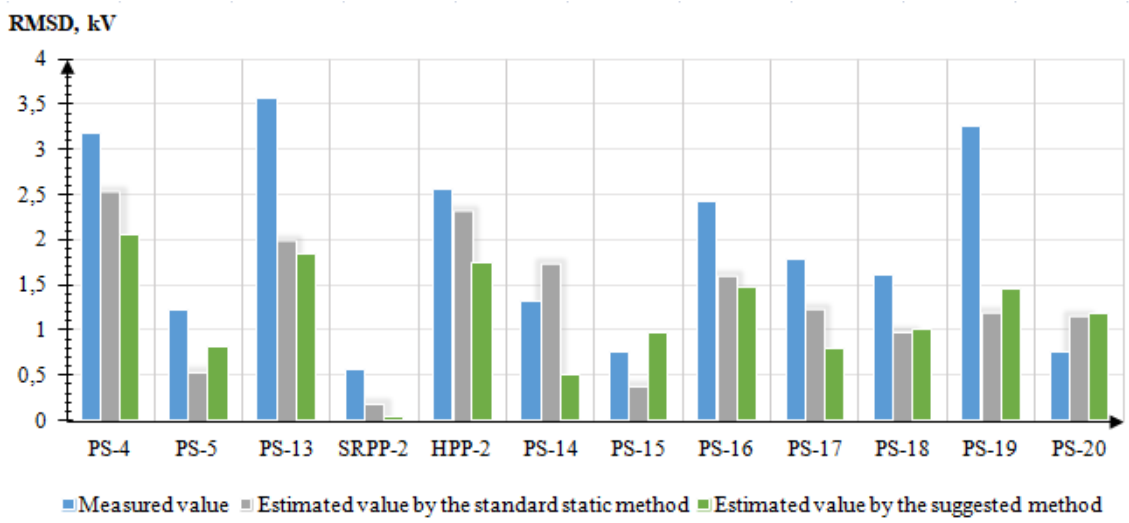

Fig.5. The voltage RMSD sharing in the steady state mode

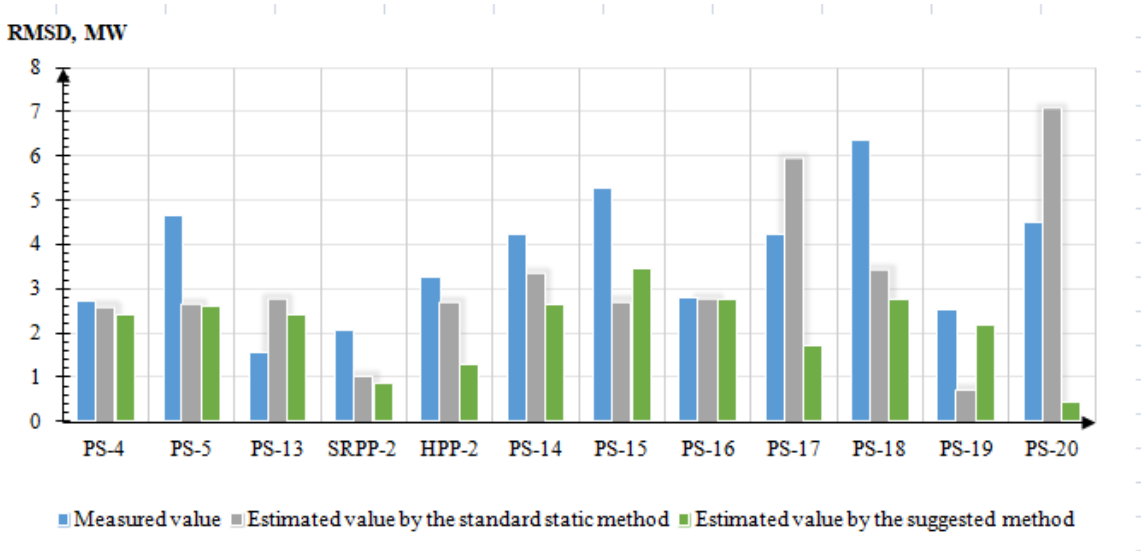

Fig.6. The active power RMSD sharing in the post-accident mode

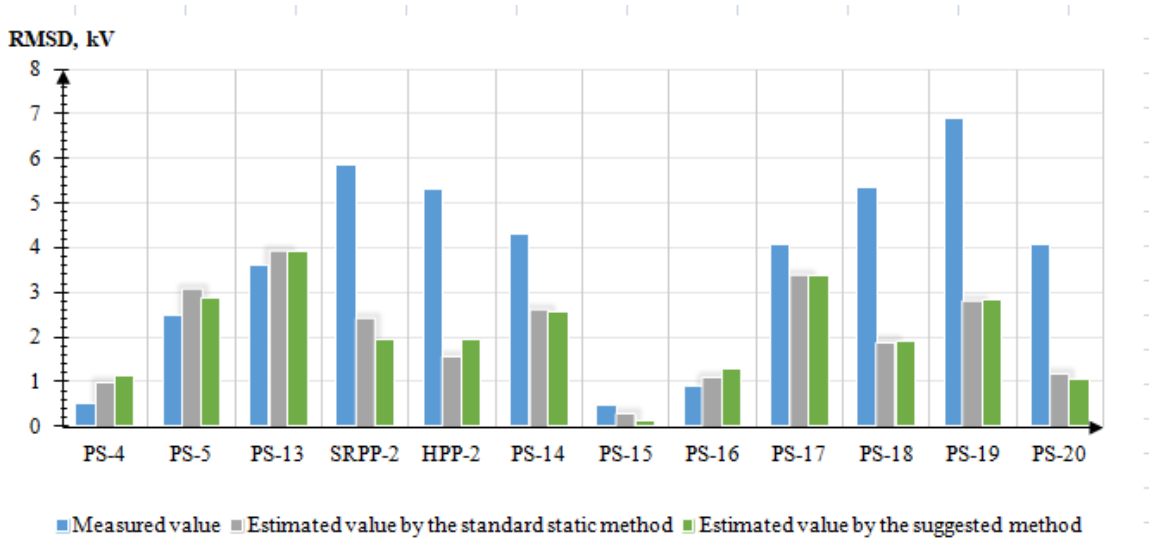

Fig.7. The voltage RMSD sharing in the post-accident mode

The high efficiency of the proposed method for nodes with SPMs is associated with the correct prediction of mode parameters based on measurements in previous time. Meanwhile, the predictive accuracy is lower for nodes with telemetry due to low data rate.

4. Conclusion

1. The SE method is formulated and tested by the high voltage power system. This method is based on the sophisticated Gauss-Newton method and the extended Kalman filter, when telemetry and synchronized phasor measurements are used in combination. The suggested method allows evaluating mode parameters with greater accuracy than a standard static SE method. It is to be noted that:

– SE operates in polar coordinates considering voltage and current angles (formulas 2 – 6), therefore, the Jacobian condition and calculation process convergence are improved.

– Even though the unscented Kalman filter has a desirable accuracy, it requires identifying additional parameters, which are initially indeterminable for all complexes of the system structures and modes. For that reason, the extended Kalman filter has been chosen for dynamic SE.

– Formula (7), which ensures convergence of the iterative process, is offered for calculating weight coefficients of a measured parameter relative to other parameters.

2. It should be noted that the suggested method improves the accuracy of active power flow estimation by 1.76 times for the steady state mode and by 1.5 times for the post-accident mode, while, voltage estimation accuracy shows a 1.2 increase for the steady state mode. These results enable the solution of technological tasks in power engineering with greater accuracy.

3. To implement this method in real-time software packages of the ICC state estimation block, an algorithm (fig.2) is developed. This algorithm includes the command option to receive data from OIC and WAMS.

4. The authors emphasize the importance of codify the theory of continuous and discrete linear Kalman filters, quasilinear filters, generalized nonlinear Kalman filters and continuous and discrete suboptimal nonlinear Pugachev filters to improve the dynamic component of the SE method [22].

5. The additional researches represented that the proposed method permits to calculate maximum allowed active power flows and control action volumes at controlled sections with greater accuracy. The mode parameters, estimated by the suggested method, is applied for calculations of maximum allowed active power flows and control action volumes at controlled sections of 14-bus IEEE electrical grid and 220 kV real power system. The obtained results show that in the steady stay mode, maximum allowed active power flows outnumber by 12 MW against the previously defined number and in the post-emergency mode it is more by 40 MW. It indicates that the total capacity of controlled sections is not used to the end. Whereas, control action volumes in the steady stay mode is more by 2 MW and 13 MW in the post-emergency mode. The use of underestimated control action volumes can not support the stability and reliability in a power system.

Conflict of interest statement
The authors declare that they have no conflict of interest in relation to this research, whether financial, personal, authorship or otherwise, that could affect the research and its results presented in this paper.

CRediT author statement
Batseva, N.L.: Conceptualization, Writing - Review & Editing; **Foos, J.A.:** Validation, Investigation, Software.
The final manuscript was read and approved by all authors.

References

1 Hoseinzadeh B., Bak C.L. (2018) Centralized coordination of emergency control and protection system using on-line outage sensivity index. *Electric Power Systems Research*, 163, 413 – 422. DOI:10.1016/j.epsr.2018.07.016.

2 Panteli M., Crossley P.A., Fitch J. (2015) Design of dependable and secure system integrity protection scheme. *Electrical Power and Energy Systems*, 68, 15 – 25. DOI:10.1016/j.ijepes.2014.12.047.

3 Ballal M.S., Kulkarni A.R., Suryawanshi H.M. (2021) Methodology for the improvements in synchrophasor based System Integrity Protection Schemes under stressed conditions. *Sustainable Energy, Grids and Networks*, 26, 1 – 19. DOI:10.1016/j.segan.2021.100465.

4 Rao A.K., Kundu P. (2023) System integrity protection scheme for minimizing curtailment considering transmission line thermal limits. *Sustainable Energy, Grids and Networks*, 33, 1 – 13. DOI:10.1016/j.segan.2022.100970.

5 Kotha S.K., Rajpathak B., Mallareddy M., Bhuvanagiri R. (2023) Wide area measurement systems based Power System State Estimation using a Robust Linear-Weighted Least Square method. *Energy Reports*, 9, 23 – 32. DOI:10.1016/j.egyr.2023.05.046.

6 Khalid H.M., Flitti F., Mahmoud M.S., Hamdan M.M., Muyeen S.M., Dong Z.Y. (2023) Wide area monitoring system operations in modern power grids: A median regression function-based state estimation approach towards cyber attacks. *Sustainable Energy, Grids and Networks*, 34, 1 – 15. DOI:10.1016/j.segan.2023.101009.

7 Phadke G., Thorp J. S. (2008) *Synchronized Phasor Measurements and Their Applications.* New York: Springer, 247. Available at: https://ieeexplore.ieee.org/document/5447627.

8 Martin K.E. (2015) Synchrophasor measurements under the IEEE Standard C37. 118.1-2011 with amendment C37.118.1a. *IEEE Transactions on Power Delivery*, 30, 3, 1 – 14. Available at: https://ieeexplore.ieee.org/abstract/document/7052413.

9 Espejo E.B., Sevilla F.R.S., Korba P. (2023) *Monitoring and Control of Electrical Power Systems Using Machine Learning Techniques*. Elsevier, 339. Available at: https://www.sciencedirect.com/book/9780323999045/monitoring-and-control-of-electrical-power-systems-using-machine-learning-techniques.

10 Karvelis G.I., Korres G.N., Darmis O.A. (2022) State estimation using SCADA and PMU measurements for networks containing classic HVDC links. *Electric Power Systems Research*, 212, 2–7. DOI:10.1016/j.epsr.2022.108544.

11 Zhenjie W., Lin Y., Pei L., Chengda L., Zhengyang Z., Suirong L., Sun J.F. (2021) State estimation of distribution network based on hybrid measurement combined with multi-source asynchronous data. *Energy Reports*, 8, 1778–1783. DOI:10.1016/j.egyr.2022.03.195.

12 Liu Y., Lin Y., Yue K. (2021) *Modern power system state estimation methods.* Elsevier, 277. Available at: https://nyuscholars.nyu.edu/en/publications/modern-power-system-state-estimation-methods.

13 Li K., Han X. (2022) A distributed Gauss–Newton method for distribution system state estimation. *International Journal of Electrical Power and Energy Systems*, 136, 1 – 14. DOI:10.1016/j.ijepes.2021.107694.

14 Ahmad F., Rashid M.A.K., Rasool A., Özsoy E.E., Sabanovic A., Elitaş M. (2017) Performance Comparison of Static and Dynamic State Estimators for Electric Distribution Systems. *International Journal of Emerging Electric Power Systems*, 18, 3, 1 – 14. DOI:10.1515/ijeeps-2016-0299.

15 Zhao J., Gomez-Exposito A., Netto M., Mili L., Abur A., Terzija V., Kamwa I., Pal B., Singh A.K., Qi J., Huang Z., Meliopoulos A.S. (2019) Power System Dynamic State Estimation: Motivations, Definitions, Methodologies, and Future Work. *IEEE Transactions on Power Systems*, 34, 4, 3188 – 3198. DOI:10.1109/TPWRS.2019.2894769.

16 Yu Y., Li Q., Chen C., Zheng X., Tan Y. (2022) Improved dynamic state estimation of power system using unscented Kalman filter with more accurate prediction model. *Energy Reports*, 8, 364 – 376. DOI:10.1016/j.egyr.2022.10.112.

17 Hong-de D., Shao-wu D., Yuan-cai C., Guang-bin W. (2012) Performance comparison of EKF/UKF/CKF for the tracking of ballistic target. *TELKOMNIKA Indonesian Journal of Electrical Engineering*, 10, 7, 1692 – 1699. DOI: 10.11591/telkomnika.v10i7.1564.

18 Mokhtari S., Yen K.K. (2023) Dynamic state estimation with additive noise for load frequency control using bilateral fuzzy adaptive unscented Kalman filter. *Electric Power Systems Research*, 220, 1 – 10. DOI: 10.1016/j.epsr.2023.109363.

19 Lorenz-Meyer N., Suchantke R., Schiffer J. (2023) Dynamic state and parameter estimation in multi-machine power systems. Experimental demonstration using real-world PMU-measurements. *Control Engineering Practice*, 135, 1 – 10. DOI: 10.1016/j.conengprac.2023.105491.

20 Batseva N.L., Foos Y.A. (2023) Effectiveness of the dynamic state estimation method application for mode parameters of a power system. *Bulletin of the Ivanovo State Power Engineering University*, 3, 5 – 15. DOI:10.17588/2072-2672.2023.3.005-015. [in Russian]

21 Veerakumar N., Cetenovic D., Kongurai K., Popov M., Jongepier A., Terzija V. (2023) PMU-based real-time distribution system state estimation considering anomaly detection, discrimination and identification. *International Jornal of Electrical Power and Energy Systems*, 148, 1 – 15. DOI: 10.1016/j.ijepes.2022.108916.

22 Pugachev V.S., Sinitsin I.N. (2004) *A theory of stochastic systems*. Moscow, Logos Publ., 999. Available at: https://search.rsl.ru/ru/record/01002457901. [in Russian]

AUTHORS' INFORMATION

Batseva, Natalia L. – Cand. Sc., Associate Professor, National Research Tomsk Polytechnic University, Tomsk, Russia; Scopus Author iD: 56486150000; https://orcid.org/0000-0003-1808-4700; batsevan@tpu.ru

Foos, Julia A. – PhD student, National Research Tomsk Polytechnic University, Tomsk, Russia; https://orcid.org/0000-0003-1216-0653; JuliaAlekseevna6797@gmail.com

EURASIAN PHYSICAL TECHNICAL JOURNAL

2024, Volume 21, No. 4 (50)

https://doi.org/10.31489/2024No4/71-78

Received: 09/04/2024 Revised: 02/09/2024 Accepted: 11/12/2024 Published online: 25/12/2024

Original Research Article

UDC 53.06.011.56

CONTROL PROBLEM FOR A VACUUM TECHNOLOGICAL COMPLEX

Melikov E.A.*, Magerramova T.M., Safarova A.A.

Electronics and Automation Department, Azerbaijan State Oil and Industry University, Baku, Azerbaijan

*Corresponding author: elchin03@mail.ru

Abstract. *Based on a comprehensive study of technological processes occurring in the vacuum block for an installation of the ELOU-AVT type, the features for the complex technological complex under consideration as a control object were analyzed. In this regard, a physically based mathematical formulation for the optimal control problem of the block under study has been developed, taking into account restrictive conditions on control and input parameters. Taking into account the compiled mathematical models for the quantitative and qualitative characteristics of the process under consideration and the algorithm for their gradient adaptation, to numerically solve the problem of optimizing the functioning for this block, the classical Lagrange method multipliers is used, which allows the transition from the problem of a conditional extremum to the problem of finding the unconditional extremum for the constructed Lagrange function. This method, as well as the proposed algorithm and control principles, were applied for the first time to the vacuum block of the primary oil refining installation of the ELOU-AVT type under study. In wide range conditions of changes in input disturbing factors in quantity and quality, as well as insufficient operational quality information on the selected petroleum products, the proposed method and principles of development algorithm for controlling the process under study allows for prompt preliminary local regulation modes correction and the selection of new optimal modes for adaptive control as a whole. This circumstance leads to an increase in the economic production efficiency and the achievement of the greatest stability in the quality for the resulting target products.*

Keywords: Model, Control problem, Vacuum block, Technological process, Oil fraction.

1. Introduction

Technological complexes for primary oil refining are, in terms of importance, the most important and integral part of the entire oil industry [1-3]. In this regard, in the practice of developing and implementing optimal control systems for complex continuous technological complexes, one of the most important research stages is a comprehensive study of the processes occurring in these technological installations [4-8]. Crude oil coming from various fields, successively passing through distillation columns, is subjected in these technological complexes to the primary distillation process, dividing the crude oil into fractions of different boiling point ranges. At the same time, as control objects, the above-mentioned technological complexes are characterized by the complexity of their constituent devices, a large number of controlled and uncontrolled technological parameters, the need to make decisions on the control of technological apparatus and processes as a whole in conditions of incomplete information about the processes occurring in them and the objects state, high production capacity, a large number of different aggregates types with complex technological connections between them, etc. [9-12].

In the presented article, a vacuum technological complex (block) for primary oil refining of the ELOU-AVT type is considered as an object of research and development an automatic control system. It is known that in vacuum blocks residual fuel oil is processed into various oil fractions used in the lubricants

production in mechanical engineering, as well as for internal combustion engines and various technological equipment.

As noted above, from a cybernetic view point, the vacuum block of the primary oil refining installation is a complex control object with a multidimensional matrix of interconnected control and controlled coordinates for the technological process under study. In this regard, solving the actual problem improving the quality of vacuum blocks automatic control in oil refining and, as a consequence, increasing the economic efficiency of petroleum products production is a great scientific and practical value.

A comprehensive analysis and study of modern automation systems for primary oil refining installations shows their primary focus on solving local control functions [13-15]. However, in this case, local automation is no longer able to satisfy the growing competitive modern market demands, which requires multifactor automatic control systems for both quantitative and qualitative characteristics of raw materials and the resulting target petroleum products.

The presented article examines the cybernetic foundations of the controlling problem the vacuum technological complex of a primary oil refining installation and proposes principles for development an algorithm for an automatic control system that allows increasing the economic efficiency and productivity of the production in question as a whole.

At the first stage, operational parametric control of the main technological aggregates for the vacuum block is carried out. This control is based on the synthesis of deterministic mathematical models in conjunction with algorithms for optimizing the control coordinates of the process.

At the second stage, the solution to the problem of technological regimes invariant stabilization in conditions of insufficient information about the state of the control object under study is provided. Here, a combined system is proposed using self-adjusting controllers that make it possible to stabilize the quality of the resulting target oil products. Let's consider a generalized automation functional scheme of the vacuum block for a primary oil refining ELOU-AVT type presented in Figure 1.

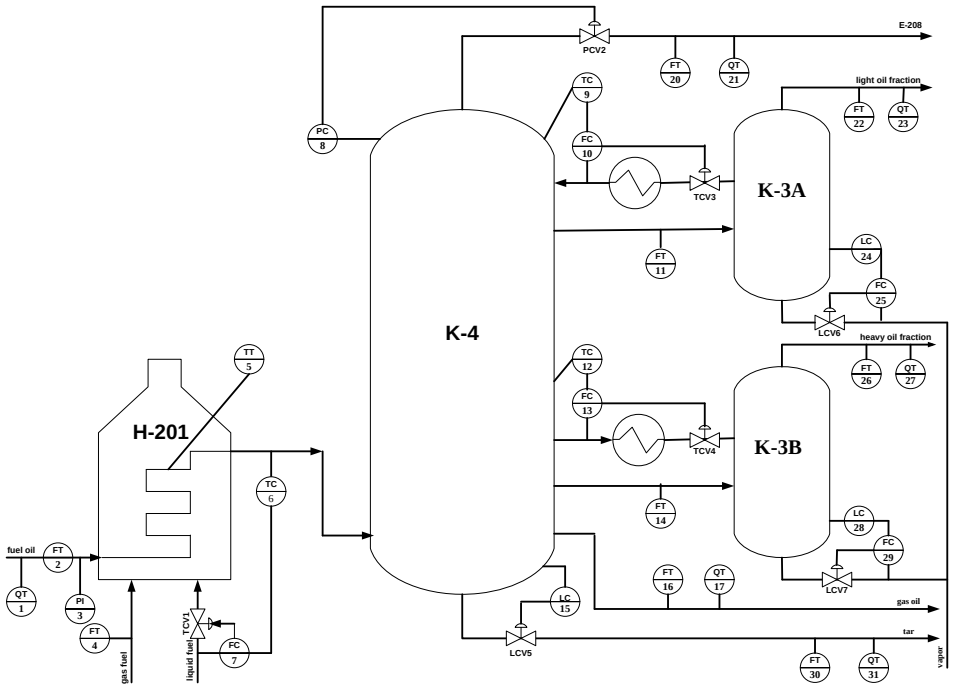

Fig.1. Automation functional scheme of the vacuum block for a primary oil refining ELOU-AVT type installation.

The conducted studies showed that the main and most significant for the effective control of technological apparatuses of the vacuum block are a tubular furnace that provides fuel oil heating, a vacuum column for fuel oil rectification and additional stripping columns.

Being a residual product of the atmospheric block, fuel oil is heated in the H-201 furnace to a temperature of 405÷415 ℃ and then enters the bottom of the K-4 vacuum column. From the top of the K-4 column, a light oil fraction is removed at a temperature of 155÷185 ℃, part of which is used here as

irrigation, and the main flow through the K-5A stripper column is fed to product section of the installation. The heavy oil fraction obtained from the middle part of the K-4 column with a temperature of 290÷310 ℃ is also used as irrigation, and the main flow of the fraction itself flows through the bottom of the K-5B stripping column also in the product section. And finally, heavy vacuum gas oil is removed from the bottom of the K-4 column, and residual tar with a temperature of 340÷345 ℃ is pumped out from the bottom. Table 1 shows the regulatory indicators of the vacuum block mode parameters. Note that the fuel oil vacuum distillation column K-4 has the greatest influence on the quality of the resulting target products. In this case, the main controlled coordinates of the technological process under consideration here are the matrices of temperature conditions and residual pressures. The disturbing factors of this process are variations in the quantitative and qualitative characteristics of the fuel oil coming from the atmospheric block.

Table 1. Regulatory indicators of the vacuum block mode parameters.

Technological parameters	Unit of measurement	Range of variations	
		lower limit	upper limit
Quality of raw materials (fuel oil)	-	Not measured	
Consumption of raw materials	kg^3/h	60	100
Temperature at the outlet flow from the furnace H-201	℃	390	400
Temperature of the vacuum column bottom K-4	℃	385	395
Temperature of the vacuum column top K-4	℃	72	88
Level in vacuum column K-4	%	40	60
Residual pressure in vacuum column K-4	mmHg	60	80
Temperature of the plate from which the light oil fraction is taken	℃	155	185
Temperature of the plate from which the heavy oil fraction is taken	℃	290	310
Light oil consumption	m^3/h	10	-
Heavy oil consumption	m3/h	15	-
Light vacuum gas oil	m3/h	45	-
Vacuum residue – tar	m3/h	10	-

2. Statement of the problem

Depending on the amount of a priori information on the controlled and control coordinates, as well as on the disturbing factors of the process under study, the vacuum block as a control object is classified by a deterministic and partially uncertain system.

In addition, significant difficulties in synthesizing a set of mathematical models that most fully describe the specifics for the ongoing processes in a vacuum block are associated with the efficiency and error of measuring technological parameters.

The practice of operating vacuum blocks in real conditions shows that for these technological installations type the main indicator is maximizing the yield and quality of the resulting oil fractions (specific gravity of the resulting product, flash temperature, kinematic viscosity, etc.) contained in the processed fuel oil with minimal energy consumption. The solution to this problem lies in consistently optimal control of the technological process under consideration.

Thus, taking into account the above, a generalized physically based mathematical formulation of the optimal control problem for a vacuum block, taking into account regulatory indicators, will be written in the following form:

$$Y_{l.o.f} = f_1(F_{f.o}, T_b, T_t, P, T_{K-3A}) \rightarrow max\ , \quad (1)$$

$$G_{l.o.f}^{s.g} = f_2(F_{f.o}, T_b, T_t, P, T_{K-3A}) \geq 0.877\ , \quad (2)$$

$$G_{l.o.f}^{k.v} = f_3(F_{f.o}, T_b, T_t, P, T_{K-3A}) \leq 8.5\ , \quad (3)$$

$$G_{l.o.f}^{f.p} = f_4(F_{f.o}, T_b, T_t, P, T_{K-3A}) \geq 135\ , \quad (4)$$

$$Y_{h.o.f} = f_5(F_{f.o}, T_b, P, T_{K-3B}) \rightarrow max\ , \quad (5)$$

$$G^{s.g}_{h.o.f} = f_6(F_{f.o}, T_b, P, T_{K-3B}) \leq 0.907\ , \quad (6)$$

$$G^{k.v}_{h.o.f} = f_7(F_{f.o}, T_b, P, T_{K-3B}) \leq 6.5\ , \quad (7)$$

$$G^{f.p}_{h.o.f} = f_8(F_{f.o}, T_b, P, T_{K-3B}) \geq 205\ . \quad (8)$$

Restrictions imposed on the control and input parameters of the vacuum block:

$$60\,\frac{m^3}{h} \leq F_{f.o} \leq 100\,\frac{m^3}{h}\ , \quad (9)$$

$$72\ ℃ \leq T_b \leq 88\ ℃\ , \quad (10)$$
$$385\ ℃ \leq T_b \leq 395\ ℃\ , \quad (11)$$
$$60\ mmHg \leq P \leq 80\ mmHg\ , \quad (12)$$
$$155\ ℃ \leq T_{K-3A} \leq 185\ ℃\ , \quad (13)$$
$$270\ ℃ \leq T_{K-3B} \leq 285\ ℃\ . \quad (14)$$

Here and respectively are the yields of light and heavy oil fractions: $G^{s.g}_{l.o.f}$, $G^{k.v}_{l.o.f}$, $G^{f.p}_{l.o.f}$, $G^{s.g}_{h.o.f}$, $G^{k.v}_{h.o.f}$ and $G^{f.p}_{h.o.f}$ accordingly, the specific gravity, kinematic viscosity and flash point of light and heavy oil fractions; $F_{f.o}$ is consumption of fuel oil supplied to the vacuum block for processing; P is residual pressure in vacuum column K-4; T_b, T_t, T_{K-3A} and T_{K-3B} are temperature conditions at control K-4 vacuum column points.

Based on the scientific and theoretical research and analysis, as well as practical experience in operating the K-4 vacuum column, we will accept generalized mathematical models for the output coordinates of the technological process occurring in the vacuum block in the following linear form:

$$y = b_0 + \sum_{i=1}^{n} b_i\, x_i \quad (15)$$

and in nonlinear form:

$$y = b_0 + \sum_{i=1}^{n} b_i\, x_i + \sum_{i=1}^{n} \sum_{j=i+1}^{n} b_{ij} x_i x_j + \sum_{i=1}^{n} b_{ii}\, x_i^2, \quad (16)$$

where y is output coordinate of the technological process under consideration, b_0 is free coefficient of regression equation, b_i, b_{ij} $(i, j = \overline{1,n},\ i \neq j)$ linear and nonlinear coefficients, respectively, b_{ii} $(i = \overline{1,n})$ are quadratic coefficients, $x_i (i = \overline{1,n})$ are input coordinates of the technological process, n is the input matrix dimension.

3. Modelling and development algorithm of control problem

As a result of the process under study analysis, it was established that when mathematically formalizing the vacuum block of a technological installation for the oil primary processing it is more appropriate to build mathematical models characterizing the quantitative indicators of the light and heavy oil fractions target products in a nonlinear form, and mathematical models describing the qualitative indicators of the above-mentioned products - in a linear form. This circumstance makes it possible to achieve the necessary adequacy of the developed mathematical models complex to the real process occurring in the vacuum technological complex. In addition, the proposed control system uses a gradient adaptation algorithm, which makes it possible to maintain the adequacy of the obtained mathematical models to the real process in an iterative mode.

In general, here it is proposed to use a well-known postulate, under which the system can be considered adaptive if the deviation of the output parameter real value for the technological process from its mathematical expectation is minimized by an arbitrarily small value ε:

$M|y_{mod} - y_{real}| \geq \varepsilon,$

where, y_{mod} is the output coordinate obtained on the basis of a linear or nonlinear mathematical model (9) or (10), y_{real} is current value of the output coordinate obtained at the control object output under study, ε is a value characterizing technological accuracy in the mathematical models development. Typically the value of ε is a very small value and is expressed as a percentage.

Here, to adapt mathematical models of the vacuum technological komplex to current situations, it seems more appropriate to use an adaptation algorithm based on the gradient method, since in this proposed adaptation algorithm, unlike other algorithms, gradients of input technological parameters are used to adapt mathematical models. The advantage of this adaptation algorithm compared to other algorithms is that each of the mathematical model's coefficients is adjusted depending on the direction of their gradients and the corresponding model error. This, in turn, makes it possible, based on a smaller operations number, to construct the most adequate mathematical models that have the required quality indicators.

Adaptation of mathematical models to current situations based on this algorithm is carried out in the following way:

- for linear models:

$$B_i^{m+1} = B_i^m + a^m\left[y_{real} - \left(B_0 + \sum_{p=1}^{k} B_p^m x_{preal}\right)\right] \cdot \left(\frac{\partial y_m^*}{\partial x_i}\right)_{x_i = x_{ireal}} \quad (17)$$

- for nonlinear models:

$$B_i^{m+1} = B_i^m + a^m[y_{real} - (B_0 + \sum_p^k B_p^m x_{preal} + \sum_t^k \sum_p^k B_{tp}^m x_{treal} x_{preal})]\left(\frac{\partial y_m^*}{\partial x_i}\right)_{x_i = x_{ireal}} \quad (18)$$

$$B_{ij}^{m+1} = B_{ij}^m + a^m[y_{real} - (B_0 + \sum_p^k B_p^m x_{preal} + \sum_t^k \sum_p^k B_{tp}^m x_{treal} x_{preal})]\left(\frac{\partial^2 y_m^*}{\partial x_i \partial x_j}\right)_{x_i = x_{ireal}, x_j = x_{jreal}} \quad (19)$$

$$i = 1,2,\dots,k; j = 1,2,\dots,k; j \geq i$$

Here y_{real} , x_{ireal} $(i = \overline{1,k})$ are accordingly, the current values of the output and input parameters of the object under study; $\left(\frac{\partial y_m^*}{\partial x_i}\right)_{x_i = x_{ireal}}$, $\left(\frac{\partial^2 y_m^*}{\partial x_i \partial x_j}\right)_{x_i = x_{ireal,}, x_j = x_{jreal}}$ are partial derivatives calculated values according to the corresponding input parameters of the model at points $\{x_{1real}, x_{2real}, \dots, x_{kreal}\}$ on the *m*-th tact, a^m is a positive number that satisfies certain conditions; y_m^* is calculated value of the output technological parameters based on model expressions (15) or (16) at the *m*-th cycle, m are tacts.

It should be noted that the optimization speed of the adaptation algorithm, performed on the expression's basis (17)-(19), depends on several factors, the most important of which is the sequence a^m choice. When developing adaptive mathematical models, it is desirable to choose such a^m coefficients that the deviation of the model coefficients current values from their desired values at each stage is minimal.

In accordance with the above, mathematical models have been obtained that have been adapted to the current situation relative to the output coordinates in the vacuum block upper part and have the following form:

$$Y_{l.o.f} = -4501.1558 + 5.7527F_{f.o} + 8.8673T_b + 45.9481T_t + 3.0525P + 8.76462T_{K-3A} + \\ + 0.0432F_{f.o}^2 - 0.0044F_{f.o}T_b - 0.164F_{f.o}T_t - 0.0079F_{f.o}P + 0.0018F_{f.o}T_{K-3A} - 0.127T_b^2 - \\ -0.127T_b^2 - 0.085T_bT_t + 0.055T_bP - 0.06T_bT_{K-3A} + 0.106T_t^2 - 0.036T_t\,P - -0.0856T_tT_{K-3A} - \\ 0.0024P^2 + 0.0019P\,T_{K-3A} - 0.00292T_{K-3A}^2 \quad (20)$$

$$G_{l.o.f}^{s.g} = 0.9236 - 0.00012F_{f.o} - 0.00117T_b - 0.00517T_t - 0.0001064P - 0.00000177T_{K-3A} \quad (21)$$

$$G_{l.o.f}^{k.v} = 0.0213 - 0.04616F_{f.o} + 0.02752T_b - 0.1339T_t - 0.003585P + 0.05854T_{K-3A} \quad (22)$$

$$G_{l.o.f}^{f.p} = 31{,}3126 - 023486F_{f.o} + 0.1164T_b - 0.3665T_t - 0.000773P + 0.259T_{K-3A} \quad (23)$$

$$Y_{h.o.f} = -3397.998 + 8.8025F_{f.o} + 2.3294T_b + 11.961P + 15.7958T_{K-3B} + 0.00798F_{f.o}^2 - \\ - 0.008F_{f.o}T_b - 0.0599F_{f.o}P + 0.00189F_{f.o}T_{K-3B} - 0.0112T_b^2 + 0.00247T_bP - \\ - 0.03949T_bT_{K-3B} + 0.0024P^2 - \ 0.03193PT_{K-3B} - 0.004949T_{K-3B}^2 \quad (24)$$

$$G_{h.o.f}^{s.g} = 0.885 + 0.000455F_{f.o} + 0.00002T_b - 0.000022P - 0.000041T_{K-3B} \quad (25)$$

$$G_{h.o.f}^{k.v} = 0.3416 + 0.002496F_{f.o} - 0.00175T_b + 0.0385P + 0.0010854T_{K-3B} \quad (26)$$

$$G_{h.o.f}^{f.p} = 120.25 - 0.26975F_{f.o} - 0.02962T_b - 0.046579P + 0.433051T_{K-3B} \quad (27)$$

As can be seen from the above, the mathematical formulation of the optimizing problem the functioning for the vacuum technological complex (1)-(14), built on the mathematical models basis (20)-(27) is by its nature a nonlinear programming problem. Based on the scientific publications analysis, it has been established that to numerically solve the above optimization problem, it is more rational and efficient to use the classical Lagrange multipliers method, since to solve this large-dimensional optimization problem, this method makes it possible to reduce it into a relatively simple subtasks complex that make it up.

As is known, the Lagrange multiplier method allows you to find the maximum or minimum of a function under equality-constraints. Based on finding the objective function partial derivatives, solving the optimization problem using the Lagrange method is reduced to finding the coordinates of the Lagrange function saddle point. Then, for the problem under consideration, the Lagrange function will be written in the following form:

$$\begin{aligned} L = {} & f_1(F_{f.o}, T_b, T_t, P, T_{K-3A}) + f_5(F_{f.o}, T_b, P, T_{K-3B}) + \lambda_1[f_2(F_{f.o}, T_b, T_t, P, T_{K-3A}) - 0.877] + \\ & + \lambda_2[8.5 - f_3(F_{f.o}, T_b, T_t, P, T_{K-3A})] + \lambda_3[f_4(F_{f.o}, T_b, T_t, P, T_{K-3A}) - 135] + \lambda_4[0.907 - \\ & - f_6(F_{f.o}, T_b, P, T_{K-3B})] + \lambda_5[6.5 - f_7(F_{f.o}, T_b, P, T_{K-3B})] + \lambda_6[f_8(F_{f.o}, T_b, P, T_{K-3B}) - 25] + \\ & + \lambda_7[T_b - 385] + \lambda_8[395 - T_b] + \lambda_9[T_t - 72] + \lambda_{10}[88 - T_t] + \lambda_{11}[P - 60] + \lambda_{12}[80 - P] + \\ & + \lambda_{13}[T_{K-3A} - 155] + + \lambda_{14}[185 - T_{K-3A}] + \lambda_{15}[T_{K-3B} - 270] + \lambda_{16}[285 - T_{K-3B}], \end{aligned} \quad (28)$$

where λ_i ($i = \overline{1,16}$) are the Lagrange multipliers.

The proposed algorithm for solving the nonlinear problem of optimizing the functioning for the vacuum block in this case consists of the following steps:

1) the Lagrange function (28) is compiled;

2) the unconditional extremum of the constructed Lagrange function is found based on the controlled coordinates of the process under consideration;

3) according to the Kuhn-Tucker theorem, necessary and sufficient conditions for the extremum point are fixed;

4) using the artificial basis method, the coordinates of the extremum point are found;

5) the optimal form of the original problem is found and the objective function values are calculated.

Below, the solving results the optimization problem under consideration (1)–(14), obtained for the vacuum block of ELOU-AVT type technological installation at an oil refinery, are summarized in tabular form (Table 2). As noted above, the use of traditional automation systems in oil refining under conditions of a wide range of changes in the quantitative and qualitative characteristics of the raw materials supplied to the installation and the insufficiency of available operational qualitative information on the selected fractions no longer meets modern market requirements and is unprofitable in terms of energy costs. In this regard, there is an urgent need to develop fundamentally new automatic control systems based on energy-saving and disturbance-invariant strategies, and also capable of functioning effectively in information deficiency conditions.

Considering various rectification processes from these concepts, it should be noted that in conditions of the existence of a changes wide range in disturbing influences at the vacuum block inlet under consideration, stabilization of the various fractions quality obtained in distillation columns to one degree or another depends from adequate and, most importantly, proactive regulation of the irrigation degree and temperature conditions at the distillation products selection points for the block under study. During transient operating modes of technological installations, in conditions of the significant variations existence in the input quantitative and qualitative incoming raw materials characteristics, only local and traditional parameters stabilization on the stripping plates of the column it is not always possible to achieve the desired result.

Table 2. Results of solving the optimization problem obtained for the vacuum block of ELOU-AVT type technological installation

Parameters	Real value	Optimal value
Raw material consumption (fuel oil), m^3/h	71.66	71.66
Column bottom temperature K-4, ℃	388.49	385.00
Column top temperature K-4, ℃	72.83	82.00
Residual pressure in column K-4, mmHg	64.18	62.00
Temperature at the light oil fraction selection plate of column K-4 (line K-3A), ℃	175.88	177.00
Temperature at the heavy oil fraction selection plate of column K-4 (line K-3B), ℃	276.13	285.00
Consumption of light oil fraction, m^3/h	14.98	17.04
Specific gravity of light oil fraction, g/m^3	0.8771	0.8772
Kinematic viscosity of light oil fraction	7.72	6.47
Flash point of light oil fraction, ℃	132.00	135.24
Consumption of heavy oil fraction, m^3/h	32.00	38.12
Specific gravity of heavy oil fraction, g/m3	0.9061	0.9073
Flash point of heavy oil fraction, ℃	206	212

4. Conclusion

This problem is also aggravated by the certain errors presence in the operational control of the process controlled coordinates under consideration, leading to a lack of adequate parametric information from the control object as a whole. The solution to this problem can be the synthesis of the proposed combined automatic control system with self-adjusting regulators that produce adequate compensation effects in response to existing input disturbances. At the same time, the main idea of developing the proposed combined automatic control system for the vacuum block is the possibility of preliminary correction for the mode parameters of the local control the column stripping trays, depending on the input disturbing factors regarding the quality and quantity of fuel oil entering the unit in question. Thus, by providing a preliminary correction signal, depending on variations in the quality and quantity of fuel oil at the inlet and changes in the irrigation degree, as well as the temperature gradient on the stripping plates, it becomes possible to adapt the settings for local regulators.

As a result, the greatest stability in the quality of the resulting fractions and invariance to input disturbances of the entire system as a whole is achieved.

The main advantage of the approach described in this article to the proposed automatic control system development compared to existing traditional systems is the ability to maintain stability of the quality characteristics for the resulting fractions with sufficiently large changes in the quality and quantity of incoming fuel oil. The proposed principle of development algorithm for a two-level control system of the process under study provides for the corrective influences implementation at both levels. At the same time, existing small disturbances can be corrected during self-tuning of installed local controllers, and large changes at the process input are corrected by choosing new optimal mode parameters for adaptive control of the technological process under consideration. The above also determines the economic feasibility of the proposed control principle, which allows, under conditions of a wide changes range in input disturbances, to achieve the greatest stability in the quality of the resulting commercial product with the lowest energy costs.

Conflict of interest statement

The authors declare that they have no conflict of interest in relation to this research, whether financial, personal, authorship or otherwise, that could affect the research and its results presented in this paper.

CRediT author statement

Melikov E.: Conceptualization, Methodology, Software, Data curation, Writing - Original draft preparation. **Magerramova T.:** Visualization, Investigation, Supervision; **Safarova A.:** Software, Validation, Writing - Reviewing and Editing. The final manuscript was read and approved by all authors.

References

1 Guseinov I.A., Melikov E.A., Khanbutaeva N.A., Efendiev I.R. (2012) Models and algorithms for a multilevel control system of primary oil refinery installations. *J. Comput. Syst. Sci. Int.*, 51, 138–146. DOI: 10.1134/S1064230711060098.

2 Guseinov I.A., Kurbanov Z.G., Melikov E.A., Efendiev A.I., Efendiev I.R. (2014) Nonstationary Multistage Process Control in the Petrochemical Industry. *J. Comput. Syst. Sci. Int.*, 53, 556-564. DOI: 10.1134/S1064230714030095.

3 Melikov E.A., Magerramova T.M., Safarova A.A. (2023) Logical-Linguistic Model for Reactor Cleaning from Impurities. Proceeding of the 15th Intern. Conf. on Applications of Fuzzy Systems, Soft Computing and Artificial Intelligence Tools – ICAFS-2022. ICAFS 2022. *Lecture Notes in Networks and Systems*, 610. Springer, Cham. DOI:10.1007/978-3-031-25252-5_44.

4 Wang L.X. (1998) Stable and optimal fuzzy control of linear systems. *IEEE Transactions on Fuzzy Systems*, 6, 137-143. Available at: https://hdl.handle.net/1783.1/25922.

5 Morari M., Arkun Y., Stephanopoulos G. (1980) Studies in the synthesis of control structures for chemical processes. *Analysis of the Optimizing Control Structures*, 220-232. DOI: 10.1002/aic.690260205.

6 Giwa A. (2012) Decoupling PID Control of a Reactive Packed Distillation Column. *International Journal of Engineering Research & Technology*, 1, 10-12. Available at: https://www.researchgate.net/publication/236899250.

7 Gupta A. (2013) Control of distillation process using neuro-fuzzy technique. *International Journal of Electrical, Electronics and Data Communication*, 1, 16-20. Available at: http://ijeedc.iraj.in/paper_detail.php?paper_id=233.

8 Aliyeva K., Jafarov R. (2023) Safety control systems for ethylene production. *Multidisciplinary Journal, Refereed & Reviewed Journal*, 35 (04), 206-213. DOI: 10.36962/PAHTEI35122023-206.

9 Žilka V., Halás M., Huba M. (2009) Nonlinear Controllers for a Fluid Tank System. Computer Aided Systems Theory - EUROCAST 2009. *Lecture Notes in Computer Science*, 5717, 618-625. Springer, Cham. DOI:10.1007/978-3-642-04772-5_80.

10 Khelassi A., Wilson J.A., Bendib R. (2004) Assessment of Interaction in Process Control Systems. *Proceedings – Dynamical Systems and Applications*, 463-471. Available at: https://www.researchgate.net/publication/228985993.

11 Attarakih M. (2013) Dynamic analysis and control of sieve tray gas absorption column using MATLAB and SIMULINK. *Applied Soft Computing*, 13 (2), 1152-1169. DOI: 10.1016/j.asoc.2012.10.011.

12 Solatian P., Abbasi S.H., Shabaninia F. (2012) Simulation Study of Flow Control Based On PID ANFIS Controller for Non-Linear Process Plants. *American Journal of Intelligent Systems*, 2(5), 104-110. DOI: 10.5923/j.ajis.20120205.04.

13 Yakubov M.S., Xoshimov B.M. (2023) Operational control of the vacuum column of the unit of oil primary distillation. "*Al-Farg'oniy Avlodlari" Electronic Scientific Journal*, 1 (1), 27-34. DOI: 10.5281/zenodo.7698708.

14 H'ng S.X., Ng L.Y., Ng D.K.S., Andiappan V. (2024) Optimisation of Vacuum Distillation Units in Oil Refineries Using Surrogate Models. *Process Integration and Optimization for Sustainability*, 8 , 351–373. DOI: 10.1007/s41660-024-00395-6.

15 Kazakova V.N., Mikhaylova P.G. (2021) Development and research of control systems with fuzzy regulators for installation of primary petroleum refining. *Scientific Journal "Advances in Chemistry and Chemical Engineering*, 35, 22-26. Available at: https://cyberleninka.ru/article/n/razrabotka-i-issledovanie-sistem-upravleniya-s-nechetkimi-regulyatorami-dlya-ustanovki-pervichnoy-pererabotki-nefti/viewer

AUTHORS' INFORMATION

Melikov, Elchin Adil - PhD, Associate Professor, Electronics and Automation Department, Azerbaijan State Oil and Industry University, Baku, Azerbaijan. Scopus Author ID: 55040103800; https://orcid.org/0000-0002-1411-125X; elchin03@mail.ru

Magerramova, Tamella Mustafa - PhD, Associate Professor, Department of Electronics and Automation, Azerbaijan State Oil and Industry University, Baku, Azerbaijan. Scopus Author ID: 58031678900, https://orcid.org/0000-0001-8367-0031; tamellatm@gmail.com

Safarova, Aygun Agamirza - PhD, Associate Professor, Department of Electronics and Automation, Azerbaijan State Oil and Industry University, Baku, Azerbaijan. Scopus Author ID: 57422312900, https://orcid.org/0000-0001-9806-6654; aygsafa@rambler.ru

EURASIAN PHYSICAL TECHNICAL JOURNAL

2024, Volume 21, No.4 (50)

https://doi.org/10.31489/2024No4/79-87

Received: 17/06/2024 Revised: 19/10/2024 Accepted: 18/12/2024 Published online: 25/12/2024

Original Research Article

UDC 53.083.7:621.396

DESIGN OF SOFTWARE DEFINED RADIO OF GROUND STATION FOR RECEIVING NANO-SATELLITES IMAGE DATA IN S-BAND

Baktybekov K.S.*, Bochkova E.N., Korol V.V., Murushkin M.S., Zhumazhanov B.R.

Ghalam LLP, Astana, Kazakhstan

*Corresponding author: k.baktybekov@ghalam.kz

Abstract. *This paper presents results for design, production and implementation of a ground station for transmitting and receiving information in the S-band for low-orbital nanosatellites for remote sensing of the Earth. A distinctive feature of the solution is that it uses universal low-cost Software Defined Radio hardware platforms based on programmable logic arrays and transceivers, such as the AD9361. Computational resources are saved by usage of a FIR filter with real coefficients and a carrier signal with a symmetrical impulse response, as well as a frequency converter using the CORDIC algorithm, which provides an efficient solution in terms of field programmable gate arrays resources. This work computes total and useful data transfer rates, as well as the required ratio of the energy of one message bit to the value of the power spectral density of the equivalent noise when used for encoding and modulation of a standard DVB-S2 MODCOD signal. Evaluation of the parameters of the Software Defined Radio field programmable gate arrays transceiver showed that it can be used in both the S and X frequency bands without significant changes in hardware, which can significantly reduce the cost of the ground station.*

Keywords: ground station, software defined radio, nanosatellite, satellite antenna, field programmable gate arrays, coding, modulation, line communication.

1. Introduction

Conventional radio systems predominantly utilize hardware-centric approaches, which offer limited adaptability in software. These solutions are distinguished by the elevated cost, intricating development process, and labor-intensive adjustment, lacking the capability for flexible system reconfiguration. Software Defined Radio (SDR) offers a programmable implementation of numerous functions compared to traditional architecture-based systems. SDR technology can be utilized for both transceivers on satellites and ground stations. The application of SDR for ground stations, in particular, in the field of remote sensing, was demonstrated in the paper [1], where X-band radio station tracking NOAA-20, Suomi-NPP, Terra, Aqua, and other low-orbit satellites was considered. The ground station architecture used by the European Space Agency was upgraded through the integration of software-defined radio technology. Based on this system, the sampling functions were implemented, reaching a rate of 8 Gsym/s, and digital conversion of the radio signal was realized in S- and X-bands [2].

Extensive investigation into the functionalities of SDR for satellite communications was initiated by the National Aeronautics and Space Administration (NASA) [3]. The research was focused on the realization of following operations onboard the spacecraft that are traditionally executed at ground stations. For example, scheduling of communication sessions and calculation of spacecraft antenna angles were discussed. Moreover, the possibility of obtaining adaptative data rate, modulation, and error-correcting coding in response to fluctuations in communication conditions was explored [4]. The flexibility of SDR-based

solutions allows systems to be reconfigured accounting for different effects such as variations in noise temperature, phase offset, and Doppler shift [5].

SDR technologies can offer advantages for low-orbit spacecraft due to due to their ability to compensate for the Doppler effect, which has a significant impact on low-orbit missions [6]. In such scenarios, SDR and specialized software such as GNURadio offer opportunities that surpass the traditional radio hardware architecture, facilitating simplified Doppler compensation for telemetry taking into account the position of the ground station [7]. SDR finds its most common applications among small satellites and ground stations which are often referred to as university projects [8-14]. The peculiarity of solutions for small satellites lies in the utilization of universal inexpensive SDR hardware platforms based on Field Programmable Gate Arrays (FPGA) and chip-based transceivers, such as AD9361.

Software-defined radio finds application in high data rate communication particularly for meteorological satellite systems, which are characterized by high-speed transmission of satellite images. This objective can be achieved even utilizing on universal SDR hardware platforms and open-source code [15-17].

2. Design SDR technology

SDR has the potential to revolutionize approaches in the field of scientific research on satellite communications and Earth sensing. One of the important functionalities provided by SDR is the ability to remove data anomalies from the payload or communication system. Additionally, this technology reduces development costs by designing adaptive, versatile space platforms that enable meeting specific mission requirements. Owing to the use of FPGA, signal processing across multiple frequency bands, filtering procedure, adaptive modulation, and encoding schemes can be executed without significant hardware alterations. Moreover, it becomes possible to transmit and receive signals across various radio protocols and update software of on-board systems during their mission in orbit.

The radio system based on SDR for the ground station was developed. The hardware platform is manufactured by Luowave. This system provides various functions, including modulation, demodulation, and decoding of digital signals. The following modulation schemes are selected for communication links: QPSK for service telemetry, CPFSK for telecommands, and 8PSK for payload data. Communication can be conducted in S and X bands, supporting different polarizations.

Figure 1 depicts a block diagram of the developed software, which is responsible for signal processing. A debugging setup intended for the development process of digital signal processing algorithms consists of the Ettus N321 SDR and the Xilinx Zynq UltraScale+ MPSoC XCZU9EG FPGA debugging board from Alinx. The integrated development environment is "Vivado" from Xilinx, with Verilog as the hardware description language. The operation system is built for the ARM Cortex-A53 processor using the PetaLinux distributive. This tool facilitates step-by-step debugging of the FPGA and allows real-time monitoring of the correct operation of the circuits and automatic testing of each individual functional block.

Testbench consisted of software part based on GNU radio and the debug board as hardware part. The testing scheme represents two signal paths from a common source. In the first case the signal is processed by GNU radio tool and is demonstrated as a reference on a spectrum analyzer. In the second case the signal goes through FPGA on the debag board and is received by second port of the spectrum analyzer.

Next, one of the important components of a satellite communication system is a Doppler compensation block, which is especially critical for the LEO satellites, is described. The motion of a spacecraft relative to a ground station leads to the signal carrier frequency shift in the frequency spectrum due to the Doppler effect. For example, for a signal operating at frequency of 8.2 GHz, the frequency variation lies in the range of 191 kHz to -191 kHz during the time the spacecraft in sight of the ground station passing from horizon to zenith.

The traditional method of Doppler frequency shift compensation consists of mixing the incoming signal with the signal from the local oscillator (LO). The frequency of the LO is dependent on the range rate and satellite trajectory and is calculated from the spacecraft flight program. After the mixer the resulting frequency is corrected compensating Doppler effect.

The Doppler-corrector mixer with a controlled master oscillator was implemented according to the CORDIC algorithm, which allows to reduce the calculation of complex functions to a cycle of addition and shift operations [18]. The Doppler corrector block receives this value via the PS-PL interface and shifts the spectrum of the received signal. Absence of direct synchronization of a transmitter and a receiver leads to a frequency error. Moreover, there is an inaccuracy in prediction of Doppler compensation frequency and additional frequency offset due to atmosphere effect. To compensate this frequency errors and enhance the

modulation quality the frequency correction unit based on band edge filters is applied [19].

The operation principle of the edge filter circuit is to maintain the symmetry of the carrier spectrum relative to zero. To estimate the carrier frequency offset, the passbands of the edge bandpass filters correspond to the lower and upper limits of the carrier frequency spectrum. There is a divergence in power indicators at the output of bandpass filters for the lower and upper boundaries of the spectrum when the spectrum shifts. When the carrier frequency deviates, a signal is sent from the master oscillator to the mixer to compensate for the frequency error.

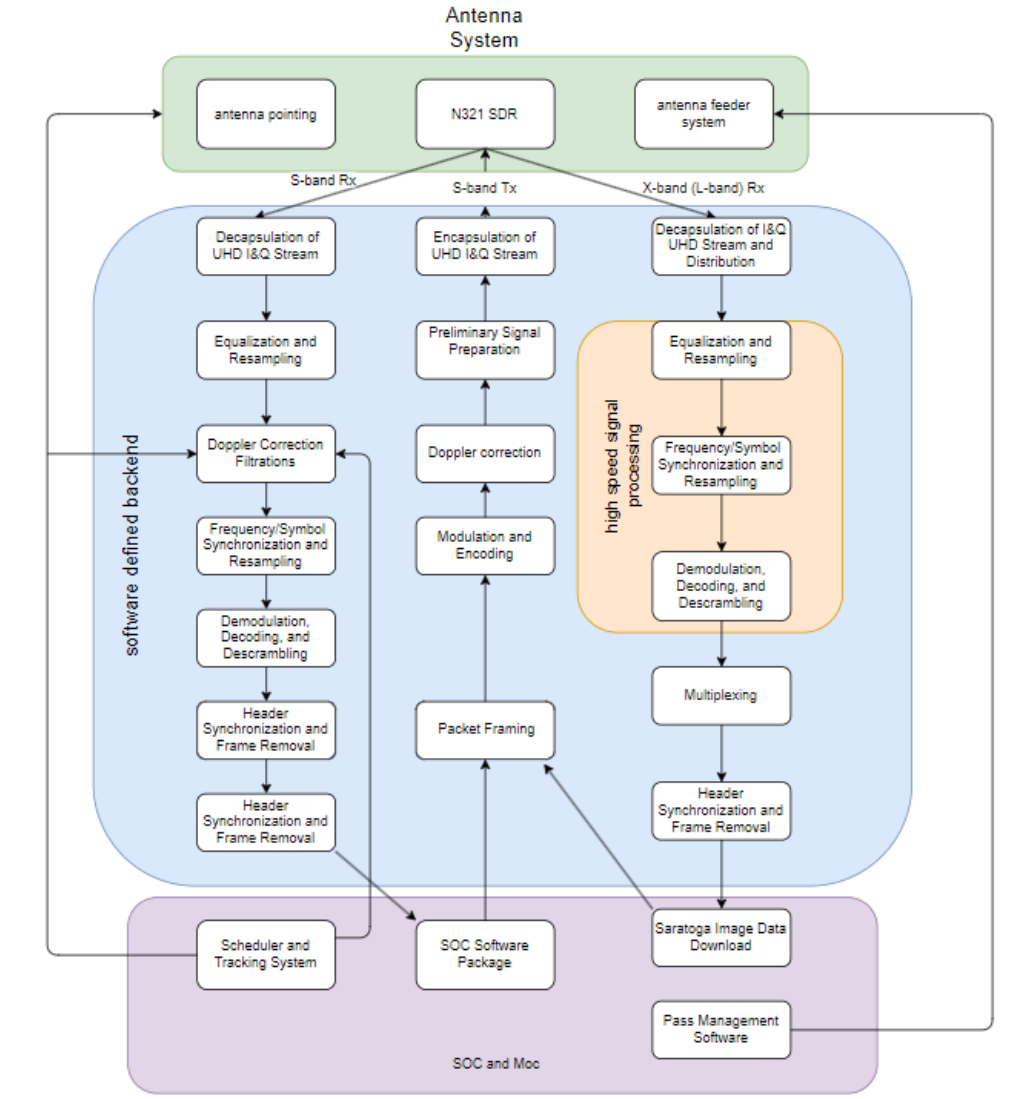

Fig.1. Block diagram of software for SDR platform.

The frequency correction block on the FPGA, as for the Doppler corrector is implemented, using the CORDIC algorithm. The correction block includes a mixer, a controlled master oscillator and edge filters based on FIR filters. Edge filters for the upper and lower boundaries of the spectrum have the same shape of the amplitude-frequency response, which is shifted in the positive and negative directions. Thus, the filters have complex coefficients. Implementing complex coefficient FIR filters on an FPGA means doubling the number of filters, with half having real coefficients and the other half having imaginary coefficients. The filtering procedure involves a multiplication operation for each filter coefficient, which when doubling the number of filters leads to the use of large FPGA resources. To save computational resources, we used a FIR filter with real coefficients and a carrier signal with a symmetrical impulse response and a frequency converter using the CORDIC algorithm. This provided a more efficient solution in terms of FPGA resources.

The above algorithm made it possible to implement Doppler correction of the received signal in order to fix the carrier frequency. This allows you to move on to the next stage of signal reception - symbol

synchronization. Symbol synchronization is the process of adjusting the timing of readings on the receiver with the transmitter timing. The source of timing pulses at the reception is the ADC timing generator, which does not have a direct connection with the transmitter timing generator. Therefore, timing data is extracted directly from the received signal (Figure 2).

The impulse responses of Nyquist filters as symbols were used, namely a filter with a raised cosine response. Nyquist filters are a trade-off between signal bandwidth and intersymbol interference. Those. with a fairly compact form of the signal spectrum, its pulses do not interfere with each other at zero points when they are located on a time interval that is a multiple of the symbol period. The zero values of the pulses are periodic and follow every interval of the symbol period. Outside these null points, pulses overlap each other and interfere with accurate recognition, intersymbol interference increases. The task of symbol synchronization comes down to finding these zero points of the pulse sequence and extracting information about the meaning of the symbol from them.

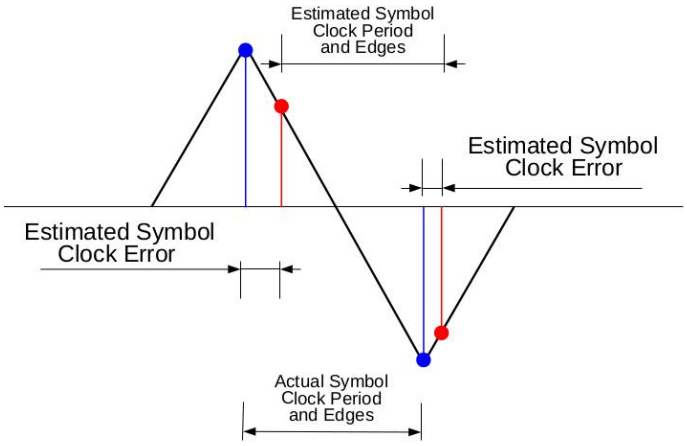

Fig.2. Symbol synchronization scheme.

It should be noted that the receiver operates according to an optimal scheme with a matched filter. This means that a correlation circuit based on a matched filter is used on the receiving side, i.e. the receiver filters out a signal of a certain shape, increasing the reliability of the decision made. The matching of the transmitter and receiver in the signal shape is achieved by using filters with the characteristic of the root of the square raised cosine RRC. Two RRC filters connected in series form a filter with the raised cosine characteristic mentioned earlier. Thus, the RRC filter solves two important problems: it provides optimal reception using a matched filter and minimizes intersymbol interference with a compact signal spectrum.

Digitization at the receiver with a sampling rate higher than the symbol frequency by SPS times is called the number of samples per symbol. Increasing this parameter allows you to find among the readings the one that is as close as possible to the zero point of the pulse. The larger the SPS, the higher the resolution of the time sequence, the higher the accuracy. However, SPS improvement is limited by the performance of the A/D converter and downstream circuitry. Therefore, increasing the resolution of the time sequence of a signal can be achieved by interpolation.

One of the interpolation options is the use of a set of matched filters, the impulse responses of which are identical, only differing in the shift in time space [20]. The filters have the same amplitude-frequency response, but the phase-frequency response differs by a certain amount of group delay time, which is less than the sampling period of the number of filters in the group. Thus, increasing the resolution of the time sequence is achieved by dividing the sampling period into the number of parallel working filters, and the choice of the reference position is achieved by selecting the appropriate filter from the group. Filters are grouped by increasing group delay time, so the time offset becomes equivalent to the filter index. This circuit has a finite number of filters, so the limited resolution of such an interpolator leads to a fixed error.

The ZCTED (Zero-Crossing Timing Error Detector) algorithm is used to estimate the inaccuracy of reference time with symbol time. This method determines the zero-crossing point on the eye diagram and, by analyzing the input sequence, produces a synchronization error signal. This signal is used in a feedback loop to influence the interpolator. In this way, the filter from the group and the sample from the SPS are selected that corresponds to the minimum ZCTED error. A symbolic synchronization scheme using a group of FIR

filters and a ZCTED error analyzer allowed us to develop an FPGA design that has sufficient performance and is acceptable in terms of resource costs.

3. Link budget calculation for S-band uplink and downlink

The link budget is calculated for the described ground station communicating with a LEO satellite. The basic idea of determining the radio link budget derives from the Friis equation, which relates characteristics of a transmitter and receiver and signal propagation path between them. The link budget analysis theoretically estimates the performance of the communication link by accounting for the most critical power gains and losses of the signal. In digital communication, the analysis results in the evaluation of such link quality characteristics as Eb/N0 - the ratio of received energy per bit to spectral noise density. The amount of energy per bit exceeding the noise level is directly proportional to the probability of an error in the bit value determination. For this reason, in communication theory, the E_b/N_0 ratio is defined for a certain bit error rate (BER). The considered radio link operates in the S-band frequency range and involves transmitting telemetry and payload data and receiving telecommands. Two different signal configurations are considered: the first one refers to digital modulation and the second one corresponds to the digital satellite transmission standard, DVB-S2. For the second case full and useful data rates are estimated. The calculations are performed for the defined signal modulations as mentioned above: QPSK for telemetry, 8PSK for payload data, and CPFSK for telecommands. The transmitter symbol rate ranges from 1 *kbit/s* to 500 *kbit/s*.

The downlink includes telemetry transmission and high-rate channel for the payload data transmission. The telemetry signals are modulated by using QPSK scheme where one symbol corresponds to 2 bits, with the required level E_b/N_0 equaling to 10.6 *dB* at BER=10^{-6}. At the same time, using 8PSK modulation 1 symbol of the message corresponds to 3 bits of information, with E_b/N_o level being equal to 14 *dB* at BER=10^{-6}. Table 1 below presents bit rate and required E_b/N_o ratios for QPSK and 8PSK modulations if the symbol rate is leveled to 100 *ksym/s*.

Table 1. Full data rate, useful data rate and E_b/N_0 for QPSK и 8PSK modulations.

Modulation	Symbol rate, [*ksym/s*]	Data rate, [*kbit/s*]	E_b/N_0 at BER=10^{-6} , [*dB*]
QPSK	100	200	10.6
8PSK	100	300	14

Enhanced coding and modulation schemes are implemented in the DVB-S2 standard, to reduce the required Eb/No level and achieve higher bit rates without increasing the signal power [21]. Table 2 demonstrates the total bit rate, useful bit rate, and required E_b/No ratio for several modulation and coding configurations according to DVB-S2. As shown, using the standard allows for achieving a high bit rate at a moderate level of required energy per bit. For example, a bit rate of 1.5 *Mbit/s* can be obtained using 8PSK modulation with a 2/3 coding rate at an Eb/No level of 3.65 *dB*.

Table 2. Full and useful data rate and required Eb/No for different MODCOD according to DVB-S2

MODCOD	Symbol rate, [*ksym/bit*]	Full bit rate, [*kbit/s*]	Useful bit rate, *[kbit/s*]	E_b/No, [*dB*]
QPSK 3/4	100	200	148.7	2.31
QPSK 2/3	100	200	132.2	1.89
QPSK 3/4	500	1000	740	2.31
QPSK 2/3	500	1000	660	1.89
8PSK 2/3	100	300	200	3.65
8PSK 2/3	500	1.5000	1000	3.65

The downlink budget is calculated using the following parameters after determining the required power level for reliable communication, the transmitter output power is 1W, the ratio of gain to the effective noise temperature of the ground station (G/T) is 12 *dB/K*, and the operating frequency is 2.3 *GHz*. The orbit altitude is 600 *km*, and the ground station is located in Astana. A single circularly polarized patch antenna with a maximum gain of 4 *dB* is utilized as the transmitting satellite antenna. Signal attenuation due to pointing inaccuracy and polarization distortion is assumed to be 0.5 *dB* each, respectively. Additionally, a

loss of 3 *dB* in the transmitter and antenna feeder path is taken into account. Atmospheric attenuation for the selected ground station is considered according to the recommendations of the International Telecommunication Union (ITU). The equivalent isotopically radiated power (EIRP) is defined as the product of the gain of the transmitting antenna in a given direction and the output radiated power. EIRP can be calculated using the Friis transmission equation. The calculated EIRP value for an output power of 1*W* and the considered patch antenna is shown in Figure 3.

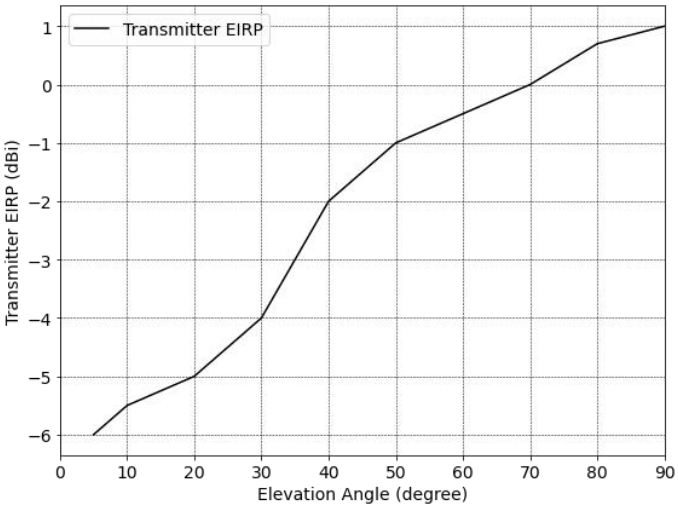

Fig.3. EIRP of the satellite antenna for downlink.

Attenuation due to free space signal propagation from the satellite to the ground station is calculated as a function of the elevation angle. The results are presented in Figure 4. The next step involves obtaining the E_b/N_o level, taking into account the calculated EIRP, free space attenuation, atmospheric loss, and other losses.

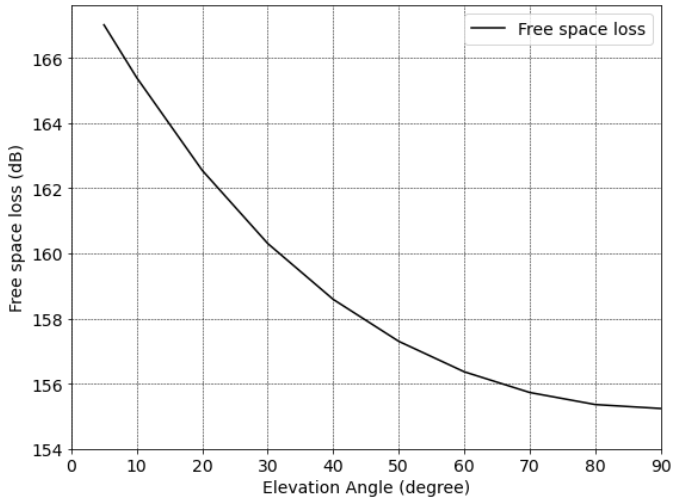

Fig.4. Free space loss depending on elevation angle.

The results for different data rates of 200 *kbit/s*, 500 *kbit/s*, and 1.5 *Mbit/s* are shown in Figure 5. The E_b/N_o level for the 1.5 *Mbit/s* bit rate exceeds 20 *dB* at the nadir position and decreases to 5 *dB* at the 10-degree elevation angle. The required E_b/N_0 level for 8PSK2/3 MODCOD should exceed 3.65 *dB* for reliable radio communication according to the DVB-S2 standard. Consequently, the transmission rate of 1.5 *Mbit/s* based on the 8PSK2/3 signal configuration can be maintained practically from the moment the satellite appears on the horizon. The E_b/N_o ratio for 200 *kbps* is 13 *dB* at a 10-degree elevation angle and grows to 30 *dB* at the nadir position, considerably exceeding the threshold for QPSK modulation. Consequently, low-speed data transmission of telemetry data can be performed using either simple QPSK modulation or according to the broadcasting standard.

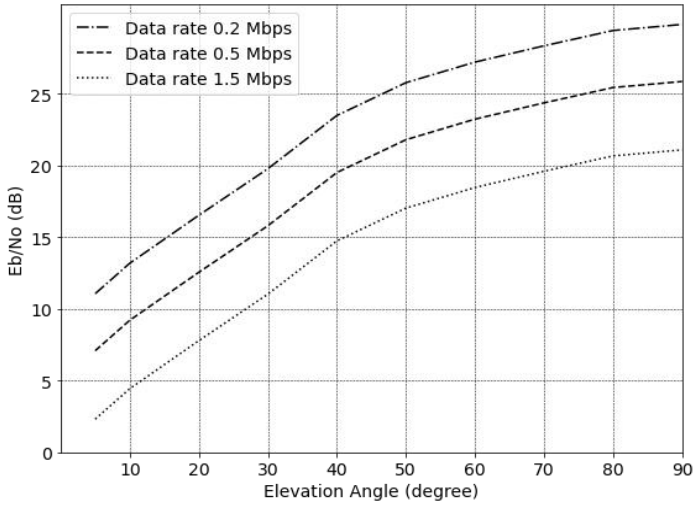

Fig.5. Calculated E_b/N_o for different data rates for downlink.

The radio link budget is estimated for the uplink based on the following parameters: the EIRP of the ground station is 44.5 *dB*, the operating frequency is 2.1 *GHz*, the orbit altitude is 600 km. The same patch antenna used for the downlink is also used as the receiving satellite antenna. The calculated G/T of the receiving antenna is demonstrated in Figure 6. The signal attenuation due to free-space propagation is close to the values obtained for the downlink due to the close operating frequencies.

The calculated E_b/N_o which is required for different bit rates of 50 *kbit/s*, 100 *kbit/s* and 200 *kbit/s* are shown in Figure 7. As it can be observed, under these communication conditions, obtained level of Eb/No is close to 15 *dB* at elevation angle of 5 degrees for a bit rate of 200 *kbit/s*. Transmission of telecommands is carried out on CPFSK modulation, for which the required level of E_b/N_o is 13.6 *dB* at BER = 10^{-6}. Consequently, the data rate of 200 *kbit/s* can be supported practically at any elevation angle from the horizon. However, the rate of 200 *kbit/s* is much higher than the typical telecommand rates in the range of 20-60 *kbps*. Thus, we can conclude that the considered communication channel has a significant power margin.

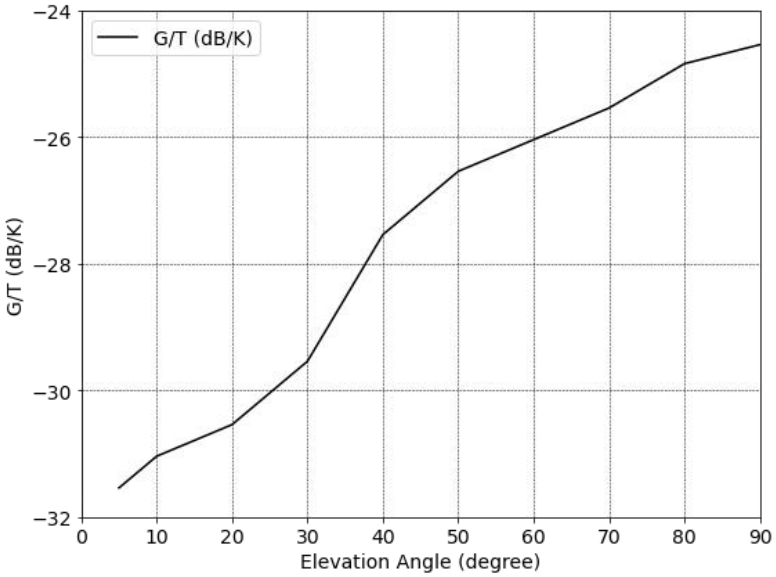

Fig.6. Calculated G/T of receiving satellite antenna depending on elevation angle.

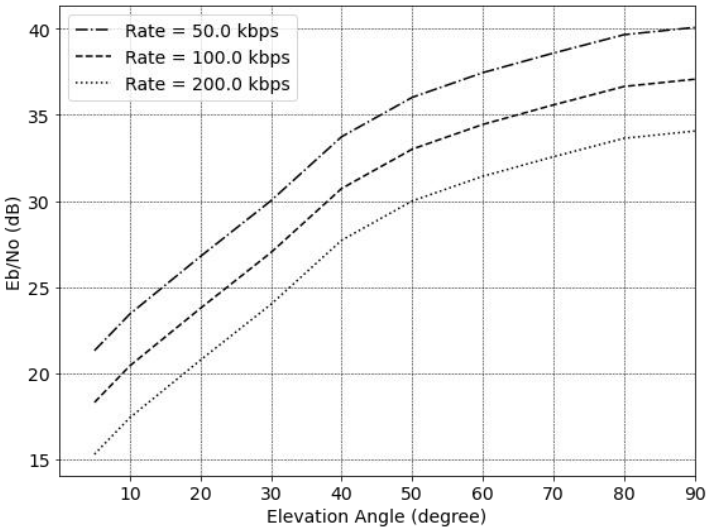

Fig.7. Calculated E_b/N_o for different data rates for uplink.

4. Conclusions

It is shown that the developed SDR transceiver using FPGA provides greater flexibility and allows it to be used in multiple frequency bands, filtering, adaptive modulation and encoding schemes without significant changes in hardware.

Advanced coding and modulation schemes are implemented in the DVB-S2 standard to reduce the required E_b/N_o level and achieve higher data rates without increasing signal power.

The E_b/N_o values were calculated for a ground station depending on the elevation angle at different transmission rates, taking into account atmospheric losses and power reserves, which make it possible to determine the ratio of the transmitter output power level and the antenna gain depending on the data transmission rate requirement.

The calculated data and S-band transceiver described in this article will be used for a ground station that provides services for a constellation of nanosatellites for Earth remote sensing, communications or IoT.

Conflict of interest statement

The authors declare that they have no conflict of interest in relation to this research, whether financial, personal, authorship or otherwise, that could affect the research and its results presented in this paper.

CRediT author statement

Baktybekov K.S.: Conceptualization, Supervision - Original Draft; **Bochkova E.N.:** Writing - Review & Editing; **Korol V.V**.: Data Curation – Writing; **Murushkin M.S.:** Data Curation, Writing; **Zhumazhanov B.R.:** Writing - Review.
The final manuscript was read and approved by all authors.

Acknowledgments

This research has been/was/is funded by the Aerospace Committee of the Ministry of Digital Development, Innovations and Aerospace Industry of the Republic of Kazakhstan (BR 21982462)

References

1 Liashkevich S.V., Saetchnikov V.A. (2021) SDR Based X-Band University Ground Station as Remote Sensing Technologies Learning Environment. *Proceeding of the 8th International Workshop on Metrology for AeroSpace*, IEEE Xplore, 127 – 131. DOI: 10.1109/MetroAeroSpace51421.2021.9511743.

2 Reinhart R., Lux J.P. (2014) Space-based reconfigurable software defined radio test bed aboard international space station. *Proceeding of the "SpaceOps" conference*, AIAA 2014-1612. DOI: 10.2514/6.2014-1612.

3 Ferreira P.V.R., Paffenroth R., Wyglinski A.M., Hackett T.M.; Sven G. Bilen S.G., Reinhart R.C. (2019) Reinforcement learning for satellite communications: From LEO to deep space operations. *IEEE Communications Magazine*, 57, 5, 70 – 75. DOI: 10.9/MCOM.2019.1800796.

4 Kozłowski S. (2018) A carrier synchronization algorithm for SDR-based communication with LEO satellite. *Radioengineering*, 27, 1, 299 – 306. DOI: 10.13164/re.2018.0299.

5 Ilco V., Levineț N., Gîrșcan., A. Margarint, A., Secrieru N. (2015) *Satellite telemetry data reception and processing via software defined radio.* Available at: http://repository.utm.md/handle/5014/2351.

6 Grayver E., Chin A., Hsu J., Stanev S., Kun D., Parower A. (2015) Software defined radio for small satellites. *Proceeding of the IEEE Aerospace Conference*, 1 – 9. DOI: 10.1109/AERO.2015.7118901.

7 Ceylan O., Caglar A., Tugrel H.B., Cakar O., Kislal A.O., Kula K., Yagci H. B. (2016) Satellites. *IEEE icrowave magazine,* 17, 3, 26 – 33. DOI: 10.1109/MMM.2015.2505700.

8 Guerra A.G.C., Ferreira A.S., Costa M., Nodar-Lopez D., Agelet F.A. (2018) Integrating ´ small satellite communication in an autonomous vehicle network: A case on oceanography. *Acta Astronautica,* 145, 229 – 237. DOI:10.1016/j.actaastro.2018.01.022.

9 Maheshwarappa M.R. (2016) *Software defined radio (SDR) architecture for concurrent multisatellite communications.* PhD dissertation. University of Surrey. Available at: https://openresearch.surrey.ac.uk/esploro/outputs/doctoral/Software-defined-radio-SDR-architecture-for/99511622502346.

10 Juang J.C., Tsai C.T., Miau J.J. (2008) A software-defined radio approach for the implementation of ground station receivers. In book: *Small Satellites for Earth Observation,* 293–298. DOI: 10.1007/978-1-4020-6943-7.

11 Quintana-Dıaz G., Birkeland R. (2018) Software-Defined Radios in Satellite Communications. *Proceeding of the conference ESA 4S Symposium*, Sorrento, Italy. Available at: https://www.researchgate.net/publication/330398017.

12 Ajith Kumar Joel, Pavan Kalyan Redd, Charan Yadav, Chandan M., Devanathan M. (2020) SDR Based Ground Station for Image Reception from Weather Satellites. *International Journal of Advance Science and Technology*, 29, No. 10S, 7694 – 7705. Available at: https://sersc.org/journals/index.php/IJAST/article/view/24092.

13 Velasco C., Tipantuña C. (2017) Meteorological picture reception system using software defined radio (SDR). *Proceeding of the IEEE 2nd Ecuador Technical Chapters Meeting*, 1-6. DOI: 10.1109/ETCM.2017.8247551.

14 Georgescu I., Angelescu N., Puchianu D.C., Predusca G., Circiumarescu L-D. (2021) Software defined radio applications-receiving and decoding images transmitted by weather satellites. *Proceeding of the 13th Intern. Conf. on Electronics, Computers and Artificial Intelligence*, 1 – 4. DOI: 10.1109/ECAI52376.2021.9515169.

15 Thabit A.A. (2020) Design and software implementation of radio frequency satellite link based on SDR under noisy channels. *Telkomnika*, 8, 6, 2852 - 2860. DOI: 10.12928/telkomnika.v18i6.16130.

16 Halté S., Chambon C., Rawson S., Dasgupita A., Neveux G., Barataud D. (2019) X-band sampling technology demonstration. *Proceeding of the TTC 2019 - 8th ESA International Workshop on Tracking, Telemetry and Command Systems for Space Applications, IEEE Xplore.* DOI: 10.1109/TTC.2019.8895295.

17 Chen W., Khan A.Q., Abid M., Ding S. (2011) Integrated design of observer-based fault detection for a class of uncertain nonlinear systems. *International Journal of Applied Mathematics and Computer Science,* 21(3), 423 – 430. DOI:10.2478/v10006-011-0031-0.

18 Pratt T., Bostian C., Allnutt J. *Satellite Communications.* Wiley, 560. Available at: https://books.google.com/books/about/Satellite_Communications.h tml?id=IqFvngEACAAJ2002.

19 Larson W.J., Wertz A.V. (1992) *Space Mission Analysis and Design.* Springer, 976, 381 – 395. Available at: https://books.google.com/books/about/Space_Mission_Analysis_and_Design.html?id=QJanyiWfvXMC.

20 Benvenuto N., Cherubini G. (2002) *Algorithms for Communications Systems and Their Applications*. John Wiley & Sons. 508. Available at: https://lib.ysu.am/open_books/413038.pdf.

21 Joseph A. Shaw. (2013) Radiometry and the Friis transmission equation. *Am. J. Phys.*, 81, 33 – 37. DOI:10.1119/1.4755780.

AUTHORS' INFORMATION

Baktybekov, Kazbek S. – Doctor of Phys. & Math. Sciences, Professor, Department of Advanced and Research Projects, Leading Design Engineer, Ghalam LLP, Astana, Kazakhstan; Scopus Author ID: 8926833000, https://orcid.org/0000-0002-6401-8053; k.baktybekov@ghalam.kz

Bochkova, Elena Nikolaevna – PhD, Department of Ground Complex and Technical Support, Leading Design Engineer, Ghalam LLP, Astana, Kazakhstan; Scopus Author ID: 56820098200; https://orcid.org/0000-0003-4851-306X; e.bochkova@ghalam.kz

Korol, Vladimir Viktorovich – PhD, Department of Design and Technical Analysis, Leading Design Engineer, Ghalam LLP, Astana, Kazakhstan; https://orcid.org/0009-0000-4081-1316; v.korol@ghalam.kz

Murushkin, Mikhail Sergeevich – PhD, Special Design Bureau of Space Technology, Leading Design Engineer, Ghalam LLP, Astana, Kazakhstan; https://orcid.org/0009-0006-9917-3842; m.murushkin@ghalam.kz

Zhumazhanov, Berik Rakhymbekuly - Head of the Office of Advanced and Research Projects, Ghalam LLP, Astana, Kazakhstan, Scopus Author ID: 57350754500; https://orcid.org/0000-0001-5926-9619; b.zhumazhanov@ghalam.kz

EURASIAN PHYSICAL TECHNICAL JOURNAL

2024, Volume 21, No.4 (50)

https://doi.org/10.31489/2024No4/88-98

Received: 02/06/2024 Revised: 07/09/2024 Accepted: 18/12/2024 Published online: 25/12/2024

Original Research Article

UDC 539.52; 669.034.011

USING COAL FLOTATION WASTE AS A HEAT-INSULATING BILLING FOR THE HEAD PART OF A FORGING INGOT

Ibraev I.K.[1], Ibraeva O.T.[1], Aitkenov N.B.[1], Sakipov K.E.[2]

[1] Karaganda State Industrial University, Temirtau, Kazakhstan

[2] L.N. Gumilyov Eurasian National University, Astana, Kazakhstan

*Corresponding author: ibraevik@yandex.ru

Abstract. *The experience of using coal flotation waste as a weakly exothermic insulating backfill for insulating the head part of forging dead-melted steel ingots is presented. It has been shown that when using weakly exothermic fills based on single-component fills in the form of coal flotation waste, it is possible to reduce the chemical heterogeneity of the ingot by producing a closed shrinkage cavity, which allows halving heat loss and depth of penetration of shrinkage looseness into the body of the ingot, reducing the segregation of impurities, compacting the head part of the ingot and increasing the yield; moreover, the profitable part of the ingot is more dense and less contaminated with nonmetallic inclusions. The studied patterns of the formation of a closed shrinkage cavity with a dense "bridge" in the head part of a dead-melted steel ingot made it possible to develop and implement a technology for casting large forging ingots of sufficiently high quality using weakly exothermic heat-insulating materials based on metallurgical waste (coke screenings, coal flotation waste).*

Keywords: shrinkage cavity, heat-insulating backfill, ingot, dead-melted steel, coal flotation waste, segregation.

1. Introduction

During the production of large forging ingots made from calm steels, special attention is given to the selection of effective thermal insulation materials to insulate the head part. This is critically important to ensure a high level of yield and the quality of the final product. Especially its head part. The shape of the shell and choice of thermal insulation materials play a key role in this process. These materials need to meet requirements to ensure macro- and micro-structural uniformity of the metal, as well as environmental safety throughout all stages of metal production and use. The main requirements for thermal insulation materials include: high thermal insulation capacity, lack of metal contamination during insulation of ingots in mills, good environmental performance. However, not all materials meet these criteria. For example, asbestos has been previously widely used in some plants, although it is a naturally occurring aquatic mineral with an affinity for fiber structure that can lead to cancerous diseases due to significant dust release when used.

A large number of exothermic thermal insulation mixtures have been developed, consisting of hot oxidizers and inert fillers. Most of these mixtures are characterized by a significant heat release but low heat utilization due to excessive formation of ash with high thermal conductivity. This leads to an increase in heat loss in profitable parts of the ingot and head trimming, as well as increased costs and explosion risks during operation and storage.

To increase the efficiency of exothermic reactions, it is required to combine a high thermal capacity with the ability to retain heat. It is more effective to use weakly exothermic filler materials based on waste materials from metallurgical production. These materials have a slow burning rate and form a porous

structure, which can retain heat over a long period of time and create an airtight, dense layer at the top of the ingot. In addition to achieving maximum thermal insulation, it is essential to develop efficient insulation techniques.

The purpose of this research is to examine the impact of different weakly exothermic metallurgical waste materials on the yield, loss, and macro- and microstructural heterogeneity of metal. It is crucial to assess the environmental consequences of using these substances and techniques for insulating the top of an ingot.

2. Literature review

When heat-insulating boards are used, the heat loss structure from the head part of the ingot changes, and the heat removal through the side surface in the upper part of the ingots decreases. Moreover, the relative amount of heat removed from the metal surface of the ingot increases, which can reduce the effect of using heat-insulating boards. Therefore, the transition to casting ingots with heat-insulating boards requires the use of more effective insulation from the metal mirror than casting ingots with profitable extensions lined with alum inosilicate refractories. The experience of individual plants shows that the difference in the size of the head trim when transferring the insulation of the head part of the ingot from one heat-insulating backfill material to another can reach 3-5% [1-4].

The general requirements for heat-insulating materials are as follows: high heat-insulating ability, no metal contamination when insulating ingots in melds, and good environmental performance. Not all materials used for thermal insulation meet these requirements. For example, asbestos, which is a group of natural aqueous minerals of the silicate class with a fine-fibre structure, causes carcinogenic diseases; when a perlite-graphite mixture is used, significant dust emission is observed.

The authors [5,6] noted that an increase in yield is achieved, in particular, by rolling ingots cast with insulation of the profitable part with exothermic mixtures. There are known developments to create mixtures based on hot, oxidizing and inert fillers [5-8]. Most of these mixtures are characterized by a significant level of heat release but a low heat utilization coefficient of exothermic reactions due to the production of cinder with excessively high thermal conductivity during combustion. This causes an increase in heat loss from the profitable part of the ingot and the head trim.

An increase in the efficiency of exothermic mixtures is achieved when the thermal properties are combined with the ability to retain the generated heat, which is ensured by obtaining a highly porous, lightweight powdered cinder [8-10]. There is no doubt that when heat is supplied to the profit metal of the ingot during solidification, the shrinkage cavity can be localized, and the volume of metal in the profit is brought to the theoretical limit. This is evidenced by the experience of using an electric arc and electro slag heating of ingots, which are currently used only on a limited scale in the production of special alloys or high-alloy steels [11, 12]. The use of effective mixtures containing nitrate leads to unacceptable pollution of the atmosphere of the casting bay with nitrogen oxides, and this process is possible only in workshops in which ventilation ensures the removal of harmful emissions [13].

Mixtures with silicone are very expensive, and their use can only be used for the production of special and alloy steels. In addition, they are explosive and can be manufactured only in specially built workshops designed to be explosion-proof. [14-16]. It is also very difficult to obtain silicone powder due to its explosiveness. Another disadvantage of the mixtures noted in [15], which reduce their manufacturability, is that as a result of their combustion, heat-conducting combustion products are formed, which require the additional introduction of a heat-insulating layer of materials.

However, the preparation of multicomponent exothermic mixtures requires special equipment, which, as a rule, is carried out in the departments of slag-forming mixtures, melds increasing the cost of mild and low-alloy steels. The choice of compositions of exothermic backfills is still made by the “trial and error” method, which is due to the lack of a sufficiently substantiated scientific analysis of the influence of such important characteristics. The location and configuration of the shrinkage cavity in the upper half of the ingot were determined, all else being equal (the mass of the ingot, its transverse dimensions, steel composition, etc.) by the cooling intensity of the ingot and especially its head, which in turn was determined by the efficiency of the insulation of the metal surface and side surfaces. The use of exothermic mixtures to heat the head part of ingots [6-12] is even more effective for bringing the shrinkage cavity upwards, especially if the duration of combustion of the mixture corresponds to the time required to remove overheating of the metal in the entire volume of the ingot above the crystallization temperature.

If the uppermost bridge consists of dense metal without fistulas, cracks or tears, then this contributes to the welding of the shrinkage cavity during hot plastic deformation because the shell itself appears to be divided into parts. If the “bridges” have gaps or discontinuities through which atmospheric oxygen can enter the volume of the shrinkage cavity, then such ingots, when rolled, behave similarly to ingots with an open shrinkage cavity. The reason for the formation of “bridges” is the insufficient effective insulation of the mirror and the side surface of the ingot.

The temperature of the liquid core in the head part of the ingot is in the crystallization range “liquidus – solidus”, i.e., in the temperature range at which the liquid metal loses its fluidity. As the metal level decreases under the layer of heat-insulating backfill and cools, a hard crust periodically forms, which can bend in the central part, tear off along the periphery, etc. Rapid crystallization from the side surface helps to obtain stronger “bridges.” Typically, the conditions of the ingots are such that 1 to 4 bridges are fixed in the head. Therefore, one of the main criteria for evaluating ingots with bridges in the head part is the quality of the “bridges” themselves. For reliable, guaranteed welding of a shrinkage cavity separated by bridges, it is necessary to have strong, defect-free “bridges” (especially the top one), which prevent atmospheric air from entering the volume of the shrinkage cavity. Somewhat separate from the problem of casting ingots with “bridges,” but still close to it, there is the problem of producing ingots with a welded shrinkage cavity. The methods for producing such ingots can be different, but an important general requirement is reliable isolation of the shrinkage cavity from the atmosphere.

In [16], two types of welded shrinkage cavities were obtained-one by the usual turning of the ingot with a still liquid core and the other by dispersing the cavity offset relative to the ingot axis-sometimes by laying the ingot on the side surface after casting. The technology for producing ingots with inversion has been known for a long time; it is used to produce ingots with a closed shell and, during rolling, a welded shell. Filling metal with water is also used for the same purpose. The use of bottle melds for casting mild steels also yielded similar results. In the latter case, the shrinkage cavity is divided into two parts-one open, in which the cinder from the heat insulator accumulates, and the other closed, with small transverse dimensions, which are welded during rolling. Metal from the upper, open shell goes into the head trim, while the yield increases.

3. Research methodology

Steel is poured from above through a collector nozzle with a diameter of 80 mm at a temperature of 1540-1550 °C into melds of type I6H with heat-insulating liners (ingot weight 16.9 tons). Thermal insulating material was applied to the head surface of the metal in the meld after the meld was filled. Carbon-containing material in the form of coal flotation waste (CFL) was used as a thermal insulation material. The chemical and fractional compositions are given in Tables 1 and 2.

Table 1. Chemical composition of the starting materials.

Material	C_t	CaO	CaO_{act}	SiO_2	Fe_2O_3	MgO	Al_2O_3	S	P_2O_5	ppp
Flotation waste	41.23	1.83	-	55.95	8.89	1.23	19.06	0.66	0.119	53.18

When rolling on a slab, head trimming on the experimental melts occurs at a level of 10-11% from the beginning of rolling and, if necessary, until shrinkage defects are completely removed. The heat-insulating properties of various mixtures of known and proposed options for insulating a metal mirror are assessed by the depth of the shrinkage cavity, i.e., according to the length of suitable slabs. The macrostructure and chemical heterogeneity of the metal are studied on transverse templates taken from the head part of the ingot and slab.

Table 2. Average particle size distribution of flotation waste.

Size sieves, mm	>1.6	1.0-1.6	0.63-1.0	0.4-0.63	0.315-0.4	0.2-0.315	< 0.2
Yield of fractions, %	1.91	15.56	23.55	24.28	9.94	11.28	13.48

To study chemical heterogeneity and contamination with nonmetallic inclusions, characteristic ingots of mild steel were isolated and deposited in the composition preparation workshop. After cooling, oxygen cutters cut the slabs parallel to the wide edge 120-150 mm above the axial plane (Figure 1, a); then, in the machine shop, they were planed to the axial plane and ground to remove the sulfuret imprint.

To study chemical heterogeneity and contamination with nonmetallic inclusions, metal samples were taken according to the scheme (Figure 1, b). Chips were collected for chemical analysis using a drill with a diameter of 12 mm. The contents of the elements [C], [Mn], [Si], [S], [P], [AL], and [N] were determined by chemical methods. Metal contamination with nonmetallic inclusions was determined by electrolytic deposition and the LT metallographic method.

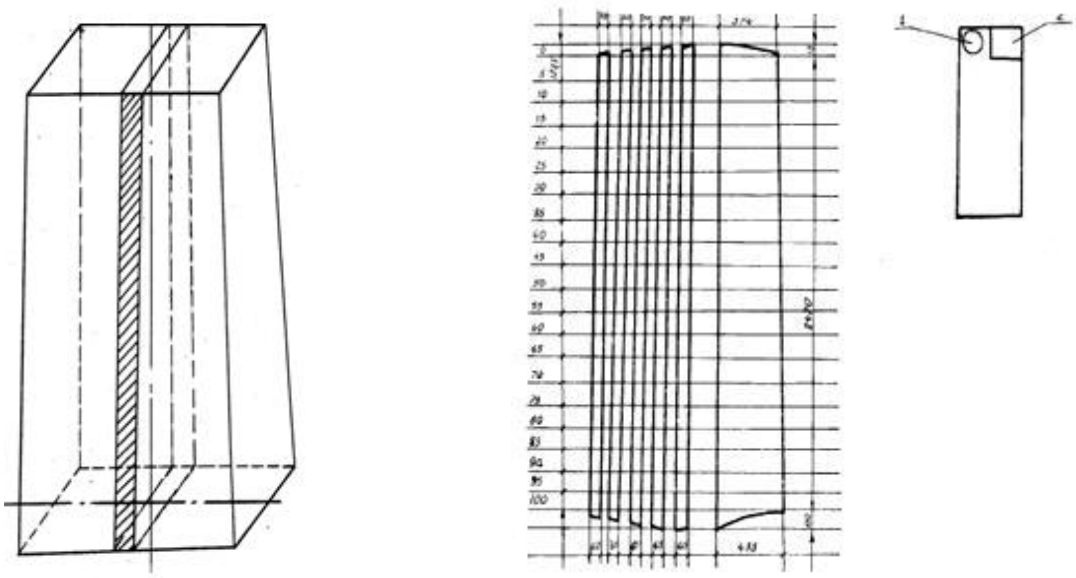

a) b)

Fig.1. Scheme of cutting out the axial plate (a) and sampling for chemical and metallographic analysis (b):
1- place of metal sampling for chemical analysis; 2- selection site for metallographic studies.

When rolling on a slab, head trimming on the experimental melts occurs at a level of 10-11% from the beginning of rolling and, if necessary, until shrinkage defects are completely removed. The heat-insulating properties of various mixtures of known and proposed options for insulating a metal mirror are assessed by the depth of the shrinkage cavity, i.e., according to the length of suitable slabs. The macrostructure and chemical heterogeneity of the metal are studied on transverse templates taken from the head part of the slabs. Metal testing for delamination in slabs was carried out using an ultrasonic method with a UDM-1 M flaw detector at a frequency of 1.8 MHz with a straight probe. The installation diagram for ultrasonic testing of the slabs is shown in Figure 2.

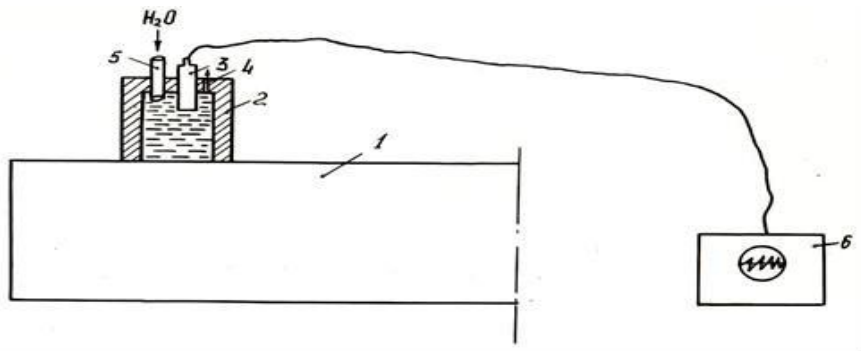

Fig.2. Installation diagram for ultrasonic testing of slabs and sheets:
1 – slab; 2 - textuality head; 3 - sensor; 4 - hole for air outlet;
5 - tube for supplying water to the head; 6 – recording device.

Before ultrasonic testing, the surface of the slab was cleaned of scale. The contact of the metal with the probe was carried out with both technical petroleum jelly and water. The depth of occurrence and the boundaries of the distribution of discontinuities in the slabs were measured using the depth gauge scale of a flaw detector previously calibrated on reference samples. To study the microstructure and contamination of steel with nonmetallic inclusions, metal samples were taken along the boundaries of the shrinkage looseness defect according to the scheme (Figure 3). Thin sections were cut from the selected samples to determine the nonmetallic inclusions and chemical composition.

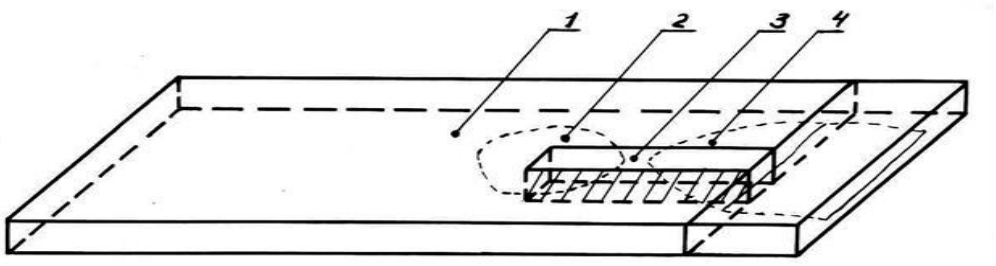

Fig.3. Scheme for sampling from defective areas:
1 – slab; 2, 4 - delamination; 3 - template.

4. Research results

Coal flotation wastes (CFW) themselves have high heat-insulating properties since, mineralogically; they consist of an organic part (carbonaceous substances) and mineral impurities (clay minerals, carbonates, sulphates, etc.). The main clay component is kaolinite. Inorganic substances are represented mainly by the clayey-hydro mica complex, the share of which is 55-65%. The density varies widely from 1400 to 1800 kg/m2, the bulk density by dry weight is 0.65-0.85 kg/m^3, and the calorific value is 2500-4200 kcal/kg.

When developing an industrial technology for casting mild and low-alloy steels using man-made waste from metallurgical production, CFW, as heat-insulating fills, it was necessary to establish the conditions for obtaining a closed shrinkage cavity in the head part of the ingot. According to the proposed method, CFW is applied to a hardened metal mirror with a layer of 20-40 mm. The optimal holding time before applying it to the head surface has been established to be 10-30 s, which makes it possible to increase the temperature state of the metal-backfill system and reduce the period of heating of the flotation waste to the ignition temperature.

Insulation of the head part of a mild steel ingot using the developed method eliminates carburization of the metal and makes it possible to effectively use the heat of a weakly exothermic combustion reaction for thermal insulation of the metal surface. Carbon-containing material, which is used as coal flotation waste, is applied to the hardened head surface of the ingot, which prevents carburization of the metal and makes it possible to obtain an ingot with a closed shrinkage cavity (Figure 4.b). When carbon from coal flotation waste burns for a longer time (more than 1.5 hours), the high temperature of the head of the ingot and, as a consequence, the metal in a liquid state under the solidified “bridge” are maintained. A gas cavity formed between the solidified “bridge” and the liquid metal, preventing heat removal in the vertical direction. In addition, the closed shrinkage cavity prevents metal splashes from occurring during the transportation and processing of ingots and during their placement in heating devices.

The research results showed that slight cooling before adding CFW, promoted the formation of a dense gas-tight bridge. The gas cavity between the solidified bridge and the liquid metal prevents heat removal like in double window frames; the high temperature of the head surface of the ingot is maintained, and as a result, a large proportion of the metal is in a liquid state under the solidified bridge.

As studies have shown, when an OFC is added to a metal mirror, earlier than 10 s after casting the ingots, the formation of an open shrinkage cavity is observed, and as a consequence, carburization of the metal occurs in the sub gross part of the ingot. In addition, oxidation of the inner surface of the shrinkage cavity occurs during the heating of the ingots in the furnace, which ultimately leads to increased head trimming (Table 3, examples 1-3).

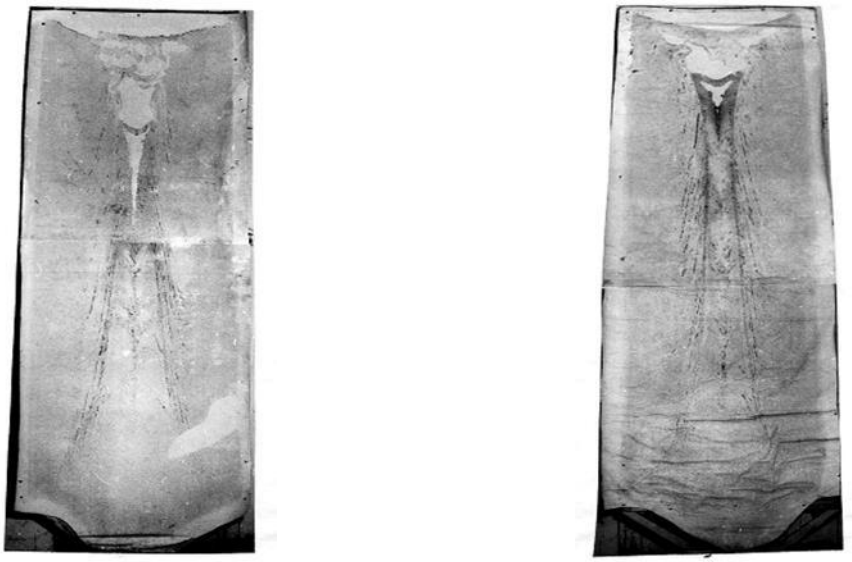

a) b)

Fig.4. Macrostructure of ingots insulated with asbestos (a) and OFU (b).

Checking the influence of the carbon insulation backfill on the degree of carburization of the head part of the ingot with metal sampling along the length of the roll at 4%, 6%, and 10% from the top and at two points along the width (edge and centre) showed that when insulating the head surface of the ingot, in the steel screenings of coke and OFU, there is a slight increase in the carbon concentration, which is typical only for the area up to 4% of the length of the roll, but this change does not affect the quality since it goes with the head trim. Therefore, the type of insulating backfill has no effect on the degree of carbon segregation. This was confirmed by the distribution of carbon along the length and width of the cold-rolled strips (Table 3).

When «OFF» is applied to the metal mirror after 30 s after the head part of the ingot is filled, the flammable components of the flotation waste slowly ignite, which worsens the thermal performance and leads to a decrease in yield in the first stage (Table 4, examples 7-9).

Data from experimental melts showed that the use of the proposed method allows not only the carburization of the metal but also the improvement of the structure of the head part of the ingots and, as a result, the increase in the yield of slabs (examples 4-6).

When applying coal flotation waste to an already hardened metal mirror, the following positive processes occur: During the holding process, flotation waste is heated to a temperature at which the combustion reaction of active carbon and hydrogen begins due to atmospheric oxygen, releasing heat and gaseous reaction products, i.e., carbon dioxide and water vapour, to obtain a solid residue in the form of ash. The presence of particles of different sizes in the waste and the presence of an inert filler in the form of ash contribute to the dispersal of combustion over time. Moreover, the combustion process lasts 30-50 minutes. Moreover, in the process of releasing volatiles contained in flotation waste and gaseous reaction products of carbon and hydrogen, the backfill layer is loosened with the formation of a porous cinder during aging, which has a volume 2-2.5 times greater than that of the original layer of flotation waste and good thermal insulation properties. This helps to reduce the rate of heat removal from the head of the crystallizing ingot.

According to actual data, the porosity of the cinder ranges from 60 - 75%. The entire volume of the cinder has a high thermal resistance, which leads to an increase in the amount of heat transferred to the head of the ingot. The main heat flow is directed to the profitable (head) part of the ingot, which slows its crystallization. During the crystallization process, liquid metal is supplied to the axial zone of the ingot, located below the profit. This helps to reduce the volume of the shrinkage cavity, which is the source of layer formation during the rolling process.

The research results showed that the maximum yield, minimum waste and dust removal are achieved when CFW is applied at a flow rate of 1.5-2.0 kg/t, which corresponds to a layer thickness of 20-40 mm.

Table 3. Changes in the carbon content of cold-rolled rolled products with respect to the length and width of strips obtained from ingots insulated with OFU and dusted asbestos.

View thermal insulation backfill	Carbon content in the ladle sample, %	Location selection by length stripes	Carbon content, %	
			edge	stripes middle stripes
Coal flotation waste	0.03	beginning	0.034	0.030
		middle	0.033	0.025
		end	0.028	0.030
	0.04	beginning	0.037	0.040
		middle	0.027	0.032
		end	0.34	-
	0.05	beginning	0.046	0.040
		middle	0.047	0.046
		end	0.044	0.040
Asbestos	0.03	beginning	0.039	0.038
		middle	0.038	0.038
		end	0.044	0.036
	0.04	beginning	0.034	0.031
		middle	0.036	0.037
		end	0.026	0.031
	0.05	beginning	0.050	0.049
		middle	0.056	0.050
		end	0.050	0.050

Table 4. Metallic logical indicators

Insulation method	Type of insulating backfill	Exposure before insulation, s	Type of shrinkage cavity	Average length of roll, m	Consumption coefficient, t/t	Naugler-living metal
Proposed						
1	flotation waste	0	open	8.9	1.236	occurs
2		3	open	9.0	1.201	occurs
3		7	open	9.1	1.198	does not occur
4		10	closed	9.3	1.176	does not occur
5		20	closed	9.35	1.175	does not occur
6		30	closed	9.38	1.171	does not occur
7		40	closed	9.2	1.189	does not occur
8		50	closed	9.15	1.191	does not occur
9		60	closed	8.95	1.197	does not occur
10	elimination coke	10	open	8.86	1.223	occurs
11		30	closed	9.35	1.175	does not occur
12		90	closed	9.30	1.179	does not occur
Famous	asbestos	0	open	8.89	1.201	does not occur

When the thickness of the layer of carbon-containing material is less than 20 mm, the combustion duration decreases, the heating efficiency of the head of the ingot decreases, and when the layer thickness is more than 40 mm, there is an overconsumption of material without improving the quality characteristics of the metal in the first stage. The novelty of this method lies in the use of heat insulation and exothermic properties of flotation waste to insulate the head part of the ingot, which solves the problem of recycling production waste and prevents contamination of land allocated for the storage of liquid waste sludge from coke and coal preparation production.

In addition, when using the proposed method with coal flotation waste as a weakly exothermic heat-insulating backfill, no harmful emissions are observed in the atmosphere. Research has shown that the dust content on casting balconies is less than 4 mg/m^3 (1.5-2.5 mg/m3); i.e., in ecological terms, these areas have significantly better characteristics (Table 5). The moment at which the insulating fill is introduced into the meld to insulate the head surface of the ingot also affects the environmental performance of the casting process. An environmental assessment of the use of carbon-containing backfill showed that the highest intensity of pollutant release is observed when the material is applied to a liquid

"mirror" of metal. Thus, the concentrations of sulfuric dioxide and carbon monoxide in the air of the pourers in the working area increase to 24.1-29.8 and 30-60 mg/m^3, respectively (Table 5).

Table 5. Environmental assessment of various modes of applying insulating backfill to a metal "mirror".

Ingredient, mg/m3	Asbestos	Coal flotation waste	
		0 -10 s	10 – 30 s
Sulfur dioxide	3.2	29.4	6.6
Ammonia	0	7.3	3.6
Carbon monoxide	0	30.3	15.3
Dust	401.7	15.3	14.62
Nitrogen dioxide	0	0	0
Phenol	0	0.010	0.16
Benzene	0	0	0
Aluminium	0	0	0

The positive aspect of the method using flotation waste as a weakly exothermic heat-insulating material in the form of a monocomposition eliminates the need for preliminary preparation-classification by size classes and mixing of components—rather than when using known exothermic mixtures. The main defects identified in the macrostructure, axial looseness and nonmetallic inclusions, do not exceed 1 point, and carbon segregation is practically absent; i.e., carbon segregation can be considered natural without the influence of insulating backfill.

5. Discussion of the research results

When the shrinkage cavity is closed, when part of the metal is consumed to form a "bridge," one can expect its deeper penetration into the body of the ingot. However, in practice, this is not observed because when the shrinkage cavity is closed, the surface area of the profit through which heat is lost is constant; when the shrinkage cavity is open, this surface increases as the level of metal in the profit decreases due to the hardened layers of metal at the walls of the profitable extension. When a closed shrinkage cavity is formed, its solidification angle decreases (the angle formed by the intersection of the tangents to the outer surface of the profit and the side surface of the cavity of the shell), which is accompanied by a decrease in the depth of the shrinkage cavity. This circumstance in which the shrinkage cavity formed under the "bridge" becomes a heat insulator led to the conclusion about the need to accelerate the formation of the "bridge". The results of the study (Table 6) show that heat loss through the surface of the profit with a closed shrinkage cavity decreases by half, and the penetration depth of the shrinkage cavity decreases from 360 to 260 mm. The quality of the 10 SP steels was studied after the head slabs were rolled onto a 12 mm thick hot-rolled sheet using samples taken at horizons of 12, 14, 16, and 18% (Table 7, 8).

Table 6. Heat loss through the surface of the open (A) and closed (B) cavities and the nature of the shrinkage cavity.

Indicators	Unit measurements	A	B
Heat flow	MJ/m^2	25.6	21.0
Radiation area	m^2	0.8	0.43
Heat loss	MJ/h	20	9
Heat loss during the crystallization process of the ingot (2.5 hours / % of the total amount of heat in profit)	%	7.0	3.2
Shell depth along the ingot axis	mm	340-380	230-275
		360	260
Peel thickness	mm	-	5-25
			15
Solidification angle	deg.	20-35	8-15
		25	10
Sink bottom area at the level of the curved walls	m^2	0.13	0.18
Sink volume	m^3	0.06	0.06

Table 7. Assessment of the quality of the metal macrostructure (to the left and right of the slash: satisfactory and unsatisfactory, respectively, (%) with open (A) and closed (B) profits.

Horizon, %	A	B
12	66.7/33.3	83.3/16.7
14	66.7/33.3	91.7/8.3
16	100.0/0	100.0/0
18	100.0/0	100.0/0

When the head of the ingot is insulated to obtain a closed shrinkage cavity, the profitable part of the ingot is more dense and less contaminated with nonmetallic inclusions. This is explained by the formation of a closed shrinkage cavity, which is clearly visible on the macrostructure of the ingot insulated with CFW (Table 8).

Table 8. Contamination of steel with nonmetallic inclusions (score) when insulating the head part of the OFU (A) and asbestos (B)

Inclusions	A	B
Sulfides	1 - 3.5	1 - 4
	2.1	2.6
Oxides	0.5 - 2.5	0.5 - 2.5
	0.7	0.9
Silicates	0 - 5	1 - 5
	2.7	3.7

6. Conclusion

Analysis of the technical literature and the results of our research show that to reduce the level of head trimming and increase the yield of forging ingots, it is not necessary to achieve complete removal of shrinkage looseness into the profitable part, which is achieved by using high-temperature insulating fills. Satisfactory results are achieved by using weakly exothermic insulating backfill materials based on industrial waste (coal flotation waste, coke screenings and aluminium shaving screenings) to obtain a closed shrinkage looseness with a dense “bridge”, which helps reduce production costs and air dust during casting and solves the problem of recycling production waste.

Analysis of the macrostructure of cast metal has shown that additional heat supply through the metal mirror is possible by using weakly exothermic backfills in the form of coal flotation waste and coke screenings, which not only reduce the volume of liquid metal while ensuring the required reserve of metal density but also affect the location and size of secondary shrinkage defects.

When burning CFW carbon, the high temperature of the head of the ingot is maintained for a longer time (more than 1.5 hours). A gas cavity formed between the solidified “bridge” and the liquid metal, preventing heat removal in the vertical direction. In addition, a closed shrinkage cavity prevents metal splashes during the transportation and processing of ingots, which makes it possible to reduce the duration of holding the ingot in the mould and reduce the time before it is seated in the heating device, i.e., increase its heat content and thereby reduce fuel or electricity consumption for subsequent heating before pressure treatment (forging, rolling).

To eliminate carburization of the metal and ensure a dense “bridge” in the head part of the ingot, a method has been developed for introducing a heat-insulating backfill onto the “mirror” of the metal, i.e., cooling for 10-30 seconds, to form a durable, no melting “bridge”, which additionally plays the role of a heat shield. A new mechanism, cause and technological factor influencing the shape and depth of penetration of the internal “shrinkage looseness” hidden in the body of the ingot have been established, and casting methods and technology for insulating mild steel ingots using man-made waste from metallurgical production have been developed to help reduce delamination.

The studied patterns of the formation of a closed shrinkage cavity with a dense “bridge” in the head part of a quiet steel ingot made it possible to develop and implement a technology for casting large forging ingots of sufficiently high quality using weakly exothermic heat-insulating materials based on metallurgical waste (coke screenings, coal flotation waste) at JSC "ArcelorMittal Temirtau".

A weakly exothermic one-component heat-insulating mixture has been developed based on waste from metallurgical production (carbon-containing sludge from coal preparation), which combines the properties of fairly high thermal properties and good heat-insulating properties due to the production of highly porous, lightweight powdered cinder.

Conflict of interest statement

The authors declare that they have no conflict of interest in relation to this research, whether financial, personal, authorship or otherwise, that could affect the research and its results presented in this paper.

CRediT author statement

Ibraev I.K.: Conceptualization, Software, Investigation.; **Ibraeva O.T.:** Data curation, Writing - Original draft preparation; **Aitkenov N.B**.: Supervision, Software, Validation, Writing - Reviewing and Editing, **Sakipov K.E.:** Methodology; Charge visualization.

The final manuscript was read and approved by all authors.

References

1 Efimov V.S., Eldarkhanov A.S. (2004) *Technologies of modern metallurgy*. Moscow: New technologies. 784. Available at: https://www.gpntb.ru/vystavki-v-gpntb-rossii/2021-god/113-chitatelyam/6/7748-metallurgiya-tekhnologii-i-innovatsii.html [in Russian]

2 Oh K.S., Lee J.D., Kim S.J., Choi J.Y. (2015) Development of a large ingot continuous caster. *Metall. Res. Technol*., 112, 203. DOI: 10.1051/metal/2015006.

3 Leushin I.O., Grachev A.N., Leushina L.I., Ryabtsev A.D. (2023) Exothermic insulation mixture for the production of stainless steel ingots. *Chernye Metally*, 5, DOI: 10.17580/chm.2023.05.03.

4 Efimov M.V., Panov V.V., Kolomoec A.N., Lobanov A.I., Pashynskyi V.V., Snizko O.A., Ryabtsev A.D. (2012) Investigation of non-metallic inclusions in large-mass ingots, produced by PJSC "Energomashspetsstal". *Proceeding of the 5th Intern. Congress on the Science and Technology of Steelmaking*, 2012, Dresden, 335–340. DOI: 10.5937/vojtehg61-3873.

5 Xu L.Yi., Wu Q., Tang Y. (2014) Control of Solidification Process and Surface Microstructure of Large Size Ingot ZALCu5MnA. *Alloy*, 620, 122 – 127. DOI: 10.4028/www.scientific.net/kem.620.122.

6 Leushin I.O., Grachev A.N., Leushina L.I., Ryabtsev A.D. (2023) Exothermic insulation mixture for the production of stainless steel ingots. *Chernye Metally Follow journal*, DOI: 10.17580/chm.2023.05.03.

7 Zhang S., Bao Y., Wang M. (2016) Influence of casting parameters on shrinkage porosity of a 19 ton steel ingot. *La Metallurgia Italiana*, 1, 37 - 44. Available at: https://www.researchgate.net/publication/295938553.

8 Leushin I.O. Exothermic mixture for thermal insulation of the head part of the ingot during casting of steels and alloys. RF Patent No. 2773977. Applied: 03/02/2022. Published: 06/14/2022. Bulletin No.17. [in Russian] DOI: 0.17580/chm.2023.05.03.

9 Toshihiro Dodo (2009) Method for producing an exothermic mixture, exothermic mixture, exothermic composition and exothermic product. Pat. EP 2009/1782780 A4. IPC: A61F7/08, C09K5/16. Available at: https://patents.google.com/patent/EP1782780A4

10 Pindor I.J., Kurka V., Kosňovská J., Štefanišinová S., Socha L., Pyszko R. (2017) Effect of Cooling of the Ingot on its Macrostructural and Chemical Heterogeneity. *Hutnické listy*, 70, 3, 47–57. Available at: https://www.hutnickelisty.cz/en/archives/content-3-2017/effect-of-cooling-of-the-ingot-on-its-macro-structural-and-chemical-heterogeneity/

11 Bettoni P., Biebricher U., Franz H., Lissignoli A., Pagerni A., Scholz H. (2014) Large ESR forging ingots and their quality in production. *Forgiatura La Metallurgia Italiana*, 10. Available at: https://www.researchgate.net/publication /293074610

12 Medovar L.B., Saenko V.Ya., Stovpchenko A.P., Tsykulenko A.K., Shevchenko N.T., Zhuravel V.M. (2010) Electroslag technology of production of large forging ingots. *Advances in Electrometallurgy*, Available at: https://www.thefreelibrary.com/Electroslag technology of production of large forging ingots.-a0319615343.

13 Bächle K., Müller D., Lagemann J. (2020) Entwicklung eines verfahrens und prüfstandes zur qualitätsprüfung exothermer speiser. *Giesserei*, 4. 32 - 37. [in German] Available at: https://www.giesserei.eu/artikel/entwicklung-eines-verfahrens-und-pruefstandes-zur-qualitaetspruefung-exothermer-speiser.

12 Leushin I.O., Grachev A.N., Leushina L.I., Ryabtsev A.D. (2023) Exothermic insulation mixture for the production of stainless steel ingots. *Chernye Metally Follow journal*, DOI: 10.17580/chm.2023.05.03.

13 Rutsky D.V., Zyuban N.A. (2015) Development of defective zones and structure of cast metal in elongated two-piece ingots of chromium-nickel-molybdenum steel. *Bulletin of Cast Iron and Steel of the CIS*, 10, 14 – 18.

Available at: https://www.researchgate.net/publication/290476154_Development_of_defect_zones_and_cast_metal_structure_in_elongared_two-piece_Cr-Ni-Mo

14 Rutskiy D.V., Zyuban N.A., Galkin A.N., Gamanyuk S.B. (2012) Effect of crystallization condirions of the forging ignots head on their structure and forging's quality. *Izvestiya. Ferrous Metallurgy*, 55(7), 32 - 37. DOI:10.17073/0368-0797-2012-7-32-37. [in Russian]

15 Nazaratin V.V., Kobelev O.A., Efimov M.V., Selyutin A.A., Yavtushenko P.M. (2013) Analysis of technologies used to make hollowingots and prospects for their improvement. *Metallurgis*, 56, 672–678. Available from: https://link.springer.com/article/10.1007/s11015-013-9634-z

16 Ibraev I.K., Ibraeva O.T., Aitkenov N.B. (2024) Experience in using coal flotation waste to insulate the head part of forging ingots. *Ferrous metallurgy. Bulletin of scientific, technical and economic information*, 80, 6, 51 – 66. DOI: 10.32339/0135-5910-2024-6-51-66.

AUTHORS' INFORMATION

Ibraev, Irshek Kazhikarimovich - Doctor of Technical Sciences, Professor, Department of Metallurgy and Metallurgy, Karaganda Industrial University, Temirtau, Kazakhstan; https://orcid.org/0000-0002-6414-6901; ibraevik@yandex.ru

Ibraeva, Orazbike Toktarkhanovna - Candidate https://orcid.org/ORCID 0000-0002-8490-1994; ibraevaot@yandex.ru

Aitkenov, Nurbek Bolatovich - PhD, Senior Lecturer, Department of Metallurgy and Metallurgy, Karaganda Industrial University, Temirtau, Kazakhstan; https://orcid.org/0000-0001-7495-6337; nurbek.aitkenov@mail.ru

Sakipov, Kamalkhan E. - Candidate of Technical Sciences, Associate Professor, Department of Thermal Power Engineering, L.N. Gumilyov Eurasian National University, Astana, Kazakhstan; https://orcid.org/0000-0003-2477-3879; sakamer2100@gmail.com

EURASIAN PHYSICAL TECHNICAL JOURNAL

2024, Volume 21, No.4 (50)

https://doi.org/10.31489/2024No4/99-108

Received: 07/06/2024 Revised: 11/10/2024 Accepted: 13/12/2024 Published online: 25/12/2024

Original Research Article

UDC 539.374.1, 539.381, 539.4.012, 621.735.3:621.983.31

MODELING IN THE DESIGN OF TECHNOLOGICAL PROCESSES FOR DRAWING WITH WALL THINNING OF HOLLOW AXISYMMETRIC PARTS FOR VARIOUS PURPOSES

Rasulov Z.[1], Olehver A.[1], Remshev E.[1], Voinash S.[2], Vornacheva I.[3], Sokolova V.[2], Malikov V.[4]*

[1] Baltic State Technical University "Voenmeh" named after D.F. Ustinov, Saint Petersburg, Russia
[2] Kazan Federal University, Kazan, Russia
[3] South-West State University, Kursk, Russia
[4] Altai State University, Barnaul, Russia
*Corresponding author: osys11@gmail.com

Abstract. *There are a number of products that operate under extremely difficult conditions of complex loading, the manufacture of which by traditional stamping operations does not provide the required properties, which leads to a large number of defects. One of the possible directions for the manufacture of products of increased strength is the introduction into the technological process of methods of intense plastic deformation, which can be either volumetric (equal-channel angular pressing, longitudinal extrusion through a channel of variable cross-section, drawing with wall thinning along the internal contour) or surface (grinding holes, rolling with rollers or balls). The study demonstrates the application of the approximate monotonicity criterion and its relationship with technological parameters, using the example of a deep drawing process with wall thinning. A case is presented where technological parameters, including friction conditions and the degree of deformation, are selected to ensure approximate monotonicity during the thinning process. The findings provide a basis for the rational selection of the "strain-stress" curve, contributing to a more accurate and efficient design of deformation processes.*

Keywords: Technological process, drawing with wall thinning, intense plastic deformation, criterion of approximate monotonicity, stress-strain state.

1. Introduction

The solution of metal forming problems through the calculation of the stress-strain state (SSS) is based on several assumptions, one of which involves adopting a specific "strain-stress" curve. According to the established classification of complex loading processes [1-9], the selection of this curve is intricately linked to the concept of monotonic deformation, a term introduced into scientific discourse by G.A. Smirnov-Alyaev [2]. This process is widely used in the manufacture of axisymmetric parts with constant and variable wall thickness [3–4]. The deforming elements are a cylindrical mandrel and a roller having a conical or torus shape. During processing, the roller rolls along a rotating workpiece with a given axial feed and ensures forced thinning of the wall to the required value. Within the geometric focus of deformation, the material is under conditions of uneven all-round compression, which greatly complicates the theoretical study of the SSS of this process. This determines that the improvement of the technology of the rotary drawing process is based mainly on the results, on the basis of which various theoretical models are developed [5–10].

The purpose – is to apply the approximate monotonicity criterion and establish its connection with technological parameters using the example of a hood with wall thinning, to develop an algorithm for selecting technological parameters, such as friction conditions and the degree of deformation, in the thinning process of a deep drawing operation is designed to ensure the approximate monotonicity of the process. This algorithm provides a systematic approach to optimizing the deformation process by maintaining stability in the strain distribution and minimizing deviations from monotonic behavior throughout the operation.

The results allow a reasonable choice of the “strain-stress” curve.

Monotonic deformation is characterized by the simultaneous fulfillment of two conditions:

1) the principal axes of the strain rate remain aligned with the same material fibers throughout the process;

2) the value of $\nu = \nu_{\dot{\varepsilon}} = \frac{2\dot{\varepsilon}_2 - \dot{\varepsilon}_1 - \dot{\varepsilon}_3}{\dot{\varepsilon}_1 - \dot{\varepsilon}_3}$ remains constant during the entire deformation.

The first condition of monotonicity means the coaxiality of the tensors T_ε and $T_{\dot{\varepsilon}}$. In other words, if denote the principal axes of tensor T_ε as X_1, X_2 and X_3 corresponding to its eigenvalues $\lambda_1 > \lambda_2 > \lambda_3$, and the principal axes of tensor $T_{\dot{\varepsilon}}$ as Y_1, Y_2 and Y_3 – then the relationships $X_1||Y_1$, $X_2||Y_2$ and $X_3||Y_3$ must hold.

Let us denote the rotation angle of the principal axes of the strain rate tensor relative to the principal axes of the strain tensor as α. he first condition for monotonicity can then be expressed as $\alpha = 0$. The second condition, by definition, is written as $\nu =$const.

For any given process, the selection of the "strain-stress" curve depends on whether both conditions are fully met, only one is satisfied, or neither holds true [1].

In practice, however, the exact fulfillment of $\alpha = 0$ and $\nu =$const, is unlikely, as these are idealized equality conditions. When addressing real-world problems, the concept of "approximate monotonicity" is typically used, although the degree of this approximation is not explicitly quantified. In general, both α and ν ary over time, expressed as $\alpha = \alpha(t)$, $\nu = \nu(t)$.

In [1], a criterion for approximate monotonicity was proposed:

$$d = max\left[\frac{1}{\pi}\max_t(\alpha(t));\ \frac{1}{2}\left(\max_t \nu(t) - \min_t \nu(t)\right)\right] \quad (1)$$

- a scalar, based on the value of which you can decide whether or not to consider a given process monotonic. The criterion for approximate monotonicity d y satisfies the inequality $0 \le d \le 1$, and for monotonic processes the equality $d = 0$ holds.

The concept of monotonic deformation by Smirnov-Alyaeva G.A. establishes a connection between the strain tensor and the strain rate tensor. The use of flow theory in solving plastic deformation problems in metal forming focuses on quantities such as flow rates, strain rates, and stresses, without involving displacements or deformations in the solution. Conversely, when the theory of small elastic deformations is applied, the analysis excludes velocities and strain rates, focusing instead on displacements and deformations.

In [11], which develops this approach, the strain rate is determined using sections in accordance with a methodology in which the deformed state is determined using microstructural analysis performed near a selected point. The authors conducted a drawing and deformation study in which a single cold drawing pass drew a 12 mm diameter circular tube with a 1 mm wall thickness made of steel into a square tube. This study determined how material properties affect the energy intensity of the manufacturing process and the strain rate when drawing a square tube.

The development of deformations has been studied in a number of other works. Khatala et al. [12] studied the deformations that occur in a non-circular pipe during processing and described the development of a mathematical model using the DEFORM software package. State variables describing the initial state of the material (such as stress, strain, and strain rate) and the flow of material during the drawing process were determined through numerical calculation. Boutenel et al. [13] studied the cold drawing of high-precision non-circular pipes using a computer model that very accurately predicted the final dimensions of the pipe and determined the effect of die angle on the drawing force and the effect of relative thickness on pipe deformation.

In [14], under a number of assumptions (including the plane nature of the problem), the stress-strain state (SSS) of the workpiece wall during drawing with thinning was calculated. The expression for the

intensity of the strain rate is the product of two functions that depend on only one variable and has a relatively simple form.

In the event that the expression for the intensity of the strain rate does not have a simple form, constructing an analytical solution to the system of equilibrium equations is very difficult. The assumption of the flat nature of the problem adopted in [14, 15] is quite restrictive for cartridge-case production, since the ratio of the wall thickness of the semi-finished case to its diameter is quite large, so it is necessary to classify the case as a thick-walled workpiece. It is also impossible to use the obtained solution for calculating the stress-strain state and assessing the degree of deformation of thick-walled workpieces during drawing with thinning. Blanks for drawing with thinning are divided into thin-walled and thick-walled blanks.

2. Practical Research

Let us demonstrate the practical application of the approximate monotonicity criteria using the example of a hood with wall thinning. In [3], a flow velocity field was constructed for drawing with thinning. Under the assumptions made there, the zone of plastic deformation (ZPD) has the form of an annular sector limited by circles of radii $r = a$ and $r = b$ ($a < b$), angular valueγ. The speeds are:

$v_r = \frac{f(\phi)}{r}$, $v_\phi = 0$, $v_\theta = 0$,

where $f(\phi)$ was calculated in [4]:

$$f(\phi) = -v_0 a \cdot e^{\frac{2}{C\sqrt{3}}\left(\sqrt{1-3C_1{}^2}-\sqrt{1-3(C_1-C\phi)^2}\right)} \tag{2}$$

and satisfies the inequality $f(\phi) < 0$. Thus, the movement of particles along the ZPD occurs in the radial direction in the direction of decreasing the radius. This movement determines the unique dependence of the radial coordinate on time, the explicit form of which is established in [4]:

$$t(\phi) = \frac{r^2-b^2}{2\cdot f(\phi)}. \tag{3}$$

By definition of current speed $v_r = \frac{du_r}{dt}$. Writing the speed v_r taking into account (3) as a function of time, find:

$$u_r = \int_0^t \frac{f(\phi)dt}{\sqrt{b^2+2t\cdot f(\phi)}} = \sqrt{b^2 + 2t \cdot f(\phi)} - b. \tag{4}$$

Note that take into account relation (3) in relation (4), obtain $u_r = r - b$, as one would expect. It's obvious that $u_\phi = 0$, $u_\theta = 0$. Knowing the displacements, calculate the deformations: $\varepsilon_r = 1$, $\varepsilon_\phi = \frac{r-b}{r}$. To search for shear strain $\gamma_{r\phi}$ use relation (4):

$$\gamma_{r\phi} = \frac{1}{r}\frac{t\cdot f'(\phi)}{\sqrt{b^2+2t\cdot f(\phi)}} = \frac{(r^2-b^2)\cdot f'(\phi)}{2r^2\cdot f(\phi)} \tag{5}$$

Thus, the strain tensors T_ε and strain rate $T_{\dot{\varepsilon}}$ (its components are taken from [3]) have the form:

$$T_\varepsilon = \begin{pmatrix} 1 & \frac{(r^2-b^2)\cdot f'(\phi)}{2r^2\cdot f(\phi)} & 0 \\ \frac{(r^2-b^2)\cdot f'(\phi)}{2r^2\cdot f(\phi)} & \frac{r-b}{r} & 0 \\ 0 & 0 & 0 \end{pmatrix} \text{ and } T_{\dot{\varepsilon}} = \begin{pmatrix} -\frac{f(\phi)}{r^2} & \frac{f'(\phi)}{2r^2} & 0 \\ \frac{f'(\phi)}{2r^2} & \frac{f(\phi)}{r^2} & 0 \\ 0 & 0 & 0 \end{pmatrix}. \tag{6}$$

The inequalities are satisfied (in the first one must take into account that $\frac{r-b}{r} < 0$):

$$det\begin{pmatrix} 1 & \frac{(r^2-b^2)\cdot f'(\phi)}{2r^2\cdot f(\phi)} \\ \frac{(r^2-b^2)\cdot f'(\phi)}{2r^2\cdot f(\phi)} & \frac{r-b}{r} \end{pmatrix} < 0, \quad det\begin{pmatrix} -\frac{f(\phi)}{r^2} & \frac{f'(\phi)}{2r^2} \\ \frac{f'(\phi)}{2r^2} & \frac{f(\phi)}{r^2} \end{pmatrix} < 0.$$

As a result, the eigenvalues of both tensors T_ε and $T_{\dot{\varepsilon}}$ include one positive, one zero, and one negative value, with the zero-eigenvalue corresponding to the eigenvector $(0 \quad 0 \quad 1)$ for both tensors. Consequently, the first and third principal axes of one tensor are generally rotated by a certain angle in the *XOY* plane relative to the corresponding axes of the other tensor. This angle is denoted as α. It is important to note that the presence of a zero eigenvalue, combined with the incompressibility condition (i.e., the zero trace condition for the tensor $T_{\dot{\varepsilon}}$) implies that $\nu = 0$. Therefore, the second condition of monotonicity is satisfied, and the expression for the measure of monotonicity becomes $d = \frac{1}{\pi} \underset{t}{max}(\alpha(t))$.

To compute the angle α between the first principal vectors of two matrices, it is advantageous for the matrices to be in their simplest form. According to the definitions of eigenvalues and eigenvectors, if X is an eigenvector of matrix A, corresponding to the eigenvalue λ, then for any $\mu \in (-\infty; +\infty)$ the vector X is an eigenvector of matrix $A + \mu E$ (where E is the identity matrix), corresponding to the eigenvalue $\lambda + \mu$.

Furthermore, when substituting matrix A with $A + \mu E$ t the order of the eigenvalues remains unchanged; thus, the largest eigenvalue of matrix A corresponds to the largest eigenvalue of matrix $A + \mu E$. Additionally, scaling a matrix by any positive constant does not affect the order of its eigenvalues or the corresponding eigenvectors. This property allows for the transformation of matrices T_ε and $T_{\dot{\varepsilon}}$ into matrices of a simpler structure. The original matrices T_ε and $T_{\dot{\varepsilon}}$ are represented as follows (see (6)):

$$T = \begin{pmatrix} c_{11} & c_{12} & 0 \\ c_{12} & c_{22} & 0 \\ 0 & 0 & 0 \end{pmatrix}$$

Let us denote the matrix obtained by this transformation from T_ε, by A, and the matrix obtained from $T_{\dot{\varepsilon}}$, by B:

$$A = \begin{pmatrix} 1 & a_{12} & 0 \\ a_{12} & -1 & 0 \\ 0 & 0 & a_{33} \end{pmatrix}, \quad B = \begin{pmatrix} 1 & b_{12} & 0 \\ b_{12} & -1 & 0 \\ 0 & 0 & 0 \end{pmatrix},$$

here

$$a_{12} = -\frac{2(b^2-r^2)}{rb} \cdot \frac{f'(\phi)}{2f(\phi)} \text{ и } b_{12} = -\frac{f'(\phi)}{2f(\phi)} \tag{7}$$

Note that b_{12} is a function only of the angle ϕ, that is, b_{12} does not change on a fixed trajectory. Note also that $a_{12} = \frac{2(b^2-r^2)}{rb} \cdot b_{12}$. The value $k = \frac{2(b^2-r^2)}{rb}$ is a certain coefficient of proportionality that depends only on the radius r, that is, changing along any fixed trajectory. Since $a \le r \le b$, then the coefficient k is positive. Moreover, since

$$k_r' = \left(\frac{2(b^2-r^2)}{rb}\right)' = -\frac{2(b^2+r^2)}{br^2} < 0,$$

then the coefficient k is a monotonically decreasing function of r, that is, when moving along the trajectory towards a decreasing radius, the coefficient k monotonically increases.

Thus, to calculate the approximate monotonicity criteria, it remains to calculate the angle α between the first eigenvectors X_1 and Y_1 matrices A and B. The angle α_1 between X_1 and the OX axis:

$$\alpha_1 = \text{arctg}\frac{a_{12}}{1+\sqrt{1+a_{12}^2}} = \frac{\text{arctg}(a_{12})}{2}.$$

Similarly, the angle α_2 between Y_1 and the OX axis:

$$\alpha_2 = \text{arctg}\frac{b_{12}}{1+\sqrt{1+b_{12}^2}} = \frac{\text{arctg}(b_{12})}{2}.$$

Consequently, $\alpha = |\alpha_1 - \alpha_2|$. Along any fixed trajectory, the angle α_2 remains constant. When $r = b$ (at the entry point to the ZPD), the condition $k = 0$ is fulfilled, resulting in $a_{12} = 0$, which indicates that X_1 aligns with the *OX* axis, making the desired angle $\alpha = \alpha_2$. The diagram illustrating the variation of angle α The diagram illustrating the variation of angle $k = 1$, matrices A and B will be identical, leading to the condition $\alpha = 0$.

By solving the equation $k = 1$, obtain the corresponding value $r_0 = \frac{\sqrt{17}-1}{4}b$). With a further increase in the coefficient k the angle α_1, which has already exceeded the angle α_2, will continue to increase, so it will be $\alpha = \alpha_1 - \alpha_2$. At some point, the equality $\alpha_1 = 2\alpha_2$, will be achieved, at which again $\alpha = \alpha_2$ will appear (by solving the equation $\alpha_1 = 2\alpha_2$, find that for $|b_{12}| < 1$ a solution exists, the corresponding coefficient $k = \frac{2}{1-b_{12}^2}$, and the radius value

$$r_1 = \frac{\sqrt{4b_{12}^4 - 8b_{12}^2 + 5} - 1}{2(1 - b_{12}^2)}b$$

(whereby the inequality $r_1 < r_0$ always holds, and for $|b_{12}| \geq 1$ the equality $\alpha_1 = 2\alpha_2$ is impossible). The value of the internal radius a determines to what value the radius will decrease when moving along the trajectory in the ZPD. There are three options:

1) if $r_0 < a$ (such a in Fig.1 is designated as a_1), then $min\,\alpha = \alpha_2 - \alpha_1(a_1)$, $max\,\alpha = \alpha_2 - \alpha_1(b) = \alpha_2$.

2) if $r_1 < a \leq r_0$ (such a in Fig.1 is designated as a_2), then $min\,\alpha = \alpha_2 - \alpha_1(r_0) = 0$, $max\,\alpha = \alpha_2 - \alpha_1(b) = \alpha_2$.

2) if $a \leq r_1$ (such a in Fig.1 is designated as a_3), then $min\,\alpha = \alpha_2 - \alpha_1(r_0) = 0$, $max\,\alpha = \alpha_1(a_3) - \alpha_2$.

It follows that on each fixed trajectory, if the thickness of the ZPD in the radial direction is not too large, then $d = \frac{1}{\pi}\alpha_2$ is achieved at the entrance to the ZPD, and if the thickness of the ZPD in the radial direction is sufficiently large, then $d = \frac{1}{\pi}(\alpha_1(a) - \alpha_2) > \frac{1}{\pi}\alpha_2$ and is achieved at the exit from the ZPD.

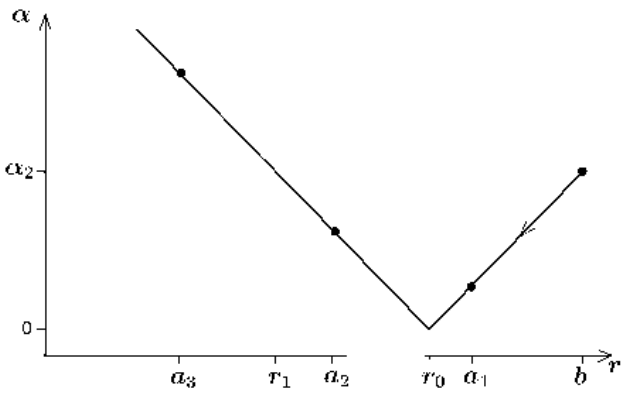

Fig.1. Variation of the angle $\boldsymbol{\alpha}$ while traversing along a trajectory is observed at point $\boldsymbol{r = b}$ — which serves as the entry point into the ZPD. The points $\boldsymbol{a_1}$, $\boldsymbol{a_2}$, $\boldsymbol{a_3}$ represent potential exit points from the ZPD, corresponding to different values of the internal radius of the ZPD under varying degrees of deformation and friction conditions.

In both cases, the angle α_2 (and, therefore, the value of d) depends on the angle ϕ f the entrance to the ZPD and the friction coefficients along the working surfaces of the punch and matrix. Let us establish this dependence explicitly. Substituting explicit expression (2) for the function $f(\phi)$ into formula (7), after transformations obtain (here $C_1 = 0.5\beta\mu_1$, $C = \frac{\beta(0.5\mu_1 - \mu)}{\alpha}$, μ is the friction coefficient on the surface matrix, μ_1 is coefficient of friction on the surface of the punch (the law of constant friction force is applied (Siebel's law, or Prandtl's law), therefore $0 \leq \mu \leq 0.5$ и $0 \leq \mu_1 \leq 0.5$), α is cone angle of the matrix drawing particle):

$b_{12} = \frac{(C_1 - C\phi)\sqrt{3}}{\sqrt{1-3(C_1-C\phi)^2}}$.

If denote $Q = C_1 - C\phi$ (the value of Q reflects the cumulative influence of friction coefficients), and take into account that $0 \le min(\beta\mu_1/2; \beta\mu) \le Q \le max(\beta\mu_1/2; \beta\mu) \le 1/\sqrt{3}$, then the value

$$\alpha_2 = \frac{\text{arctg}(b_{12})}{2} = \frac{1}{2}\text{arctg}\frac{Q\sqrt{3}}{\sqrt{1-3Q^2}}$$

monotonically increases from 0 to $\pi/4$. In order for the inequality $|b_{12}| < 1$ to be satisfied, it is necessary and sufficient to satisfy the inequality $\frac{Q\sqrt{3}}{\sqrt{1-3Q^2}} < 1$, from which obtain $|Q| < 1/\sqrt{6}$ (for such Q there will be $\alpha_2 < \pi/8$). In this case have: $r_1 = \frac{\sqrt{153Q^4-54Q^2+5}-(1-3Q^2)}{2(1-6Q^2)}b$. Graphs of α_2 and r_1/b as functions of Q are shown in Fig.2.

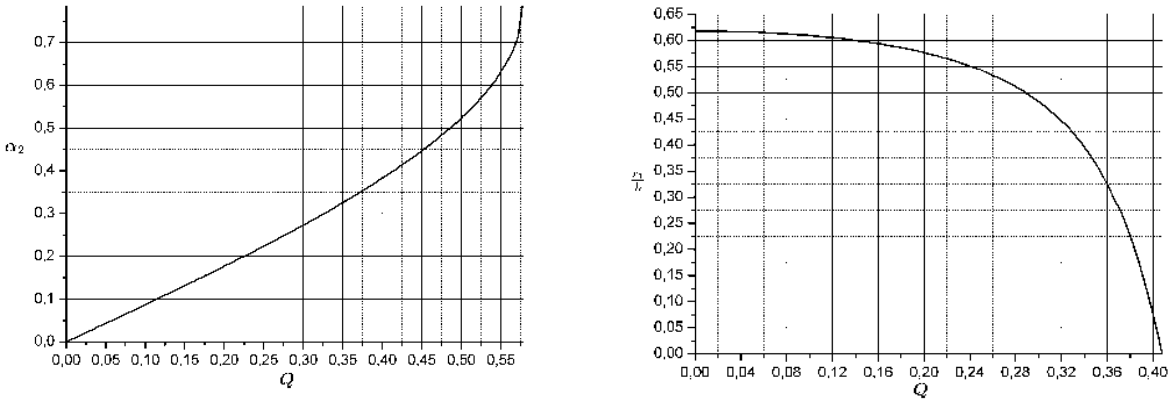

a) b)

Fig.2. a) Dependence of angle α_2 (in radians) on Q; б) Dependence of the value r_1/b on Q

So, will show how to evaluate the monotonicity of the drawing process with wall thinning.

First, let us consider the problem of selecting technological parameters so that the deformation can be considered approximately monotonic. Establish the threshold value for the criterion of approximate monotonicity as $d_n = \frac{1}{18}$ which corresponds to an allowable deviation of the principal axes of the deformation tensor from one another by an angle not exceeding 10°. Assume that if the inequality $d \le d_n$, is satisfied, the process can be considered monotonic; conversely, if $d > d_n$ monotonicity cannot be guaranteed. This threshold value d_n corresponds to $\alpha_{2n} = \pi \cdot d_n = 0.17453$. Based on the relationship between the angle α_2 от Q (see Fig. 2a), calculate the threshold value:

$$Q_n = \frac{1}{\sqrt{3}}sin(2\alpha_{2n}) = \frac{1}{\sqrt{3}}sin\frac{\pi}{9} = 0.19747.$$

Then the limits are achieved by the coefficient of friction:

$$max(\beta\mu_1/2; \beta\mu) \le \frac{1}{\sqrt{3}}sin\frac{\pi}{9} \Leftrightarrow \begin{cases} \mu_1 \le \frac{2}{\beta\sqrt{3}}sin\frac{\pi}{9} \approx 0.34202, \\ \mu \le \frac{1}{\beta\sqrt{3}}sin\frac{\pi}{9} \approx 0.17101. \end{cases} \quad (8)$$

Moreover, since $Q_n < 1/\sqrt{6} \approx 0.40825$ (that is, $|b_{12}| < 1$), then, depending on the extent of deformation, any of the three cases is possible (which correspond to points a_1, a_2, a_3 of the exit from the ZPD). To obtain case 1 from the inequality $r_0 < a$ and formulas for the radii of the OPD [3, p. 279, (15.23)] $b = (R_{нд} - r_в)/sin(\gamma)$ and $a = (R_{нп} - r_в)/sin(\gamma)$ (here $R_{нд}$ is the outer radius before drawing with thinning, $R_{нп}$ is the outer radius after drawing, $r_в$ is inner radius, γ is cone angle of the exhaust part of the matrix) find that $R_{нп}$ should not be too small, that is, the degree of deformation should not be too big:

$$R_{нп} > \frac{\sqrt{17}-1}{4} R_{нд} + \frac{5-\sqrt{17}}{4} r_в \approx 0.78078 R_{нд} + 0.21922 r_в.$$

To obtain case 2, firstly, it is required that $R_{нп}$ be small enough

$$r_в < R_{нп} \leq \frac{\sqrt{17}-1}{4} R_{нд} + \frac{5-\sqrt{17}}{4} r_в \approx \approx 0.78078 R_{нд} + 0.21922 r_в$$

(the degree of deformation must be quite large), and, secondly, the inequality $r_1 < a$, must be satisfied, that is:

$$\frac{\sqrt{153Q^4-54Q^2+5}-(1-3Q^2)}{2(1-6Q^2)} (R_{нд} - r_в) + r_в < R_{нп}.$$

To obtain case 3, firstly, the inequality is required

$$r_в < R_{нп} < \frac{\sqrt{153Q^4-54Q^2+5}-(1-3Q^2)}{2(1-6Q^2)} (R_{нд} - r_в) + r_в,$$

and, secondly, since in case 3 $max\,\alpha = \alpha_1(a_3) - \alpha_2$, s satisfied, then for approximate monotonicity it should be $max\,\alpha = \alpha_1(a_3) - \alpha_2 \leq \frac{\pi}{18} \approx 0.17453$, that is

$$max\,\alpha = \alpha_1(kb_{12}) - \alpha_2 = \frac{1}{2}\text{arctg}(kb_{12}) - \frac{1}{2}\text{arctg}(b_{12}) \leq \frac{\pi}{18}.$$

Thus, if need to get it an approximately monotonic drawing with wall thinning, it is necessary to set the value of the radius R_{np} (the radii R_{nd}, r_v can be regarded as fixed parameters, allowing the selection of R_{np} to uniquely determine the resulting degree of deformation while ensuring that the friction coefficients remain at acceptable (relatively low) levels. Depending on the relative values of the radii R_{nd}, R_{np}, r_v an approximately monotonic drawing will be achieved in one of the scenarios outlined in cases 1-3.

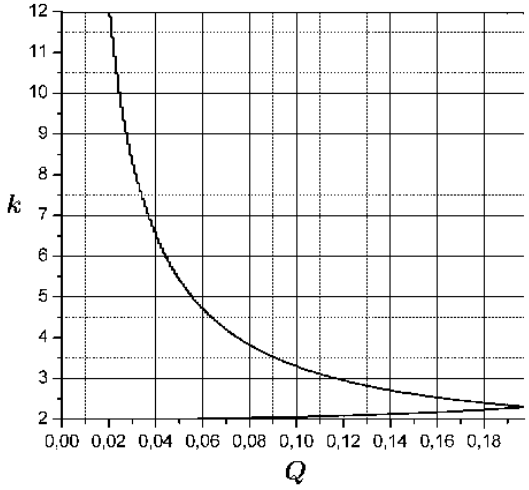

Fig.3. Admissible values of parameters Q and k (located to the left of the curve), at which the third case of approximate monotonicity is realized.

To address the inverse problem of determining whether a specific hood with a thinning wall can be classified as monotonic, it is essential to first evaluate the range of values for Q: $min(\beta\mu_1/2;\ \ \beta\mu) \leq Q \leq max(\beta\mu_1/2;\ \ \beta\mu)$. Next, the angle α_2 should be calculated (or estimated from Fig. 2a). If the resulting angle $\alpha_{2n} = 0.17453$, the drawing cannot be considered monotonic. Conversely, if the inequality $\alpha_2 \leq \alpha_{2n} = 0.17453$ holds true, it is then necessary to compute (or estimate from Fig. 2b) the value of r_1. Now, using the known outer radius of the part before drawing $R_{нд}$, the outer radius after drawing $R_{нп}$, the inner

radius $r_в$ and the taper angle γ it is necessary to calculate the outer b and inner radii a of the ZPD and check the inequality $a \geq r_1$. f this is done, then the hood can be considered monotonous. If the inequality $a < r_1$, is satisfied, then it is necessary to check the fulfillment of the inequality

$$\frac{1}{2}\operatorname{arctg}\left(\frac{2(b^2-a^2)}{ab}\frac{Q\sqrt{3}}{\sqrt{1-3Q^2}}\right) - \frac{1}{2}\operatorname{arctg}\frac{Q\sqrt{3}}{\sqrt{1-3Q^2}} \leq \frac{\pi}{18}. \quad (9)$$

If it is done, then the hood can be considered monotonous; if it is not done, then it cannot be.

3. Results and discussion

Let us consider the application of the above calculations to solve practical problems in the field of designing a working tool for a drawing operation with wall thinning:

Example 1. Let $R_{нд} = 40$ mm, $R_{нп} = 38.5$ mm, $r_в = 30$ mm, $\gamma = 2°$,$\mu = 0.1$, $\mu_1 = 0.1$. Calculate: $0.058 \leq Q \leq 0.115$, $0.05 \leq \alpha_2 \leq 0.101$. Since the inequality $\alpha_2 \leq \alpha_{2п} = 0.17453$ is satisfied, we calculate the range of variation of r_1: $173.7 \leq r_1 \leq 176.3$ and radii: $b = 286.5$mm, $a = 243.6$mm. Since the inequality $a \geq r_1$, holds, the drawing can be considered monotonic.

Example 2. Let $R_{нд} = 40$mm, $R_{нп} = 38.5$mm, $r_в = 30$mm, $\gamma = 2$, $\mu = 0.2$, $\mu_1 = 0.1$. Calculate: $0.058 \leq Q \leq 0.231$, $0.05 \leq \alpha_2 \leq 0.206$. Since some of the α_2 values exceed the threshold value $\alpha_{2п} = 0.17453$, the hood cannot be considered monotonic. This happened because the friction coefficient μ does not satisfy inequality (8). In general, inequalities (8) are the main conditions on which approximate monotonicity depends.

Example 3. Let $R_{нд} = 40$mm, $R_{нп} = 36$mm, $r_в = 30$mm, $\gamma = 2°$,$\mu = 0.1$, $\mu_1 = 0.1$. Calculate: $0.058 \leq Q \leq 0.115$, $0.05 \leq \alpha_2 \leq 0.101$. Since the inequality $\alpha_2 \leq \alpha_{2п} = 0.17453$ is satisfied, calculate the range of changes: r_1: $173.7 \leq r_1 \leq 176.3$ and radii: $b = 286.5$mm, $a = 171.9$mm. Since the inequality $a < r_1$, it is necessary to check the fulfillment of inequality (9) over the entire range of changes in Q. For Q_{min}: $0.056 < \pi/18 \approx 0.175$ - fulfilled, for Q_{max}: $0.105 < \pi/18 \approx 0.175$ - fulfilled. Thus, the hood can be considered monotonous. It is necessary to check inequality (8) even if for part of the range of variation r_1 the inequality $a < r_1$ is satisfied, but for part it is not.

In the examined model, the parameters that define the geometric dimensions of the exhaust section of the matrix are the radii $R_{нд}$, $R_{нп}$ and $r_в$. Consequently, it can be concluded that approximate monotonicity is influenced by the cone angle solely through the radii b and a (similar to how the degree of deformation for the exhaust with wall thinning is calculated in [4]), given that any arbitrary matrix thickness (greater than 115 mm, as illustrated in example 3) is deemed acceptable. However, if the matrix thickness is treated as a fixed parameter, then a drawing with a significant degree of thinning will inherently necessitate a larger taper angle. Let's say, increasing the taper angle for the data from example 3 to $\gamma = 12$ (and keeping the remaining data), obtain $b = 48.1$mm, $a = 28.9$mm, $29.2 \leq r_1 \leq 29.6$ while keeping the ranges for Q and α_2 and the left sides of inequality (9) for Q_{min} and Q_{max} and with still approximately monotonic stretching.

4. Conclusion

In engineering technological practice, monotonic processes are rare. At the same time, a huge number of technological problems are associated with the analysis of processes close to monotonic, due to the limitations imposed on engineering calculation models. In this regard, an assessment of the proximity of a specific technological process being developed to a monotonic or other special cases of complex loading is necessary, since this allows us to assess the validity of using a particular rheological model of the processed material, which underlies this technological problem.

At the current stage of research, the developed technological recommendations allow the process engineer to assess the "level of monotonicity" of the process and, if necessary, make changes to the deformation modes of the semi-finished product. Providing the operation with the condition of a "monotonic" process allows us to minimize errors in the application of a rheological model of material hardening (for example, based on the results of a tensile test) and, thereby, predict the possibility of hardening the material and ensuring tactical and technical requirements, the possibility of loss of stability or destruction.

The result of the implementation of this tool is a stable technological process, where a balance is maintained between the level of material hardening acquired during stamping operations and heat treatment, which leads to a reduction in defects and an increase in the quality of manufactured products.

Conflict of interest statement

The authors declare that they have no conflict of interest in relation to this research, whether financial, personal, authorship or otherwise, that could affect the research and its results presented in this paper.

CRediT author statement

Rasulov Z.- Conceptualization, Methodology; **Olehver A**. - Software; **Voinash S.A. -** Validation; **Vornacheva I and Sokolova V**. - Writing - Review & Editing; **Malikov V.** - Supervision.
The final manuscript was read and approved by all authors.

Acknowledgements

This work was carried out with financial support from the Ministry of Science and Higher Education of the Russian Federation (research and development project "Research and prediction of gradient fields of strength and plastic characteristics of metals in cold forming processes under complex loading" FZWF-2024-0006).

References

1 Vinnik P.M., Ivanov K.M. (2016) Processes of complex loading in technological problems. *News of higher educational institutions. Mechanical engineering.* 6, 675, 62-72. Available at: https://www.researchgate.net/publication/308389554_ Combined_Loading_Processes_in_Technological_Problems

2 Smirnov-Alyaev G.A. (1978) Resistance of materials to plastic deformation. Leningrad, Mashinostroenie Publ., 368 p. Available at: https://studfile.net/preview/19957333/ [in Russian]

3 Haghshenas M., Klassen R.J. (2015) Mechanical characterization of flow formed FCC alloys. *Materials Science and Engineering*, 641, 249 – 55. DOI: 10.1016/j.msea.2015.06.046.

4 Bhatt R.J., Raval H.K. (2017) Investigation of effect of material properties on forces during flow forming process. *Procedia Engineering*, 173, 1587 – 1594. DOI: 10.1016/j.proeng.2016.12.265.

5 Davidson M.J., Balasubramanian K., Tagorea G.R.N. (2008) An experimental study on the quality of flowformed AA6061 tubes. *Journal of Materials Processing Technology*, 203 (1–3), 321 – 325. DOI:10.1016/j.jmatprotec.2007.10.021.

6 Bedekar V., Pauskar P., Shivpuri R. (2017) Microstructure and texture evolutions in AISI 1050 steel by flow forming. *J. HoweProcedia Engineering*, 81, 2355 – 2360. DOI: 10.1016/j. proeng.2014.10.333.

7 Marini D., Corney J. (2008) A methodology for assessing the feasibility of producing components by flow forming. *Journal of Materials Processing Technolog*, 5(1), 210–234. DOI: 10.1080/21693277.2017.1374888.

8 Wang X., Xia Q., Cheng X. (2017) Deformation behavior of Haynes 230 superalloy during backward flow forming. *Int. J. Precis. Eng. Manuf.*, 18(1), 77 – 83. DOI: 10.1007/s12541-017-0009-4.

9 Udalov A.A., Parshin S.V., Udalov A.V. (2018) Theoretical investigation of the effect of the taper angle of the deforming roller on the limiting degrees of deformation in the process of flow forming. *MATEC Web of Conferences*, 224, 01040. DOI: 10.1051/matecconf/201822401040.

10 Udalov A.A., Parshin S.V., Udalov A.V. (2019) Influence of the profile radius of the deforming roller on the limit degree of deformation in the process of flow forming. *Materials Science Forum*, 946, 800 – 806. DOI:10.4028/www.scientific.net/msf.946.800.

11 Okulov R.A., Semenova N.V. (2019) Modeling the Drawing of Square-Cross-Section Pipes/Tubes Made from Various Materials. *Metallurgist*, 65, 571-577. Available at: https://link.springer.com/article/10.1007/s11015-021-01192-z.

12 Hatala M., Botko F., Peterka J., Bella P., Radic P. (2020) Evaluation of strain in cold drawing of tubes with internally shaped surface. *Materials Today: Proceedings*, 22, 287 – 292. Available at: https://www.sciencedirect.com/science/article/abs/pii/S2214785319330962

13 Boutenel F., Delhomme M., Velay V., Boman R. (2018) Finite element modelling of cold drawing for high-precision tubes. *Comptes Rendus – Mecanique*, 346, 665 – 677. Available at: https://www.sciencedirect.com/science/article/pii/S1631072118301220

14 Vorontsov A.L. (2014) Theory and calculations of metal forming processes. Vol. 2. Moscow, BMSTU Publ., 441. Available at the: https://www.labirint.ru/books/541059/ [in Russian]

15 Vinnik P.M., Ivanov K.M., Danilin G.A., Remshev E.Yu., Vinnik T.V. (2015) Prediction of the mechanical properties of a part obtained by drawing with thinning. *Metalloobrabotka*, 88, 31 – 36. Available at: https://polytechnics.ru/arhmo/2015/product-details/365-metalloobrabotka-4-88-2015.html.

AUTHORS' INFORMATION

Rasulov, Zainodin Nurmukhamedovich – Candidate of Technical Sciences, Head of the Youth Laboratory, BSTU "VOENMEKH" named after D.F.Ustinova, Saint Petersburg, Russia; https://orcid.org/0000-0002-6966-7060; rasulov_zn@voenmeh.ru

Olehver, Alexey Ivanovich – Candidate of Technical Sciences, Associate Professor, BSTU "VOENMEKH" named after D.F. Ustinova, BSTU "VOENMEKH" named after D.F. Ustinova, Saint Petersburg, Russia; https://orcid.org/0009-0003-8630-344X; leshicher@mail.ru

Remshev, Evgenii Uri'evich – Candidate of Technical Sciences, Associate Professor, BSTU "VOENMEKH" named after D.F. Ustinova, Saint Petersburg, Russia; https://orcid.org/0000-0002-7630-0398; remshev@mail.ru

Voinash, Sergey Aleksandrovich – Master, Leading Engineer, Research laboratory "Intelligent Mobility", Institute of Design and Spatial Arts, Kazan Federal University, Kazan, Russia; Scopus Author ID: 57194339935; https://orcid.org/0000-0001-5239-9883; sergey_voi@mail.ru

Vornacheva, Irina Valerievna – Candidate of Technical Sciences, Associate Professor, South-West State University, Kursk, Russia; https://orcid.org/0009-0003-5511-235X; vornairina2008@yandex.ru

Sokolova, Viktoriia Alexandrovna – Candidate of Technical Sciences, Associate Professor, Leading Researcher, Research Laboratory "Intelligent Mobility", Institute of Design and Spatial Arts, Kazan Federal University, Kazan, Russia; https://orcid.org/0000-0001-6880-445X; sokolova_vika@inbox.ru

Malikov, Vladimir Nickolaevich – Candidate of Technical Sciences, Associate Professor, Department of General and Experimental Physics, Altai State University, Barnaul, Altai Territory, Russia; https://orcid.org/0000-0003-0351-4843; osys11@gmail.com

EURASIAN PHYSICAL TECHNICAL JOURNAL

2024, Volume 21, No. 4 (50)

https://doi.org/10.31489/2024No4/109-117

Received: 02/07/2024 Revised: 16/10/2024 Accepted: 17/12/2024 Published online: 25/12/2024

Original Research Article

UDC 532.5.032

DETERMINATION OF THE FLOW RATE AND TEMPERATURE OF THE LIQUID WHEN IT IS FORCED THROUGH THE THROTTLE OPENINGS

Nussupbekov B.R.[1,2] *, Oshanov Y.Z.[1], Ovcharov M.S.[1], Kongyrbayeva A.K.[1]

[1] E.A. Buketov Karaganda University, Karaganda, Kazakhstan

[2] A. Saginov Karaganda Technical University, Karaganda, Kazakhstan

*Corresponding authors: bek_nr1963@mail.ru

Abstract. *The article presents laboratory findings from studies conducted on a specially developed setup for analyzing liquid flow through throttle holes. The liquid flow rate depends on various factors, such as hole diameter, upstream pressure, liquid viscosity, and the channel's length and shape. As the liquid passes through the throttle, pressure drops, velocity increases, and kinetic energy rises, subsequently converting to thermal energy due to molecular friction. This throttling process raises the liquid's temperature, making it suitable for heating applications in industrial, laboratory, and heating systems. This throttling process increases the liquid's temperature through molecular friction, making it a practical solution for heating applications across industrial and laboratory systems.*

Keywords: liquid flow rate, throttle openings, hydraulic heating systems, thermal energy conversion

1. Introduction

The conversion of electrical energy to thermal energy is increasingly essential across industries that rely on efficient heating solutions to maintain specific temperature levels. One effective approach to achieve this involves forcing liquids through throttle openings, where a controlled pressure drops and increase in liquid velocity generate kinetic energy that is subsequently transformed into thermal energy via molecular friction. This process provides advantages over traditional heating methods by minimizing heat loss over long distances, making it suitable for applications in hydraulic systems operating in cold climates and heating systems in isolated environments [1-3].

Recent advancements in thermal energy conversion have emphasized the design of throttle-based systems, including vortex and cavitation heat generators, which enhance energy efficiency by leveraging fluid dynamics. For example, vortex energy converters with integrated boundary layers show potential for improving heat transfer in turbulent pipe flows, significantly impacting thermal boundary layer thickness and energy transfer efficiency [6, 7]. Similarly, cavitation-based systems utilize swirling flow effects to achieve effective fluid heating, particularly in hydraulic systems where stable operational temperatures are crucial [8].

Despite these advancements, conventional throttling methods remain a simple yet effective solution for fluid heating in hydraulic systems, especially in northern regions with demanding environmental conditions [9, 10]. Given the importance of these applications, further investigation is warranted to optimize liquid heating in throttle systems under specific operational conditions. This study examines the factors influencing flow rate and temperature in liquids forced through throttle openings, contributing to the development of energy-efficient, high-performance heating solutions in hydraulic systems.

In this process, electrical energy is converted by transmitting the rotor's rotational motion, imparting centrifugal acceleration to each liquid particle from the rotation axis outward. This acceleration generates pressure and facilitates the displacement of liquid through throttle openings on the side walls. A sharp pressure drop results, releasing accumulated compression energy as heat. Notably, in a uniformly rotating rotor, a balance is maintained between the inflow and ejection of liquid through the chokes, allowing low-power motors to efficiently convert electrical energy to thermal energy.

2. Literature review and problem statement

In [6], a solution for investigating the heat transfer characteristics of a pipe with turbulent decaying swirl flow using an integrated boundary layer circuit is considered. The influence of the inlet Reynolds number, inlet swirl intensity and Prandtl number on the thermal boundary layer thickness and Nusselt number is also studied. The work [7] shows patented devices that allow using the vortex and cavitation effect to provide space heating. The hydrodynamic heater includes a pump with an electric motor, an input pipeline, a vortex energy converter, a device for forming a vortex installed at some distance from the vortex former, a confuser at the outlet of the vortex tube. Nevertheless, the process deserves a good assessment, but it is impossible to determine whether vortices appear.

In [8], the authors propose a cavitation-vortex heat generator featuring a vortex chamber with two angled injection pipes (45-90°) at varying heights. A braking device is positioned at the base of the housing opposite the vortex chamber, which also includes an additional bypass braking device. Cylindrical bushings with helical interiors are installed at the pipe entrances to induce flow swirling. The housing connects to the vortex chamber via a curved pipe. However, this concept remains largely theoretical and has not been fully implemented.

In [9], it is shown that pumping liquid through throttle holes can increase the liquid's temperature, providing necessary heat. These throttles are typically installed along pressure lines, as they are simple and effective for heating working fluids to operational temperatures in hydraulic systems, particularly in northern climates. However, they are rarely used specifically for liquid heating in practice.

As is known, on supersonic jet aircraft, due to aerodynamic heating of the skin, the environment surrounding the hydraulic system has a temperature significantly exceeding the permissible temperature for the liquids used. In this regard, the problem of forced heat removal arises, i.e. it is necessary to artificially cool the hydraulic system [10]. Therefore, individual questions and tasks arise that must be solved and a cooling mode must be selected. However, especially for airbuses, whose hydraulic systems have high capacities, convective heat exchange with the environment is insufficient and does not ensure the maintenance of the required liquid temperature. In this regard, it is necessary to select a specific cooling mode.

The proposed study introduces a unique approach to analyzing fluid flow and thermal energy conversion in throttle-based heating systems. Unlike conventional methods, this research emphasizes the optimization of throttle geometry and operational parameters to enhance energy efficiency under controlled experimental conditions. The developed experimental setup allows precise differentiation between theoretical calculations and real-world observations, providing valuable insights for industrial and laboratory applications. Furthermore, this study integrates findings from vortex and cavitation-based systems, highlighting improvements in performance and applicability, particularly for heating systems in extreme climates.

The theauthorsproposed a throttle-type heat generator designed for heat and hot water supply of industrial and domestic facilities, as well as for heating process liquids [11]. In this case, the throttle is made as a narrowing device in the form of a conoid nozzle, i.e. having the shape of a jet coming out of the hole, and at the outlet of which in the pipeline of the route at a given distance a braking device is installed.

Therefore, to more accurately determine the flow rate and temperature of the liquid as it is forced through the throttle openings, it is necessary to take into account factors associated with specific operating conditions and the design of the system.

3. Experimental stand for determining the flow rate through throttle holes

For an ideal fluid without friction, the fluid flow rate through an orifice can be calculated using the Torricelli-Chasele equation. However, in practice, due to friction and other losses, the fluid flow rate may be less than that calculated using the Torricelli-Chasele equation. Therefore, to more accurately calculate the

fluid flow rate through an orifice, it is necessary to take into account factors related to the specific operating conditions and system design.

The heat generator unit we use does not allow us to set the flow rate of liquid through the throttle holes, so an experimental stand was developed and manufactured. Some results obtained using this setup are published in papers [12-13], which consider issues related to the design of a throttle-type hydrodynamic heater. The maximum angular velocities for cylindrical and conical shapes are determined from the condition of no liquid splashing out of the rotating vessel. Theoretical studies have shown that the conical skirt shape is more optimal, since with an increase in the liquid level in the vessel within 0.02–0.09 m, the angular velocity decreases from 37.566 rad/s to 17.709 rad/s, respectively. In addition, with a vessel wall taper of 5° and a liquid level height of 0.02 m, the liquid volume is 11.0 10-5 m^3. If the liquid level is increased to 0.09 m, the liquid volume will increase to 55.0 10-5 m^3.

Experimental studies have shown air locking during the formation of a liquid ring in the rotor cavity. In addition, it was found that the smaller the inner radius of the liquid ring, the higher the temperature of the liquid supplied through the throttle holes. However, creating pressure in front of the throttle holes using the inertial forces of the rotating mass of liquid is a promising direction. [14] shows radial-cylindrical spraying devices using water-coal fuels for combustion. The authors of the works developed nozzles with cylindrical radial flow rotation and aerodynamic (tangential) flow rotation for fuel injection. As practice shows, the use of these forms and technology instead of the corresponding nozzles with diameters up to 3 mm will allow increasing the liquid temperature.

The design of the stand is made in such a way that it allows changing the height of the liquid column (Fig.1), as well as creating pressure in the system using the central water supply. In addition, it is possible to determine the flow rate through the throttle holes by changing the direction of the jet (Fig. 2). The stand includes a drain tank 1 with guides along which crossbars 2 and 3 move in the vertical direction. An electric motor 4 with a hollow rotor 5 is installed on crossbar 2, which has tubes 6 with throttle nozzles 7, as well as a nipple 8 for connection to the supply line 9. Tubes 6 have an external thread for adjusting the radial position of the throttle nozzles 7 relative to the axis of rotation of the rotor 5. A pressure gauge 10, a flow meter 11, an accumulator 12 and a valve 13 are installed on the supply line 9. Water from the drain tank 1 is discharged into the sewer through a pipeline 15. Regulation of the angular velocity of the rotor ω is ensured by a «ВЕСПЕР» frequency converter 14.

Fig.1. General view of the experimental setup for determining the flow rate through throttle holes.

The stand allows for conducting research by forcing liquid through throttle holes with a diameter of 1.5, 2, 3 mm, located at a distance of 0.235 m from the center of rotation of the rotor, with a static height of the liquid column equal to 1.0 m (9796.462 Pa). Opening valve 13 ensures the start of water flow through supply line 9 to the throttle openings, as soon as the liquid column in accumulator 12 reaches a specified level, readings are taken from flow meter 11. Liquid flow readings (Q_n) are recorded for rotor angular velocities changing in the range of 0...314 rad/s. When the electric motor (4) is activated, the liquid mass within the rotor begins to rotate. This rotation generates inertial forces that push the liquid radially outward, creating pressure in front of the throttle openings.

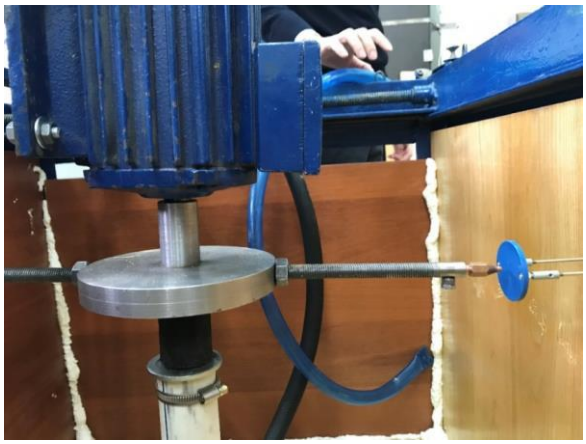

Fig.2. Front view of the experimental setup.

To determine the optimal operating conditions of the heating unit, nozzles with varying diameters were used as throttle openings, facilitating a controlled jet formation and offering a high liquid flow coefficient, which is beneficial for use in heat-generating systems [12, p.46].

4. Results and discussion

In this thermal setup, cylindrical nozzles extend outward from the vessel. When the nozzle length is at least three times the diameter of the hole, the liquid flow rate increases by approximately 30% compared to flow through a thin-wall opening. For simplified calculations with low-viscosity liquids exiting a round hole, a jet compression coefficient is applied, approximated at [15] $\varepsilon = 0.64$.

For the adopted openings, the flow coefficient μ is established after conducting experimental studies using the expression

$$\mu = \frac{Q}{Q_m}, \tag{1}$$

where Q represents the actual flow rate through the opening, and Q_m is the theoretical flow rate.

The theoretical flow rate of the throttle holes is calculated by the expression

$$Q_m = S\sqrt{\frac{2Pg}{\gamma}}, \tag{2}$$

where S is the area of the throttle opening, P represents the pressure differential across the throttle, γ is the specific weight of the fluid.

According to expression (2), we determine the theoretical flow rate of liquid (Q_{m3}) at different positions of the liquid ring using the calculated pressures, results are shown in Table 1.

According to the data in Table 1, the larger the throttle hole diameter, the higher the theoretical fluid flow rate. However, the throttle hole diameter cannot be increased indefinitely, as this will complicate the creation of pressure at the throttle holes. Since the stand (Fig. 2) provides preliminary static pressure of the liquid inside the rotor, expression (2) takes the following form:

$$Q_{\Sigma m} = S\sqrt{\frac{2(P+P_n)g}{\gamma}}, \tag{3}$$

where $Q_{\Sigma m}$ is the total theoretical flow rate of the liquid, S is the area of the throttle opening, P is the current pressure, P_n is the preliminary static pressure of the liquid in the supply line, γ is the specific weight of the fluid.

Table 1. Theoretical flow results for 3mm orifice diameter.

ω, (rad/s)	Q_{m3} (m^3/s)			
	r_1 = 0.4 (m)	r_2 = 0.3 (m)	r_3 = 0.2 (m)	r_4 =0.0 (m)
0	0.00	0.00	0.00	0.00
42	0.00027871	0.000372	0.000426	0.000465
76	0.00050433	0.000672	0.00077	0.000841
136	0.00090249	0.001203	0.001379	0.001504
215	0.00142673	0.001902	0.002179	0.002378
314	0.0020837	0.002778	0.003183	0.003473

Using expression (3), we determine the total theoretical flow rate Q_{m1} for throttle hole diameters of 3 mm, taking into account the preliminary static pressure of the liquid in the system, results are shown in Table 2. The results presented in Tables 1 and 2 distinguish between theoretical and experimental data. Theoretical values were derived using the Torricelli-Chasele equation (Equation 2), which calculates the ideal fluid flow rate based on pressure differentials and throttle geometry. Experimental values, on the other hand, were obtained from direct measurements using the developed experimental setup (Figures 1 and 2). This setup allowed for precise control of variables such as throttle diameter and liquid column height, ensuring reliable data collection under consistent conditions. As is known, the preliminary static pressure in the supply line has a significant effect on the flow rate only at low rotor speeds (up to ω = 76 rad/s), and with an increase in the angular velocity, its effect decreases and the coefficient k tends to 1. This is due to the fact that with an increase in the angular velocity of the rotor, the liquid pressure at the throttle holes is several times higher than the static pressure in the supply line.

Table 2. Total theoretical flow results for 3mm orifice diameter.

ω (rad/s)	Q_{m1}, m^3/s			
	r_1 = 0.4 (m)	r_2 = 0.3 (m)	r_3 = 0.2 (m)	r_4 =0.0 (m)
0	0.00	0.00	0.00	0.00
42	0.000295438	0.000384318	0.000436869	0.000474743
76	0.000513767	0.000679547	0.000776593	0.000846248
136	0.000907799	0.001207306	0.001382057	0.001507343
215	0.001430094	0.001904833	0.002181573	0.002379909
314	0.002085999	0.002779988	0.003184405	0.003474208

It should also be noted that the value of the coefficient of distribution of liquid flow from static pressure k depends on the angular velocity of the rotor and the inner radius of the liquid ring in the drum, but does not depend on the diameter of the throttle opening. The reliability of the experimental results was ensured through the use of calibrated instruments, such as the flow meter and pressure gauge, which were regularly checked for accuracy. Additionally, the experimental setup was carefully designed to minimize errors caused by external factors, such as temperature fluctuations or inconsistencies in liquid viscosity. All measurements were repeated multiple times to confirm the consistency of the results. While some experimental errors could arise from slight variations in rotor speed and liquid pressure, these were minimized by maintaining strict control over the experimental conditions. The observed discrepancies between theoretical and experimental results are likely due to inherent system limitations, including friction losses and variations in liquid properties. To assess the effectiveness of the proposed throttle-based heating system, a comparative analysis was conducted between the results obtained from our experimental setup and existing systems used for thermal energy conversion. The key parameters, such as system efficiency (COP), power output, and

temperature increase, were compared. Table 3 summarizes these comparisons, highlighting the improvements observed with our system.

The results indicate that at similar operational conditions, the proposed system achieves a significantly higher thermal efficiency and a more substantial temperature increase, which makes it particularly suitable for industrial applications in cold climates. For instance, at rotor speeds of 200 rad/s, our system demonstrated a 20% improvement in temperature rise compared to traditional vortex-based heating systems [6].

The current results suggest that, as expected, increasing the throttle hole diameter improves the flow rate. However, the temperature rise in the liquid, while directly proportional to the flow rate, shows diminishing returns as the speed of the rotor increases. This suggests a non-linear relationship between energy input and temperature output in this experimental setup.

Compared to previous studies, such as [6] and [7], our results indicate a more efficient heat conversion at lower rotor speeds, potentially offering significant advantages for applications in colder environments, where minimizing energy loss is crucial.The large growth coefficient of flow through the nozzles is due to the fact that the cross-section of the jet at its outlet is approximately equal to the diameter of the hole. In addition, the viscosity of the liquid is a factor reducing the coefficient φ relative to the outflow through the holes. If we consider the movement of liquid inside a rotating rotor, then in addition to centrifugal forces and acceleration of gravity, Coriolis forces act on it [16].

It is evident from Fig. 3 that when the rotor rotates, forces act on the flowing liquid that change its direction and cause a bend in the trajectory.

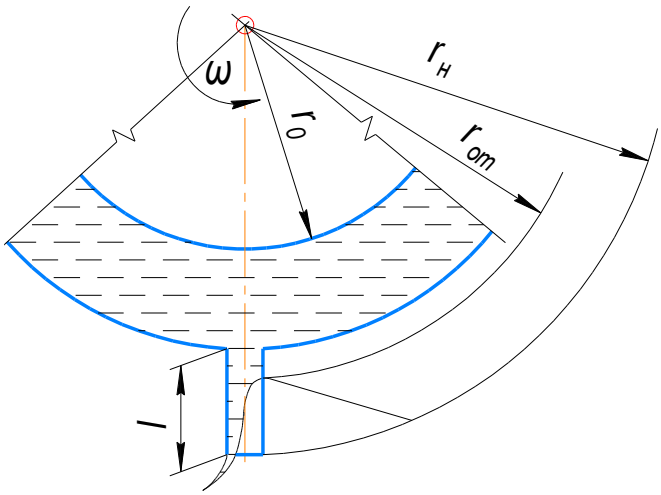

Fig.3. Jet separation under the action of Coriolis inertial forces.

This is due to the fact that each particle of liquid is affected by inertial forces that depend on its speed and the angular velocity of rotation of the vessel. However, in most practical situations, the effect of Coriolis forces on the flow of liquid through the orifices of a rotating vessel is insignificant and can be ignored. This is because the effect of Coriolis forces on the flow of liquid depends on many factors, such as the rotation speed of the vessel, the diameter of the orifices, and other parameters that are not critical for the flow of liquid in most cases.

The flow rate of liquid through throttle orifices with diameters of 1.5, 2.0, and 3.0 mm as a function of the rotor's angular velocity was experimentally determined at an initial static pressure of 0.01 MPa in the supply pipeline (Fig. 4). The analysis of Fig. 4 demonstrates two distinct behaviors of liquid flow rate depending on the rotor's angular velocity. At angular velocities between 0 and 21 rad/s, the flow rate increases gradually, indicating minimal influence of inertial forces. This trend suggests that the static pressure primarily drives the liquid through the throttle orifices in this range.

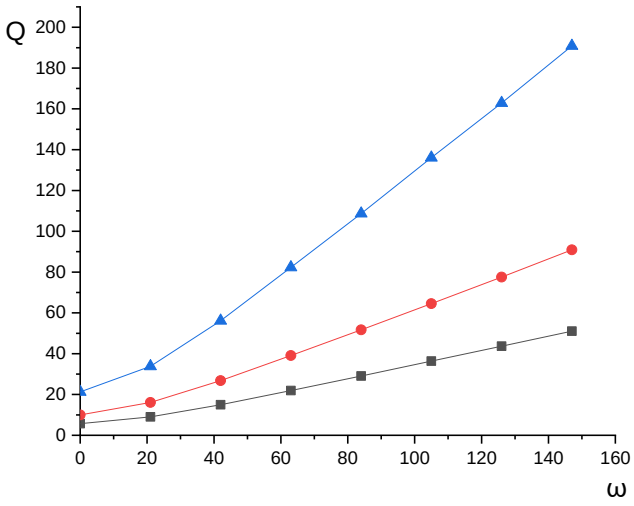

■ - 1.5 mm; ● - 2.0 mm; ▲ - 3.0 mm

Fig.4. Graph of the total liquid flow rate as a function of the rotor's angular velocity.

Beyond 21 rad/s, a significant rise in flow rate is observed. This can be attributed to the substantial increase in liquid pressure near the throttle orifices due to the combined effects of centrifugal forces and dynamic pressure. This relationship highlights the nonlinear dependence of flow rate on angular velocity at higher speeds, emphasizing the dominant role of inertial forces in this regime.

Fig. 5 shows graphs of the dependence of the liquid temperature T on the operating time of the thermal unit t, with the total areas of the throttle holes δ = 64.34*10 $^{-6}$ m ^{2,} respectively.

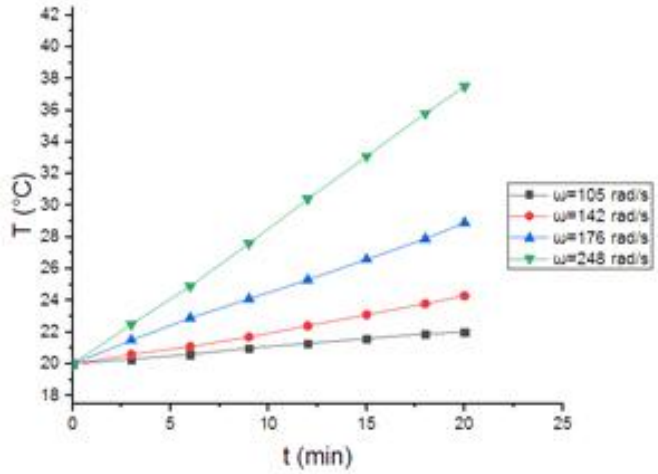

Fig.5. Change in liquid temperature depending on time with the total area of the heat generator throttling holes δ = 64.34*10^{-6} m ^{2} [13, p. 27].

Increasing the area of the throttle holes by two times (Fig. 3.2) gave a minute-by-minute average temperature increase for the first curve of 0.11ºC, for the second 0.18ºC, for the third 0.45ºC, for the fourth 0.72ºC. Comparison of the results of the curves showed that only when the rotor rotates at an angular velocity of 105 rad/s, the minute-by-minute temperature increase with a two-fold increase in the total area of the throttle holes was 1.66 times, and in other cases the indicators were lower, although some small increase was observed.

If a liquid passes through a throttle, its kinetic energy increases and its potential energy decreases. Some heat transfer from the surrounding medium to the liquid may also occur. If the radius of the throttle opening is doubled, the fluid flow velocity will decrease by half (according to the Couette-Poiseuille equation). Consequently, the kinetic energy of the flow will decrease by four times (since it is proportional to the square

of the velocity). At the same time, if we assume that the potential energy in the rotor does not change, then the internal energy of the fluid should increase in accordance with the law of conservation of energy.

This increase in the temperature of the liquid can be described by the heat balance equation, where the change in the internal energy of the liquid will be equal to the work done by the liquid when passing through the orifice and the heat flow passing through the walls of the orifice and absorbed by the liquid. Thus, an increase in the radius of the orifice can lead to an increase in the temperature of the liquid.

5. Conclusion

The study demonstrated that as the angular velocity of the rotor increases, the proportion of liquid flow driven by preliminary static pressure decreases. Specifically, when the rotor speed was 0 rad/s, the proportion of flow due to static pressure was 100%, whereas at a rotor speed of 147 rad/s, this proportion decreased to just 0.8% of the total flow. These findings emphasize the diminishing impact of static pressure at higher rotor speeds, suggesting that inertial forces become more dominant in fluid movement.

Additionally, the research confirmed that the coefficient for distributing liquid flow from static pressure depends on the rotor's angular velocity and the cross-sectional area of the liquid ring in the drum, but it remains independent of the diameter of the throttle opening. This result provides insights into the factors influencing flow behavior in throttling systems.

Furthermore, it was established that the temperature increase of the liquid during throttling is not solely dependent on the cross-sectional area of the annular liquid layer in the heat-generating unit. The flow rate plays a significant role, as it directly influences the turnover of the liquid and the efficiency of thermal energy conversion. These findings highlight the importance of optimizing both flow rate and throttle geometry to enhance the system's thermal performance.

The practical implications of this research suggest that the developed throttle-based heating system could be particularly beneficial for industrial and hydraulic applications, especially in cold environments where energy efficiency is critical. Future research could explore the optimization of throttle hole design and the scalability of this technology for larger systems, as well as the potential use of alternative fluids and advanced materials for throttling to further improve system efficiency.

Conflict of interest statement

The authors declare that they have no conflict of interest in relation to this research, whether financial, personal, authorship or otherwise, that could affect the research and its results presented in this paper.

CRediT author statement

Nussupbekov B.R.: Conceptualization, Methodology, Supervision; **Oshanov Y.Z.:** Investigation, Writing – Original Draft Preparation; **Ovcharov M.S**.: Data Curation, Formal Analysis; **Kongyrbayeva A.K.:** Writing – Review & Editing, Visualization. The final manuscript was read and approved by all authors.

Funding

This research is funded by the Science Committee of the Ministry of Science and Higher Education of the Republic of Kazakhstan (Grant no. AP19678501).

References

1 Concept of Transition to a "Green Economy" in the Republic of Kazakhstan. Available at: http://strategy2050.kz [in Russian].

2 Trukhniy A.D., Povarov O.A., Izyumov M.A. (2011) Basics of Modern Energy. Volume 1. Modern Heat Energy: A Textbook for Higher Educational Institutions. Moscow: Publishing House of the Moscow Power Engineering Institute, 472 p. Available at: http://nt-mpei.ru/biblio/osnovy-sovremennoy-energetiki-1/ [in Russian].

3 Tergemes K.T., Duisembaev M.S. (2014) Vortex heat generator with an adjustable energy conversion coefficient for heating farm-houses. Research, results. Available at: https://articlekz.com/article/126542.

4 Guo G., Lu K., Xu S., Yuan J., Bai T., Yang K., He Z. (2023) Effects of in-nozzle liquid fuel vortex cavitation on characteristics of flow and spray: Numerical research. *International Communications in Heat and Mass Transfer*, 148, 107040. DOI: 10.1016/j.icheatmasstransfer.2023.107040.

5 Usychenko V.G. (2012) The Ranque effect as a self-organization phenomenon. *Technical Physics*, 57(3), 379–385. DOI: 10.1134/s1063784212030164.

6 Aghakashi V., Saidi M.H. (2018) Turbulent Decaying Swirling Flow in a Pipe. *Heat Transfer Research*, 49(16), 1559–1585. DOI: 10.1615/HeatTransRes.2018021519.

7 Patent RU №2415350. Cavitation-Vortex Heat Generator / Kovrizhkin M.G. IPC: F24J 3/00, published on March 27, 2011. Available at: https://patents.s3.yandex.net/RU2415350C1_20110327.pdf [in Russian].

8 Mujtaba M., Cuntang W., Yasin F.M., Fangwei X. (2018) Throttle Valve as a Heating Element in Wind Hydraulic Thermal System. *Journal of Advance Research in Mechanical and Civil Engineering*, 5(2), 01-08. DOI:10.53555/nnmce.v5i2.304.

9 Mohammad A.A., Good I.A., Titov M.A., Kulikova N.P. (2015) Calculation of a Throttle Device for Heating a Hydraulic Fluid with Automatic Control Depending on Temperature. *Vestnik KrasGAU*, 12, 38–44. Available at: https://cyberleninka.ru/article/n/raschyot-drosselnogo-ustroystva-razogreva-rabochey-zhidkosti-gidrop [in Russian].

10 Shumilov I.S. (2016) Fluid Temperature of Aero Hydraulic Systems. *Machines and Plants: Design and Exploiting*, MSTU N.E. Bauman, 16, 2. DOI: 10.7463/aplts.0216.0837432.

11 Marinin M.G., Mosalev S.M., Naumov V.I., Sysa V.P., (2009) Throttle Type Heat Generator, RF Patent RU2357161C1, filed November 6, 2007, issued May 27. DOI: 10.1615/HeatTransRes.2022038753.

12 Nussupbekov B., Oshanov Y., Ovcharov M., Duisenbayeva M., Sharzadin A., Kongyrbayeva A., Amanzholova M. (2024) The influence of the rotor shape on the efficiency of the hydrodynamic heater. *Eastern-European Journal of Enterprise Technologies*, 4, 8(130), 42–49. DOI: 10.15587/1729-4061.2024.310140.

13 Nussupbekov B., Oshanov Y., Ovcharov M., Kutum B., Duisenbayeva M., Kongyrbayeva A. (2023) Identifying regularities of fluid throttling of an inertial hydrodynamic installation. *Eastern-European Journal of Enterprise Technologies*, 6(7), 26–32. DOI: 10.15587/1729-4061.2023.292522.

14 Nussupbekov B., Khassenov A., Nussupbekov U., Akhmadiyev B., Karabekova D., Kutum B., Tanasheva N. (2022) Development of technology for obtaining coal-water fuel. *Eastern-European Journal of Enterprise Technologies*, 3(8), 39–46. DOI: 10.15587/1729-4061.2022.259734.

15 Bashta T.M. (1971) Mechanical Engineering Hydraulics. Mechanical Engineering, 672 p. Available at: https://lib-bkm.ru/10007 [in Russian].

16 Grishin N.S., Ponikarov I.I., Ponikarov S.I., Grishin D.N. (2012) Extraction in a Field of Variable Forces. Hydrodynamics, Mass Transfer, Apparatus (Theory, Designs and Calculations). Part 1., 468. Available at: https://e.lanbook.com/book/73493 [in Russian].

AUTHORS' INFORMATION

Nussupbekov, Bekbolat – Candidate of Technical Sciences, Professor, E.A. Buketov Karaganda University; Vice-rector, A. Saginov Karaganda Technical University, Karaganda, Kazakhstan; Scopus Author ID: 56289675900; https://orcid.org/0000-0003-2907-3900; bek_nr1963@mail.ru

Oshanov, Yerlan – Senior Lecturer, E.A. Buketov Karaganda University, Karaganda, Kazakhstan; Scopus Author ID: 57217303890; https://orcid.org/0000-0003-4419-2625; oshanovez@mail.ru

Ovcharov, Michael – Candidate of Technical Sciences, Associate Professor, E.A. Buketov Karaganda University, Karaganda, Kazakhstan; Scopus Author ID: 57217311794; https://orcid.org/0000-0001-7436-813; mihail.ovcharov.40@mail.ru

Kongyrbayeva, Aitkul – PhD student, Department of Engineering Thermophysics named after prof. Zh.S. Akylbaev, E.A. Buketov Karaganda University, Karaganda, Kazakhstan; Scopus Author ID: 58866370500; https://orcid.org/0009-0008-4241-0346; konyrbaevaak@gmail.com

EURASIAN PHYSICAL TECHNICAL JOURNAL

2024, Volume 21, No.4 (50)

https://doi.org/10.31489/2024No4/118-130

Received: 12/04/2024 Revised: 09/09/2024 Accepted: 11/12/2024 Published online: 25/12/2024

Original Research Article

UDC: 539.192; 539.194

ANALYTICAL SOLUTION OF THE CLASS OF INVERSELY QUADRATIC YUKAWA POTENTIAL WITH APPLICATION TO QUANTUM MECHANICAL SYSTEMS

Inyang E.P.[1], Nwachukwu I. M.[1], Ekechukwu C.C.[2], Ekong I.B.[2], William E.S.[3], Lawal K.M.[1], Simon J.[1], Momoh K.O.[1], Oyelami O.A.[4]

[1] National Open University of Nigeria, Jabi-Abuja, Nigeria
[2] University of Calabar, Calabar, Nigeria
[3] Federal University of Technology, Ikot Abasi, Nigeria
[4] Open University of Nigeria, Lagos, Nigeria
*Corresponding author: einyang@noun.edu.ng

Abstract. *In our study, we applied the Exact Quantization Rule approach to tackle the radial Schrödinger equation analytically, specifically addressing the class of inversely quadratic Yukawa potential. Through this method, we successfully predicted the mass spectra of heavy mesons, including charmonium and bottomonium, across a range of quantum states by leveraging the energy eigenvalues. When compared to experimental data and other researchers' findings, our model exhibited a remarkable degree of accuracy, with a maximum error of* $0.0065\ GeV$*. We reduced our potential model to the Kratzer potential in order to further expedite our computations, and we ensured mathematical accuracy by imposing particular boundary conditions. By utilizing the acquired energy spectrum, we broadened our examination to investigate the energy spectra of homonuclear diatomic molecules, like nitrogen* (N_2) *and hydrogen* (H_2)*. One remarkable finding was that the energy spectrum reduced as the angular momentum quantum number increased in the case where the principal quantum number stayed fixed. In a similar vein, the energy spectrum consistently decreases when the angular momentum quantum number is varied. The complex interaction between the kinetic and potential energies of the electron causes this decreasing trend in the energy spectrum as the angular momentum quantum number increases in a diatomic molecule. The energy spectrum is systematically reduced as the electron's orbit lengthens and its distance from the nucleus increases, shifting the balance between these energies.*

Keywords: Schrödinger equation; Exact Quantization Rule; Homonuclear diatomic molecules; Heavy mesons; Class of Inversely Quadratic Yukawa potential

1. Introduction

Diatomic molecules are important components of the fascinating field of molecular physics. They consist of two atoms bonded together. These molecules are important because they are simple and useful for understanding molecular behavior and chemical bonding in a variety of fields such as chemistry, physics, and materials science. They are divided into two categories: homonuclear diatomic molecules, which are made up of two atoms of the same element such as oxygen (O_2), nitrogen (N_2), hydrogen (H_2), and chlorine (Cl_2), and heteronuclear diatomic molecules, which are created when two distinct elements combine. Nitric oxide (NO), hydrogen chloride (HCl), and carbon monoxide (CO) are a few examples. The electronic, vibrational, and

rotational spectra of diatomic molecules reveal important details about their composition, states of energy, and chemical properties. These molecules have recently been studied by authors [1-3]. The solution of the radial Schrödinger equation (SE) is crucial in modern physics [4], but it requires knowledge of the particular confining potential (CP) that governs a system. Quark confinements and Coulombic interactions are captured for quarkonium systems by the Cornell potential, which combines Coulomb and linear potentials [5]. The Schrödinger and semi-relativistic wave equations are usually used to solve this potential [6,7]. While the constituent quark model describes heavy mesons (HM) like charmonium and bottomonium as non-relativistic bound states of a quark-antiquark pair [8], the full description in particle physics relies on Quantum Chromodynamics (QCD) to account for the strong interaction mediating their dynamics [9]. In essence, the non-relativistic approach offers a simplified picture, whereas QCD provides a more rigorous framework. Numerous researchers have explored the Cornell potential and its variations using diverse analytical techniques [10,11]. Such as, the asymptotic iteration method (AIM) [12], Laplace transformation method [13], and others [14–17] have been proposed to solve the Schrödinger equation for such potentials. Recently, exponential-type potentials have garnered attention for studying heavy meson mass spectra [18-20]. For instance, Inyang et al. [21] investigated heavy meson mass spectra using the Yukawa potential, while Ibekwe et al. [22] examined the effect of an improved screened Kratzer potential with the mass spectra. Akpan et al. [23] presented mass spectra using a combination of the Hulthen and Hellmann potential models, and Inyang et al. [24] studied heavy meson mass spectra with the Varshni potential. Motivated by these studies, we utilize the class of inversely quadratic Yukawa potential (CIQYP) to predict heavy meson mass spectra like charmonium and bottomonium, along with the energy spectra of homonuclear diatomic molecules (HDM) such as hydrogen (H_2) and nitrogen (N_2), employing the exact quantization rule (EQR) to solve the Schrödinger equation. Furthermore, the meson is assumed to be a spinless particle for ease [26, 27]. The theory describes diatomic molecules and heavy mesons by modeling their interactions with the class of inversely quadratic Yukawa potential. It captures vibrational-rotational spectra in molecules and energy spectra in mesons, accounting for quantum effects like tunneling and binding energies. This approach bridges atomic-scale molecular behavior and quarkonium systems' fundamental particle interactions.

The class of inversely quadratic Yukawa potential is given as:

$$V(r_q) = -\frac{A_a}{r_q} - \frac{A_b}{r_q^{\,2}} + \frac{A_c e^{-\alpha r_q}}{r_q^{\,2}} \tag{1}$$

where α is the screening parameter, A_a, A_b, *and* A_c are potential strength parameters that will be determined subsequently. The potential is more appropriate compared to other potentials inspired by QCD, for example, the Cornell Potential, because it has more fitting parameters. The class of inversely quadratic Yukawa potential could find great applications in atomic physics, nuclear physics, and molecular physics. Modeling the potential to interact in the quarkonium system, Taylor series expansion is carried out in the exponential term, resulting in Eq. (2).

$$V(r_q) = \frac{\beta_{00}}{r_q^{\,2}} - \frac{\beta_{11}}{r_q} + \beta_{22} r_q^{\,2} + \beta_{33} r_q + \beta_{44}\,, \tag{2}$$

where

$$\beta_{00} = A_c - A_b, \beta_{11} = A_a - A_c\alpha, \beta_{22} = \frac{\alpha^4 A_c}{24}, \beta_{33} = -\frac{\alpha^3 A_c}{6}, \beta_{44} = \frac{A_c\alpha^2}{2} \tag{3}$$

2. Exact Quantization Rule formalism

This section provides a concise overview of the exact quantization rule. For a comprehensive understanding of the exact quantization rule and its implications, readers are directed to the extensive discussions available in references [28, 29].

The Schrödinger equation in one dimension is written as:

$$\frac{d^2\psi_1(\mathrm{y})}{dy^2} + \frac{2\mu_a}{\mathrm{h}^2}\left[E_{nl} - V(\mathrm{y})\right]\psi_1(\mathrm{y}) = 0 \tag{4}$$

The expression represented by Equation (4) can be alternatively formulated as follows:

$$\phi'(\mathrm{y}) + \phi(\mathrm{y})^2 + k(\mathrm{y})^2 = 0 \tag{5}$$

.

with

$$k(\mathrm{y}) = \sqrt{\frac{2\mu_a}{\mathrm{h}^2}\left[E_{nl} - V(\mathrm{y})\right]} \tag{6}$$

In the equation provided, $\phi(\mathrm{y}) = \psi_1'(\mathrm{y})/\psi_1(\mathrm{y})$ represents the logarithmic derivative of the wave function (WF), μ_a denotes the reduced mass of the quarkonium particles, $k(\mathrm{y})$ stands for momentum, and $V(\mathrm{y})$ represents a piecewise continuous real potential function of x_c. The phase angle of the SE corresponds to the logarithmic derivative $\phi(\mathrm{y})$. As indicated by Equation (6), when x increases across a node of the wave function $\psi_1(\mathrm{y})$, $\phi(\mathrm{y})$, decreases to $-\infty$, undergoes a jump to $+\infty$, and then decreases once more. We can extend the exact quantization rule to encompass the three-dimensional radial SE with spherically symmetric potential by simply substituting the variables $y \to r$ and $V(\mathrm{y}) \to V_{eff}(r)$ accordingly, as detailed in references [28, 29].

$$\int_{r_a}^{r_b} k(r_q)dr_q = N\pi + \int_{r_a}^{r_b} \phi(r_q)\left[\frac{dk(r_q)}{dr_q}\right]\left[\frac{d\phi(r_q)}{dr_q}\right]^{-1} \tag{7}$$

$$k(r_q) = \sqrt{\frac{2\mu_a}{\hbar^2}\left[E_{nl} - V_{eff}(r_q)\right]} \tag{8}$$

In this context, r_a *and* r_b refers to two turning points identified by $E = V_{eff}(r)$. $N = n+1$, which represents the number of nodes $\phi(r)$ within the region $E_{nl} = V_{eff}(r)$ is incremented by 1 compared to the count of nodes in the wave function $\psi_1(r_q)$. The expression can be decomposed into two terms: $N\pi$, originating from the nodes of the logarithmic derivatives of the wave function, and a second term known as the quantum correction. Notably, the quantum correction, denoted as (Q_c), primarily concerns the ground state, simplifying the calculation process. i.e.,

$$Q_c = \int_{r_a}^{r_b} k_0'(r_q)\frac{\phi_0}{\phi_0'}dr_q \tag{9}$$

3. Analytical solutions of the Schrödinger equation with the class of inversely quadratic Yukawa potential

The Schrödinger equation is given by [30].

$$\frac{d^2R(r_q)}{dr_q^{\,2}} + \frac{2\mu_a}{\mathrm{h}^2}\left[E_{nl} - V(r_q) - \frac{l(l+1)\mathrm{h}^2}{2\mu_a r_q^{\,2}}\right]R(r_q) = 0 \tag{10}$$

In this equation, l, corresponds to the angular momentum, μ_a, is the reduced mass, r_q represents the distance between the interacting particles, and $\hbar$ denotes the reduced Planck constant.

By substituting Equation (2) into Equation (10), we derive

$$\frac{d^2R(r_q)}{dr_q^{\,2}} + \frac{2\mu_a}{\mathrm{h}^2}\left[E_{nl} - V_{eff}(r_q)\right]R(r_q) = 0 \tag{11}$$

where

$$V_{eff}(r_q) = \frac{\beta_{00}}{r_q^{\,2}} - \frac{\beta_{11}}{r_q} + \beta_{22}r_q^{\,2} + \beta_{33}r_q + \beta_{44} + \frac{l(l+1)\mathrm{h}^2}{2\mu_a r_q^{\,2}} \tag{12}$$

Transformation of the coordinate of Eq. (11) from r_q to s is given below;

$$s = \frac{1}{r_q} \tag{13}$$

After substituting Equation (13) into Equation (12), we obtain Equation (14).

$$V_{eff}(\mathrm{s}) = \beta_{00}s^2 - \beta_{11}s + \frac{\beta_{22}}{s^2} + \frac{\beta_{33}}{s} + \beta_{44} + \frac{l(l+1)\mathrm{h}^2 s^2}{2\mu_a} \tag{14}$$

To simplify the analysis of the third and fourth terms in equation (14), we introduce an approximation strategy. This strategy involves assuming a characteristic radius, r_0, for the meson. We will then proceed by expanding $\frac{\beta_{33}}{s}$ and $\frac{\beta_{22}}{s^2}$ in a power series around r_0; i.e. around $\delta \equiv \frac{1}{r_0}$, up to the second order. This is similar to the Pekeris-type approximation which helps to deform the centrifugal term [31].

Setting $z_c = s - \delta$ and around $z_c = 0$ it can be expanded as

$$\frac{\beta_{33}}{s} = \frac{\beta_{33}}{z_c + \delta} = \frac{\beta_{33}}{\delta\left(1 + \frac{z_c}{\delta}\right)} = \frac{\beta_{33}}{\delta}\left(1 + \frac{z_c}{\delta}\right)^{-1} \tag{15}$$

which yields

$$\frac{\beta_{33}}{s} = \beta_{33}\left(\frac{3}{\delta} - \frac{3s}{\delta^2} + \frac{s^2}{\delta^3}\right) \tag{16}$$

Similarly,

$$\frac{\beta_{22}}{s^2} = \beta_{22}\left(\frac{6}{\delta^2} - \frac{8s}{\delta^3} + \frac{3s^2}{\delta^4}\right) \tag{17}$$

The next step involves utilizing equations (16) and (17) within equation (14). This substitution leads to

$$V_{eff}(\mathrm{s}) = \xi_{11} + \xi_{22}s + \xi_{33}s^2 \tag{18}$$

where

$$\left.\begin{aligned} \xi_{11} &= \frac{6\beta_{22}}{\delta^2} + \frac{3\beta_{33}}{\delta} + \beta_{44}, \quad \xi_{22} = -\beta_{11} - \frac{3\beta_{33}}{\delta^2} - \frac{8\beta_{22}}{\delta^3} \\ \xi_{33} &= \frac{3\beta_{33}}{\delta^4} + \frac{\beta_{33}}{\delta^3} + \beta_{00} + \frac{l(l+1)\mathrm{h}^2}{2\mu_a} \end{aligned}\right\} \tag{19}$$

We can express the non-linear Riccati equation describing the ground state using a new variable, denoted by s as**,**

$$-s^2\phi'(\mathrm{s}) + \phi^2(\mathrm{s}) = k(\mathrm{s}), \tag{20}$$

where

$$k(\mathrm{s}) = \sqrt{\frac{2\mu_a}{\mathrm{h}^2}\left[\xi_{33}s^2 + \xi_{22}s + \xi_{11} - E\right]} \tag{21}$$

The quantization rule comes into play as we analyze the potential. The first step involves calculating the turning points, labeled s_a and s_b. We achieve this by solving the equation within the square brackets of Eq. (21).

$$\left.\begin{aligned} s_a &= \frac{-\xi_{22} - \sqrt{\xi_{22}{}^2 - 4\xi_{33}(\xi_{11} - E)}}{2\xi_{33}} \\ s_b &= \frac{-\xi_{22} + \sqrt{\xi_{22}{}^2 - 4\xi_{33}(\xi_{11} - E)}}{2\xi_{33}} \end{aligned}\right\} \tag{22}$$

From Eq. (22) we get,

.

$$\left.\begin{aligned} s_a s_b &= \frac{\xi_{11}-E}{\xi_{33}} \\ s_a + s_b &= -\frac{\xi_{22}}{\xi_{33}} \end{aligned}\right\} \tag{23}$$

Also, from Eq. (21) we have

$$k(\mathrm{s}) = \sqrt{\frac{2\mu_a}{\mathrm{h}^2}\xi_{33}\left(x_c{}^2 + \frac{\xi_{22}}{\xi_{33}}x + \frac{\xi_{11}-E}{\xi_{33}} \right)} \tag{24}$$

Substituting Eq. (23) into Eq. (24) gives

$$k(\mathrm{s}) = \sqrt{\frac{2\mu_a\xi_{33}}{\mathrm{h}^2}(s-s_a)(s-s_b)} \tag{25}$$

where $k(\mathrm{s})$ is the momentum between the two turning points s_a and s_b.

Because the logarithmic derivative possesses only one zero and lacks poles for the ground state, we propose a trial solution for the ground state wave function

$$\phi_0(\mathrm{s}) = A_1 + B_2 s \tag{26}$$

We can solve for the ground state energy by incorporating Eq. (26) into Eq. (20). This involves solving the resulting non-linear Riccati equation, which yields

$$E_0 = \xi_{11} - \frac{\mathrm{h}^2 A_1^2}{2\mu_a} \tag{27}$$

Also, A_1 and B_2 are obtained as follows

$$\left.\begin{aligned} A_1 &= \frac{\mu_a\xi_{22}}{B_2\mathrm{h}^2} \\ B_2 &= \frac{1}{2} + \sqrt{\frac{1}{4} - \frac{2\mu_a\xi_{33}}{\mathrm{h}^2}} \end{aligned}\right\} \tag{28}$$

The positive sign is chosen for the square root of B_2. This selection is crucial because it ensures that the logarithmic derivatives $\phi_0(\mathrm{s})$ behave as needed, specifically by decaying exponentially. Having established this, we can now determine the quantum correction, which is

$$\int_{r_a}^{r_b}\phi(r_q)\left[\frac{dk(r_q)}{dr_q}\right]\left[\frac{d\phi(r_q)}{dr_q}\right]^{-1} dr_q = -\int_{s_a}^{s_b}\frac{k_0'(\mathrm{s})}{s^2}\frac{\phi_0(\mathrm{s})}{\phi_0'(\mathrm{s})}ds \tag{29}$$

From Eq. (29) we have

$$= \sqrt{\frac{2\mu_a\xi_{33}}{\mathrm{h}^2}}\int_{s_a}^{s_b}\left(\frac{\frac{A_1}{B_2} - \frac{s_a+s_b}{2}}{s\sqrt{(s-s_a)(s-s_b)}} + \frac{\frac{A_1}{B_2}\left(\frac{s_a+s_b}{2}\right)}{s^2\sqrt{(s-s_a)(s-s_b)}} \right)ds \tag{29a}$$

By referring to the integrals in Appendix A, we achieved the following

$$= \pi\sqrt{\frac{2\mu_a\xi_{33}}{\mathrm{h}^2}}\left[\frac{\frac{A_1}{B_2} - \frac{s_a+s_b}{2}}{\sqrt{1+(s_a+s_b)+s_a s_b}} + \frac{\frac{A_1}{B_2}\left(\frac{s_a+s_b}{2}\right)\left(\sqrt{s_a s_b} - \frac{1}{2(s_a+s_b)}\right)}{\sqrt{s_a s_b}} \right] \tag{29b}$$

We substitute Eq. (23) into Eq.(29b) and obtain

$$= \pi\sqrt{\frac{2\mu_a\xi_{33}}{\mathrm{h}^2}}\left[\frac{\frac{A_1}{B_2}+\frac{\xi_{22}}{2\xi_{33}}}{\sqrt{\frac{\mathrm{h}^2}{2\mu\xi_3}}\left(A_1+B_2\right)}-\frac{\frac{A_1\xi_{22}}{2B_2\xi_{33}}\left(\sqrt{\frac{\mathrm{h}^2}{2\mu_a\xi_{33}}}A_1+\frac{\xi_{33}}{2\xi_{22}}\right)}{\sqrt{\frac{\mathrm{h}^2}{2\mu_a\xi_{33}}}A_1}\right] \tag{29c}$$

Inserting Eq. (29c) into Eq. (7), Eq.(29d) is gotten as;

$$= \pi\sqrt{\frac{2\mu_a\xi_{33}}{\mathrm{h}^2}}\left[\frac{\frac{A_1}{B_2}+\frac{\xi_{22}}{2\xi_{33}}}{\sqrt{\frac{\mathrm{h}^2}{2\mu_a\xi_{33}}}\left(A_1+B_2\right)}-\frac{\frac{A_1\xi_{22}}{2B_2\xi_{33}}\left(\sqrt{\frac{\mathrm{h}^2}{2\mu_a\xi_{33}}}A_1+\frac{\xi_{33}}{2\xi_{22}}\right)}{\sqrt{\frac{\mathrm{h}^2}{2\mu_a\xi_{33}}}A_1}\right]+N\pi \tag{29d}$$

Furthermore, the integral of Eq.(9) is obtain as

$$\int_{r_a}^{r_b}k(r_q)dr_q=-\int_{s_a}^{s_b}\frac{k(\mathrm{s})}{s^2}ds \tag{30}$$

From Eq.(30) we have

$$=-\sqrt{\frac{2\mu_a\xi_{33}}{\mathrm{h}^2}}\int_{s_a}^{s_b}\frac{\sqrt{\left(s-s_a\right)\left(s-s_b\right)}}{s^2}ds \tag{30a}$$

After utilizing Eq. (31), Eq. (30a) takes the following form

$$=-\sqrt{\frac{2\mu_a\xi_{33}}{\mathrm{h}^2}}\left[\frac{\left(s_a+s_b\right)-\sqrt{s_as_b}}{2\sqrt{s_as_b}}\right] \tag{30b}$$

Incorporating Eq. (23) into Eq. (30b), we get

$$-\sqrt{\frac{2\mu_a\xi_{33}}{\mathrm{h}^2}}\left[\frac{-\frac{\xi_{22}}{\xi_{33}}-\sqrt{\frac{\xi_{11}-E}{\xi_{33}}}}{2\sqrt{\frac{\xi_{11}-E}{\xi_{33}}}}\right] \tag{30c}$$

Since Eq. (27a) lacked a solution in standard integral tables, we employed Maple software to evaluate it. This resulted in the following valuable integral:

$$\int_a^b\frac{\sqrt{\left(s-a\right)\left(b-s\right)}}{s^2}ds=\frac{\left(a+b\right)-\sqrt{ab}\pi_a}{2\sqrt{ab}} \tag{31}$$

The energy equation governing the CIQYP is obtained by equating Eqs. (29d) and (30c). We achieve this after incorporating Eqs. (19), (28), and (3).

$$E_{nl}=\frac{\alpha^4A_c}{4\delta^2\mathrm{h}^2}-\frac{\alpha^3A_c}{2\delta\mathrm{h}^2}-\frac{\frac{\mu_a}{2\mathrm{h}^2}\left(\frac{\alpha^4A_c^2}{3\delta^3}-\frac{\alpha^3A_c}{2\delta^2}+A_c\alpha^2+A_a^2-A_c\alpha\right)}{\left[n+\frac{1}{2}+\sqrt{\frac{4\mu_a\alpha^3A_c}{3\delta^3\mathrm{h}^2}+\left(l+\frac{1}{2}\right)^2+\frac{2\mu_a(A_c-A_b)}{\mathrm{h}^2}+\frac{\mu_a\alpha^2A_c}{\delta^4\mathrm{h}^2}}\right]^2} \tag{32}$$

4. Application to Diatomic Molecules

Diatomic molecules, which are made up of just two atoms bonded together are the basic building blocks of physics and chemistry. These combinations are essential to everything in our world, including the materials we use and the air we breathe. By setting $A_a=2D_er_e, A_b=-D_er_e^2, A_c=0$ of Eq.(1), we have the Kratzer potential [32] and the energy equation is given as Eq.(33),

.

$$E_{nl} = -\frac{2\mu_a}{\hbar^2} D_e^2 r_e^2 \left[n + \frac{1}{2} + \sqrt{\left(l + \frac{1}{2} \right)^2 + \frac{2\mu_a D_e r_e^2}{\hbar^2}} \right]^{-2} \tag{33}$$

5. Application to Heavy Mesons

Based on the theoretical framework provided in references [33, 34], we compute the mass spectra for heavy meson

$$M_x = 2m_w + E_{nl} \tag{34}$$

where m_w is quarkonium mass and E_{nl} is energy eigenvalues.

The mass spectra of the class of inversely quadratic Yukawa potential for heavy mesons can be derived by incorporating Eq. (32) into Eq. (34).

$$M_x = 2m_w + \frac{\alpha^4 A_c}{4\delta^2 \hbar^2} - \frac{\alpha^3 A_c}{2\delta \hbar^2} - \frac{\dfrac{\mu_a}{2\hbar^2}\left(\dfrac{\alpha^4 A_c^2}{3\delta^3} - \dfrac{\alpha^3 A_c}{2\delta^2} + A_c\alpha^2 + A_a^2 - A_c\alpha \right)}{\left[n + \dfrac{1}{2} + \sqrt{\dfrac{4\mu_a \alpha^3 A_c}{3\delta^3 \hbar^2} + \left(l + \dfrac{1}{2} \right)^2 + \dfrac{2\mu_a (A_c - A_b)}{\hbar^2} + \dfrac{\mu_a \alpha^2 A_c}{\delta^4 \hbar^2}} \right]^2} \tag{35}$$

In this work, we rely on the Chi-square function [24] to determine how closely our numerical predictions match the actual values.

$$\chi^2 = \frac{1}{k_a} \sum_{j=1}^{k_a} \frac{\left(M_j^{\text{Exp.}} - M_j^{Theo.} \right)}{\nabla_j} \tag{36}$$

where k_a represent number of mesons sample, $M_j^{\text{Exp.}}$ is the experimental value of mesons, while $M_j^{Theo.}$ is the corresponding theoretical prediction. The ∇_j quantity is the experimental uncertainty of the masses. Intuitively, $\nabla_j = 1$.

6. Discussion of results

The analytical calculations agree with experiments involving diatomic molecular spectroscopy, where potential energy curves match spectroscopic constants. They align with data on vibrational-rotational spectra, energy levels in quantum dots, and heavy quarkonium mass spectra, validating models in plasma and condensed matter systems under the class of inversely quadratic Yukawa interactions.

Our predictions for the mass spectra of heavy mesons in various quantum states are summarized in Tables 1 and 2. To achieve these predictions, we first needed to determine the free parameters in equation (35). This was accomplished by solving a system of two algebraic equations. The specific values used for bottomonium and charmonium systems, as referenced in [35], are $m_b = 4.823\,GeV$, and $m_c = 1.209\,GeV$, respectively. The experimental data is taken from [36, 37]. The predicted mass spectra for charmonium and bottomonium, shown in Tables 1 and 2, exhibit excellent agreement with experimental data. This represents a significant improvement compared to earlier works like Refs. [12, 13]. This simply implies that one approach to understanding the behavior of quark-antiquark pairs in mesons is to use potential models. These models describe the interaction between quarks and antiquarks as an effective potential energy. The potential energy includes contributions from the strong force as well as other forces. Our predictions agree with experimental data within a maximum margin of error of $0.0065\,GeV$. Our potential model was simplified to the Kratzer potential through the application of specific boundary conditions, ensuring the mathematical precision of our analytical calculations. Additionally, we utilized the energy spectrum outlined in Eq. (33) to examine the energy spectra of HDM such as hydrogen (H_2) and nitrogen (N_2). The spectroscopic data for these molecules, sourced from references [38], are presented in Table 3. The calculations were carried out utilizing the conversions outlined by 1 amu = 931.494028 MeV/c^2 and $\hbar c = 1973.29$ eV Å [1-3].

The selection of these diatomic molecules was based on extensive applications and studies conducted by various researchers. Tables 4 and 5 present the numerical energy eigenvalues for the chosen homonuclear diatomic molecules across different quantum numbers n and l. Notably, for a fixed principal quantum number

n, the energy spectrum decreases with an increase in angular momentum quantum l. Similarly, maintaining the angular momentum quantum l constant while varying the principal quantum number n yields the same observed trend. This suggests that the behavior of the angular momentum and its impact on the energy levels, specifically, are the fundamental principles of quantum mechanics and explain the decrease in the energy spectrum with increasing angular momentum quantum number for a fixed principal quantum number in a HDM. An electron orbiting a nucleus in a diatomic molecule, for example, has quantized angular momentum in quantum mechanics, which means it can only take on specific discrete values determined by the quantum numbers n and l. Both the angular momentum quantum number and the principal quantum number of an electron in an atom or molecule define its energy. The electron's orbit grows more elliptical and farther from the nucleus as the angular momentum quantum number rises while the principal quantum number remains constant. The electron's potential energy decreases with increasing distance, resulting in lower energy levels or, to put it another way, a reduction in the energy spectrum. These findings align well with results previously obtained using diverse analytical and numerical methods [39, 40].

Table 1. Mass spectra of charmonium in (GeV) (m_c =1.209 GeV, μ_a = 0.6045 GeV, $A_a = -19252.67309\ GeV$, $A_b = -1.94850856910^6\ GeV$, $A_c = -1.9497828810^6 GeV$, $\alpha = 0.01\ GeV$, $\delta = 0.371\ GeV$)

State	Present work	AIM [12]	LTM [13]	Experiment [36,37]
1s	3.09588	3.096	3.0963	3.096
2s	3.68568	3.686	3.5681	3.686
1p	3.52447	3.214	3.5687	3.525
2p	3.77234	3.773	3.5687	3.773
3s	4.04010	4.275	4.0400	4.040
4s	4.26322	4.865	4.5119	4.263
1d	3.77110	3.412	4.0407	3.770
2d	4.15909	-	-	4.159

Table 2. Mass spectra of bottomonium in (GeV) (m_b = 4.823 GeV, μ_a = 2.4115 GeV, $A_a = -11852.70018\ GeV$, $A_b = -1.19335194110^6\ GeV$, $A_c = -1.19413808310^6\ GeV$, $\alpha = 0.01\ GeV$, $\delta = 0.371\ GeV$).

State	Present work	AIM [12]	LTM [13]	Experiment [36,37]
1s	9.46023	9.460	9.745	9.460
2s	10.02345	10.023	10.023	10.023
1p	9.89923	9.492	10.025	9.899
2p	10.26098	10.038	10.303	10.260
3s	10.35587	10.585	10.302	10.355
4s	10.58076	11.148	10.580	10.580
1d	10.16467	9.551	10.303	10.164

Table 3. Spectroscopic parameters of the selected HDM [38]

Molecules	$D_e(eV)$	$r_e\left(\overset{g}{A}\right)$	$\mu_a(MeV)$
H_2	4.7446000000	0.7416	0.05021684305
N_2	11.938190000	1.0940	0.65235787010

In addition, Fig. 1 is the variation of energy spectra against the angular quantum number, which shows an asymptotic convergence of the energy. Understanding the stability of diatomic molecules requires an understanding of the asymptotic convergence of energy, which occurs when the internuclear separation approaches a certain value as it grows very large. When they approach each other, electron sharing attracts them together and creates a stable bound state with a minimum energy configuration. The most precise framework for characterizing the energy states of diatomic molecules is provided by quantum mechanics.

.

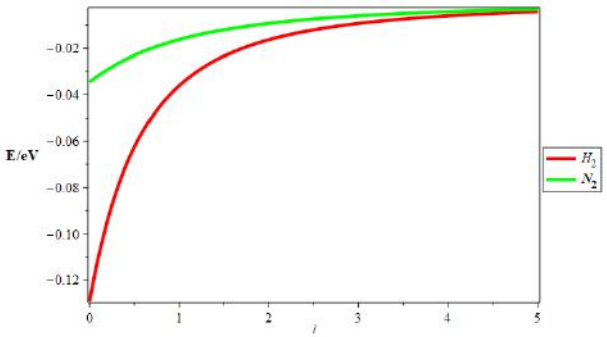

Fig.1. The correlation between the angular momentum quantum number (ℓ) and the variation in energy levels for the homonuclear diatomic molecules.

Table 4. Energy spectra (in eV) for the various *n* and *l* quantum numbers for a HDM at constant n

n	*l*	N_2	H_2
0	0	−11.88375321672634	−4.565204473204863
	1	−11.883257920816611	−4.551938675793838
	2	−11.882267452916444	−4.525638129919935
	3	−11.88078206078689	−4.4867549364956085
1	0	−11.776112900792786	−4.238616688471602
	1	−11.775624318967708	−4.226747699496392
	2	−11.774647277141154	−4.203210857813765
	3	−11.773182018884329	−4.168399926608872
	4	−11.771228909364144	−4.122884944668811
2	0	−11.669928460893514	−3.945860680848302
	1	−11.669446472347172	−3.9351990851508365
	2	−11.668482615027564	−3.914051903440431
	3	−11.667037128406324	−3.882763865567736
	4	−11.665110371504726	−3.8418344039298025
	5	−11.662702822670521	−3.7918979616955264
3	0	−11.565173759877975	−3.6824199205172485
	1	−11.564698246509348	−3.6728073518278963
	2	−11.563747337538615	−3.653736983693575
	3	−11.562321268425762	−3.625512072868766
	4	−11.560420392178223	−3.588572275743318
	5	−11.558045179132064	−3.5434766480219393
	6	−11.555196216660608	−3.490882938850404

Table 5. Energy spectra (in eV) for the various *n* and *l* quantum numbers for a HDM at constant *l*

l	n	N_2	H_2
0	0	−11.88375321672634	−4.565204473204863
	1	−11.776112900792786	−4.238616688471602
	2	−11.669928460893514	−3.945860680848302
	3	−11.565173759877975	−3.6824199205172485
1	0	−11.883257920816611	−4.551938675793838
	1	−11.775624318967708	−4.226747699496392
	2	−11.669446472347172	−3.9351990851508365
	3	−11.564698246509348	−3.6728073518278963
	4	−11.4613540908605	−3.4358103946306726
2	0	−11.882267452916444	−4.525638129919935
	1	−11.774647277141154	−4.203210857813765
	2	−11.668482615027564	−3.914051903440431
	3	−11.563747337538615	−3.653736983693575
	4	−11.460415899344495	−3.418553558957142
	5	−11.358463323244653	−3.2053677272267476
3	0	−11.88078206078689	−4.4867549364956085
	1	−11.773182018884329	−4.168399926608872
	2	−11.667037128406324	−3.882763865567736
	3	−11.562321268425762	−3.625512072868766
	4	−11.45900890150587	−3.3930046311567494
	5	−11.357075058128967	−3.182166919054122
	6	−11.256495321607867	−2.990387440908319

7. Conclusion

Our investigation utilized the exact quantization rule approach to obtain the approximate solutions of the Schrödinger equation for energy eigenvalues using a recently proposed potential known as the class of inversely quadratic Yukawa potential. Using the current findings, we calculated the heavy-meson masses (charmonium and bottomonium) for various quantum states. We observe that the mass spectra of the mesons acquired in this work are consistent with findings from other investigations and the experimental measurements. This simply implies that one approach to understanding the behavior of quark-antiquark pairs in mesons is to use potential models. These models describe the interaction between quarks and antiquarks as an effective potential energy. The potential energy includes contributions from the strong force as well as other forces. Also, our potential model was simplified to the Kratzer potential through the application of specific boundary conditions, ensuring the mathematical precision of our analytical calculations.

We utilized the energy spectrum to examine the energy spectra of homonuclear diatomic molecules such as hydrogen (H_2) and nitrogen (N_2). Notably, for a fixed principal quantum number n, the energy spectrum decreases with an increase in angular momentum quantum l. Similarly, maintaining the angular momentum quantum number l constant while varying the principal quantum number n yields the same observed trend. This implies that the decrease in the energy spectrum with increasing angular momentum quantum number for a fixed principal quantum number in a diatomic molecule arises from the interplay between the electron's kinetic and potential energies as its orbit becomes more elongated and its distance from the nucleus increases. The analytical solution notably differs by incorporating quantum mechanical principles, capturing discrete energy spectra and wavefunction behaviors that are absent in classical solutions. It accounts for state quantization, and potential-specific features, enabling precise predictions in microscopic systems—unlike classical approaches, which treat energy as continuous and overlook quantum phenomena.

Conflict of interest statement

The authors declare that they have no conflict of interest in relation to this research, whether financial, personal, authorship or otherwise, that could affect the research and its results presented in this paper.

CRediT author statement

Inyang E.P.: Conceptualization, Methodology, Writing-Original draft preparation, Funding acquisition; **Nwachukwu I. M.:** Software Funding acquisition; **William E.S:** Data curation; **Ekechukwu C.C.**: Visualization; **Ekong I.B.**: Investigation; **Lawal K. M.:** Validation, Funding acquisition; **Simon J., Momoh K O., Oyelami O.A.:** Writing- Reviewing and Editing. The final manuscript was read and approved by all authors.

Funding

This research was supported by the 2024 Senate Research Grant from the National Open University of Nigeria: with grant number NOUN/DRA/SRG/AW/045.

Acknowledgements

Inyang, E.P., Nwachukwu, I.M., and Lawal, K.M. gratefully acknowledge the National Open University of Nigeria for the 2024 Senate Research Grant award. The authors also thank the reviewers for valuable suggestions that have significantly enhanced the quality of the manuscript

References

1 Inyang E.P., Ayedun F., Ibanga E.A., Lawal K.M., Okon I. B., William E.S., Ekwevugbe O., Onate C.A., Antia A. D., Obisung E. O. (2022) Analytical Solutions of the N-Dimensional Schrödinger equation with modified screened Kratzer plus Inversely Quadratic Yukawa potential and Thermodynamic Properties of selected Diatomic Molecules. *Results in Physics*, 43, 106075. DOI:10.1016/j.rinp.2022.106075.

2 Inyang E.P., Ali N., Endut R., Aljunid S.A. (2024) Energy Spectra, Expectation Values, and Thermodynamic Properties of HCl And LiH Diatomic Molecules. *Eurasian Physical Technical Journal*, 21, 1(47), 124 – 137. DOI:10.31489/2024No1/124-137.

3 Inyang E.P., Ntibi J.E., Obisung E.O., William E.S., Ibekwe E.E., Akpan I.O., Inyang E.P. (2022) Expectation Values and Energy Spectra of the Varshni Potential in Arbitrary Dimensions. *Jordan Journal of Physics*, 5, 495 – 509. DOI: 10.47011/15.5.7.

4 Kumar R., Chand F. (2013) Asymptotic study to the N-dimensional radial Schrödinger equation for the quark-antiquark system. *Communications in Theoretical Physics*, 59(5), 528. DOI: 10.1088/0253-6102/59/5/02.

.

5 Mutuk H. (2018) Mass Spectra and Decay constants of Heavy-light Mesons: A case study of QCD sum Rules and Quark model. *Advances in High Energy Physics, 2018*. DOI: 10.1155/2018/8095653.

6 William E.S., Inyang S.O., Ekerenam O.O., Inyang E.P., Okon I.B., Okorie U.S., Ita B.I., Akpan I.O., Ikot A.N. (2024) Theoretic analysis of non-relativistic equation with the Varshni-Eckart potential model in cosmic string topological defects geometry and external fields for the selected diatomic molecules. *Molecular Physics*, *122*(3), e2249140. DOI: 10.1080/00268976.2023.2249140.

7 Hassanabadi S., Rajabi A.A., Zarrinkamar S. (2012) Cornell and kratzer potentials within the semirelativistic treatment. *Modern Physics Letters A*, *27*(10), 1250057. DOI: 10.1142/S0217732312500575.

8 Vega A., Flores J. (2016) Heavy quarkonium properties from Cornell potential using variational method and supersymmetric quantum mechanics. *Pramana*, *87*, 1-7. DOI: 10.1007/s12043-016-1278-7.

9 Ciftci H., Kisoglu H.F. (2018) Nonrelativistic-Arbitrary l-states of quarkonium through Asymptotic Iteration method. Advances in High Energy Physics, 4549705. DOI: 10.1155/2018/4549705.

10 Carrington M.E., Czajka A., Mrówczyński S. (2020) Heavy quarks embedded in glasma. *Nuclear Physics A*, *1001*, 121914. DOI: 10.1016/j.nuclphysa.2020.121914.

11 Allosh M., Mustafa Y., Khalifa Ahmed N., Sayed Mustafa A. (2021) Ground and Excited state mass spectra and properties of heavy-light mesons. *Few-Body Systems*, *62*(2), 26. DOI: 10.1007/s00601-021-01608-1.

12 Rani R., Bhardwaj S.B., Chand F. (2018) Mass spectra of heavy and light mesons using asymptotic iteration method. *Communications in Theoretical Physics*, *70*(2), 179. DOI: 10.1088/0253-6102/70/2/179.

13 Abu-Shady M., Khokha E.M. (2018) Heavy-light mesons in the nonrelativistic quark model using laplace transformation method. *Advances in high energy physics*, *2018*. DOI: 10.1155/2018/7032041.

14 Abu-Shady M., Inyang, E.P. (2022) Heavy-meson masses in the framework of trigonometric Rosen-Morse potential using the generalized fractional Derivative. *arXiv preprint arXiv:2209.00566*. DOI: 10.26565/2312-4334-2022-4-06.

15 Inyang E.P., Obisung E.O., Amajama J., Bassey D.E., William E.S., Okon I.B. (2022) The Effect of Topological Defect on The Mass Spectra of Heavy and Heavy-Light Quarkonia. *Eurasian Physical Technical Journal*, 9, 4(42), 78 – 87. DOI: 10.31489/2022No4/78-87.

16 Ikot A.N., Obagboye L.F., Okorie U.S., Inyang E.P., Amadi P.O., Abdel-Aty A. (2022) Solutions of Schrodinger equation with generalized Cornell potential (GCP) and its applications to diatomic molecular systems in D-dimensions using Extended Nikiforov–Uvarov (ENU) formalism. *The European Physical Journal Plus*, 137, 1370 DOI:10.1140/epjp/s13360-022-03590-x.

17 Omugbe E., Eyube E.S., Onate C.A., Njoku *I*.J., Jahanshir A., Inyang E.P., Emeje K.O. (2024) Nonrelativistic energy equations for diatomic molecules constrained in a deformed hyperbolic potential function. *Journal of Molecular Modeling*, *30*(3), 1-10. DOI: 10.1007/s00894-024-05855-x.

18 Purohit K.R., Jakhad P., Rai A.K. (2022) Quarkonium spectroscopy of the linear plus modified Yukawa potential. *Physica Scripta*, *97*(4), 044002. DOI: 10.1088/1402-4896/ac5bc2.

19 Purohit K.R., Rai A.K., Parmar R.H. (2023) Spectroscopy of heavy-light mesons (cs^{-}, cq^{-}, bs^{-}, bq^{-}) for the linear plus modified Yukawa potential using Nikiforov–Uvarov method. *Indian Journal of Physics*, 1-13. DOI:10.1007/s12648-023-02852-3.

20 Inyang E.P., Inyang E.P., Akpan I.O., Ntibi J.E., William E.S. (2021) Masses and thermodynamic properties of a Quarkonium system. *Canadian Journal Physics*, 99, 982 – 990. DOI: 10.1139/cjp-2020-0578.

21 Inyang E.P., Inyang E.P., Ntibi J. E., Ibekwe E. E., William E. S. (2021) Approximate solutions of D-dimensional Klein-Gordon equation with Yukawa potential via Nikiforov-Uvarov method. *Indian Journal of Physics*, 95, 2733 - 2739. DOI: 10.1007/s12648-020-01933-x.

22 Ibekwe E.E., Okorie U.S., Emah J.B., Inyang E.P., Ekong S.A. (2021) Mass spectrum of heavy quarkonium for screened Kratzer potential (SKP) using series expansion method. *European Physical Journal Plus*, 87, 1- 11. DOI:10.1140/epjp/s13360-021-01090-y.

23 Akpan I.O., Inyang E.P., William E.S. (2021) Approximate solutions of the Schrödinger equation with Hulthen-Hellmann Potentials for a Quarkonium system. *Revista mexicana de fisica*, 67(3), 482-490. DOI:10.31349/revmexfis.67.482.

24 Inyang E.P., Inyang E.P., William E.S. (2021). Study on the applicability of Varshni potential to predict the mass-spectra of the Quark-Antiquark systems in a non-relativistic framework. *Jordan Journal of Physics*, *14*(4), 339-347. DOI: 10.47011/14.4.8.

25 Patrick I.E., Joseph N., Akpan I.E., Funmilayo A., Peter I.E., Sunday W.E. (2023). Thermal properties, mass spectra and root mean square radii of heavy quarkonium system with class of inversely quadratic Yukawa potential. *In AIP Conference Proceedings*, AIP Publishing, 2679, 1. DOI: 10.1063/5.0112829.

26 Grinstein B. (2000) A modern introduction to quarkonium theory. *International Journal of Modern Physics A*, 15(04), 461-495. DOI: 10.1142/S0217751X00000227.

27 Lucha W., Schöberl F. F., Gromes D. (1991). Bound states of quarks. *Physics reports*, *200*(4), 127-240. DOI:10.1016/0370-1573(91)90001-3.

28 Ma Z.Q., Xu B.W. (2005) Quantum correction in exact quantization rules. *Europhysics Letters*, 69(5), 685. DOI: 10.1209/epl/i2004-10418-8.

29 Ma Z.Q., Xu B.W. (2005) Exact quantization rules for bound states of the Schrödinger equation. *International Journal of Modern Physics E*, 14(04), 599-610. DOI: 10.1142/S0218301305003429.

30 William E.S., Inyang E.P., Thompson E.A. (2020) Arbitrary -solutions of the Schrödinger equation interacting with Hulthén-Hellmann potential model. *Revista Mexicana Fisica*, 66, 730 - 741. DOI: 10.31349/RevMex Fis.66.730.

31 Abu-Shady M., Edet C.O., Ikot A.N. (2021) Non-relativistic quark model under external magnetic and Aharanov–Bohm (AB) fields in the presence of temperature-dependent confined Cornell potential. *Canadian Journal of Physics*, 99(11), 1024-1031. DOI: 10.11139/cjp-2020-0101.

32 Bayrak O., Boztosun I., Ciftci H. (2007) Exact analytical solutions to the Kratzer potential by the asymptotic iteration method. *International Journal of Quantum Chemistry*, 107(3), 540-544. DOI: 10.1002/qua.21141.

33 Omugbe E., Osafile O.E., Okon I.B., Inyang E.P., William E.S., Jahanshir A. (2022) Any L-state energy of the spinless Salpeter equation under the Cornell potential by the WKB Approximation method: An Application to mass spectra of mesons. *Few-Body Systems*, 63, 1-7. DOI: 10.1007/s00601-021-01705-1.

34 Inyang E.P., Ali N., Endut R., Rusli N., Aljunid S.A., Ali N.R., Asjad M.M. (2024) Thermal Properties and Mass Spectra of Heavy Mesons in the Presence of a Point-Like Defect. *East European Journal of Physics*, (1), 156-166. DOI: 10.26565/2312-4334-2024-1-13.

35 Olive R., Groom D. E., Trippe T.G. (2014) Particle Data Group, *Chinese Physics C.*, 38, 60. DOI: 10.1088/1674-1137/38/9/090001.

36 Barnett R.M., Carone C.D., Groom D.E., Trippe T.G., Wohl C.G. Particle Data Group. *Physical Review D.*, 92,656. DOI: 10.1103/PhysRevD.54.1.

37 Tanabashi M., Carone, C. D., Trippe T.G., Wohl C.G. (2018) Particle Data Group. *Physical Review D.*, 98, 546. DOI:10.1103/PhysRevD.98.030001.

38 Inyang E.P., William E.S., Ntibi J.E., Obu J.A., Iwuji P.C., Inyang E.P. (2022) Approximate solutions of the Schrödinger equation with Hulthén plus screened Kratzer Potential using the Nikiforov–Uvarov–functional analysis (NUFA) method: an application to diatomic molecules. *Canadian Journal of Physics*, 100(10), 463-473. DOI:10.1139/cjp-2022-0030.

39 Flügge S. (2012) *Practical quantum mechanics*. Springer Science & Business Media. DOI:10.1007/978-3-642-6199.

40 Vigo-Aguiar J., Simos T.E. (2005) Review of multistep methods for the numerical solution of the radial Schrödinger equation. *International journal of quantum chemistry*, 103(3), 278-290. DOI: 10.1002/qua.20495.

AUTHORS' INFORMATION

Inyang, Etido Patrick – Dr. (Sci.), Department of Physics, Faculty of Science, National Open University of Nigeria, Abuja, Nigeria; https://orcid.org/0000-0002-5031-3297; etidophysics@gmail.com

Nwachukwu, Iheke Michael – Dr. (Sci.), Department of Physics, Faculty of Science, National Open University of Nigeria, Abuja, Nigeria; https://orcid.org/0000-0003-2237-7805; inwachukwu@noun.edu.ng

Ekechukwu, Christopher Chinasa – Master (Sci.), Department of Physics, Faculty of Physical Science, University of Calabar, Calabar, Nigeria; https://orcid.org/0000-0001-7559-4112; ekehmore@gmail.com

Ekong, Isaac Bassey – Master (Sci.), Department of Physics, Faculty of Physical Science, University of Calabar, Calabar, Nigeria; https://orcid.org/0000-0002-0645-6768; ekongisaac@unical.edu.ng

William, Eddy Sunday – Dr. (Sci.), Department of Physics, School of Pure and Applied Sciences, Federal University of Technology, Ikot Abasi, Nigeria; https://orcid.org/0000-0002-5247-5281; williameddyphysics@gmail.com

Lawal, Kolawole M. – Dr. (Sci.), Professor, Department of Physics, Faculty of Science, National Open University of Nigeria, Abuja Nigeria; kmlawal@noun.edu.ng

Simon, John – Dr. (Sci.), Department of Physics, Faculty of Science, National Open University of Nigeria, Abuja, Nigeria; https://orcid.org/0000-0002-5477-9043; jsimon@noun.edu.ng

Momoh, Kabir O. – Master (Sci.), Department of Physics, Faculty of Science, National Open University of Nigeria, Abuja, Nigeria; https://orcid.org/0009-0006-4512-6397; kmomoh@noun.edu.ng

Oyelami, Oyewole Abiodun – Master (Sci.), Department of Mathematics, Faculty of Science, National Open University of Nigeria, Abuja, Nigeria; https://orcid.org/0000-0002-2599-0595; ooyelami@noun.edu.ng

.

Appendix A

Some Useful Standard Integrals

$$\int_{r_a}^{r_b} \frac{1}{\sqrt{(r-r_a)(r_b-r)}} dr = \pi_a \tag{A1}$$

$$\int_{r_a}^{r_b} \frac{1}{(a+br)\sqrt{(r-r_a)(r_b-r)}} dr = \frac{\pi_a}{\sqrt{(a+br_b)(a+br_a)}} \tag{A2}$$

$$\int_{r_a}^{r_b} \frac{1}{r}\sqrt{(r-r_a)(r_b-r)} dr = \frac{\pi_a}{2}(r_a+r_b) - \pi_a\sqrt{r_a r_b} \tag{A3}$$

$$\int_{r_a}^{r_b} \frac{1}{r\sqrt{(r-r_a)(r_b-r)}} dr = \frac{\pi_a}{\sqrt{r_a r_b}} \tag{A4}$$

EURASIAN PHYSICAL TECHNICAL JOURNAL

2024, Volume 21, No.4 (50)

https://doi.org/10.31489/2024No3/131-139

Received: 22/05/2024 Revised: 17/10/2024 Accepted: 19/12/2024 Published online: 25/12/2024

Original Research Article

UDC 535.8, 54.057

ENHANCEMENT OF POWER CONVERSION EFFICIENCY OF DYE-SENSITIZED SOLAR CELLS VIA INCORPORATION OF GAN SEMICONDUCTOR MATERIAL SYNTHESIZED IN HOT-WALL CHEMICAL VAPOR DEPOSITION FURNACE

Toktarbaiuly O.[1], Baisariyev M.[1], Kaisha A.[1], Duisebayev T.S.[1,2], Ibrayev N.Kh.[3], Serikov T.M.[3], Ibraimov M.K.[2], Khaniyev B.A.[2], Tezekbay Y.Zh.[1,2], Zhambyl A.N.[2], Nuraje N.[1,4], Sugurbekova G.K.[5]

[1] National Laboratory Astana, Nazarbayev University, Astana, Kazakhstan
[2] Al-Farabi Kazakh National University, Almaty, Kazakhstan
[3] Institute of Molecular Nanophotonics, E.A. Buketov Karaganda University, Karaganda, Kazakhstan
[4] School of Engineering and Digital Science, Nazarbayev University, Astana, Kazakhstan
[5] L.N. Gumilyov Eurasian National University, Astana, Kazakhstan
*Corresponding author: olzat.toktabaiuly@nu.edu.kz

Abstract. *This study discusses the results of plasma enhanced chemical vapor deposition synthesis of GaN on sapphire and silicon substrates using specific parameters: a forward output voltage of 150 watts, a N_2 gas flow rate of 60 standard cubic centimeters per minute, a chamber pressure of 2.48 mmHg, and a synthesis time of 2hours. Characterization by scanning electron microscope, Raman and energy dispersive X-ray revealed the non-stoichiometric formation of GaN, with Ga clearly predominating in the composition. scanning electron microscope analysis of the substrate surface morphology revealed the presence of small islands, which are considered to be the first step in the chemical vapor deposition process. The research also examined the effects of incorporating GaN into the photoanode of dye-sensitized solar cells. The study investigated the optimal amount of GaN powder in the TiO_2 matrix. The initial experiments used commercial GaN powder to determine the optimal weight percentage. Four different weight percentages (wt%) 10 wt%, 20 wt%, 30wt % and 40 wt% GaN were selected for the study. Among them, the 20 wt% GaN had the highest power conversion efficiency of 0.75%. The fill factor values showed a tendency to decrease as the weight fraction of GaN increased.*

Keywords: power conversion, semiconductor, dye, TiO_2, GaN.

1. Introduction

The special physical and chemical properties of semiconductor nanostructures inspire their use as functional devices and basic components for electronic and optoelectronic nanodevices [1]. Gallium-based semiconductor materials are currently of great practical importance and are widely used in the production of high-efficiency optical information storage devices, displays, field-grade lasers, environmental detectors and other applications [2, 3]. The production of semiconductor materials, particularly gallium nitride, for solid-state lighting and high-performance electronic devices represents a promising and cost-effective technology

for producing light-emitting devices. The goal of this advancement is to provide consumers with a viable alternative to highly efficient and less reliable lighting technologies [4].

The strategic design and modification of structures based on gallium compounds with the aim of reducing costs in the end product is based on their environmentally friendly and chemically inert nature. Therefore, there is an urgent need to further develop technologies that can improve living standards by reducing energy consumption and thereby minimizing environmental impact. III-nitride semiconductor materials, including aluminum nitride (AlN), gallium nitride (GaN), and indium nitride (InN), similar to silicon, have the potential to serve as the basis for semiconductor devices with novel functionalities and the ability to upgrade existing technologies [5].

To achieve high-efficiency LEDs with high brightness, the development of bulk or free-standing GaN structures with GaN as a substrate is required. Established crystal growth techniques such as high-pressure nitrogen solution (HPNS), the sodium (Na) flow method, ammon thermal growth and hydride vapor phase epitaxy (HVPE) are used to obtain gallium nitride (GaN) crystals in large quantities. In recent years, Nobel Prize-winning physicist Prof. Shuji Nakamura introduced two-component Metal-Organic Chemical Vapor Deposition (MOCVD) technology, a breakthrough for growing high-quality GaN [6].

Dye solar cells represent a low-cost, easy-to-produce third-generation solar cell technology with promising applications in certain markets, including wearable electronics and indoor and outdoor applications such as smart labels, posters and decorative tiles for building facades. However, the widespread adoption of dye-sensitized solar cells faces two key performance challenges: limited lifetime and low energy conversion efficiency. This project focuses on maximizing the power conversion efficiency of dye solar cells [7].

Despite the discovery of dye-sensitized solar cells several decades ago, improvement in power conversion efficiency has been slower compared to other solar cell technologies. Various methods have been introduced to improve the power conversion efficiency of dye-sensitized solar cells (DSSCs). The approach taken in this study involves the development of composite GaN-TiO_2 photoanode material. The hypothesis is that the distinctive physical and chemical properties of GaN and TiO_2 will synergistically contribute to the overall improved performance of dye-sensitized solar cells.

One of the predominant materials in DSSCi s titanium dioxide (TiO_2). TiO_2 is used as a photoelectrode in solar cells due to its resistance to UV-A radiation. TiO_2 has a large band gap on the order of 3–3.6 eV [8]. To improve the properties of TiO_2, structures are modified by adding impurities and various organic dyes on the surface to accelerate the charge transfer process. The electronic charge transfer properties in DSSC problems are influenced by crystal defects and structural porosity [9] material thickness [10], the efficiency of power conversion depends on charge transfer and recombination processes. There is an optimal film thickness parameter at which these two processes are most balanced. In the choice of the optimal thickness of TiO_2 to balance the processes of the electronic transition layer is given. The GaN material has a band gap of 3.4 eV and UV-A resistance. As we can see, they are in the same range as TiO_2 [11]. This suggests the possibility of sharing these materials [12].

Use of the GaN/TiO_2 structure in literature reviews indicates excellent performance as UV-activated oxygen sensors at room temperatures, but there is no information on use as a DSSC. In this regard, we assume that physical and chemical properties of GaN and TiO_2 will synergistically contribute to the overall improved performance of dye-sensitized solar cells.

2. Experimental process

2.1 Synthesis of GaN films

Plasma enhanced chemical vapor deposition (PECVD) system with comprising a 500 Watts R.F. plasma source, a 2” split tube furnace, a 4-channel precision mass flow meter with a gas mixer tank, an oil-less Pfeiffer High-Speed (226 L/min) vacuum pump, and a dual-zone furnace were used. The R.F. source's output power is adjustable within the range of 5-500 W with a stability of ±1. The plasma source operates at an RF frequency of 13.56 MHz with ±0.005% stability, and the reflection power can reach up to 200 Watts.

In the synthesis procedure, metallic Ga and powdered ammonium chloride served as the sources of Ga and N atoms, positioned at the entrance of a 20 mm diameter quartz tube with respect to gas flow. This tube was centrally aligned within the main furnace tube to enhance activation by the plasma. Pure nitrogen, with a flow rate of 20 ml/h, was employed as the carrier gas. A vacuum of $5x10^{-2}$ Torr was achieved inside the main tube using the furnace's vacuum pump. Substrates, consisting of sapphire and quartz glass, were positioned at varying distances from the plasma source after the source reagents in the high-temperature zone.

The oven followed a three-stage temperature gradient program, initially heating to 320 °C to prevent boiling of the ammonium chloride but to ensure its uniform evaporation. The oven was then gradually heated up for the actual deposition process and kept at 500 °C. When the set temperature was reached, the plasma source was activated at 120 W and the process was maintained for 2 hours. After the deposition process, the oven was gradually cooled and the substrates were subjected to further examination to determine the presence of heterostructures. Our methods are not complicated compared with this study [13].

2.2 Paste Formulation

The pastes for our dye-sensitized solar cells were made according to the recipe from Hee-Je Kim et al [14] formulated. In this phase of the project, we prepared four different pastes with different weight percentages of GaN in the TiO_2 matrix, in line with our research objectives. Additionally, a reference TiO_2 paste was created. The amounts of chemicals used in the formulation of TiO_2 and 10–40 wt% GaN/TiO_2 pastes are listed in Table 1, following established procedures in the literature [15].

The preparation process adhered to standard protocols. Initially, the measured GaN was ground on an alumina mortar for approximately 10 minutes, with the addition of 400 uL of ethanol during grinding. Grinding continued until a uniformly sized powder was achieved. Following GaN grinding, TiO_2 and polyvinylpyrrolidone (PVP) were incorporated as per the formulation, and the mixture underwent an additional 10 minutes of grinding. Acetyl acetone and ethanol were gradually introduced in specified quantities to prevent aggregation. Subsequently, acetic acid (99.9%) was added, followed by Triton X-100 as a dispersing agent and ethanol. If necessary, the prepared solution could be heated at 90 ºC for 10 minutes to enhance the viscosity of the resulting pastes.

Table 1. Composition of TiO_2, GaN and composite pastes for DSSCs.

Materials	10wt%GaN	20wt%GaN	30wt%GaN	40wt%GaN
Poly(vinylpyrrolidone) (g)	0.08	0.0432	0.0432	0.04
TiO_2 nanoparticles (g)	0.09	0.0432	0.0378	0.03
GaN (g)	0.01	0.0108	0.0162	0.02
Triton X-100 (mL)	0.2	0.108	0.108	0.1
Acetyl acetone (mL)	0.07	0.0324 (0.07)	0.0324 (0.07)	0.03 (0.07)
Acetic acid (mL)	0.07	0.0216 (0.07)	0.0216 (0.07)	0.02 (0.07)
Ethanol (mL)	1	0.54 (1)	0.54 (1)	1

2.3 DSSC construction

To fabricate dye-sensitized solar cells, fluorine-doped tin oxide (FTO) and Pt-coated glass substrates were subjected to a thorough cleaning process. This included a 10-minute ultrasonic bath in deionized water, followed by another 10-minute ultrasonic bath in ethanol. Subsequently, the FTO substrate with Pt coating was determined as a counter electrode after the cleaning process was completed. A Pt layer was then electrochemically deposited on this substrate at a potential of -0.5 V using an aqueous solution containing H_2PtCl_6 (10 mM) and KCl (10 mM) at room temperature. The deposition process took 5 minutes. The cleaned glasses were then air-dried for 5 minutes at ambient temperature.

Next, four different pastes were applied to the FTO-coated side of the glass plates using the squeegee method. A polymer film, specifically Meltonix 1170–25 (Solaronix, Switzerland), served as a spacer between the electrodes in the DSSC cell. To improve the contacts when measring the efficiency of DSSC cells, a tin layer was applied to the edges using the ultrasonic soldering station CS55–X151 (CHEERSONIC) with a frequency of 55 kHz and ECOSOLDER RMA98 SUPER as soldering material. This film effectively prevented short circuits between the electrodes.

After application and drying, the samples were sintered step by step in a muffle furnace (8.21100, Snol) at specific temperatures and durations: 325 °C – 5 minutes; 375 °C – 5 minutes; 450 °C – 15 minutes; 500 °C – 15 minutes. The sintered glass plates were then immersed in a 0.25 mM solution of the commercial ruthenium-based dye N719 for 24 hours. After this period of time, the dye-sensitized photoanodes were rinsed with ethanol and allowed to dry. After drying, 2 μL of an electrolyte consisting of 0.1 M LiI, 1.0 M 1,2-dimethyl-3-propylimidazolium iodide (DMPII), 0.12 M I2, and 0.5 M 4-TBP were applied to the surface of the sensitized films. The sequential steps to construct the dye-sensitized solar cell are shown in Figure 1.

.

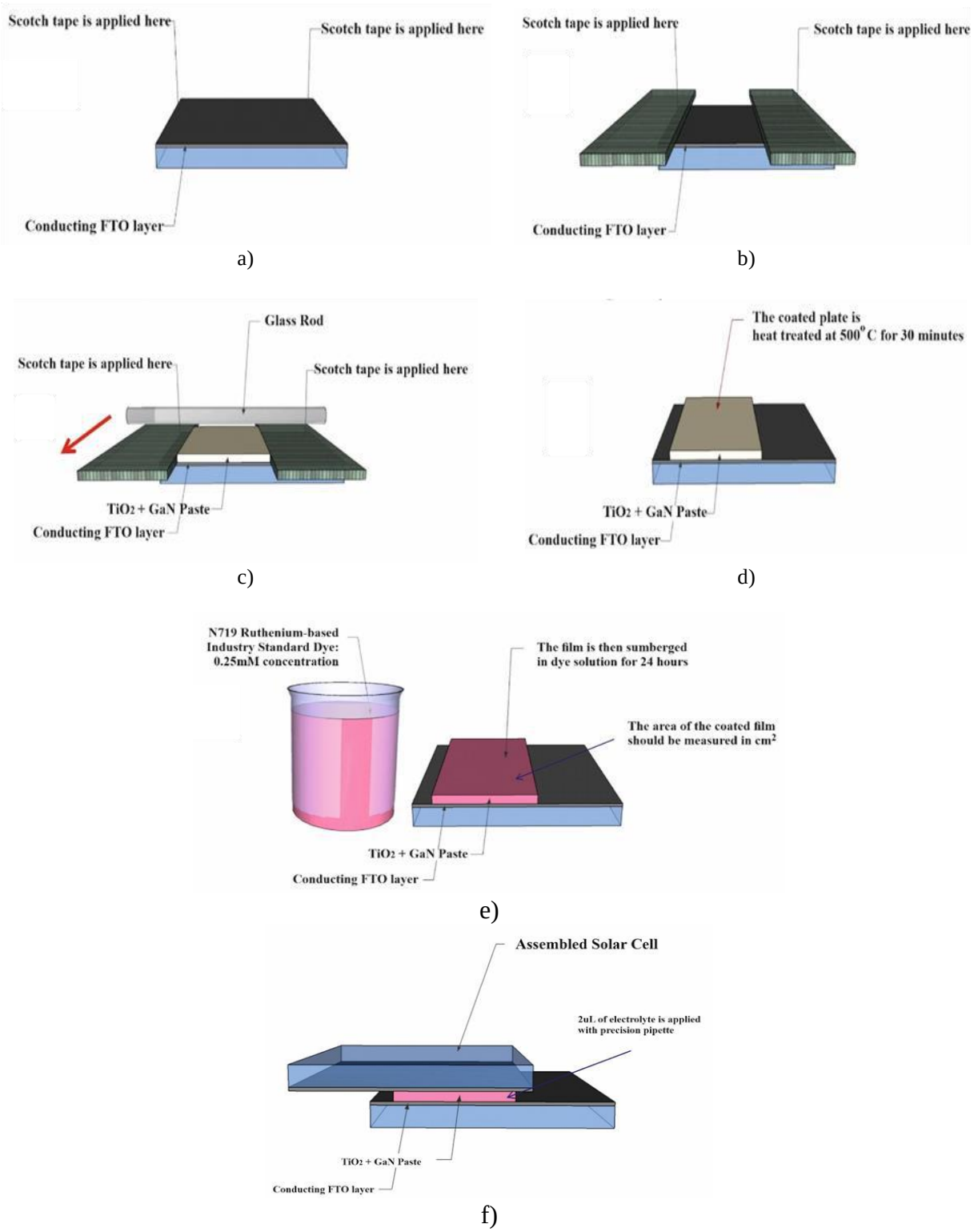

Fig.1. The graphical depiction of the sequential steps in assembling DSSCs.

3. Discussion of results

Surface analyzes of the sapphire and quartz substrates used in PECVD synthesis included scanning electron microscopy, Raman spectroscopy, and X-ray elemental analysis (EDX). According to the SEM results, GaN crystal structures in the form of different islands were observed on both types of substrates (Fig.2). These structures then expanded on the substrate surface and formed a continuous thin polycrystalline film, which is characteristic of Chemical Vapor Deposition **(**CVD) processes.

The results suggest that the deposition technology used, operating at relatively low temperatures with plasma enhancement, is effective in producing polycrystalline GaN structures[4]. The relatively low deposition rate is due to the selected temperature of 500 ºC and can be increased by increasing the temperature if necessary [16]. While the PECVD oven allows temperature increases of up to 1100 ºC, achieving such high temperatures requires additional adjustments to parameters such as gas flow rate, vacuum level and plasma source power [17]. Observations from SEM images indicate that a uniform thin film was not formed on the surfaces of the sapphire and quartz substrates, except for small scattered islands that islands were observed in a previous report [18, 19], as shown in Figure 2.

To confirm the absence of a uniform thin film, Raman spectroscopy analysis was performed (see Fig.3). The absence of GaN-specific peaks corresponding to the zone boundary phonons E1 (high) and A1 (LO) in the spectra confirms the absence of a uniform thin film on the surfaces of sapphire and quartz substrates.

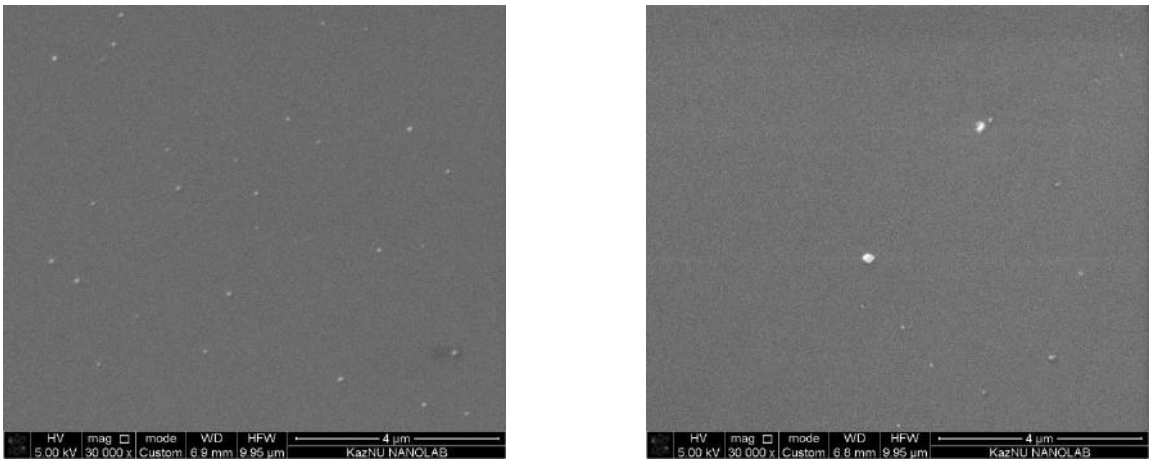

a) b)

Fig.2. The SEM images of GaN islands deposited on different substrates, where (a) Al_2O_3 and (b) SiO_2 substrates

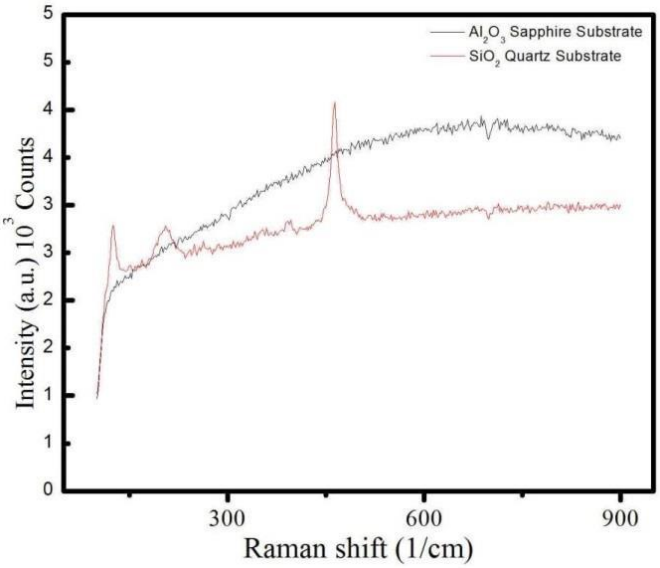

Fig.3. Raman spectra of Al_2O_3 sapphire and SiO_2 quartz substrate samples obtained from a PECVD reactor.

EDX spectroscopy was used to study the surface composition of the substrates, as shown in Figure 4. The chemical composition data of the substrate surfaces show that the ratio of Ga to N exceeds the stoichiometric ratio of GaN. This discrepancy arises from the condensation of Ga from chemical vapors at low temperature and low gas flow rate. The optimal conditions for higher purity GaN films include higher temperatures, a slower cooling rate, and an increased gas flow rate during the post-deposition phase.

.

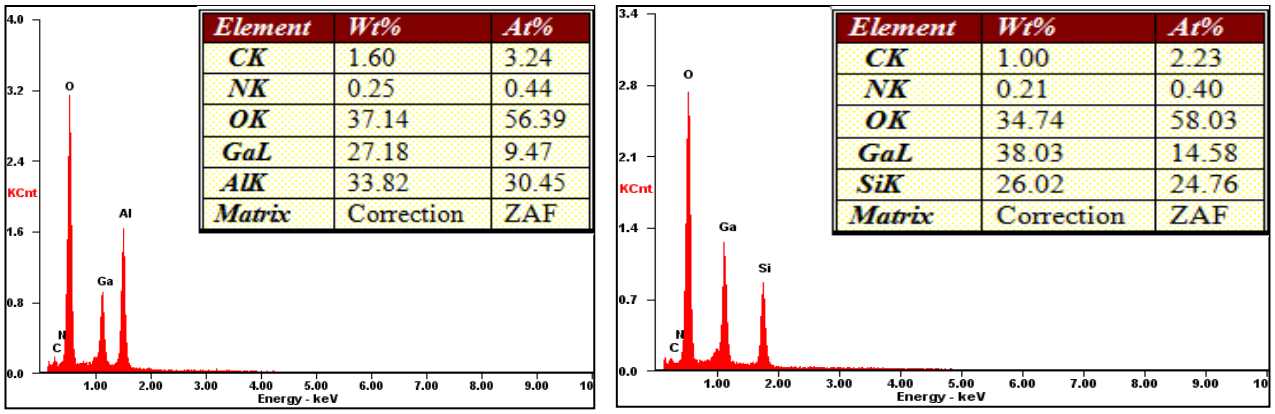

a) b)

Fig.4. EDX data of GaN samples deposited on (a) sapphire-Al_2O_3 and (b) quartz-SiO_2 substrates.

In addition to conducting characterization studies on samples prepared using the plasma-enhanced chemical vapor deposition method, we have expanded our research to investigate the influence of GaN powder in dye-sensitized solar cells. This extension of our work specifically focuses on studying how different amounts of GaN affect photovoltaic performance in mixed structure composite photoanodes. The results of the photovoltaic characterization of solar cells are listed in Table 2. The volt-ampere characteristics and efficiency were then adjusted using a solar simulator, the ST150AAA (PET PHOTO Emission TECH.), under AM 1.5 conditions with the power of the source determined at 100 mW/cm².

Table 2. The photovoltaic parameters of the DSSCs.

Samples	V_{oc} (mV)	I_{sc} (mA)	Fill Factor	Eficiency (%)	Active Area (cm^2)
TiO_2, Reference DSSC	598.60	1.853	0.63	1.76	0.40
10 wt% GaN/TiO_2, mixed DSSC	561.21	0.459	0.65	0.50	0.34
20 wt% GaN/TiO_2, mixed DSSC	656.96	1.049	0.62	0.75	0.58
30wt%GaN/TiO_2, mixed DSSC	591.51	1.148	0.59	0.72	0.60
40wt%GaN/TiO_2, mixed DSSC	491.87	0.480	0.57	0.25	0.55

Due to the time-consuming synthesis process and the limited availability of laboratory-synthesized GaN powder, we initially decided to use commercially available GaN powder. The aim was to determine the optimal weight fraction of GaN in the TiO_2 matrix, which could later be reproduced using GaN powders synthesized in the laboratory. When examining the fill factor (FF) values of the solar cells, it becomes clear that in a mixed structure the FF values decrease with increasing weight proportion of GaN in the TiO_2 matrix. FF values provide information about the level of internal resistance within the solar cell, suggesting that higher amounts of GaN lead to increased parasitic resistance [20].

Conversely, the behavior of the next photovoltaic parameter, power conversion efficiency, differs from FF. Power conversion efficiency starts to increase from 0.50 % for the 10 wt% GaN sample and reaches a maximum of 0.75% for the 20 wt% GaN sample, after which the value starts to decrease that confirmed in a previous report [21, 22]. Therefore, the results of the current experiments suggest that the optimal amount of GaN in the composite photoanode is 20 wt% and our results are consistent with this work [23].

The commercial GaN was analyzed using Raman spectroscopy, as shown in Figure 5. Raman spectroscopy analysis of commercial GaN shows the same three distinct peaks of phonon modes such as zone boundary, E2 (high, 572.81) and A1 (LO) observed in our laboratory synthesized GaN flakes. More E_2 (high) peaks were also found in this report as well [24, 25].

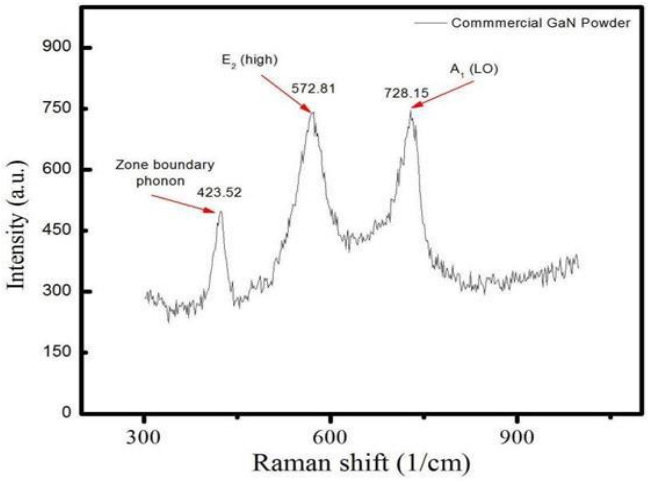

Fig. 5. Raman spectra of commercial GaN powder.

4. Conclusion

In summary, characterization studies were performed on GaN samples cultured on sapphire and quartz substrates. Elemental analysis revealed an excess of Ga on the substrate surfaces, indicating nonstoichiometric formation of GaN with abundant evaporation of liquid Ga at the synthesis temperature of 500 °C. To mitigate this, it is recommended to lower the deposition temperature and/or increase the RF power to improve the delivery of nitrogen-active species to the surface reaction sites and obtain a stoichiometric GaN thin film.

Results were demonstrated for the optimal weight fraction of GaN powder in a mixed photoanode structure. Different GaN weight fractions were incorporated into the TiO_2 matrix to determine the optimal power conversion efficiency of the mixed powder photoanode film. The most favorable result in terms of power conversion efficiency was observed with a GaN composition of 20 wt%, reaching a value of 0.75%. Conversely, the highest fill factor value was achieved with a GaN composition of 10 wt%. Through parameter adjustments, we identified the optimal conditions that resulted in high power conversion efficiencies and fill factor values.

Conflict of interest statement

The authors declare that they have no conflict of interest in relation to this research, whether financial, personal, authorship or otherwise, that could affect the research and its results presented in this paper.

CRediT author statement

Toktarbaiuly O.: Conceptualization, Methodology, Supervision; **Baisariyev M.:** Investigation, Writing; **Kaisha A.:** Investigation, Formal Analysis; **Duisebayev T.S.:** Writing - original draft; **Ibrayev N.Kh. and Serikov T.M.:** Review and Editing; **Ibraimov M.K. and Khaniyev B.A.:** Software and Analysis; **Tezekbay Y.Zh. and Zhambyl A. N.:** Investigation; **Nuraje N. and Sugurbekova** G.: Writing-Reviewing and Editing and Supervision. The final manuscript was read and approved by all authors.

Funding

This research was funded by the Science Committee of the Ministry of Science and Higher Education (MHES) of the Republic of Kazakhstan under Grant No. AP19678266.

Acknowledgments

The authors acknowledge the assistance from the Targeted Program of the MHES of the Republic of Kazakhstan, Grant No. BR21882439.

References

1 Hardin B.E., Snaith H.J., McGehee M.D. (2012) The renaissance of dye-sensitized solar cells. *Nature Photonics*, 6(3), 162–169. DOI: 10.1038/nphoton.2012.22.

.

2 Sharma K., Sharma V., Sharma S.S. (2018) Dye-sensitized solar cells: Fundamentals and current status. *Nanoscale Research Letters,* 13, Article 2760. DOI:10.1186/s11671-018-2760-6.

3 Abdullayev J.SH., Sapaev I.B. (2024) Optimizing the influence of doping and temperature on the electrophysical features of p-n and p-i-n junction structures. *Eurasian physical technical journal*, 21, 21-28. DOI:10.31489/2024No3/21-28.

4 Wei D. (2010) Dye sensitized solar cells. *International Journal of Molecular Sciences,* 11(3), 1103–1113. DOI:10.3390/ijms11031103.

5 Gong J., Sumathy K., Qiao Q., Zhou Z. (2017) Review on dye-sensitized solar cells (DSSCs): Advanced techniques and research trends. *Renewable and Sustainable Energy Reviews,* 68 (Part 1), 234–246. DOI:10.1016/j.rser.2016.09.097.

6 Nakamura S., Harada Y., Seno M. (1991) Novel metalorganic chemical vapor deposition system for GaN growth. *Applied Physics Letters,* 58(18), 2021–2023. DOI: 0.1063/1.105239.

7 Muñoz-García A.B., Benesperi I., Boschloo G., Concepcion J.J., Delcamp J.H., Gibson E.A., Meyer, Pavone M., Pettersson H., Hagfeldt A., Freitag M. (2021) Dye-sensitized solar cells strike back. *Chemical Society Reviews,* 50(22), 12450 – 12450. DOI: 10.1039/D0CS01336F.

8 Tian G.L., He H.B., Shao J.D. (2005) Effect of microstructure of TiO2 thin films on optical band gap energy. *Chinese Physics Letters,* 22(7), 1787–1790. DOI: 10.1088/0256-307X/22/7/062.

9 Serikov T.M., Ibrayev N.K., Nuraje N., Savilov S.V., Lunin V.V. (2017) Influence of surface properties of the titanium dioxide porous films on the characteristics of solar cells. *Russian Chemical Bulletin,* 66(4), 614–621. DOI:10.1007/s11172-017-1781-0.

10 Green M.L., Gusev E.P., Degraeve R., Garfunkel E.L. (2001) Ultrathin (<4 nm) SiO_2 and Si-O-N gate dielectric layers for silicon microelectronics: Understanding the processing, structure, and physical and electrical limits. *Journal of Applied Physics,* 90(5), 2057–2121. DOI: 10.1063/1.1385803.

11 Mukametkali T.M., Ilyassov B.R., Aimukhanov A.K., Serikov T.M., Baltabekov A.S., Aldasheva L.S., Zeinidenov A.K. (2023) Effect of the TiO_2 electron transport layer thickness on charge transfer processes in perovskite solar cells. *Physics B: Condensed Matter,* 659, Article 414784. DOI: 10.1016/j.physb.2023.414784.

12 Gong J., Liang J., Sumathy K. (2012) Review on dye-sensitized solar cells (DSSCs): Fundamental concepts and novel materials. *Renewable and Sustainable Energy Reviews,* 16(8), 5848–5860. DOI: 10.1016/j.rser.2012.04.044.

13 Fong C.Y., Ng S.S., Yam F.K., Abu Hassan, H., Hassan Z. (2015) Growth of GaN on sputtered GaN buffer layer via low cost and simplified sol-gel spin coating method. *Vacuum,* 119, 119–122. DOI:10.1016/j.vacuum.2015.04.042.

14 Liu H.L., Chen C.C., Chia C.T., Yeh C.C., Chen C.H., Yu M.Y., Keller S., DenBaars S.P. (2001) Infrared and Raman-scattering studies in single-crystalline GaN nanowires. *Chemical Physics Letters,* 345(3–4), 245–251. DOI:10.1016/S0009-2614(01)00858-2.

15 Zhang M., Wang Y., Teng F., Chen L., Li J., Zhou J., et al. (2016) A photoelectrochemical type self-powered ultraviolet photodetector based on GaN porous films. *Materials Letters,* 162, 117–120. DOI:10.1016/j.matlet.2015.10.001.

16 Beechem T., Christensen A., Graham S., Green D. (2008) Micro-Raman thermometry in the presence of complex stresses in GaN devices. *Journal of Applied Physics,* 103(12), Article 121. DOI: 10.1063/1.2940131.

17 Hassan Z., Lee Y.C., Yam F.K., Ibrahim K., Kordesch M.E., Halverson W., Colter P.C. (2005) Characteristics of low-temperature-grown GaN films on Si (111). *Solid State Communications,* 133(5), 283–287. DOI:10.1016/j.ssc.2004.11.022.

18 Dedkova A.A., Nikiforov M.O., Mitko S.V., Kireev V.Y. (2019) Investigation of gallium nitride island films on sapphire substrates via scanning electron microscopy and spectral ellipsometry. *Nanotechnologies in Russia,* 14(3–4), 176–183. DOI: 10.1134/S1995078019020046.

19 Mosconi E., Yum J.H., Kessler F., Gómez García C.J., Zuccaccia C., Cinti A., Nazeeruddin M.K., Grätzel M., De Angelis F.(2012) Cobalt electrolyte/dye interactions in dye-sensitized solar cells: A combined computational and experimental study. *Journal of the American Chemical Society,* 134(47), 19438–19453. DOI: 10.1021/ja3079016.

20 Lee Y.J., Lee M.H., Cheng C.M., Yang C.H. (2011) Enhanced conversion efficiency of InGaN multiple quanta well solar cells grown on a patterned sapphire substrate. *Applied Physics Letters,* 98(26), 1–4. DOI:10.1063/1.3585485.

21 Hagfeldt A., Boschloo G., Sun L., Kloo L., Pettersson H. (2010) Dye-sensitized solar cells. *Chemical Reviews,* 110(11), 6595–663. DOI: 10.1021/cr900356p.

22 Chiba Y., Islam A., Watanabe Y., Komiya R., Koide N., Han L. (2006) Dye-sensitized solar cells with conversion efficiency of 11.1%. *Japanese Journal of Applied Physics, Part 2: Letters,* 45(24–28), 23–26. DOI:10.1143/JJAP.45.L638.

23 Lidow A., Strydom J., Strittmatter R., Zhou C. (2015) GaN: A reliable future in power conversion dramatic performance improvements at a lower cost. *IEEE Power Electronics Magazine,* 2(1), 20–26. DOI:10.1109/MPEL.2014.2381457.

24 Robins L.H., Horneber E., Sanford N.A., Bertness K.A., Brubaker M.D., Schlager J.B. (2016) Raman spectroscopy, based measurements of carrier concentration in n-type GaN nanowires grown by plasma-assisted molecular beam epitaxy. *Journal of Applied Physics*, 120(12), 1–10. DOI: 10.1063/1.4963291.

25 Bagnall K.R., Moore E.A., Badescu S.C., Zhang L., Wang E.N. (2017) Simultaneous measurement of temperature, stress, and electric field in GaN HEMTs with micro-Raman spectroscopy. *Review of Scientific Instruments*, 88(11), 1–6. DOI: 10.1063/1.5010225.

AUTHORS' INFORMATION

Toktarbaiuly, Olzat – PhD, National Laboratory Astana, Nazarbayev University, Astana, Kazakhstan; https://orcid.org/0000-0003-4594-3435; olzat.toktarbaiuly@nu.edu.kz

Baisariyev, Murat K. – Master (Sci.), National Laboratory Astana, Nazarbayev University, Astana, Kazakhstan; https://orcid.org/0009-0001-9209-1768, murat.baisariyev@nu.edu.kz

Kaisha, Aitkazy – PhD, National Laboratory Astana, Nazarbayev University, Astana, Kazakhstan; https://orcid.org/0000-0001-7203-9842 ; kaishaa@tcd.ie

Duisebayev, Tolagay S. – Master (Sci.), Department of Physics and Technology, Al-Farabi Kazakh National University, Almaty, Kazakhstan; https://orcid.org/0000-0002-4992-0495; tola.d@yandex.ru

Ibrayev, Niyazbek Kh. – Doctor of Phys. and Math. Sciences, Professor, Director of the Institute of Molecular Nanophotonics, E.A. Buketov Karaganda University, Karaganda, Kazakhstan; Scopus Author ID: 9333698600; https://orcid.org/0000-0002-5156-5015; niazibrayev@mail.ru

Serikov, Timur M. – PhD, Associate Professor, E.A. Buketov Karaganda University, Karaganda, Kazakhstan; https://orcid.org/0000-0003-4302-96744; serikov-timur@mail.ru

Ibraimov, Margulan K. – PhD, Assosiate Professor, Al-Farabi Kazakh National University, Almaty, Kazakhstan; https://orcid.org/0000-0002-8049-3911; margulan.Ibraimov@kaznu.edu.kz

Khaniyev, Bakyt A. – PhD, Head of Department of Solid state and Nonlinear Physics, Al-Farabi Kazakh National University, Almaty, Kazakhstan; https://orcid.org/0000-0002-0103-9201; khaniyev.bakyt@gmail.com

Tezekbay, Yerbolat Zh. - Master (Sci.), Department of Physics and Technology, Al-Farabi Kazakh National University, Almaty, Kazakhstan; https://orcid.org/0000-0001-7479-6898; yerbolattezekbay@gmail.com

Zhambyl, Azamat Nurlanuly - Master (Sci.), Department of Physics and Technology, Al-Farabi Kazakh National University, Almaty, Kazakhstan; https://orcid.org/0009-0005-5340-3262; azamatzhambyl8@gmail.com

Nuraje, Nurxat – PhD, Associate Professor, Department of Chemical and Materials Engineering, School of Engineering and Digital Sciences, Head of laboratory "Renewable Energy", National Laboratory Astana, Nazarbayev University, Astana, Kazakhstan; https://orcid.org/0000-0002-4335-8905; nurxat.nuraje@nu.edu.kz

Sugurbekova, Gulnar K. – Doctor of Chemical Sciences, Department of Chemistry, Faculty of Natural Sciences, L.N. Gumilyov Eurasian National University, Astana, Kazakhstan; https://orcid.org/0000-0002-6894-7247; gulnar.sugurbekova@nu.edu.kz

EURASIAN PHYSICAL TECHNICAL JOURNAL

2024, Volume 21, No.4 (50)

https://doi.org/10.31489/2024No4/140-148

Received: 04/06/2024 Revised: 13/10/2024 Accepted: 20/12/2024 Published online: 25/12/2024

Original Research Article

UDC 537.533, 535.31

ANALYTICAL DESCRIPTION OF THE POTENTIAL OF ELECTROSTATIC MULTIPOLE SYSTEMS BASED ON A CONDUCTING CIRCULAR CYLINDER

Shugayeva T.Zh.[1], Spivak-Lavrov I.F.[1], Seiten A.B.[1*], Trubitsyn A.A.[2]

[1] Aktobe Regional University named after K. Zhubanov, Aktobe, Kazakhstan
[2] Ryazan State Radio Engineering University named after. V.F. Utkin, Ryazan, Russia
* *Corresponding author*: aizhanat_bolatovna@mail.ru

Abstract. *An urgent task of corpuscular optics and scientific instrumentation is the creation of new methods for calculating the physical and instrumental parameters of mass spectrometers. Leveraging the increased capabilities of computational technology, these methods provide a solid basis for the design and calculation of instruments with improved analytical capabilities. In this work, a method was developed for calculating the electrostatic field of multipole systems based on a conducting circular cylinder. This method uses the broad analytical capabilities of the theory of functions of a complex variable. Analytical expressions are found for the electrostatic field potential of a quadrupole system for the case of infinitely narrow gaps between the electrodes. Analytical expressions for the derivatives of the potential are also obtained. A study was carried out of the influence of the finite size of the gaps between the electrodes on the field configuration. For this purpose, numerical simulations of planar electric fields satisfying the Laplace equation were carried out. The calculation of the electrostatic field potential was carried out using the boundary element method in two stages. First, the distribution of electric charge at the boundary was calculated according to the known boundary potential distribution, that is, the "inverse" problem was solved. Then, using the found values of the charge distribution and the found potential values, the "direct" problem was solved. To solve this problem, a method was developed for solving integral equations with singular and quasi-singular kernels, which provides high accuracy in field calculations for electron-optical systems with rectilinear boundaries. The inaccuracies in the calculations resulted solely from rounding mistakes. In the case of an Equation of State electron-optical systems characterized by curved boundaries, the precision is dependent exclusively on how accurately the boundaries are represented using linear segments. For the purpose of segmenting the curved borders of the second-order electron-optical systems, these boundaries were broken down into arcs with an angular measurement not exceeding one degree.*

Keywords: multipole system, potential, conducting circular cylinder, equipotential lines, anti-resonance system.

1. Introduction

At present, quadrupole mass spectrometers are extensively utilized. This type of mass analyzer is categorized under anti-resonance mass spectrometers, where a portion of the ions is subjected to an electric field comprising both static and oscillating components as they navigate through. In this setup, some ions are able to traverse a specific field with a constrained oscillation amplitude, while the oscillation amplitude for the remaining ions escalates indefinitely over time, causing them to exit the beam [1,2]. The behavior of these charged particles is influenced by their mass-to-charge ratios, enabling the electric field to function as a mass

filter. Consequently, it selectively permits only those ions that possess a designated mass-to-charge ratio to pass through.

The main element of a quadrupole mass analyzer is a linear quadrupole, which is a structure of four cylindrical rods located parallel to each other. Direct and alternating radio frequency voltage is applied to the electrodes.

Quadrupole electrostatic fields are widely used in analytical instrumentation. Quadrupole, sextupole and octupole electrostatic systems are used to correct aberrations of electrostatic lenses and mirrors [3-5]. Quadrupole mass spectrometers, as well as various ion traps that use quadrupole fields, are now widespread. The linear ion trap was proposed by W. Paul in 1952, who was awarded the Nobel Prize in 1989 for these developments [6]. The linear ion trap essentially functions as a quadrupole mass spectrometer, differing primarily due to specific design modifications that allow for stable three-dimensional confinement of charged particles [6-9]. Presently, a variety of linear traps have emerged, including the ion surface trap [10], a microtrap designed for surface studies of a quantum processor [11], and a toroidal ion trap [12]. The fundamental principles of the quadrupole mass spectrometer remain unchanged, despite variations in the spatial configuration and alignment of the electrodes [13]. Furthermore, ion traps hold potential for application in the development of quantum computers [16].

2. Research method

As shown in Fig. 1., a quadrupole electrostatic field is created by setting the potential values $\pm V$ on the surface of a conducting circular cylinder of radius R. In what follows, we will measure linear dimensions in units of R. Thus, a boundary problem arises on the unit circle, the solution of which leads to the Poisson integral for the φ potential [17]:

$$\varphi(\rho,\psi)=\frac{1-\rho^2}{2\pi}\int_0^{2\pi}\frac{V(t)dt}{1+\rho^2-2\rho\cos(t-\psi)}\ . \tag{1}$$

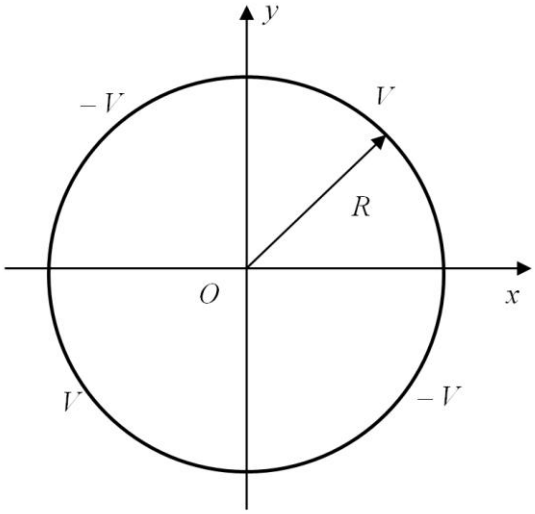

Fig.1. Quadrupole on a cylinder.

Here $V(t)$ – is the angular distribution of potential on the surface of the cylinder.

Let us transform expression (1) to the following form:

$$\varphi(\rho,\psi)=\frac{1-\rho^2}{2\pi}\int_0^{2\pi}\frac{V(t)dt}{1+\rho^2-2\rho(\cos t\cos\psi+\sin t\sin\psi)}\ . \tag{2}$$

To calculate integral (2) we use the following well-known formula:

$$\int\frac{dx}{a+b\cos x+c\sin x}=\frac{2}{\sqrt{a^2-(b^2+c^2)}}\operatorname{arctg}\frac{(a-b)\operatorname{tg}\frac{x}{2}+c}{\sqrt{a^2-(b^2+c^2)}}\ . \tag{3}$$

.

3. Results and discussion

Using formula (3), we write the following expression for potential (2):

$$\varphi(\rho,\psi)=\frac{V}{\pi}\operatorname{arctg}\frac{\left(1+\rho^2+2\rho\cos\psi\right)\operatorname{tg}\frac{t}{2}-2\rho\sin\psi}{1-\rho^2}\Bigg|_0^{\frac{\pi}{2}}-$$

$$-\frac{V}{\pi}\operatorname{arctg}\frac{\left(1+\rho^2+2\rho\cos\psi\right)\operatorname{tg}\frac{t}{2}-2\rho\sin\psi}{1-\rho^2}\Bigg|_{\frac{\pi}{2}}^{\pi^-}+$$

$$\frac{V}{\pi}\operatorname{arctg}\frac{\left(1+\rho^2+2\rho\cos\psi\right)\operatorname{tg}\frac{t}{2}-2\rho\sin\psi}{1-\rho^2}\Bigg|_{\pi^+}^{\frac{3\pi}{2}}-$$

$$-\frac{V}{\pi}\operatorname{arctg}\frac{\left(1+\rho^2+2\rho\cos\psi\right)\operatorname{tg}\frac{t}{2}-2\rho\sin\psi}{1-\rho^2}\Bigg|_{\frac{3\pi}{2}}^{2\pi}. \qquad (4)$$

In cartesian coordinates *x, y, z*, the found potential can be written as:

$$\varphi(x,y)=\frac{2V}{\pi}\left(\operatorname{arctg}\frac{1+\rho^2+2x-2y}{1-\rho^2}-\operatorname{arctg}\frac{1+\rho^2+2x+2y}{1-\rho^2}+\operatorname{arctg}\frac{2y}{1-\rho^2}\right). \qquad (5)$$

Here $\rho=\sqrt{x^2+y^2}$. It is easy to check that, as one would expect, the potential vanishes on the coordinate axes $\varphi(x,0)=\varphi(0,y)=0$. Differentiating expression (3), we find the derivatives of the potential:

$$\frac{\partial\varphi}{\partial x}=\frac{2V}{\pi}\left\{\frac{2\left(1-\rho^2\right)+4x\left(1+x-y\right)}{\left(1-\rho^2\right)^2+\left[1+\rho^2+2\left(x-y\right)\right]^2}-\frac{2\left(1-\rho^2\right)+4x\left(1+x+y\right)}{\left(1-\rho^2\right)^2+\left[1+\rho^2+2\left(x+y\right)\right]^2}+\right.$$

$$\left.+\frac{4xy}{\left(1-\rho^2\right)^2+4y^2}\right\}=V\,f_1(x,y). \qquad (6)$$

$$\frac{\partial\varphi}{\partial y}=\frac{2V}{\pi}\left\{\frac{-2\left(1-\rho^2\right)+4y\left(1+x-y\right)}{\left(1-\rho^2\right)^2+\left[1+\rho^2+2\left(x-y\right)\right]^2}-\frac{2\left(1-\rho^2\right)+4y\left(1+x+y\right)}{\left(1-\rho^2\right)^2+\left[1+\rho^2+2\left(x+y\right)\right]^2}+\right.$$

$$\left.+\frac{2\left(1-\rho^2+2y^2\right)}{\left(1-\rho^2\right)^2+4y^2}\right\}=V\,f_2(x,y). \qquad (7)$$

The derived formulas also characterize the monopole field generated by a segment of a cylindrical electrode at a specific potential, alongside two perpendicular half-planes, xz and yz, which maintain a potential of zero. Figure 2 illustrates the monopole field, depicting equipotential lines at potentials of 0.1V, 0.2V, …, up to 0.9V. These equipotential lines were obtained through the numerical integration of differential equations.

Equipotential lines were found by numerical integration of differential equations:

$$\frac{dy}{dx}=-\frac{\partial\varphi}{\partial x}\Big/\frac{\partial\varphi}{\partial y}\qquad \frac{dx}{dy}=-\frac{\partial\varphi}{\partial y}\Big/\frac{\partial\varphi}{\partial x}. \qquad (8)$$

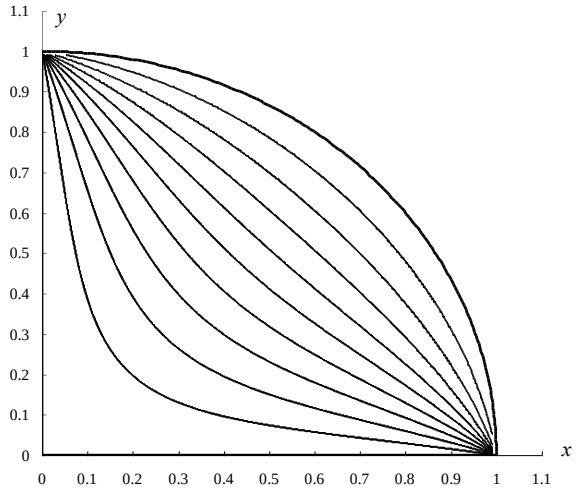

Fig.2. Picture of equipotentials of the field of a cylindrical monopole.

The initial conditions for equations (8) were set on the straight line $y = x$ and according to formula (5) such values were found at which the potential takes the values 0.1 V, 0.2 V, ..., 0.9V. These x values are shown below in Table 1.

Table 1. Values of the x coordinate of equipotential lines on the straight line $y = x$.

φ/V	0.1	0.2	0.3	0.4	0.5	0.6	0.7	0.8	0.9
$x = y$	0.19840	0.28143	0.34648	0.40307	0.45510	0.50475	0.55354	0.60274	0.65348

Using formula (3), we write the following expression for the potential of the sextupole system:

$$\varphi(\rho,\psi)=\frac{V}{\pi}\operatorname{arctg}\frac{\left(1+\rho^2+2\rho\cos\psi\right)\operatorname{tg}\frac{t}{2}-2\rho\sin\psi}{1-\rho^2}\Bigg|_0^{\frac{\pi}{3}}-$$

$$-\frac{V}{\pi}\operatorname{arctg}\frac{\left(1+\rho^2+2\rho\cos\psi\right)\operatorname{tg}\frac{t}{2}-2\rho\sin\psi}{1-\rho^2}\Bigg|_{\frac{\pi}{3}}^{\frac{2\pi}{3}}+$$

$$+\frac{V}{\pi}\operatorname{arctg}\frac{\left(1+\rho^2+2\rho\cos\psi\right)\operatorname{tg}\frac{t}{2}-2\rho\sin\psi}{1-\rho^2}\Bigg|_{\frac{2\pi}{3}}^{\pi}+\ldots\cdot \tag{9}$$

In Cartesian coordinates x, y, z, the found potential can be written as:

$$\varphi(x,y)=\frac{2V}{\pi}\left(\operatorname{arctg}\frac{2y}{1-\rho^2}+\operatorname{arctg}\frac{\left(1+\rho^2+2x\right)\frac{1}{\sqrt{3}}-2y}{1-\rho^2}-\operatorname{arctg}\frac{\left(1+\rho^2+2x\right)\sqrt{3}-2y}{1-\rho^2}+\right.$$

.

$$-\operatorname{arctg}\frac{\left(1+\rho^2+2x\right)\frac{1}{\sqrt{3}}+2y}{1-\rho^2}+\operatorname{arctg}\frac{\left(1+\rho^2+2x\right)\sqrt{3}+2y}{1-\rho^2}\Bigg). \tag{10}$$

It is easy to check that on the *x* coordinate axis the potential becomes zero $\varphi(x,0)=0$. Now let's find the derivatives of the potential:

$$\frac{\partial\varphi}{\partial x}=\frac{2V}{\pi}\Bigg\{\frac{4xy}{\left(1-\rho^2\right)^2+y^2}+\frac{2\left[(x+1)\frac{1}{\sqrt{3}}\left(1-\rho^2\right)+x\left(1+\rho^2+2x\right)\frac{1}{\sqrt{3}}-2xy\right]}{\left(1-\rho^2\right)^2+\left[\left(1+\rho^2+2x\right)\frac{1}{\sqrt{3}}-2y\right]^2}-$$

$$-\frac{2\left[(x+1)\frac{1}{\sqrt{3}}\left(1-\rho^2\right)+x\left(1+\rho^2+2x\right)\frac{1}{\sqrt{3}}+2xy\right]}{\left(1-\rho^2\right)^2+\left[\left(1+\rho^2+2x\right)\frac{1}{\sqrt{3}}+2y\right]^2}+$$

$$-\frac{2\left[(x+1)\sqrt{3}\left(1-\rho^2\right)+x\left(1+\rho^2+2x\right)\sqrt{3}-2xy\right]}{\left(1-\rho^2\right)^2+\left[\left(1+\rho^2+2x\right)\sqrt{3}-2y\right]^2}+$$

$$+\frac{2\left[(x+1)\sqrt{3}\left(1-\rho^2\right)+x\left(1+\rho^2+2x\right)\sqrt{3}+2xy\right]}{\left(1-\rho^2\right)^2+\left[\left(1+\rho^2+2x\right)\sqrt{3}+2y\right]^2}\Bigg\}=V\,f_1(x,y), \tag{11}$$

$$\frac{\partial\varphi}{\partial y}=\frac{2V}{\pi}\Bigg\{\frac{2\left(1-\rho^2+2y^2\right)}{\left(1-\rho^2\right)^2+4y^2}+\frac{2\left[\left(1-\rho^2\right)\left(\frac{y}{\sqrt{3}}-1\right)+\left(1+\rho^2+2x\right)\frac{y}{\sqrt{3}}-2y^2\right]}{\left(1-\rho^2\right)^2+\left[\left(1+\rho^2+2x\right)\frac{1}{\sqrt{3}}-2y\right]^2}-$$

$$-\frac{2\left[\left(1-\rho^2\right)\left(\frac{y}{\sqrt{3}}+1\right)+\left(1+\rho^2+2x\right)\frac{y}{\sqrt{3}}+2y^2\right]}{\left(1-\rho^2\right)^2+\left[\left(1+\rho^2+2x\right)\frac{1}{\sqrt{3}}+2y\right]^2}-$$

$$-\frac{2\left[\left(1-\rho^2\right)\left(y\sqrt{3}-1\right)+\left(1+\rho^2+2x\right)y\sqrt{3}-2y^2\right]}{\left(1-\rho^2\right)^2+\left[\left(1+\rho^2+2x\right)\sqrt{3}-2y\right]^2}-$$

$$+\frac{2\left[\left(1-\rho^2\right)\left(y\sqrt{3}+1\right)+\left(1+\rho^2+2x\right)y\sqrt{3}+2y^2\right]}{\left(1-\rho^2\right)^2+\left[\left(1+\rho^2+2x\right)\sqrt{3}+2y\right]^2}\Bigg\}=V\,f_2(x,y). \tag{12}$$

We find equipotential lines by numerical integration of differential equations:

$$\frac{dy}{dx}=-\frac{\partial\varphi}{\partial x}\Big/\frac{\partial\varphi}{\partial y},\qquad \frac{dx}{dy}=-\frac{\partial\varphi}{\partial y}\Big/\frac{\partial\varphi}{\partial x}. \tag{13}$$

Table 2. values of the y coordinate equipotential lines on the axis at $x=0$.

φ/V	0.1	0.2	0.3	0.4	0.5	0.6	0.7	0.8	0.9
y/R	0.4285433	0.5410501	0.6215145	0.6874778	0.7454322	0.7987091	0.8493886	0.8989876	0.9487817

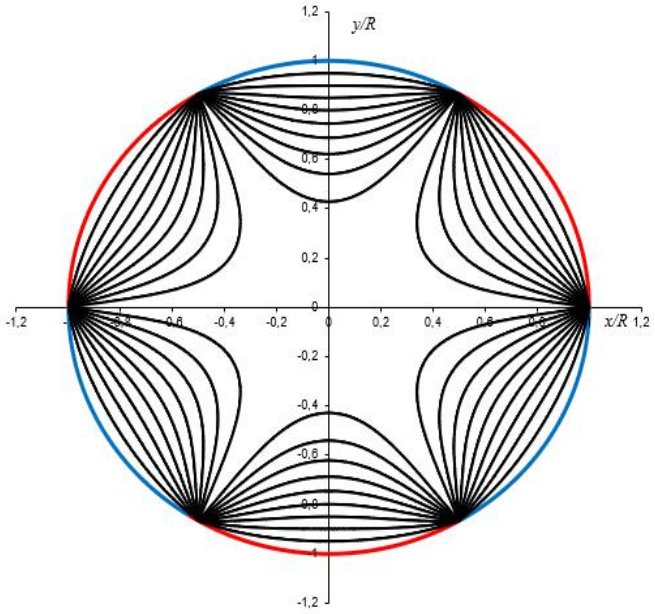

Fig.3. Picture of equipotentials of the field of a cylindrical sextupole.

To confirm the adequacy of the analytical expressions for calculating the electrostatic field proposed in [18], numerical methods for modeling planar electric fields using the boundary element method were used [19].

To tackle the problem numerically, we convert the integral equation that relates the potentials of simple and double layers into a discrete format. This involves dividing the boundary Γ into N boundary elements Γj. By assuming that the potential remains constant along each circuit (electrode) and that the normal derivative of the potential is constant across each boundary element, we can express the integral equation in the following manner:

$$u(\xi)+\sum_{j=1}^{N}u_j H_j(\xi)=\sum_{j=1}^{N}q_j F_j(\xi), \qquad (14)$$

where $\xi\in G\cup\Gamma$ and $\gamma=\pi$ at $\xi\in$G for two-dimensional tasks, $\gamma=2\pi$ at $\xi\in\Gamma$ and $\gamma=4\pi$ at $\xi\in$G for three-dimensional tasks, and the functions $F_j(\xi)$ and $H_j(\xi)$ represent integrals of the fundamental solution and the normal derivative of the fundamental solution of the Laplace equation, respectively [18]. In typical scenarios, these can be computed using standard Gaussian quadrature methods.

The computation of the electrostatic field occurs in two phases. Initially, the unknown vector q_j is derived from the known boundary distribution of the potential $u(\xi\in\Gamma)$ by employing equation (14), effectively addressing the "inverse" problem. Following this, the obtained values of q_j alongside the given u_j are utilized to compute the function $u(\xi)$, for $\xi\in\Omega$ using equation (9), there by resolving the "direct" problem. The author's approach to tackling both inverse and direct problems, as well as the methods for calculating integrals featuring singular and quasi-singular kernels, is thoroughly outlined in the monograph [21].

Figure 4 shows the color-coded potential distribution in the internal region of an antiresonant quadrupole system based on a circular conducting cylinder, obtained using the specified numerical technique.

.

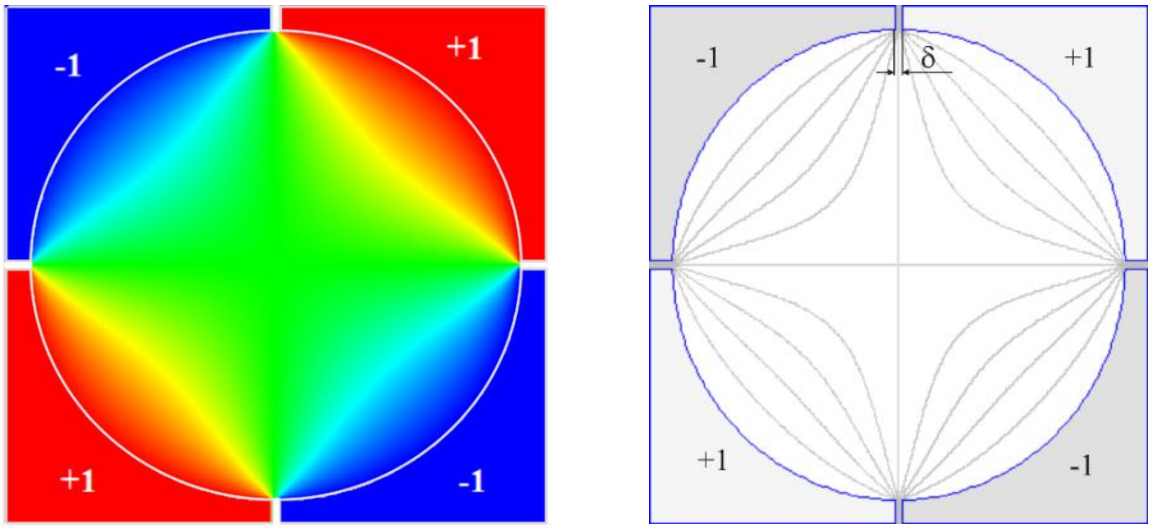

(a) (b)

Fig.4. Two-dimensional potential distribution in a quadrupole system:
a) color coded, b) equipotential lines.

The techniques introduced by the authors [21] for computing integrals in equation (9) involving singular and quasi-singular kernels ensure a high degree of modeling precision. In electron-optical systems (EOS) with straight boundaries, the calculation error is primarily influenced by rounding errors, while for systems with curved boundaries, it is affected by the precision of approximating the boundary using straight line segments. When segmenting the second-order geometric curves that define the electron-optical systems (EOS) into arcs with a 1° angular increment and approximating these arcs with straight line segments in test scenarios-like a cylindrical capacitor or a quadrupole mass filter featuring hyperbolic electrodes, for which analytical solutions exist-the resulting potential calculation error is found to be no greater than 10^{-3} %.

For the modeled anti-resonance system, when the insulating gap between the electrodes is small and does not exceed the value δ/R=0.1%, the values of the potentials calculated numerically by the boundary element method and by analytical formulas obtained in [18] and in which δ/R=0, also coincide within the error limits of the specified value of 10^{-3} %.

An important fact is the impact of the dimensions of the insulating gap on the deviation of potentials in a quadrupole system from analytically calculated ones, which should be taken into account in the manufacture of real devices. Table 3 presents the results of calculations of potentials along a vertical line located at a certain distance from the origin, which is located at the center of symmetry of the system.

Table 3. Dependence of the potential value in a quadrupole system on *y* at *x/R*=0.1

y/R	0.9	0.8	0.7	0.6	0.5	0.4	0.3	0.2	0.1
δ/*R*=0	0,529976	0,322127	0,22747	0,172661	0,134517	0,103957	0,076791	0,050948	0.025461
δ/*R*=0.2%	0.530	0.3221	0.22747	0.17267	0.13452	0.103965	0.07680	0.050959	0.025474
δ/*R*=3.5%	0.528	0.3216	0.22726	0.17257	0.13446	0.103922	0.07677	0.050928	0.025446
δ/*R*=10%	0.514	0.3173	0.22572	0.17187	0.13408	0.103683	0.07660	0.050822	0.025388

From the analysis of the table data, we can conclude that as we move away from the center and approach the cylindrical boundary of the quadrupole system, the deviation of the potential from the analytical value increases and can exceed 1% with a gap width δ/R=10%; while in the region adjacent to the center of symmetry and which is the working region of the system, the potential deviation does not exceed 0.01%.

4. Conclusion

Using TFCV methods, analytical expressions were obtained for the electrostatic potential of multipole systems based on a conducting circular cylinder for the case of infinitely narrow gaps between the electrodes. In the considered multipole systems based on a conducting circular cylinder, there is no need to use conducting rods to create a multipole field. The ion beam will move unhindered along the cylinder axis. In this case, we will localize the edge fields using grounded screens at the limits of the system.

The obtained analytical expressions describing the potential distribution in an antiresonance multipole system based on a circular conducting cylinder were tested, and the correctness of the results obtained was confirmed by numerical modeling of the electric field using the boundary element method. The influence of the width of the insulating gap between the electrodes on the magnitude of the potential and on its deviation from the "ideal" one, analytically calculated for the case of an infinitely narrow electrode, has been studied.

Conflict of interest statement

The authors declare that they have no conflict of interest in relation to this research, whether financial, personal, authorship or otherwise, that could affect the research and its results presented in this paper.

CRediT author statement

Spivak-Lavrov I: Conceptualization, Methodology, Supervision ; **Shugayeva T.:** Investigation, Formal Analysis, Writing-Reviewing and Editing ; **Seiten A.:** Writing - original draft, Review and Editing; **Trubitsyn A.:** Software and Analysis. The final manuscript was read and approved by all authors.

Funding

The work was carried out within the framework of a project with grant funding from the Ministry of Science and Higher Education of the Republic of Kazakhstan (AR22685992)

The work was performed as part of the state assignment of the Ministry of Science and Higher Education of the Russian Federation (FSSN-2024-0001)

References

1. Kambarova Z. (2023) Expansion of the functional capacities of electrostatic mirror analyzers for electron spectroscopy. *Eastern-European Journal of Enterprise Technologies*, 5(5(125)), 53–61. DOI: 10.15587/1729-4061.2023.289781.

2. Saulebekov A.O., Kambarova Zh.T., Omarova G.S. (2023) Miniature highly sensitive electron spectrometer for the analysis of corpuscular fluxes. *Eurasian Physical Technical Journal*, 20(2-44), 112–117. DOI: 10.31489/2023NO2/112-117.

3. Preikszas D., Rose H. (1997) Correction properties of electron lenses and mirrors. *Electron microscopy*, 46, 1, 1–9. DOI: 10.1093/oxfordjournals.jmicro.a023484.

4. Szilagyi M. (1990) *Electronic and ion optics*. Moscow, Mir, 639 p. Available at: https://www.libex.ru/detail/book491431.html [in Russian]

5. Hawkes P.W., Spence J.C.H. (2019) *Springer Handbook of Microscopy*, Springer Handbooks, Springer Nature Switzerland AG, 1543 p. DOI: 10.107/978-3-030-00069-1.

6. Paul V. (1990) Electromagnetic traps for charged and neutral particles. *UFN*, 60, 12, 109–127. DOI: 10.3367/UFNr.0160.199012d.0109.

7. Douglas D.J., Frank A.J., Mao D.M. (2005) Linear ion traps in mass spectrometry. *Mass Spectrom. Rev.*, 24 (1), 1–29. DOI: 10.1002/mas.20004.

8. Hager J.W. (2002) A new linear ion trap mass spectrometer. *Rapid Commun. Mass Spectrom.*, 16, 512–526. DOI: 10.1002/rcm.607.

9. March R.E, Todd J.F.J. (2005) *Quadrupole Ion Trap Mass Spectrometry*. Ed. by J.D. Winefordner. Vol. 165., P. 1–78. DOI: 10.1002/0471717983

10. Qiao H., Gao C., Mao D., Konenkov N., Douglas D.J. (2011) Spacecharge effects with mass selective axial ejection from a linear quadrupole ion trap. *Rapid Commun. Mass Spectrom.*, 25, 3509–3520. DOI: 10.1002/rcm.5255.

11. Amini J.M., Britton J., Leibfried D., Wineland D.J. (2011) Microfabricated Chip Traps for Ions Atom Chips. Ed. by J. Reichel, V. Vuletic WILEY-VCH Verlag GmbH & Co.´KGaA, Weinheim. DOI: 10.48550/arXiv.0812.3907.

12. Douglas D.J., Konenkov N.V.(2012) Ion Cloud Model for a Linear Quadrupole Ion Trap. *Euro. J. Mass Spectrom.*, 18, 419–429. DOI: 10.1255/ejms.1200.

13. Douglas D.J., Berdnikov A.S., Konenkov N.V. (2015) The effective potential for ion motion in a radio frequency quadrupole field revisited. *Int. J. Mass Spectrom.*, 377, 345–354. DOI:10.1016/j.ijms.2014.08.009.

14. Rozhdestvensky Yu.V., Rudy S.S. (2017) Linear ion trap with a deterministic voltage of a general form. *Technical Physics*, 87, 4, 625–632. DOI: 10.1134/s1063784217040259.

15. Dawson R.H. (1976) *Quadrupole Mass Spectrometry and its Application*, Amsterdam: Elsevier, 1976. Available at: Quadrupole Mass Spectrometry and Its Applications - 1st Edition | Elsevier Shop

.

16. Baumeester D., Eckert A., Zeilinger A. (2002) *Physics of quantum information*, Moscow: Postmarket, 375 p. Available at: https://www.amazon.com/Physics-Quantum-Information-Cryptography-Teleportation/dp/3540667784

17. Lavrentiev M.A., Shabat B.V. *(*1976) *Methods of the theory of functions of a complex variable*, Moscow: Nauka, 716 p. Available at: https://lib.ysu.am/open_books/93130.pdf

18. Spivak-Lavrov I.F., Shugaeva T.Zh., Seiten A.B. (2023) Anti-resonance quadrupole system based on a circular conducting cylinder. Recent Contributions to Physics, №4 (87), 23-29. DOI:10.26577/RCPh.2023.v87.i4.03. [in Russian]

19. Cheng A. H.-D., Cheng D.T. (2005) Heritage and early history of the boundary element method. *Engineering Analysis with Boundary Elements*, 29, 268–302. DOI: 10.1016/j.enganabound.2004.12.001.

20. Brebbia C.A., Telles J.C.F., Wrobel L.C. (2012) *Boundary Element Techniques: Theory and Applications in Engineering*, London: Springer, 464 p.

21. Gurov V.S., Saulebekov A.O., Trubitsyn A.A. (2015) *Analytical, Approximate-Analytical and Numerical Methods in the Design of Energy Analyzers*, Advances in Imaging and Electron Physics, ed. Peter W. Hawkes, Vol. 192, AIEP, UK: Academic Press, 209 p. DOI: 10.1016/S1076-5670(15)00103-2.

AUTHORS' INFORMATION

Shugayeva, Tilektes Zh. – PhD, K. Zhubanov Aktobe Regional University, Aktobe, Kazakhstan; https://orcid.org/0000-0002-4797-4529; tlektes.tleubaeva@gmail.com

Spivak-Lavrov, Igor F. – Doctor of Physical and Mathematical Sciences, Professor, K. Zhubanov Aktobe Regional University, Aktobe, Kazakhstan; https://orcid.org/0000-0001-6235-3897; spivakif@rambler.ru

Seiten, Aizhanat B. – PhD student, K. Zhubanov Aktobe Regional University, Aktobe, Kazakhstan; https://orcid.org/0009-0001-5530-1658; aizhanat_bolatovna@mail.ru

Trubitsyn, Andrey A. – Doctor of Physical and Mathematical Sciences, Professor; Ryazan State Radio Engineering University; Ryazan; Russia; https://orcid.org/0000-0002-9337-8947; assur@bk.ru

EURASIAN PHYSICAL TECHNICAL JOURNAL

2024, Volume 21, No. 4 (50)

https://doi.org/10.31489/2024No4/149-157

Received: 28/08/2024 Revised: 14/11/2024 Accepted: 20/12/2024 Published online: 25/12/2024

Original Research Article

UDC 537.533.3; 537.534.3

INFLUENCE OF THE INTERELECTRODE GAP WIDTH ON THE QUALITY OF FOCUSING OF ELECTROSTATIC MIRRORS WITH ROTATIONAL SYMMETRY

Bimurzaev S.B. *, Sautbekova Z.S.

G. Daukeev Almaty University of Power Engineering and Telecommunication, Almaty, Kazakhstan
**Corresponding author:* bimurzaev@mail.ru

Abstract. *The influence of the width of the interelectrode gap on the focusing quality of electrostatic mirrors with rotational symmetry, the electrodes of which are coaxial cylinders of equal diameter separated by gaps of finite width, has been studied. Formulas, convenient for the numerical calculation of the exact values of the axial potential distribution in such mirrors, are proposed. Using the obtained formulas in numerical calculations and taking into account the width of the interelectrode gap, the geometric and electrical parameters of two- and three-electrode mirrors were determined, which provide spatial focusing of beams of charged particles simultaneously with the elimination of time-of-flight chromatic aberrations and spherical and axial chromatic spatial aberrations, the most important factors in terms of influence on the resolution of time-of-flight mass spectrometers and electron microscopes. It is shown that the width of the interelectrode gap has a significant effect on the quality of focusing of electrostatic mirrors with cylindrical electrodes.*

Keywords: time-of-flight mass spectrometer, electron microscope, electrostatic mirror, space-time-of-flight focusing, spherical aberration, axial chromatic aberration.

1. Introduction

Electrostatic mirrors are the most important structural elements of modern time-of-flight reflector-type mass spectrometers [1-5] and electron microscopes [6-14], performing the roles of an ion reflector and an aberration corrector, respectively. The resolution and sensitivity of such devices largely depend on the focusing quality of such mirrors. In this regard, electrostatic mirrors formed by fields with rotational symmetry are of particular interest. Such fields, which play the role of centered electron-optical focusing systems with respect to charged particles, are capable of creating a correct electron-optical image of an object. However, the most studied and widely used designs of such mirrors for practical implementation are sets of coaxial circular cylinders. The advantage of cylindrical electrodes is the ability to shield a beam of charged particles from scattered electric fields.

In [5, 12-14], where the quality of focusing of electrostatic mirrors with cylindrical electrodes was studied, the calculation of the axial potential distribution was performed using exact formulas under the assumption that the width of the interelectrode gap is infinitely small. However, the practical use of such mirrors places high demands on the accuracy of determining the geometric and electrical parameters, taking into account the width of the interelectrode gap, which ensures the quality of focusing in devices with high

resolution. In addition, high requirements for the width of the interelectrode gap are necessary to ensure electrostatic strength at high field strengths.

It is well known that the quality of focusing is determined by aberrations – distortions in the image of an object caused by various reasons. One of the main tasks of charged particle optics is to identify the types of aberrations inherent in a given system, and then eliminate or reduce the most important ones. In this regard, electrostatic mirrors with cylindrical electrodes have unique properties: firstly, they can provide spatial focusing of beams of charged particles simultaneously with time-of-flight energy focusing [5], i.e., eliminate time-of-flight chromatic aberrations that limit the resolution of time-of-flight mass spectrometers; secondly, they can be free from spherical and axial chromatic aberrations simultaneously [12-14] or act as a corrector for these aberrations [12], which are the main factors limiting the resolution of electron microscopes.

The aim of this work is to study the influence of the width of the interelectrode gap on the quality of focusing of two- and three-electrode mirrors with rotational symmetry, the electrodes of which are made in the form of coaxial cylinders of equal diameter, separated by gaps of finite width.

2. Two-electrode mirror with space-time focusing

2.1. Axial potential distribution of a two-electrode mirror

Figure 1 shows a schematic diagram of a two-electrode mirror, the electrodes of which are coaxial cylinders of equal diameter d separated by a gap of finite width.

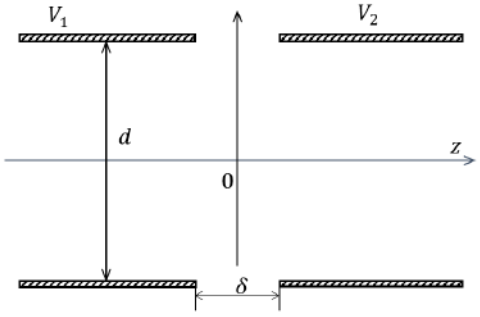

V_1, V_2 are potentials on the electrodes; d is the cylinder diameter; δ is the gap width between electrodes

Fig.1. Two-electrode electrostatic mirror.

The potential distribution along the optical axis z of such a mirror can be written in the form

$$\Phi(z) = \frac{1}{2}(V_1 + V_2) + (V_2 - V_1)U(z). \quad (1)$$

Here V_1 and V_2 are potentials at the mirror electrodes, and $U(z)$ is a function described by the exact expression [15]:

$$U(z) = \frac{1}{\pi}\int_0^\infty \frac{\sin(kz)}{k}\frac{\sin(k\delta/R)}{k\delta/R}\frac{dk}{I_0(k)}, \quad (2)$$

where $I_0(k)$ is a modified Bessel function of the first kind of zero order, and R is the radius of the cylindrical electrode. To avoid the difficulties that arise when calculating integral (2) due to its weak convergence, we transformed it into a form convenient for calculations.

To simplify the notation, we will further use $R = 1$, i.e. all linear dimensions will be measured in cylinder radii. Then

$$U(z) = \frac{1}{\pi}\int_0^\infty \frac{\sin(kz)}{k}\frac{\sin(k\delta)}{k\delta}\frac{dk}{I_0(k)}. \quad (3)$$

Let us rewrite (3), writing out the product of sines:

$$U(z) = \frac{1}{2\delta}(U_1 + U_2), \quad (4)$$

where

$$U_1 = \frac{1}{\pi}\int_0^\infty \frac{\cos k(z-\delta)}{k^2}\frac{dk}{I_0(k)}, \tag{5}$$

$$U_2 = -\frac{1}{\pi}\int_0^\infty \frac{\cos k(z+\delta)}{k^2}\frac{dk}{I_0(k)}. \tag{6}$$

Taking into account the parity of the integrand, and also having written the cosine, we rewrite (5) in the form

$$U_1(z) = \frac{1}{4\pi}\left[\int_{-\infty}^\infty \frac{\exp\left[ik(z-\delta)\right]}{k^2}\frac{dk}{I_0(k)} + \int_{-\infty}^\infty \frac{\exp\left[-ik(z-\delta)\right]}{k^2}\frac{dk}{I_0(k)}\right]. \tag{7}$$

It is convenient to calculate integral (7) can using contour integrals:

$$U_1(z) = \frac{1}{4\pi}\int_{\Gamma_+} \frac{\exp\left[ik(z-\delta)\right]}{k^2}\frac{dk}{I_0(k)} + \frac{1}{4\pi}\int_{\Gamma_-} \frac{\exp\left[-ik(z-\delta)\right]}{k^2}\frac{dk}{I_0(k)}, \tag{8}$$

where Γ_+ is the contour of integration along the real axis, which goes around the origin of the coordinate system from below as a narrow loop and closes it in the upper half-plane of the complex variable k by a semicircle of an infinite radius, Γ_- is a contour that consists of the real axis and closes, accordingly, in the lower half-plane (Figure 2).

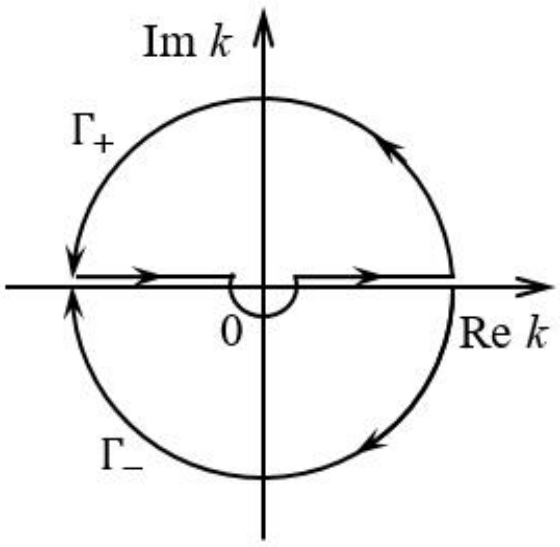

Fig.2. Integration contours on the complex plane.

Note that the contours of integration Γ_+ and Γ_-, with the exception of the vicinity of the point $k=0$, are located mirror symmetrically to each other, where the contour Γ_+ contains a second-order pole inside itself.

As the integrand is meromorphic inside the contour, the integral is equal to the sum of the residues at the poles $k = i\alpha_s$, where α_s $(s = \pm1, \pm2, ...)$ are the zeros (roots) of the zero-order modified Bessel function.

Taking into account the residue at the point $k=0$, which is a simple pole of the second order

$$\mathrm{Res}\left(\frac{\exp\left(ik|z-\delta|\right)}{I_0(k)}, k=0\right) = i|z-\delta|, \tag{9}$$

we can calculate the integral:

$$\frac{1}{4\pi}\int_{\Gamma_+} \frac{\exp\left[ik(z-\delta)\right]}{k^2 I_0(k)}dk = -\frac{1}{2}\left[|z-\delta| + \frac{1}{2}\sum_{s=1}^\infty \frac{B_s}{\alpha_s}\exp\left(-\alpha_s|z-\delta|\right)\right]. \tag{10}$$

Here

.

$$B_s = \prod_{s\neq m=1}^{\infty}\left(1-\alpha_s^2/\alpha_m^2\right)^{-1} \tag{11}$$

are the coefficients of the series, which follow from the representation of the modified Bessel function of zero order in the form of an infinite product:

$$I_0^*(ia_s) = \lim_{k\to i\alpha_s}\frac{I_0(k)}{k-i\alpha_s} = \frac{2i}{a_s B_s} = -I_0^*(-ia_s). \tag{12}$$

Similarly to (10), we calculate the integral:

$$\frac{1}{4\pi}\int_{\Gamma_-}\frac{\exp\left[-ik(z-\delta)\right]}{k^2}\frac{dk}{I_0(k)} = -\frac{1}{4}\sum_{s=1}^{\infty}\frac{B_s}{\alpha_s}\exp\left(-\alpha_s|z-\delta|\right). \tag{13}$$

Then, taking into account (9) - (12), expression (6) takes the form:

$$U_1 = \int_0^{\infty}\frac{\cos k(z-\delta)}{k^2 I_0(k)}dk = -\frac{1}{2}\pi\left[|z-\delta| + \sum_{s=1}^{\infty}\frac{B_s}{\alpha_s}\exp\left(-\alpha_s|z-\delta|\right)\right], \tag{14}$$

which is also valid for the case $z-\delta<0$.

Substituting $z-\delta\to z+\delta$ we can write (6) as

$$U_2 = -\int_0^{\infty}\frac{\cos k(z+\delta)}{k^2 I_0(k)}dk = \frac{1}{2}\pi\left[|z+\delta| + \sum_{s=1}^{\infty}\frac{B_s}{\alpha_s}\exp\left(-\alpha_s|z+\delta|\right)\right]. \tag{15}$$

Taking into account (3) and (13) - (14), we finally obtain integral (3) in the form of an exponentially convergent infinite series:

$$U(z) = -\frac{1}{4\delta}\left\{\left(|z-\delta|-|z+\delta|\right) + \sum_{s=1}^{\infty}\frac{B_s}{\alpha_s}\left[\exp\left(-\alpha_s|z-\delta|\right)-\exp\left(-\alpha_s|z+\delta|\right)\right]\right\}. \tag{16}$$

Hence, expression (3) can be written as:

$$U(z) = \frac{1}{2}\left\{\begin{pmatrix}1\\ z/\delta\\ -1\end{pmatrix} - \sum_{s=1}^{\infty}\frac{B_s}{\delta\alpha_s}\begin{bmatrix}\exp(-\alpha_s z)Sh(\alpha_s\delta), & z>\delta\\ \exp(-\alpha_s\delta)Sh(\alpha_s z), & |z|<\delta\\ -\exp(\alpha_s z)Sh(\alpha_s\delta), & z<-\delta\end{bmatrix}\right\}, \tag{17}$$

or

$$U(z) = \frac{1}{2}\begin{Bmatrix} sign(z)\left[1-\sum_{s=1}^{\infty}\frac{B_s}{\alpha_s\delta}\exp\left(-\alpha_s|z|\right)Sh(\alpha_s\delta), & |z|\geq\delta\right],\\ z/\delta - \sum_{s=1}^{\infty}\frac{B_s}{\alpha_s\delta}\exp(-\alpha_s\delta)Sh(\alpha_s z), & |z|<\delta,\end{Bmatrix}. \tag{18}$$

For $\delta\to 0$ formula (18) transforms into a well-known expression [16]:

$$U(z) = \frac{1}{2}sign(z)\left[1-\sum_{s=1}^{\infty}B_s\exp\left(-\alpha_s|z|\right)\right], \tag{19}$$

obtained in the other way from the exact expression [17]

$$U(z) = \frac{1}{\pi}\int_0^{\infty}\frac{\sin(kz)}{k}\frac{dk}{I_0(k)}, \tag{20}$$

also following from (3).

2.2. Space-time focusing conditions

The time-of-flight characteristics of the mirror, precise to the third smallest value inclusive, are completely determined by specifying four quantities that depend only on the axial distribution of the mirror potential [18]: $z = z_T^{(0)}$ – position of the effective plane of rotation of the central (with zero energy spread) particle in the mirror; $z = z_T^{(k)}$ $(k=1,2,3)$ – positions of the nodal planes of time-of-flight focusing of the k - order.

Here and below, under the condition of time-of-flight focusing of the k -th order it is assumed that the time of flight of particles does not depend on the spread of their initial energies, i.e., the coefficient of time-of-flight chromatic aberration of the k -th order is equal to zero.

The condition of time-of-flight focusing is determined by the equation [18]:

$$z_1 + z_2 = z_T^{(k)} \qquad (k = 1,2,3), \tag{21}$$

which means that time-of-flight focusing of the k -th order is achieved if the planes $z = z_1$ (object plane) and $z = z_2$ (time-of-flight image plane) are located symmetrically with respect to the plane $z = z_T^{(k)}$ $(k = 1,2,3)$.

The effective drift distance, which characterizes the time-of-flight mass dispersion of the mirror, is determined by the equality [18]:

$$L = z_T^{(0)} - z_T^{(1)}, \tag{22}$$

where $z = z_T^{(1)}$ is the position of the main plane of time-of-flight focusing of the mirror [5].

When the condition

$$z_T = z_T^{(1)} = z_T^{(2)} = z_T^{(3)} \tag{23}$$

is satisfied, in the plane $z = z_T$, time-of-flight focusing up to the third order inclusive can be achieved.

The condition for spatial focusing simultaneously with time-of-flight focusing, i.e., the condition for space-time-of-flight focusing is determined by equality [18]:

$$z_{1,2} = z_T \pm \sqrt{(z_T - z_C)(z - z_V)}, \tag{24}$$

where $z = z_C$ and $z = z_V$ are the positions of the center of curvature and the vertex of the mirror, respectively, also depending only on the axial distribution of the mirror potential [21] and representing the spatial cardinal elements of the mirror.

When $z_C = z_T$ or $z_V = z_T$ equality (4) takes the form:

$$z_1 = z_2 = z_T. \tag{25}$$

Thus, there are two types of electrostatic mirrors in which the space-time focusing condition is satisfied. However, mirrors corresponding to the type $z_C = z_T$ have higher aperture compared to the systems corresponding to the type $z_V = z_T$ [18].

2.3. Calculation of a two-electrode mirror

The calculation of an electrostatic mirror usually starts with determining the value of the blocking potential –the potential on the reflecting electrode. In a two-electrode mirror, the blocking potential is the potential at the second electrode V_2. Its value is determined from equality (1) if the condition $\Phi(z_u) = 0$ is satisfied, where $z = z_u$ is the position of the plane of rotation of the central particle.

The calculation of a two-electrode mirror is performed as follows. For the given values of the width δ of the interelectrode gap and potentials V_1 and V_2 on the mirror electrodes, which determine the axial distribution of the potential $\Phi(z)$, the position of the main plane of time-of-flight focusing $z = z_T^{(1)}$ [5] and the effective drift distance (22) of the mirror are determined when the space-time-of-flight focusing condition (24) is satisfied in the mode $z_C = z_T$. Here and below, in order to maintain the possibility of shielding the beam from scattered electric fields, the width of the interelectrode gap is limited to the value $\delta / d <= 0.2$.

The results of calculating the time-of-flight characteristics of a two-electrode mirror depending on the width δ of the interelectrode gap are presented in Table 1. Here and below, the values of electrical parameters are given in the units of the first electrode potential V_1, and the values of geometric parameters are given in the units of the cylinder diameter d. It is accepted that a beam of charged particles falls on the mirror from the side of the field-free space having the potential V_1, and after reflection returns to the same space. In this case, the positive direction of the axis z coincides with the direction of movement of the particles falling on the mirror, and the origin of coordinates is placed in the middle of the gap (Figure 1).

As it follows from the calculated data, the relative change in the values of the blocking potential and time-of-flight characteristics compared to their values at $\delta = 0$ does not exceed one percent at the gap width

.

$\delta / d \le 0.1$, whereas at the gap width $\delta / d = 0.2$ such a change is about three percent. Note that for $\delta = 0$, the results of these calculations completely coincide with the results of [5].

Table 1. Time-of-flight characteristics of a two-electrode mirror.

δ / d	$-V_2 / V_1$	$-z_T / d$	L / d
0	0.345	3.30	4.17
0.05	0.345	3.30	4.17
0.1	0.344	3.32	4.20
0.15	0.342	3.35	4.24
0.2	0.340	3.40	4.29

3. Three-electrode mirror with space-time focusing

3.1. Axial potential distribution of a three-electrode mirror

Figure 3 shows a scheme of a three-electrode mirror consisting of coaxial cylinders of equal diameter.

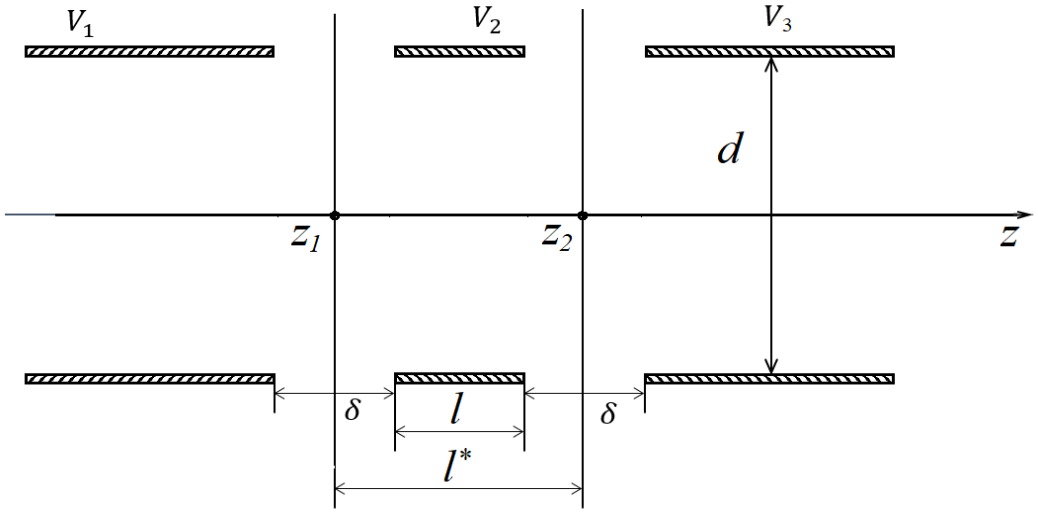

Fig.3. Three-electrode axisymmetric mirror:
V_1, V_2, V_3 are potentials on the electrodes; δ is the width of the gaps between the electrodes;
z_1, z_2 are coordinates of the middle of the gaps; d is the cylinder diameter.

Using the solution to the Dirichlet problem for two cylinders of equal diameter and the superposition principle, we can write an exact formula for the axial potential distribution of a three-electrode mirror in the form:

$$\Phi(z) = \frac{1}{2}(V_1 + V_3) + \sum_{1=1}^{2} (V_{i+1} - V_i) U(z - z_i). \tag{26}$$

Here

$$U(z - z_i) = \frac{1}{2} \left\{ \begin{array}{l} sign(z - z_i) \left[1 - \sum_{s=1}^{\infty} \frac{B_s}{\alpha_s \delta} \exp(-\alpha_s |z - z_i|) Sh(\alpha_s \delta), \quad |z - z_i| \ge \delta \right], \\ (z - z_i)/\delta - \sum_{s=1}^{\infty} \frac{B_s}{\alpha_s \delta} \exp(-\alpha_s \delta) Sh[\alpha_s (z - z_i)], \ |z - z_i| < \delta, \end{array} \right\} \tag{27}$$

where z_i $(i = 1,2)$ is z coordinate of the middle of the i-th gap.

For $\delta \to 0$ formula (27) takes the well-known form [16]:

$$U\left(z-z_i\right)=\frac{1}{2}sign(z-z_i)\left[1-\sum_{s=1}^{\infty}B_s\exp\left(-\alpha_s\left|z-z_i\right|\right)\right]. \quad (28)$$

3.2. Calculation of a three-electrode mirror

In a three-electrode mirror, compared to a two-electrode mirror, two additional parameters appear in the form of the length of the second (middle) electrode and the potential on it, which affect the distribution of the mirror potential. The introduction of a middle electrode allows, at a given potential ratio on the outer electrodes, to control the field distribution and thereby influence the quality of space-time focusing.

In a three-electrode mirror, the blocking potential is the potential on the third electrode V_3, the value of which is determined from equality (26) when the condition $\Phi\left(z_u\right)=0$ is satisfied.

The calculation of the three-electrode mirror is carried out as follows. For a given value of the gap width δ between the electrodes, the values of the control potential V_2 (potential on the second electrode), the blocking potential V_3 and the effective length of the second electrode (the distance between the middles of the first and second gaps) $l^*=l+\delta$, where l is the length of the second electrode, are determined. These parameters ensure fulfillment of the conditions for time-of-flight focusing of ions in energy up to the third order inclusive (3) simultaneously with spatial focusing (4) in the mode $z_C=z_T$.

The results of calculation of a three-electrode mirror with high-quality space-time focusing are presented in Table 2. In this case, the origin of coordinates is in the middle of the gap between the first and second electrodes of the mirror. As it follows from the calculated data, the relative change in the values of electrical parameters and time-of-flight characteristics compared to their values for $\delta=0$ is of the same order of magnitude as in a two-electrode mirror.

Table 2. Time-of-flight characteristics of a three-electrode mirror

δ/d	l^*/d	V_2/V_1	$-V_3/V_1$	$-z_T/d$	L/d
0	0.666	0.0432	0.342	5.56	7.22
0.05	0.668	0.0433	0.342	5.57	7.24
0.1	0.672	0.0439	0.342	5.60	7.28
0.15	0.680	0.0449	0.343	5.65	7.34
0.2	0.690	0.0461	0.343	5.72	7.43

4. Three-electrode mirror free of spherical and axial chromatic aberration

The calculation of the spherical and axial chromatic aberrations of the three-electrode mirror was carried out according to the formulas [19, 20]. In this case, a mirror is calculated with a second electrode length equal to $l/d=0.6$, and the object plane of the mirror is combined with its focal plane, as in [13].

The mirror was calculated using the same method as in the previous section. For a given value of the width δ of the interelectrode gap, the values of the control potential V_2 (potential on the second electrode) and the blocking potential V_3, ensuring fulfillment of the conditions for simultaneous elimination of the third-order spherical aberration and the second-order axial chromatic aberration, are determined.

The calculation results are presented in Table 3, which presents the dependences of the relative changes in the values of the cardinal elements of the mirror (focus coordinate z_F and focal length f) and the potential ratios on its electrodes (V_2 and V_3) on the width of the interelectrode gap. In this case, the calculation results are presented for the case when the object plane of the mirror is combined with its focal plane, as it was done earlier for an infinitesimal width of the interelectrode gap $\left(\delta=0\right)$ [13].

It should be noted that the width of the interelectrode gap has a significant (an order of magnitude or more) influence on the values of the electrical parameters and cardinal elements of the mirror, which is simultaneously free of spherical and axial chromatic aberrations.

For $\delta=0$ the results of these calculations completely coincide with the results of [13].

.

Table 3. Three-electrode mirror free of spherical and axial chromatic aberrations.

δ / d	V_2 / V_1	$-V_3 / V_1$	$-z_F / d$	f / d
0	0.0255	0.292	0.948	1.85
0.05	0.0258	0.294	0.982	1.88
0.1	0.0266	0.303	1.10	1.99
0.15	0.0285	0.318	1.38	2.24
0.2	0.0328	0.347	2.14	2.96

5. Conclusion

The exact formula for the axial distribution of the potential of an electrostatic system consisting of coaxial cylinders of equal diameter separated by gaps of finite width is reduced to a form convenient for numerical calculations. Using the obtained formula in numerical calculations, the influence of the width of the interelectrode gap on the quality of focusing of two- and three-electrode electrostatic mirrors with rotational symmetry, the electrodes of which are coaxial cylinders of equal diameter separated by gaps of finite width, is studied. As the results of these studies have shown, taking into account the width of the interelectrode gap allows not only to obtain more accurate values of geometric and electrical parameters that provide the conditions for high-quality space-time focusing in such mirrors, but also to provide them additional functionality, in particular, with increasing width of the interelectrode gap the effective distance of the mirror increases, which, accordingly, leads to an increase in the resolution of the time-of-flight mass spectrometer.

It should be noted that the width of the interelectrode gap has a significant impact on the values of the electrical parameters and cardinal elements of the mirror, which is free of spherical and axial chromatic aberrations simultaneously. This confirms the particular relevance of such studies from the point of view of the accuracy of calculations in the field of high-voltage electron microscopy, where the interelectrode gaps must have a width sufficient to ensure the electrostatic strength of the mirror electrodes of a real design.

The results and formulas obtained in this work can be used in the development of new designs of time-of-flight mass spectrometers and electron microscopes with high resolution and sensitivity.

Conflict of interest statement

The authors declare that they have no conflict of interest in relation to this research, whether financial, personal, authorship or otherwise, that could affect the research and its results presented in this paper.

CRediT author statement

S. Bimurzaev: Conceptualization, Methodology, Writing - original draft; **Z. Sautbekova:** Methodology, Software.
The final manuscript was read and approved by all authors.

Funding

This research has been funded by the Science Committee of the Ministry of Science and of Higher Education the Republic of Kazakhstan (Grant No. AP14869293).

Acknowledgements

The authors are grateful to Professor E.M. Yakushev for attention to this work and useful advice. They are also grateful to L.E. Strautman for her help in translating the text into English.

References

1 Mamyrin B.A. (2001) Time-of-flight mass spectrometry (concepts, achievements, and prospects). *Int. J. Mass Spectrometry*, 206 (3), 251-266. DOI: 10.1016/S1387-3806(00)00392-4.

2 Wollnik H., Casares A. (2003) An energy-isochronous multi-pass time-of-flight mass spectrometer consisting of two coaxial electrostatic mirrors. *Int. J. Mass Spectrometry*, 227 (2), 217-222. DOI: 10.1016/S1387-3806(03)00127-1.

3 Yavor M., Verentchikov A., Hasin Y., Kozlov B., Gavrik M., Trufanov A. (2008) Planar multi-reflecting time-of-flight mass analyzer with a jig-saw ion path. *Physics Procedia,* 1 (1), 391-400. DOI: 10.1016/j.phpro.2008.07.120.

4 Spivak-Lavrov I., Baisanov O., Yakushev E., Nazarenko L. (2019) TOF mass spectrometers based on a wedge-shaped electrostatic mirror with a two-dimensional field. *Rapid Communications in Mass Spectrometry***,** 34(4). DOI:10.1002/rcm.8590.

5 Bimurzaev S.B., Aldiyarov N. U., Sautbekova Z.S. (2020) High Dispersive Electrostatic Mirrors of Rotational Symmetry with the Third Order Time-of-Flight Focusing by Energy. *Technical Physics*, 65, 1150–1155. DOI:10.1134/S1063784220070051.

6 Rempfer G.F. (1990) A theoretical study of the hyperbolic electron mirror as a correcting element for spherical and chromatic aberration in electron optics. *J.Appl. Phys*., 67 (10), 6027-6040. DOI: 10.1063/1.345212.

7 Preikszas D., Rose H. (1997) Correction properties of electron mirrors. *Microscopy*, 46 (1), 1-9. DOI:10.1093/oxfordjournals.jmicro.a023484.

8 Hartel P., Preikszas D., Spehr R., Muller H., Rose H. (2002) Mirror corrector for low-voltage electron microscopes. *Adv. Imaging & Electron Phys*., 120, 41-133. DOI: 10.1016/S1076-5670(02)80034-9.

9 Hawkes P.W. (2009) Aberration correction past and present. *Phil. Trans. R. Soc.* DOI: 10.1098/rsta.2009.0004.

10 Tromp R.M., Hannon J.B., Wanb W., Berghaus A., Schaff O. (2010) A new aberration-corrected, energy-filtered LEEM/PEEM instrument. I. Principles and design. *Ultramicroscopy*, 110 (7), 852-861. DOI:10.1016/j.ultramic.2010.03.005.

11 Tromp R.M., Hannon J.B., Wanb W., Berghaus A., Schaff O. (2013) A new aberration-corrected, energy-filtered LEEM/PEEM instrument. II. Operation and results. *Ultramicroscopy*, 127, 25-39. DOI:10.1016/j.ultramic.2012.07.016.

12 Bimurzaev S.B., Aldiyarov N.U., Yakushev E.M. (2017) The objective lens of the electron microscope with correction of spherical and axial chromatic aberrations, *Microscopy*, 66 (5), 356-365. DOI: 10.1093/jmicro/dfx023.

13 Bimurzaev S.B., Serikbaeva G.S., Yakushev E.M. (2003) Electrostatic Mirror Objective with Eliminated Spherical and Axial Chromatic Aberrations. *Microscopy*, 52 (4), 365-368. DOI: 10.1093/jmicro/52.4.365.

14 Bimurzaev S.B., Yakushev E.M. (2022) Relativistic Theory of Aberrations of Electrostatic Electron-Optical Systems. *Nucl. Instr. Meth. Phys. Res. A*., 1022, 1-10. DOI: 10.1016/j.nima.2021.165956.

15 Zhu X., Munro E. (1995) Second-Order Finite Element Method and its Practical Application in Charged Particle Optics. *Journal of Microscopy*, 179(2), 172 – 180. DOI: 10.1111/j.1365-2818.1995.tb03629.x.

16 Bobykin B.V., Nevinnyi Yu.A., Yakushev E.M. (1975). Electron-optical lens as a preliminary accelerator of slow electrons in beta-spectrometry. *Zhurnal Tekhnicheskoi Fiziki*, 45, 2368–2372.

17 Gray F. Electrostatic electron-optics (1939) *Bell. Syst. Techn. Journ*., 18(1), 1-31. DOI: 10.1002/j.1538-7305.1939.tb00805.x.

18 Bimurzaev S.B., Bimurzaeva R.S., Sarkeev B.T. (1991) Spatial and time-of-flight focusing in an electrostatic lens-mirror system with two planes of symmetry. *Radiotekhnika I Elektronika*, 36, 2186–2195.

19 Yakushev E.M., Sekunova L.M. (1986) Theory of electron mirrors and cathode lenses. *Advances in Electronics and Electron Physics*, 68, 337–416. DOI: 10.1016/S0065-2539(08)60856-2.

20 Yakushev, E. M. (2013). Theory and computation of electron mirrors: The central particle method. *Advances in Imaging and Electron Physics*, *178*, 147–247. Elsevier. DOI: 10.1016/B978-0-12-407701-0.00003-0.

AUTHORS' INFORMATION

Bimurzaev, Seitkerim - Professor, Doctor of Physics and Mathematics, Chief Researcher, G. Daukeev Almaty University of Power Engineering and Telecommunication, Almaty, Kazakhstan; Scopus Author ID: 6603367014, Web of Science Researcher ID: Q-9680-2016, https://orcid.org/0000-0001-7778-1536; bimurzaev@mail.ru

Sautbekova, Zerde – PhD, Researcher, G. Daukeev Almaty University of Power Engineering and Telecommunication, Almaty, Kazakhstan; Scopus Author ID: 55946640100, https://orcid.org/0000-0001-9198-4524, zerdesautbekova@yandex.ru

.

SUMMARIES	ТҮСІНІКТЕМЕЛЕР	АННОТАЦИИ

Маханов Қ.М., Смагулов Ж.К., Бурамбаева Н.А., Асильбекова А.М., Солдатхан Д., Құттыбек А.А., Сулейменова А.К., Кеңес Т.К., Кеңесбеков С.Е., Серікова А.А., Кеңесбек Б.Ш.

Эпоксиялық шайырдағы графит бөлшектері негізіндегі радиожұтқыш материалдар.

Бұл жұмыста 78-118 ГГц өте жоғары жиілік диапазонында радиожұтқыш материалдарды зерттеу нәтижелері берілген. Кристал типті графит ұнтағы (өлшемдері 0,1 мм бөлшектер) негізгі радиожұтқыш материал болып қарастырылды. Төсеніш және байланыстырушы материал эпоксидті шайыр болып табылады. Үлгілер ұнтақты эпоксидті шайыр қоспасында араластыру арқылы дайындалды. Эпоксидті шайырдың ең тиімді жұмыс қалыңдығы эксперименттік анықталды. Сигналдың ең тиімді жазылуы байқалатын орнату компоненттерінің орналасуының геометриялық өлшемдері есептелді. Зерттеу нәтижелері эпоксидті шайырдағы графит бөлшектерінен тұратын қабыршақ 3 миллиметрлік диапазондағы радиосәулеленуді тиімді жұтатынын көрсетті.

Кілт сөздері: Радиожұтқыш материалдар, радиожиілік диапазоны, электрмагниттік толқындарды жұту, графит, аттенюатор, радиожиілік генераторы, калориметр, рупорлы антенна.

Маханов К.М., Смагулов Ж.К., Бурамбаева Н.А., Асильбекова А.М., Солдатхан Д., Куттыбек А.А., Сулейменова А.К., Кенес Т.К., Кенесбеков С.Е., Серикова А.А., Кенесбек Б.Ш.

Радиопоглощающие материалы на основе частиц графита в эпоксидной смоле.

В данной работе представлены результаты исследования радиопоглощающих материалов в сверхвысокочастотном диапазоне 78-118 ГГц. В качестве основного радиопоглощающего материала рассмотрен порошок графита кристаллического типа (частицы размером 0,1 мм). В качестве подложки и связующего использовалась эпоксидная смола. Образцы готовились путем диспергирования порошка графита по поверхности подложки из эпоксидной смолы. Экспериментальным путем установлена наиболее эффективная рабочая толщина эпоксидной смолы. Рассчитаны геометрические размеры расположения компонентов установки, при котором наблюдается наиболее эффективная регистрация сигнала. Результаты исследований показали, что пленка, состоящая из частиц графита на поверхности эпоксидной смолы эффективно поглощает радиоизлучение в 3-х миллиметровом диапазоне.

Ключевые слова: Радиопоглощающие материалы, радиочастотный диапазон, поглощение электромагнитной волны, графит, аттенюатор, генератор радиочастот, калориметр, рупорная антенна.

Дүйсембаев М.Ш., Хабиев А.Т., Рафикова Х.С., Афанасьев Д.А.

Литий-ионды аккумуляторлар мен суперконденсаторларда қолдануға арналған көміртекті материалдарға шолу.

Бұл шолу мақаласы литий-ионды аккумуляторлар мен суперконденсаторлар үшін электродтар ретінде қолданылатын көміртекті материалдарды талдауға арналған. Жұмыста материалдардың үш негізгі класы қарастырылады: белсендірілген көмір, көміртекті аэрогельдер және нанокеуекті көміртек. Мақалада екі қабатты электрхимиялық конденсаторлар, псевдоконденсаторлар және гибридті конденсаторлар сияқты конденсаторлық жүйелердің әртүрлі түрлерінің жұмыс принциптері егжей-тегжейлі сипатталған. Қарастырылып отырған көміртекті материалдардың синтез әдістеріне, құрылымдық сипаттамаларына және электрхимиялық қасиеттеріне ерекше назар аударылады. Зерттеу кеуектердің құрылымы, бет ауданы және функционалдық топтардың болуы электродтардың өнімділігіне қалай әсер ететінін қарастырады. Термиялық өңдеу және химиялық модификация процестерінің параметрлері, мысалы, температура режимі мен ұзақтығы синтезделген көміртегі құрылымдарының сипаттамаларына қалай әсер ететіні зерттелді. Материалдың әр түрінің артықшылықтары мен кемшіліктері, соның ішінде олардың меншікті сыйымдылығы, циклдің тұрақтылығы және экономикалық тиімділігі талқыланды. Жұмыс электрхимиялық қасиеттерді жақсарту үшін синтез процесін мұқият реттеу қажеттілігіне назар аударады және энергияны сақтаудың озық жүйелерінде осы материалдарды пайдалану әлеуетін ашады. Бұл шолу литий-ионды аккумуляторлар мен суперконденсаторларға арналған инновациялық материалдарды жасаумен айналысатын мамандар үшін маңызды ақпарат көзі болып табылады және электрхимиялық энергия сақтау саласындағы әрі қарайғы зерттеулердің перспективті бағыттарын көрсетеді.

Кілт сөздері: литий-ионды аккумуляторлар, суперконденсаторлар, көміртекті материалдар, белсендірілген көмір, көміртекті аэрогельдер, нанокеуекті көміртек.

Дүйсембаев М.Ш., Хабиев А.Т., Рафикова Х.С., Афанасьев Д.А.

Обзор углеродных материалов для применения в литий-ионных аккумуляторах и суперконденсаторах

Данная обзорная статья посвящена анализу углеродных материалов, используемых в качестве электродов для литий-ионных аккумуляторов и суперконденсаторов. В работе рассматриваются три основных класса

материалов: активированный уголь, углеродные аэрогели и нанопористый углерод. В статье подробно описаны принципы работы различных типов конденсаторных систем, включая двойнослойные электрохимические конденсаторы, псевдоконденсаторы и гибридные конденсаторы. Особое внимание уделяется методам синтеза, структурным характеристикам и электрохимическим свойствам рассматриваемых углеродных материалов. Исследование рассматривает, как структура пор, площадь поверхности и наличие функциональных групп влияют на производительность электродов. Было изучено, как параметры процессов термической обработки и химической модификации, такие как температурный режим и продолжительность, воздействуют на характеристики синтезируемых углеродных структур. Обсуждаются преимущества и недостатки каждого типа материала, включая их удельную емкость, стабильность при циклировании и экономическую эффективность. Работа акцентирует внимание на необходимости тщательной настройки процесса синтеза для улучшения электрохимических свойств и освещает потенциал использования данных материалов в передовых системах хранения энергии. Этот обзор представляет собой важный источник информации для специалистов, занимающихся созданием инновационных материалов для литий-ионных батарей и суперконденсаторов, и указывает на перспективные направления дальнейших исследований в области электрохимических накопителей энергии.

Ключевые слова: литий-ионные аккумулятор, суперконденсатор, углеродные материалы, активированный уголь, углеродные аэрогель, нанопористый углерод.

Тажибаев С.К., Алексеев А.М., Аймуханов А.К., Ильясов Б.Р., Бейсембеков М.Қ., Рожкова К.С., Мұсабекова, Ә.Қ., Зейниденов А.К.

Перовскиттік күн ұяшықтарының құрылымдық және электрлік қасиеттеріне Spiro-OMeTAD қабықшасы қалыңдығының әсері.

Бұл жұмыста Spiro-OMeTAD-тың кемтік тасымалдау қабатының (HTL) қалыңдығының перовскитті күн батареяларының (PSC) электрлік тасымалдау қасиеттеріне әсері зерттелді. Spiro-OMeTAD қабықшалары 2000-нан 7000 айн/мин жылдамдықпен центрифугалау әдісі арқылы алынды. Spiro-OMeTAD қабықшаларының қалыңдығы мен морфологиясы атомды-күштік микроскопия (AFM) арқылы зерттелді. AFM кескіндерінен алынған деректерге сәйкес, қабықша қалыңдығы азайған сайын бетінің орташа квадраттық ауытқуының (rms) мәні артады. Қабықша қалыңдығын азайтқанда тыйым салу аймағының (Eg) 2,97 эВ-тен 3,01 эВ-ке дейін артуына әкеледі. Қабат қалыңдығы 260 нм болғанда, күн батареяларының тиімділігі ең жоғары мәніне жететіні байқалды; қабат қалыңдығының одан әрі артуы тиімділікті төмендетеді. PSC-ның импеданс спектрлерін талдау көрсеткендей, оңтайлы қабат қалыңдығы HTL кедергісін азайтып, перовскит/HTL интерфейсіндегі рекомбинация кедергісін арттырады, бұл заряд тасымалдаушылардың тиімді өмір сүру уақытын ұлғайтады. Spiro-OMeTAD-тың перовскит қабатының беткі қабатындағы токтың таралуы және беткі құрылымы зерттелді. Үлгілердің бетінде токтың біркелкі таралмағаны анықталды, ал жоғары өткізгіштікке ие, жоғары фотоэлектрлік сипаттамалары бар аймақтар перовскит кванттық нүктелері ретінде түсіндіріледі.

Кілт сөздері: перовскитті күн ұяшықтары, кемтіктерді тасымалдау қабаты, Spiro-OMeTAD, өткізгіштік-АКМ, вольт-ампер сипаттамалары, импеданс өлшеулері.

Тажибаев С.К., Алексеев А.М., Аймуханов А.К., Ильясов Б.Р., Бейсембеков М.Қ., Рожкова К.С., Мусабекова А.К., Зейниденов А.К.

Влияние толщины пленки Spiro-OMeTADa на структурные и электрические свойства перовскитных солнечных ячеек.

В данной работе исследуется влияние толщины слоя транспортировки дырок (HTL) Spiro-OMeTAD на электрические транспортные свойства перовскитных солнечных элементов (PSC). Плёнки Spiro-OMeTAD были получены методом центрифугирования при скоростях вращения от 2000 до 7000 об/мин. Толщина и морфология плёнок Spiro-OMeTAD изучались методом атомно-силовой микроскопии (AFM). На основе данных изображений AFM было обнаружено, что с уменьшением толщины плёнки наблюдается увеличение среднего квадратичного отклонения поверхности (rms). С уменьшением толщины плёнки запрещенная зона (Eg) увеличивается с 2,97 эВ до 3,01 эВ. Было установлено, что при толщине слоя 260 нм эффективность солнечных элементов достигает максимального значения; дальнейшее увеличение толщины слоя снижает эффективность. Анализ импедансных спектров PSC показал, что оптимальная толщина слоя уменьшает сопротивление HTL и увеличивает сопротивление рекомбинации на интерфейсе перовскит/HTL, что повышает эффективное время жизни носителей заряда. Были исследованы изображения поверхности и распределения тока Spiro-OMeTAD на поверхности перовскитного слоя. Обнаружено неравномерное распределение тока на поверхности образцов; наблюдаемые области с высокой проводимостью интерпретируются как перовскитные квантовые точки, которые обладают лучшими фотоэлектрическими характеристиками.

Ключевые слова: перовскитные солнечные элементы, слой транспортировки дырок, Spiro-OMeTAD, проводящий АСМ, вольт-амперные характеристики, измерения импеданса.

Лисицын В.М., Ваганов В.А., Алпысова Г.К., Канева Е.В., Лисицына Л.А., Стрелкова А., Денисов И.П.
Вольфраммен белсендірілген барий магний фториді керамикасының радиациялық синтезі: құрылымы және оның люминесценциясы.
Жұмыста вольфраммен белсендірілген барий магний фториді жүйесінің мысалында қалыптасқан керамикаға активаторлар мен модификаторларды енгізу мүмкіндігі көрсетілген. Радиациялық синтездің бірегей қасиеттерін пайдалана отырып, жоғары синтез жылдамдығына қол жеткізілді. Вольфраммен белсендірілген магний фториді, вольфраммен белсендірілген барий фториді және вольфраммен белсендірілген барий магний фториді керамикасын қуаттылығы 15 кВт/см^2, 1,4 МэВ энергиясы бар электрондар ағынының зарядына әсер ету арқылы синтездеу мүмкіндігі көрсетілген. Рентген сәулелерінің дифракциялық спектрлері, фотоқозу және люминесценция спектрлері, импульстік катодолюминесценцияның интегралды спектрлері және оның ыдырау кинетикасы радиациялық синтез процесінде вольфрам керамиканың кристалдық торына енетінін көрсетті. Алынған вольфрам гексафторидтің ұшпа қосылыстары синтез процесі кезінде реакция аймағынан шығып үлгермейді. Синтездің тиімділігі 99% жетеді. Шихтаға вольфрам оксидін жалпы массаның 2%-ға дейінгі мөлшерінде қосу керамиканың түзілуіне әсер етпейді.
Түйінді сөздер: керамика; люминесценция; радиациямен басқарылатын синтез, рентгендік дифракциялық спектрлер, керамиканың оптикалық қасиеттері.

Лисицын В.М., Ваганов В.А., Алпысова Г.К., Канева Е.В., Лисицына Л.А., Стрелкова А., Денисов И.П.
Радиационный синтез керамики фторид бария магния, активированный вольфрамом: структура и его люминесценция.
В работе на примере системы фторид бария магния, активированный вольфрамом показано существование возможности введения в формируемую керамику активаторов, модификаторов. Используя уникальные свойства радиационного синтеза, достигнута высокая скорость синтеза. Показана возможность синтеза керамики фторид магния активированный вольфрамом, фторид бария активированный вольфрамом и фторид магния активированный вольфрамом путем воздействия на заряд потока электронов с энергией 1,4.МэВ с плотностью мощности 15 кВт/см^2. Рентгеновские дифракционные спектры, спектры фотовозбуждения и люминесценции, интегральные спектры импульсной катодолюминесценции и кинетика ее распада показали, что в процессе радиационного синтеза вольфрам входит в кристаллическую решетку керамики. Образующиеся летучие соединения гексафторида вольфрама не успевают покинуть реакционную зону в процессе синтеза. Эффективность синтеза достигает 99%. Добавление в шихту оксида вольфрама в количестве до 2 % от общей массы не влияет на образование керамики.
Ключевые слова: керамика; люминесценция, радиационно-управляемый синтез, рентгеновские дифракционные спектры, оптические свойства керамики.

Сабденов Қ. О., Ерзада М., Жолдыбаева Г.Т.
Еркін жұмыс поршені бар Стирлинг қозғалтқышында жоғары электр қуаты мен тиімділікке қол жеткізу жағдайларын модельдеу.
Стирлинг қозғалтқышының модельдеуі жүргізіліп, онда салқындатқыш пен жылытқыштағы температураның өзгергіштігі ескерілді, ал қозғалтқыштың өзі электр тогын өндіреді. Зерттеу поршень мен ығыстырғыштың синхронды қозғалысы кезінде температуралар аймағында жүргізілді. Регенератордағы гидравликалық кедергіні азайту арқылы қозғалтқыштың қуатын арттыру мүмкіндігі көрсетілді. Сонымен қатар, генераторға түсетін электрлік жүктеменің артуымен қозғалтқыш өндіретін жұмыстың да артуы мүмкін екені анықталды. Бұл жүктемеге байланысты электр энергиясын өндірудің максимумы болатынын көрсетеді. Қозғалтқыш қуаты мен оның ПӘК-ін арттыруға ығыстырғыштың серіппесінің жоғары қаттылығы ықпал етеді.
Кілт сөздер: Стирлинг қозғалтқышы, еркін жұмыс істейтін поршень, регенератор, ығыстырғыш.

Сабденов К. О., Ерзада М., Жолдыбаева Г.Т.
Моделирование условий достижения высокой электрической мощности и КПД в двигателе Стирлинга со свободным рабочим поршнем.
Проведено моделирование двигателя Стирлинга, где учитывается переменность температуры в охладителе и нагревателе, а сам двигатель вырабатывает электрический ток. Исследование проведено в области температур, когда поршень и вытеснитель двигаются синхронно. Показана возможность повышения мощности двигателя путем уменьшения гидравлического сопротивления в регенераторе. Также обнаружено, что вместе с ростом электрической нагрузки на генератор может расти и производимая двигателем работа. Это указывает на наличие максимума производства электрической энергии в зависимости от нагрузки. К росту мощности двигателя и ее КПД способствует большая жесткость пружины вытеснителя.
Ключевые слова: двигатель Стирлинга, свободный рабочий поршень, регенератор, вытеснитель.

Бацева Н.Л., Фоос Ю.А.

Энергожүйелердің режимдік параметрлерінің жағдайын телеметрия және синхрондалған векторлық өлшемдер бойынша бағалау.

Энергия жүйелерін диспетчерлік басқару нақты уақыттағы бағдарламалық кешендерден алынған нәтижелерге негізделеді. Нақты уақыттағы бағдарламалық кешендердің жағдайын бағалау модулі маңызды, себебі бұл модульден алынған режим параметрлерін бағалау нәтижелері негізінде энергия жүйелерінің тұрақтылығы мен сенімділігіне жауап беретін неғұрлым ауқымды режим параметрлері анықталады. Қазіргі уақытта режим параметрлерін бағалау үшін тек телеөлшемдер ғана емес, сонымен қатар синхрондалған векторлық өлшемдер де қолданылады, сондықтан жағдайды бағалау әдістерін дамыту өзекті мәселе болып табылады. Жағдайды бағалаудың ұсынылған әдісі жағдайды бағалау дәлдігін және диспетчерлік шешімдердің сапасын арттыруға мүмкіндік береді. Әдіс телеөлшемдер мен синхрондалған векторлық өлшемдер массивтерін бірлесіп пайдалану кезінде Гаусс-Ньютон әдісі мен кеңейтілген Калман сүзгісінің математикалық аппаратына негізделген. Эксперименттер нәтижелері бойынша жағдайды стандартты бағалау әдісімен салыстырғанда, ұсынылған әдіс қалыпты және апаттан кейінгі режимдерде сұлба түйіндеріндегі кернеуді бағалау және байланыстардағы белсенді қуат ағындарын бағалау дәлдігін арттыратыны анықталды. Әзірленген алгоритм әдісті нақты уақыттағы бағдарламалық кешендердің жағдайын бағалау модуліне енгізуге мүмкіндік береді. Энергия жүйелерінің динамикалық жұмыс режимдерінде күйді бағалау әдістерін дамытудың перспективті бағыттары анықталды.

Кілт сөздері: жағдайды бағалаудың синтезделген әдісі, Гаусс-Ньютон әдісі, кеңейтілген Калман сүзгісі, телеөлшемдер массивтері, синхрондалған векторлық өлшемдер.

Бацева Н.Л., Фоос Ю.А.

Оценивание состояния режимных параметров энергосистем по телеметрии и синхронизированным векторным измерениям.

Диспетчерское управление энергосистемами базируется на результатах, полученных из программных комплексов реального времени. Модуль оценивания состояния программных комплексов реального времени является ключевым, так как на основании результатов оценки режимных параметров, полученных из этого модуля, определяются более ёмкие режимные параметры, отвечающие за устойчивость и надёжность работы энергосистем. В настоящее время для оценивания режимных параметров применяются не только телеизмерения, но и синхронизированные векторные измерения, поэтому развитие методов оценивания состояния является актуальной задачей. Предлагаемый метод оценивания состояния позволяет повысить точность оценивания состояния и качество принимаемых диспетчерских решений. Метод базируется на математическом аппарате метода Гаусса-Ньютона и расширенном фильтре Калмана при совместном использовании массивов телеизмерений и синхронизированных векторных измерений. По результатам экспериментов установлено, что по сравнению со стандартным методом оценивания состояния, предлагаемый метод повышает точность оценивания напряжения в узлах схемы и перетоков активной мощности в связях в нормальных и послеаварийных режимах. Разработанный алгоритм позволяет внедрить метод в модуль оценивания состояния программных комплексов реального времени. Определены перспективные направления развития методов оценивания состояния в динамических режимах работы энергосистем.

Ключевые слова: синтезированный метод оценивания состояния, метод Гаусса-Ньютона, расширенный фильтр Калмана, массивы телеизмерений, синхронизированные векторные измерения.

Меликов Э.А., Магеррамова Т.М., Сафарова А.А.

Вакуумды технологиялық кешенді басқару міндеті

ЭЛОУ-АВТ типтегі қондырғының вакуумды блогында жүретін технологиялық процестерді кешенді зерттеу негізінде басқару объектісі ретінде қарастырылып отырған күрделі технологиялық кешеннің ерекшеліктеріне талдау жүргізілді. Осыған байланысты басқарылатын және кіріс параметрлерге шектеу жағдайларын ескеруімен зерттелетін блокты оңтайлы басқару есебі үшін физикалық негізделген математикалық тұжырымдама әзірленді. Қарастырылған процестің сандық және сапалық сипаттамаларының математикалық модельдері мен олардың градиенттік бейімделу алгоритмдерін ескере отырып, аталған блоктың жұмысын оңтайландыру есебін сандық шешу үшін Лагранж көбейткіштерінің классикалық әдісі қолданылады. Бұл әдіс шектеулі экстремум есебінен Лагранж функциясын құру арқылы шексіз экстремумды табу есебіне ауысуға мүмкіндік береді. Аталған әдіс, сондай-ақ ұсынылған алгоритм мен басқару принциптері алғаш рет ЭЛОУ-АВТ типтегі мұнайды алғашқы өңдеу қондырғысының зерттелетін вакуумды блогына қолданылды. Кіріс әсер етуші факторлардың саны мен сапасының кең диапазонында өзгеруі жағдайында және таңдалған мұнай өнімдерінің сапасы туралы жеткіліксіз жедел ақпарат болған кезде, зерттелетін процесті басқару алгоритмін әзірлеу әдісі мен принциптері реттеу режимдерін алдын ала жергілікті түзетуді жедел жүзеге асыруға және бейімделгіш басқарудың жаңа оңтайлы режимдерін таңдауға мүмкіндік береді. Бұл өндірістің экономикалық тиімділігін арттыруға және алынған мақсатты өнімдердің сапасының ең жоғары тұрақтылығына қол жеткізуге әкеледі.

Кілт сөздер: математикалық модель, басқару есебі, вакуумды блок, технологиялық процесс, май фракциясы

Меликов Э.А., Магеррамова Т.М., Сафарова А.А.
Задача управления вакуумным технологическим комплексом.
На основе комплексного исследования технологических процессов, протекающих в вакуумном блоке установки типа ЭЛОУ-АВТ, проанализированы особенности рассматриваемого сложного технологического комплекса как объекта управления. В связи с этим разработана физически обоснованная математическая формулировка для задачи оптимального управления исследуемым блоком с учетом ограничительных условий на управляющие и входные параметры. С учетом составленных математических моделей количественных и качественных характеристик рассматриваемого процесса и алгоритма их градиентной адаптации для численного решения задачи оптимизации функционирования данного блока используется классический метод множителей Лагранжа, позволяющий перейти от задачи условного экстремума к задаче нахождения безусловного экстремума для построенной функции Лагранжа. Данный метод, а также предложенные алгоритм и принципы управления впервые применены для вакуумного блока исследуемой установки первичной переработки нефти типа ЭЛОУ-АВТ. В условиях широкого диапазона изменения входных возмущающих факторов по количеству и качеству, а также недостаточной оперативной информации о качестве выбранных нефтепродуктов предложенный метод и принципы разработки алгоритма управления исследуемым процессом позволяют оперативно проводить предварительную локальную коррекцию режимов регулирования и подбор новых оптимальных режимов адаптивного управления в целом. Данное обстоятельство приводит к повышению экономической эффективности производства и достижению наибольшей стабильности качества получаемых целевых продуктов.
Ключевые слова: математическая модель, задача управления, вакуумный блок, технологический процесс, масляная фракция.

Бақтыбеков Қ.С., Бочкова Е.Н., Король В.В., Мурушкин М.С., Жұмажанов Б.З.
S **диапазонындағы наноспутниктік кескін деректерін қабылдау SDR жер станциясының жобалау және есептеу сипаттамалары**.
Мақалада S-диапазонында Жерді қашықтықтан зондтаудың төмен орбиталық наноспутниктері үшін ақпаратты беретін және қабылдайтын жер станциясын жобалау, құру және сынақ нәтижелері сипатталған. Шешімнің ерекшелігі - бағдарламаланатын клапан матрицаларына (FPGA) негізделген әмбебап, арзан SDR аппараттық платформаларын және AD9361 сияқты чипті қабылдағыштарды пайдалану. Ақпараттың берудің жалпы және пайдалы жылдамдығы және қажетті Eb/No қатынасы есептелген, мұндағы Eb-хабарламаның бір бит энергиясы, No- DVB-S2 MODCOD стандарттың сигналын кодтау және модуляциялау үшін пайдаланылған кезде эквивалентті шу қуатының спектрлік тығыздығының мәні.
Кілт сөздері: Жер станциясы, бағдарламалық жасақтамамен анықталған радиостанция, наноспутник.

Бактыбеков К.С., Бочкова Е.Н., Король В.В., Мурушкин М.С., Жумажанов Б.З.
Проектирование и расчетные характеристики SDR наземной станции приема данных изображения наноспутников в S-диапазоне.
В статье описаны результаты проектирования, создания и испытаний земной станции передачи и приема информации для низкоорбитальных наноспутников дистанционного зондирования Земли в S-диапазоне. Особенностью решения является использование универсальных недорогих аппаратных платформ SDR на базе программируемых вентильных матриц (FPGA) и микросхемных приемопередатчиков, таких как AD9361. Рассчитаны общая и полезная скорости передачи данных и необходимое соотношение Eb/No, где Eb – энергия одного бита сообщения, No – значение спектральной плотности мощности эквивалентного шума при использовании для кодирования и модуляции сигнала стандарт DVB-S2 MODCOD .
Ключевые слова: Земная станция, программно-определяемая радиостанция, наноспутник.

Ибраев И.К., Ибраева О.Т., Айткенов Н.Б., Сакипов К.Е.
Көмір флотациясы қалдықтарын тынық болаттан жасалған құйма бастарын оқшаулау үшін пайдалану.
Бұл жұмыста көмір флотациясы қалдықтарын тынық болаттан жасалған соғу құймаларының бас бөлігін оқшаулау үшін әлсіз экзотермиялық жылу оқшаулағыш толтырғыш ретінде пайдалану тәжірибесі ұсынылған. Зерттеу нәтижелері көмір флотациясы қалдықтарын негізіндегі бір компонентті толтырғыштарды қолдану құйманың химиялық біртектілігін айтарлықтай төмендетуге және жабық шөгу қуысының түзілуіне ықпал ететінін көрсетеді. Бұл, өз кезегінде, жылу шығынын екі есе азайтуға, шөгу борпылдақтығының құйма денесіне ену тереңдігін төмендетуге, қоспалардың ликвациясын азайтуға, құйма басының тығыздығын арттыруға және жарамды өнім шығуының жоғарылауына әкеледі. Бұдан бөлек, құйманың пайдалы бөлігі тығыз әрі металл емес қоспалармен аз ластанады. Тынық болаттан жасалған құйманың бас бөлігінде тығыз «көпірі» бар жабық шөгу қуысының түзілу заңдылықтарын зерттеу нәтижесінде, коксша ұнтақтары мен көмір флотациясы қалдықтары сияқты металлургиялық өндіріс қалдықтары негізінде әлсіз экзотермиялық жылу оқшаулағыш материалдарды қолдана отырып, жоғары сапалы ірі ұсталық құймаларын құю технологиясын әзірлеуге және енгізуге мүмкіндік берді.

Кілт сөздер: шөгу қуысы, жылу оқшаулағыш толтырғыш, құйма, тынық болат, көмір флотациясы қалдықтары, ликвация.

Ибраев И.К., Ибраева О.Т., Айткенов Н.Б., Сакипов К.Е.

Использование отходов флотации угля для утепления головной части кузовного слитка спокойной стали.

В данной работе представлен опыт использования отходов флотации угля в качестве слабоэкзотермических теплоизоляционных засыпок для утепления головной части кузнечных слитков спокойной стали. Результаты исследования демонстрируют, что применение однокомпонентных засыпок на основе отходов флотации угля способствует значительному снижению химической неоднородности слитка, что приводит к образованию закрытой усадочной раковины. Это, в свою очередь, способствует двукратному уменьшению теплопотерь, снижению глубины проникновения усадочной рыхлости в тело слитка, уменьшению ликвацию примесей, уплотнению головной части слитка и повышению выхода годного продукта. Кроме того, прибыльная часть слитка становится более плотной и менее загрязненной неметаллическими включениями. Изучение закономерностей формирования закрытой усадочной раковины с плотным «мостом» в головной части слитка спокойной стали позволило разработать и внедрить технологию разливки крупных кузнечных слитков высокого качества с использованием слабоэкзотермических теплоизоляционных материалов на основе отходов металлургического производства, таких как отсевы коксика и отходы флотации угля.

Ключевые слова - усадочная раковина, теплоизолирующая засыпка, слиток, спокойная сталь, отходы флотации угля, ликвация.

Расулов З.Н., Олехвер А.И., Ремшев Е.Ю., Войнаш С.А., Ворначева И.В., Соколова В.А., Маликов В.Н.

Әртүрлі мақсаттағы қуыс осьсимметриялық бөлшектердің қабырғасын жұқарту арқылы созу технологиялық процестерін жобалау кезіндегі модельдеу.

Күрделі жүктеме жағдайында жұмыс істейтін бірқатар бұйымдар бар, оларды дәстүрлі штамптау операцияларымен дайындау қажетті қасиеттерді қамтамасыз етуге мүмкіндік бермейді, бұл ақаулардың көп мөлшеріне әкеледі. Жоғары беріктікке ие бұйымдарды дайындаудың мүмкін бағыттарының бірі - технологиялық процеске қарқынды пластикалық деформация әдістерін енгізу, ол көлемді (тең арналы бұрыштық престеу, айнымалы қима арнасы арқылы бойлық сығымдау, ішкі контур бойынша қабырғаны жұқарту арқылы созу) және беттік (тесіктерді дорндау, роликтермен немесе шарлармен айналдыру) болуы мүмкін. Жуықталған монотондылық критерийін қолдану техникасы, оның қабырғаны жұқарту арқылы созу мысалында технологиялық параметрлермен байланысы көрсетілген. Процестің жуықталған монотондылығын қамтамасыз ететін жұқарту арқылы созудың технологиялық параметрлерін (үйкеліс жағдайлары мен деформация дәрежесін) таңдау мысалы келтірілген. Нәтижелер, атап айтқанда, «деформация ─ кернеу» қисығын негізді түрде таңдауға мүмкіндік береді.

Кілт сөздер: технологиялық процесс, қабырғаны жұқарту арқылы созу, қарқынды пластикалық деформация, жуықталған монотондылық критерийі, кернеулі-деформацияланған күй.

Расулов З.Н., Олехвер А.И., Ремшев Е.Ю., Войнаш С.А., Ворначева И.В., Соколова В.А., Маликов В.Н.

Моделирование при проектировании технологических процессов вытяжки с утонением стенки полых осесимметричных деталей различного назначения.

Существует целый ряд изделий, работающих в крайне тяжелых условиях сложного нагружения, изготовление которых традиционными штамповочными операциями не позволяет обеспечить требуемые свойства, что приводит к большому количеству брака. Одним из возможных направлений для изготовления изделий повышенной прочности является внедрение в технологический процесс способов интенсивной пластической деформации, которая может быть, как объемной (равноканальное угловое прессование, продольное выдавливание через канал переменного сечения, вытяжка с утонением стенки по внутреннему контуру), так и поверхностной (дорнование отверстий, обкатка роликами или шариками). Показана техника применения критерия приближенной монотонности, его связь с технологическими параметрами на примере вытяжки с утонением стенки. Приведен пример подбора технологических параметров (условий трения и степени деформации) вытяжки с утонением, обеспечивающих приближенную монотонность процесса. Результаты позволяют, в частности, обоснованно выбирать кривую «деформация ─ напряжение».

Ключевые слова: Технологический процесс, вытяжка с утонением стенки, интенсивная пластическая деформация, критерий приближенной монотонности, напряженно-деформированное состояние.

Нусупбеков Б. Р., Ошанов Е. З., Овчаров М. С., Қоңырбаева А.

Дроссель саңылаулары арқылы сығылған кезде сұйықтықтың ағыны мен температурасын анықтау.

Мақалада сұйықтықтарды дроссель саңылаулары арқылы итеру кезінде жасалған стендтегі зертханалық зерттеулердің нәтижелері келтірілген. Дроссель саңылаулары арқылы сұйықтық ағыны саңылау диаметрі, саңылау алдындағы сұйықтық қысымы, сұйықтықтың тұтқырлығы, саңылау алдындағы арнаның ұзындығы мен пішіні сияқты бірнеше факторларға байланысты екені белгілі. Дроссельдік саңылауы арқылы итеру кезінде

қысымның төмендеуі және сұйықтықтың қозғалу жылдамдығының жоғарылауы байқалады. Бұл оның кинетикалық энергиясының жоғарылауына әкеледі, содан кейін сұйықтық молекулалары арасындағы үйкеліске байланысты жылу энергиясына айналады. Осылайша, сұйықтықты дроссельдеу кезінде оның температурасы көтеріледі. Бұл принципті жылыту жүйелері, өндірістік процестер немесе зертханалық зерттеулер сияқты әртүрлі жүйелердегі әртүрлі сұйықтықтарды жылыту үшін пайдалануға болады.
Кілт сөздері: сұйықтық ағыны, дроссель саңылаулары, гидравликалық тазарту жүйелері, жылу энергиясын түрлендіру.

Нусупбеков Б.Р., Ошанов Е.З., Овчаров М.С., Қоңырбаева А.
Определение расхода и температуры жидкости при ее продавливании через дроссельные отверстия.
В статье приведены результаты лабораторныхх исследований на разработанном стенде при продавливании жидкостей через дроссельные отверстия. Известно, что расход жидкости через дроссельные отверстия зависит от нескольких факторов, таких как диаметр отверстия, давление жидкости перед отверстием, вязкость жидкости, длина и форма канала перед отверстием. При продавливании через дроссельное отверстие, происходит снижение давления и увеличение скорости движения жидкости. Это приводит к повышению ее кинетической энергии, которая затем преобразуется в тепловую энергию из-за трения между молекулами жидкости. Таким образом, при дросселировании жидкости происходит повышение ее температуры. Этот принцип может быть использован для нагрева различных жидкостей в различных системах, таких как системы отопления, промышленные процессы или лабораторные исследования.
Ключевые слова: расход жидкости, дроссельные отверстия, гидравлические системы очистки, преобразование тепловой энергии.

Inyang E.P., Nwachukwu I. M., Ekechukwu C.C., Ekong I.B., William E.S., Lawal K.M. , Simon J., Momoh K.O., Oyelami O.A.
Кері квадраты Юкава потенциалы класының аналитикалық шешімі және оның кванттық-механикалық жүйелерге қолданылуы.
Бұл зерттеуде радиалды Шредингер теңдеуін аналитикалық шешу үшін нақты кванттау ережесі қолданылды, атап айтқанда, кері квадраты Юкава потенциалы класына жүгінілді. Бұл әдіс арқылы ауыр мезондардың, соның ішінде чармоний мен боттомонийдің, энергияның меншікті мәндерін пайдалана отырып, кванттық күйлер ауқымындағы массалық спектрлері сәтті болжанды. Эксперименттік деректермен және басқа зерттеушілердің нәтижелерімен салыстырғанда, бұл модель ең жоғары қателік 0.0065 ГэВ бола отырып, тамаша дәлдік көрсетті.
Потенциал моделі есептеулерді жеделдету және математикалық дәлдікке қол жеткізу үшін белгілі шекаралық шарттарды қолдана отырып, Кратцер потенциалына келтірілді. Алынған энергиялық спектрді пайдалана отырып, бұл зерттеу азот (N_2) және сутегі (H_2) сияқты гомоядролы екі атомды молекулалардың энергия спектрлерін зерттеу үшін кеңейтілді. Зерттеудің бір маңызды жаңалығы - негізгі квант саны тұрақты болған кезде, бұрыштық моменттің квант саны артқан сайын энергия спектрдің төмендейтіні анықталды. Сол сияқты, бұрыштық момент квант санының өзгеруі кезінде энергия спектрі жүйелі түрде азаяды. Электронның кинетикалық және потенциалдық энергиялары арасындағы күрделі өзара әрекет бұл төмендеу үрдісін тудырады, әсіресе бұрыштық момент квант санының артуы кезінде екі атомды молекулада. Электрон орбитасының ұзаруы және ядродан қашықтығының артуы энергия балансын ығыстырып, бұл энергиялардың арасындағы тепе-теңдікті өзгертеді, нәтижесінде энергия спектрінің жүйелі түрде төмендеуіне әкеледі.
Кілт сөздер: Шредингер теңдеуі; квантталудың нақты ережесі; гомоядролы екі атомды молекулалар; ауыр мезондар; Юкаваның кері квадрат потенциалының класы.

Inyang E.P., Nwachukwu I. M., Ekechukwu C.C., Ekong I.B., William E.S., Lawal K.M. , Simon J., Momoh K.O., Oyelami O.A.
Аналитическое решение класса обратно квадратичного потенциала Юкавы с применением к квантово-механическим системам.
В данном исследовании применен подход точного правила квантования для аналитического решения радиального уравнения Шредингера, в частности, обращаясь к классу обратно квадратичного потенциала Юкавы. С помощью этого метода успешно предсказаны массовые спектры тяжелых мезонов, включая чармоний и боттомоний, в диапазоне квантовых состояний, используя собственные значения энергии. По сравнению с экспериментальными данными и выводами других исследователей данная модель показала замечательную степень точности с максимальной ошибкой 0.0065 ГэВ. Потенциальную модель сведена к потенциалу Кратцера, чтобы еще больше ускорить наши вычисления, и обеспечить математическую точность, наложив определенные граничные условия. Используя полученный энергетический спектр, данное исследование расширено, чтобы изучить энергетические спектры гомоядерных двухатомных молекул, таких как азот (N_2) и водород (H_2). Одним из замечательных открытий было то, что энергетический спектр уменьшался по мере увеличения квантового числа углового момента в случае, когда главное квантовое число оставалось фиксированным. Аналогичным образом энергетический спектр последовательно уменьшается при

изменении квантового числа углового момента. Сложное взаимодействие между кинетической и потенциальной энергиями электрона вызывает эту тенденцию к уменьшению в энергетическом спектре по мере увеличения квантового числа углового момента в двухатомной молекуле. Энергетический спектр систематически уменьшается по мере удлинения орбиты электрона и увеличения его расстояния от ядра, смещая баланс между этими энергиями.

Ключевые слова: уравнение Шредингера; точное правило квантования; гомоядерные двухатомные молекулы; тяжелые мезоны; класс обратно квадратичных потенциалов Юкавы.

Тоқтарбайұлы О., Байсариев М., Қайша А., Дуйсебаев Т.С., Ибраев Н.Х., Сериков Т.М., Ибраимов М.К., Ханиев Б.А., Тезекбай Е.Ж., Жамбыл А.Н., Нураже Н., Сугурбекова Г.К.

Ыстық қабырғалы газ фазасынан химиялық тұндыру пешінде синтезделген GaN жартылай өткізгіш материалын пайдалану арқылы бояғышқа сезімтал күн батареяларындағы энергияны түрлендіру тиімділігін арттыру.

Бұл зерттеуде сапфир және кремний төсеніштерінде плазманың көмегімен бу фазасынан химиялық тұндыру әдісімен келесі белгілі параметрлерін, яғни, шығыс кернеуі 150 Вт, N_2 газ ағынының жылдамдығы минутына 60 стандарт текше сантиметр, камера қысымы 2,48 сынап бағанасы миллиметрі және синтез уақыты 2 сағат GaN синтездеу нәтижелері талқыланды. Сканерлеуші электронды микроскоп (СЭМ), жарықтың комбинациялық шашырауы және энергия дисперсиялық рентген сәулелері әдістерімен алынған сипаттамалар GaN-нің стехиометриялық емес құрылымын және құрамында айқын Ga элементінің басымдылығын көрсетті. Төсеніш бетінің морфологиясын СЭМ-талдау арқылы бу фазасынан химиялық тұндыру процесінің алғашқы кезеңі болып табылатын шағын аралдардың бар екендігі айқындалды. Жұмыста, сондай-ақ, бояғышқа сезімтал күн элементтерінің фотоанодына GaN қосу әсерлері зерттелді. Зерттеу барысында TiO_2 матрицасында GaN ұнтағының оңтайлы мөлшері көрсетілді. Алғашқы эксперименттерде коммерциялық GaN ұнтағы қолданылып, массалық пайызбен оңтайлы құрам анықталды. Зерттеу үшін төрт түрлі массалық пайыз таңдалды: 10 %, 20 %, 30 % және 40 %. Олардың арасында 20 % GaN ең жоғары энергияны түрлендіру тиімділігіне ие болды – 0,75%. Толықтық коэффициентінің мәндері GaN массалық үлесі артқан сайын төмендеу тенденциясын көрсетті.

Кілт сөздері: қуатты түрлендіру, жартылай өткізгіш, матрица,TiO_2, GaN.

Тоқтарбайұлы О., Байсариев М., Қайша А., Дуйсебаев Т.С., Ибраев Н.Х., Сериков Т.М., Ибраимов М.К., Ханиев Б.А., Тезекбай Е.Ж., Жамбыл А.Н., Нураже Н., Сугурбекова Г.К.

Повышение эффективности преобразования энергии в солнечных элементах, чувствительных к красителям, за счет использования полупроводникового материала GaN, синтезированного в печи химического осаждения из газовой фазы с горячими стенками.

В этом исследовании обсуждаются результаты синтеза GaN методом химического осаждения из газовой фазы с использованием плазмы на сапфировых и кремниевых подложках с использованием определенных параметров: прямое выходное напряжение 150 Вт, расход газа N_2 60 стандартных кубических сантиметров в минуту, давление в камере 2,48 мм рт.ст. и время синтеза 2 часа. Определение характеристик с помощью сканирующего электронного микроскопа (СЭМ), комбинационного рассеяния света и энергодисперсионного рентгеновского излучения выявило нестехиометрическое образование GaN с явным преобладанием Ga в составе. СЭМ-анализ морфологии поверхности подложки выявил наличие небольших островков, которые считаются первым этапом процесса химического осаждения из газовой фазы. В исследовании также изучены эффекты включения GaN в фотоанод солнечных элементов, чувствительных к красителю. В ходе исследования было определено оптимальное количество порошка GaN в матрице TiO_2. В первоначальных экспериментах использовался коммерческий порошок GaN для определения оптимального процентного содержания по массе. Для исследования были выбраны четыре различных весовых процента (мас.%) GaN: 10 %, 20 %, 30 % и 40 %. Среди них GaN с 20 % имел самую высокую эффективность преобразования энергии - 0,75%. Значения коэффициента заполнения имели тенденцию к снижению по мере увеличения массовой доли GaN.

Ключевые слова: преобразование мощности, полупроводник, матрица, TiO_2, GaN.

Шугаева Т.Ж., Спивак-Лавров И.Ф., Сейтен А.Б., Трубицын А.А.

Өткізгіш дөңгелек цилиндр негізінде электрстатикалық мультиполь жүйелерінің потенциалын аналитикалық сипаттау.

Дәл физикалық және математикалық теорияларға негізделген және жақсартылған аналитикалық мүмкіндіктері бар құрылғыларды жобалауға және есептеуге мүмкіндік беретін есептеу технологияларының мүмкіндіктерін пайдаланатын масс-спектрометрлердің физикалық және аспаптық сипаттамаларын есептеу әдістерін әзірлеу корпускулалық оптика мен ғылыми аспап жасаудың өзекті есебі болып табылады. Жұмыста өткізгіш дөңгелек цилиндр негізінде мультипольдік жүйелердің электрстатикалық өрісін есептеу әдісі ұсынылды. Әдіс күрделі айнымалы функциялар теориясының әдістерін қолдануға негізделген. Электродтар арасындағы шексіз тар

саңылаулар үшін квадруполь өрісінің электрстатикалық потенциалы үшін аналитикалық өрнектер табылды. Потенциал туындылары үшін аналитикалық өрнектер алынды. Электродтар арасындағы саңылаулардың шекті шамасының өріс конфигурациясына әсерін зерттеу жүргізілді. Ол үшін шекаралық элементтер әдісімен Лаплас теңдеуін қанағаттандыратын жазықтық электр өрістерін сандық модельдеу орындалды. Өрістің электрстатикалық потенциалын есептеу екі кезеңде жүргізілді. Алдымен белгілі шекаралық потенциалды бөлу бойынша шекарадағы зарядтың таралуы есептелді, яғни «кері» есеп шешілді. Содан кейін табылған зарядты бөлу мәндерін және берілген потенциал мәндерін қолдана отырып, «тікелей» есеп шешілді. Бұл есепті шешу үшін түзу сызықты шекаралары бар электронды-оптикалық жүйелер (ЭОЖ) үшін өрісті модельдеудің жоғары дәлдігін қамтамасыз ететін сингулярлық және квазисингулярлық ядролары бар интегралдық теңдеулерді шешу әдісі жасалды. Есептеу қатесі тек дөңгелектеу қателіктерімен анықталады. Қисық сызықты шекаралары бар электронды-оптикалық жүйелер үшін ол электронды-оптикалық жүйелердің шекараларын түзу сызық сегменттерімен жуықтау дәлдігімен анықталады. Электронды-оптикалық жүйені құрайтын екінші ретті геометриялық қисықтарды бөлу кезінде олар бұрыштық шамасы бір градусқа дейінгі доғаларға бөлінеді.
Кілт сөздері: көпполюсті жүйе, потенциал, өткізгіш дөңгелек цилиндр, эквипотенциалдық сызықтар, антирезонанс жүйесі.

Шугаева Т.Ж., Спивак-Лавров И.Ф., Сейтен А.Б., Трубицын А.А.

Аналитическое описание потенциала электростатических мультипольных систем на основе проводящего кругового цилиндра.

Разработка методов расчета физических и приборных характеристик масс-спектрометров, основанных на корректных физических и математических теориях и использующих возросших возможности вычислительных технологий, которые позволяют проектировать и рассчитывать приборы с улучшенными аналитическими возможностями, является актуальной задачей корпускулярной оптики и научного приборостроения.
В работе разработан метод расчета электростатического поля мультипольных систем на основе проводящего кругового цилиндра. Метод основан на использовании методов теории функций комплексной переменной (ТФКП). Найдены аналитические выражения для электростатического потенциала поля квадрупольной системы для случая бесконечно узких зазоров между электродами. Получены аналитические выражения для производных потенциала. Проведено исследование влияния конечной величины зазоров между электродами на конфигурацию поля. Для этого выполненно численное моделирования планарных электрических полей, удовлетворяющих уравнению Лапласа, методом граничных элементов. Вычисление электростатического потенциала поля проводилось в два этапа. Сначала рассчитывалось распределение заряда на границе по известному граничному распределению потенциала, то есть решалась «обратная» задача. Затем с использованием найденных значений распределения заряда и заданных значений потенциала решалась «прямая» задача. Для решения этой задачи был разработан метод решения интегральных уравнений с сингулярными и квазисингулярными ядрами обеспечивающий высокую точность моделирования поля: для электронно-оптических систем (ЭОС) с прямолинейными границами. Ошибка вычисления определяется лишь ошибками округления. Для электронно-оптических систем с криволинейными границами, она определяется точностью аппроксимации границы электронно-оптических систем отрезками прямых линий. При разбиении геометрических кривых второго порядка, образующих электронно оптическую систему, они разбиваются на дуги с угловой величиной до одного градуса.
Ключевые слова: многополюсная система, потенциал, проводящий круговой цилиндр, эквипотенциальные линии, антирезонансная система.

Бимурзаев С.Б, Сауытбекова З.С.

Айналмалы симметриялы электрстатикалық айналардың тоғыстау сапасына электрод-аралық саңылау енінің әсері.

Электродтары ені шекті саңылаулармен бөлінген диаметрлері бірдей коаксиалды цилиндрлер болып табылатын айналмалы симметриялы электрстатикалық айналардың тоғыстау сапасына электрод-аралық саңылау енінің әсері зерттелді. Мұндай айналардағы осьтік потенциал таралуының мәндерін дәл сандық есептеуге ыңғайлы формулалар ұсынылған. Алынған формулалар негізінде, электрод-аралық саңылау енін ескере отырып, сандық есептеулер арқылы зарядталған бөлшектер шоғының кеңістіктік тоғысталуымен ұшу-уақыттық хроматикалық аберрацияларды, сфералық және осьтік хроматикалық кеңістіктік аберрацияларды жоюды бір мезгілде қамтамасыз ететін екі және үш электродты айналардың геометриялық және электрлік параметрлері анықталды. Бұл аберрациялар сәйкесінше ұшу-уақыттық масс-спектрометрлердің және электрондық микроскоптардың ажырату қабілетіне әсер ету тұрғысынан ең маңыздылары болып табылады. Цилиндрлік электродты электрстатикалық айналардың тоғыстау сапасына электрод-аралық саңылау енінің айтарлықтай әсер ететіні көрсетілген.
Кілт сөздері: ұшу уақыттық масс-спектрометр, электрондық микроскоп, электрстатикалық айна, кеңістіктік-уақыттық тоғыстау, сфералық аберрация, осьтік хроматикалық аберрация.

Бимурзаев С.Б, Сауытбекова З.С.

Влияние ширины межэлектродного зазора на качество фокусировки электростатических зеркал с вращательной симметрией.

Исследовано влияние ширины межэлектродного зазора на качество фокусировки электростатических зеркал с вращательной симметрией, электродами которых служат соосные цилиндры равного диаметра, разделенные зазорами конечной ширины. Предложены формулы, удобные для численного расчета точных значений осевого распределения потенциала в таких зеркалах. На основании полученных формул путем численных расчетов определены геометрические и электрические параметры двух- и трех-электродных зеркал при учете ширины межэлектродного зазора, обеспечивающие пространственную фокусировку пучков заряженных частиц одновременно с устранением времяпролетных хроматических аберраций и сферической и осевой хроматической пространственных аберраций, наиболее важных с точки зрения влияния на разрешающую способность времяпролетных масс-спектрометров и электронных микроскопов соответственно. Показано, что ширина межэлектродного зазора оказывает значительное влияние на качество фокусировки электростатических зеркал с цилиндрическими электродами.

Ключевые слова: времяпролетный масс-спектрометр, электронный микроскоп, электростатическое зеркало, пространственно-времяпролетная фокусировка, сферическая аберрация, осевая хроматическая аберрация.